This is to certify that the
dissertation entitled

REACTIVE EUTECTIC BRAZING OF NITINOL

presented by

KE-BIN LOW

has been accepted towards fulfillment
of the requirements for the

Ph.D. degree in MATERIALS SCIENCE AND ENGINEERING

Major Professor's Signature

APRIL 27, 2009

Date

REACTIVE EUTECTIC BRAZING OF NITINOL

By

Ke-Bin Low

A DISSERTATION

Submitted to
Michigan State University
in partial fulfillment of the requirements
for the degree of

DOCTOR OF PHILOSOPHY

Materials Science and Engineering

2009

ABSTRACT

REACTIVE EUTECTIC BRAZING OF NITINOL

By

Ke-Bin Low

Although NiTiNb alloys are well known as wide-hysteresis shape-memory alloys with important applications as coupling materials, the significance of one aspect of the Ni-Ti-Nb ternary system has not been fully appreciated. Based on the existence of a quasibinary NiTi-Nb eutectic isopleth in this ternary system, a novel braze method has been devised to fabricate metallurgical bonds between functional nitinol (NiTi) sections. When NiTi and pure Nb are brought into contact at temperatures above 1170 °C, spontaneous melting occurs, forming a liquid that is extremely reactive and not only wets NiTi surfaces, but also apparently dissolves oxide scales, obviating the need for fluxes and providing for efficient capillary flow into joint crevices. The melting process is diffusion-controlled and rate-limited by the diffusivity of Nb in the liquid. The braze liquid will subsequently solidify into microstructures containing predominantly ordered NiTi and disordered bcc-Nb. Mechanical tests revealed that the braze joints are strong, ductile, and biocompatible. With appropriate post-braze aging, the functional performance of the parent NiTi alloy can be restored. Micro-alloying the Nb filler metal with Zr or tungsten showed great potential for solution-strengthening of the braze joints. For applications where biocompatibility is not an issue, Nb metal can be substituted by pure vanadium as the braze filler, which is demonstrated to possess tensile strengths that can be potentially superior to the Nb counterparts.

This dissertation is dedicated

to my dear wife, Ting

and to my beloved daughter, Sophie

ACKNOWLEDGEMENTS

I would like to thank my academic advisor/PhD committee chairman, Professor David S. Grummon, for his guidance in not just research, but also in teaching. Professor Grummon has taught me how to think out-of-the-box and has given me a lot of opportunities to develop my interpersonal and leadership skills through teaching and public-speaking at professional conferences. He is both a great mentor and a great friend. I would also wish to express my gratitude towards Nitinol Devices and Components for supplying the materials and generously funding the brazing project. I am also grateful towards my PhD committee members, Professor Martin A. Crimp, Associate Professor Thomas R. Bieler, from the Department of Chemical Engineering and Materials Science, and Associate Professor Farhang Pourboghrat, from the Department of Mechanical Engineering, for giving valuable comments and suggestions during my comprehensive examination. I am also grateful towards Dr. Xudong Fan, from the Center for Advanced Microscopy, for the scientific discussions on specimen preparations and transmission electron microscopy. His knowledge and experience in this field has helped contribute significantly towards the success of this dissertation. Lastly, I would like to thank my colleagues, Xueling Fei, Jason W. Carter and John W. Foltz for all the help and laughter in the laboratory. Without them, a lot of work will not be accomplished.

PREFACE

The shape-memory/superelastic properties and excellent biocompatibility of nitinol (NiTi) have made it an ideal candidate material for biomedical, aerospace and micro-actuation applications. Many of these applications require nitinol to function in tandem with another nitinol component or with dissimilar alloy systems. For example, the nitinol core of a surgical guidewire has to be bonded to a platinum-tungsten alloy outer coil for proper function; radio-opaque markers, such as tantalum, has to be attached to nitinol stents reliably in order to improve radio-opacity; porous nitinol needs to be bonded onto monolithic nitinol bone implant surfaces to improve osteo-conductivity.

However, joining nitinol to itself or to dissimilar alloy systems is very difficult due to wettability issues and strong tendency for brittle intermetallics and oxides to form within the joint. Many joining techniques, such as tungsten-inert gas (TIG), laser, resistance welding under Ar or He environments and soldering, have been explored. These methods have not gained significant popularity, either due to the need for aggressive fluxes, poor wetting, or reproducibility issues. In addition, most filler materials for brazing or soldering are not biocompatible and hence cannot be employed in biomedical applications.

Recently, a reactive eutectic braze method has been successfully devised for joining separate nitinol components. It relies on the existence of a quasi-binary NiTi-Nb

eutectic isopleth in the ternary system. The joining process involves vacuum brazing using pure Nb as the filler material. Preliminary work shows that brazing occurs promptly above 1170°C; and upon cooling, the joints solidify mainly into a pro-eutectic phase based on NiTi, and eutectic microstructure consisting of Nb plates or rods in a NiTi matrix. Nitinol butt-joints, mechanically-tested in tension, strongly suggests that the brazed joints are strong and ductile as long as braze duration does not extend beyond a few minutes. With appropriate post-braze annealing, the NiTi base-alloy is still capable of exhibiting shape-memory and transformational superelasticity.

This joining method demonstrates definitive potential for cost-effective industrial applications because (1) the braze process does not destroy the shape-memory or transformational superelastic properties of the base-alloy; (2) joints made by this process have excellent mechanical strength and toughness; (3) the braze filler metal is biocompatible, allowing the joining approach to be extended to medical device applications. But to fully realize its potential, process optimization is of paramount importance, which can only be achieved through thorough understanding of the relevant phase equilibria, contact melting, and factors influencing the microstructure of the solidified braze.

It is commonly known that metallurgical joining of Ti-based alloys tend to yield brittle intermetallic compounds that have detrimental effects on the mechanical performance of the joints. Besides mechanical and microstructural aspects, understanding the driving force for contact melting between NiTi and Nb during braze

processing, the melting kinetics and isothermal solidification are also of critical importance for optimizing braze parameters. For example, the knowledge of the melting kinetics will allow one to predict, based on simulations, the braze duration required for complete dissolution of various thicknesses of the Nb filler metal.

The objectives of this research are: (1) to address the thermodynamic and kinetic aspects of contact melting between NiTi and Nb during braze processing; (2) to study contact melting kinetics and microstructural evolution of the joints as a function of braze time; (3) to investigate the effects of post-braze thermal processing on mechanical properties of the braze joints and base-alloys; and (4) to explore micro-alloying of braze joints for possible improvements in mechanical performance.

The dissertation is organized into 6 chapters. Chapter 1 provides background and literature review on phase equilibria, physical metallurgy, and joining of NiTi. In addition, some theories on ternary phase equilibria, brazing, liquid phase diffusion, and alloy solidification are introduced. Chapter 2 documents the methodologies associated with the experimental and numerical work. Chapter 3 presents results on the kinetic studies of contact melting and numerical simulations of this process. Solidification products from brazing, and the evolution of microstructures as a function of time and temperature are discussed. Chapter 3 also provides a qualitative analysis of the phase field evolution in the Ni-Ti-Nb system that is based on current experimental findings. Chapter 4 focuses on the mechanical properties of NiTi braze joints. Results were derived from nanoindentation and tensile experiments. The effects of post-braze heat

treatments on mechanical properties of these joints, and preliminary attempts to join NiTi to Ta and alumina, are also discussed. Chapter 5 presents results of indentation and tensile experiments on braze joints alloyed with Zr and tungsten. In addition, vanadium was explored as an alternative braze filler metal and as a possible alloying element for Nb. The microstructure, phase equilibria and mechanical properties of pure V-based joints and V-alloyed joints will be discussed in this chapter. Finally, Chapter 6 provides concluding remarks for the dissertation and lists possible future work pertaining to the reactive eutectic braze process.

TABLE OF CONTENTS

LIST OF TABLES

LIST OF FIGURES

CHAPTER 1: BACKGROUND AND LITERATURE REVIEW

1.1 Introduction

In this chapter, the NiTi system will be reviewed with emphasis being placed on its transformation properties, mechanical properties, phase equilibria, composition variations, thermo-mechanical treatments and ternary alloying possibilities. Problems and recent development associated with joining NiTi components will also be reviewed. A brief overview of the principles of brazing, transient liquid phase bonding, liquid-phase diffusion, and principles of ternary phase equilibria are also provided.

1.2 The NiTi System

Nickel-titanium is an ordered intermetallic compound. It was discovered by the Naval Ordnance Laboratory in the 1960s to exhibit shape-memory effect, where a deformed or strained body is able to revert to its pre-programmed geometry and dimension upon exposure to a thermal stimulus. Given its discovery by the Naval Ordnance Laboratory, NiTi is also commonly referred to as NiTi-NOL or nitinol.

1.2.1 Transformation Properties

At elevated temperature, NiTi exists in the form of an ordered cubic *B2* (CsCl – type) superlattice, which is commonly known as the 'austenite' phase. It has a superlattice parameter of 0.3015 nm [Plietsch et al. 1997]. However, as temperature decreases below the martensite start temperature, M_S, the austenite phase begins to transform into martensite phase, which has a *B19'* monoclinic crystal structure. The

martensite transformation proceeds as temperature decreases. At M_f, which is the martensite finish temperature, all *B2* phase become fully transformed into the *B19'* phase. Such transformation is athermal, diffusionless and does not involve significant change in overall volume in NiTi. Similarly, the martensite phase will begin to transform back into the austenite phase when temperature increases beyond the austenite start temperature, A_S. The transformation will only be complete beyond the austenite finish temperature, A_f. It is important to highlight that phase transformation in NiTi does not always involve a direct *B2*-to-*B19'* pathway. In some cases, *R*-phase transformation may occur preceding the *B19'* transformation in thermomechanically-treated NiTi alloys [Miyazaki et al. 1982, 1986]. As the properties of *R*-phase and the mechanism of transformation are beyond the scope of this dissertation work, they will not be reviewed. It is the intrinsic nature of shape-memory alloys to exhibit thermal hysteresis in martensite-austenite phase transformations. Specifically, M_S (M_f) is lower than M_f (A_S) and the width of the hysteresis loop is typically about 30°C for NiTi. The hysteretic behavior of shape-memory alloy is shown in Figure 1.1. Note that it is possible for M_S to be lower than A_S.

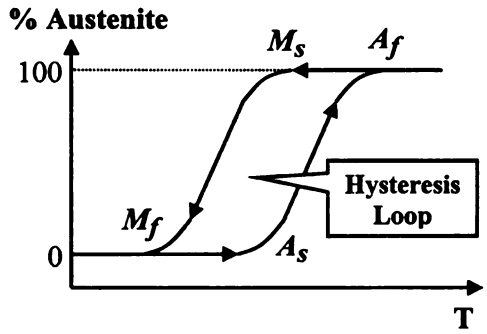

Figure 1.1 Hysteresis loop involved during Martensite-Austenite transformation with M_S, M_f, A_S and A_f indicated.

Given the lower symmetry of the *B19'* structure, it may first be expected that the austenite to martensite transformation will result in volume or shape changes. However, based on the Wechsler-Lieberman-Read theory [Wechsler et al., 1953, Lieberman et al. 1955], it was predicted that up to 24 martensite habit plane variants can form in one austenite crystal [Otsuka et al. 1998]. The internal twinning of martensite variants will eliminate the macroscopic shear strain associated with the transformation. Hence, the self-accommodating capability of these martensite variants will not result in shape change during transformation from austenite to martensite.

On the other hand, when NiTi is deformed below M_f, biased martensite variant distributions will be created in response to the macroscopic strain through twinning. The material appears to suffer permanent deformation due to the reorientation of martensite variants. Slip mechanisms associated with typical plastic deformation do not play a role in this case, unless the external stress applied exceeds the critical slip stress of the martensite phase. Shape recovery begins to occur when the material is heated above A_s, and is completed at A_f. The shape recovery capability stems from the inherent ordering across the martensite-austenite interface resulting in the detwinning of martensite variants through an exactly reversed pathway taken during twinning.

Besides the shape-memory effect, NiTi also possesses a transformational superelasticity or pseudoelasticity characteristic, which is an isothermal form of shape-memory. While decreasing temperature can cause the austenite-to-martensite

transformation to occur, externally applied stresses can also drive the austenite-to-martensite transformation even when temperature of the material is above A_f. This is known as the stress-induced martensite (SIM) transformation and it is the underlying principle for transformational superelasticity. The SIM transformation is a thermodynamic phenomenon and is governed by the modified Clausius-Clayperon equation expressed in Eq. (1.1).

$$\frac{dT_{trans}}{d\sigma} = \frac{T\Delta\varepsilon}{-\Delta H} \qquad \text{Eq. (1.1)}$$

where T_{trans} is the stress-induced transformation temperature, T is the stress-free *B2*-to-*B19'* transformation temperature, σ is the externally-applied stress, $\Delta\varepsilon$ is the stress-induced strain and ΔH is the martensite transformation enthalpy.

Figure 1.2 qualitatively illustrates how the Clausius-Clayperon relation [Wollants et al. 1979] governs the dependence of A_S, A_f, M_S and M_f on externally-applied stress. It is important to highlight that the plots in Figure 1.2 have positive slopes because the martensite transformation is an exothermic process. If NiTi is subjected to sufficient external stress at $T > A_f$, the austenite phase becomes thermodynamically unstable and transforms into martensite phase when magnitude of stress crosses into the M_S boundary (vertical upward line in Figure 1.2). The martensite variants will have crystallographic orientations dictated by the stress states and, hence, give rise to macroscopic strain in a

similar fashion described in the previous section. However, given that $T > A_f$, the material will spontaneously revert to austenite phase upon removal of the applied stress (vertical downward line in Figure 1.5). If the applied stress magnitude remained below the critical stress for slip, M_d, full strain recovery will be possible. But if the applied stress magnitude exceeds M_d, conventional slip mechanisms will be initiated, resulting in permanent deformation with only partial strain recovery.

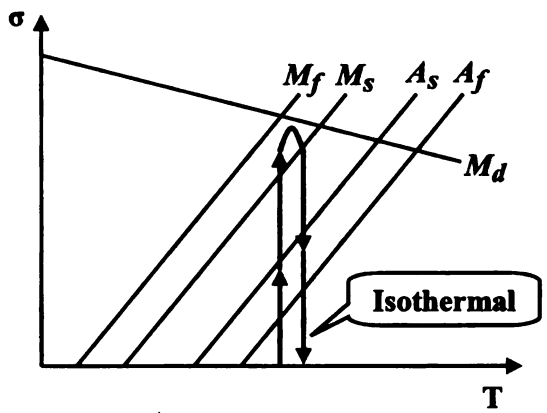

Figure 1.2 Graphical representation of modified Clausius-Clayperon equation showing change in M_s as a function of applied stress.

1.2.2 Mechanical Properties

The shape-memory effect and transformational superelasticity of NiTi are graphically summarized in Figure 1.3, which show the typical stress-strain curves of NiTi when it is deformed in the martensite and austenite state. The stress-strain behavior of martensitic shape-memory NiTi mainly appears to be analogous to conventional metallic systems. But when the martensitic NiTi is heated beyond A_f, prior deformation strain is recovered. For superelastic or austenitic NiTi, stress plateaus appear in each of the stress-

strain curves for mechanical loading and unloading. The upper-plateau is attributed to SIM transformation during loading, while the lower-plateau is associated with martensite to austenite transformation during unloading. The upper-plateau stress of NiTi alloys varies greatly, but most alloys with useful superelastic performance tend to possess upper-plateau stresses around 400 MPa.

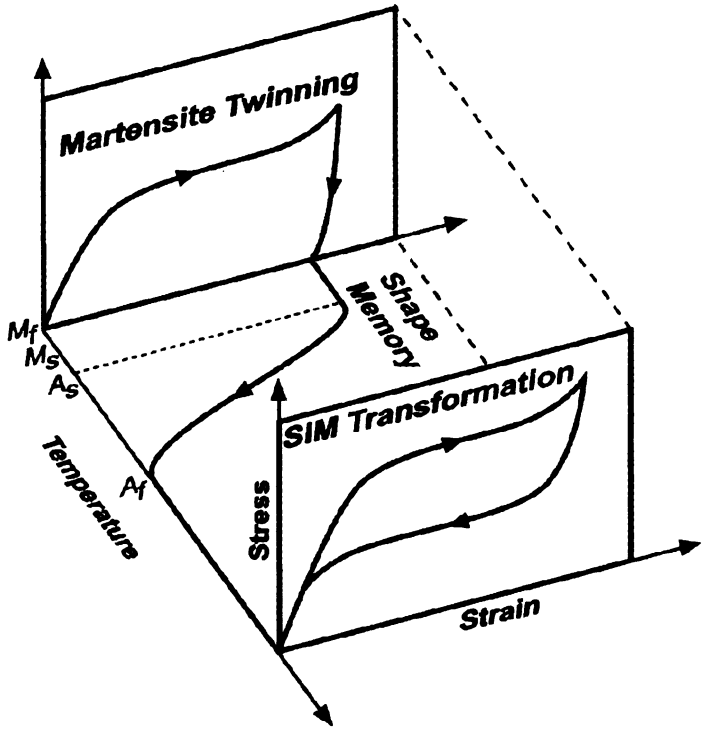

Figure 1.3 Shape-memory effect and transformational superelasticity of NiTi alloys.

Typically, full strain recovery can be achieved in NiTi if it is not strained more than 6%. However, Miyazaki et al. has shown that recoverable strain of up to 10% can be achieved through thermomechanical treatment of NiTi [Miyazaki et al. 1982, 1986].

Determination of elastic modulus of NiTi has been a challenging problem. This is due to the highly non-linear slope of the unloading stress-strain curve. Furthermore, the elastic modulus of NiTi is also dependent on temperature [Melton 1990]. Experimental work has determined that NiTi can have elastic modulus ranging from about 30 to 100 GPa [Melton 1990, Zadno et al. 1990]. Ultimate tensile strengths of NiTi alloys vary significantly and are highly-dependent on compositions and thermo-mechanical treatments. However, most alloys tend to have strengths in excess of 1 GPa.

1.2.3 Phase Equilibria in the Ni-Ti Binary System

The binary phase diagram of Ni-Ti is shown in Figure 1.4. The phase diagram indicates that NiTi melts congruently at 1310°C. Besides NiTi, there are two other stable intermediate compounds in the binary system, namely, the Ti_2Ni and Ni_3Ti phases. The former melts peritectically near 984°C and the latter melts congruently around 1380°C. The Ni_4Ti_3 and the Ni_3Ti_2 phases are two metastable compounds that exist in the Ni-rich side of the NiTi – phase field [Nishida et al. 1986, Otsuka et al. 2005]. When subjected to elevated temperature anneals for prolong period of time, these metastable phases will eventually transform into the stable Ni_3Ti phase. As discussed in Section 1.2.1, NiTi is an ordered intermetallic compound in the Ni-Ti binary system. However, it is not a line-compound of fixed composition at elevated temperatures. The binary Ni-Ti phase diagram in Figure 1.4 shows that excess Ni of about 6 at.% is soluble in NiTi above 1000°C. On the other hand, the steep NiTi phase boundary on the Ti-rich side does not permit excess Ti to be soluble in NiTi at any temperature. At temperatures below 630°C,

the phase diagram indicates that the NiTi – phase field degenerates into an equi-atomic line-compound.

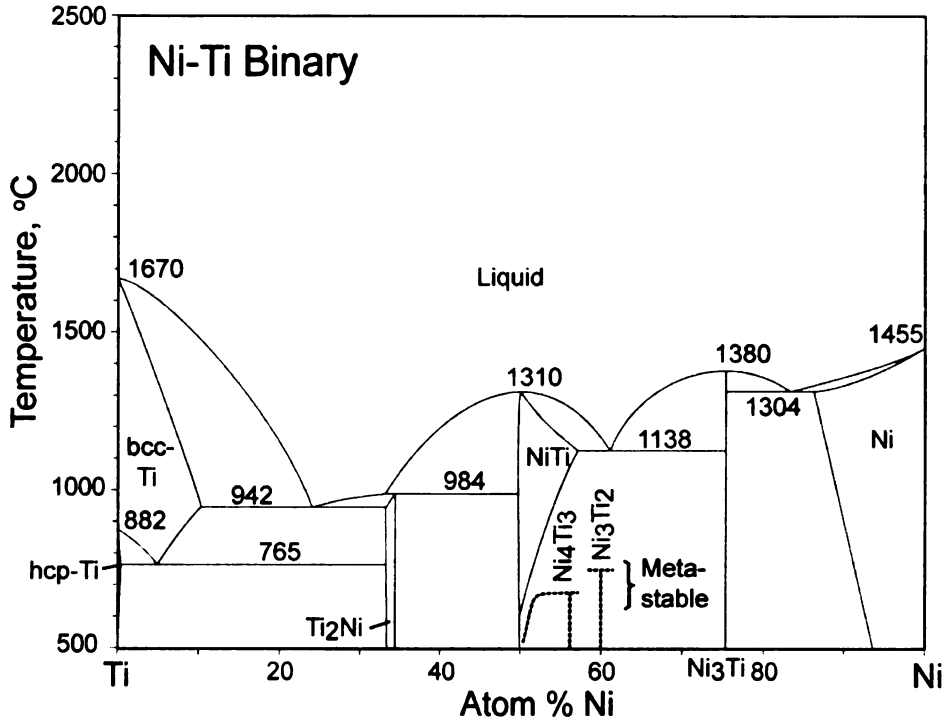

Figure 1.4 Ni-Ti binary phase diagram [Massalski 1990].

With such limited solubility of Ni and Ti in the NiTi phase at low temperatures, any alloy composition that deviates from 50Ni-50Ti (at.%) will result in precipitations of either Ti_2Ni or Ni_3Ti in NiTi. It has been reported that Ti_2Ni precipitates exist within the matrix or at the grain boundaries of NiTi when initial composition of Ti exceeds 50.4 at% [Surbled et al. 2001, Lehnert et al. 2002]. On the other hand, Nishida and coworkers [Nishida et al. 1986] claimed that their 52 at.% Ni alloy decomposed into metastable phases (first Ni_4Ti_3 then Ni_3Ti_2), then finally into the thermodynamically-stable Ni_3Ti upon thermal aging. The reaction path taken depends on the aging time and temperature, which is illustrated in the TTT diagram of Figure 1.5.

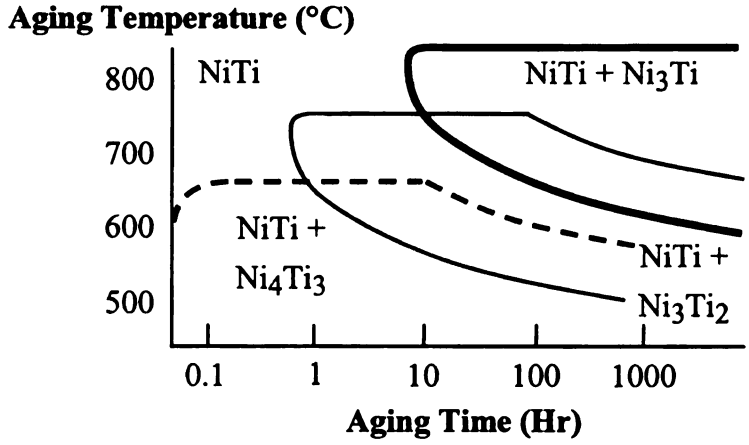

Figure 1.5 TTT diagram of 52 at.% Ni-Ti alloy [Nishida et al. 1986].

1.2.4 Effects of Composition on Transformation Temperature

Transformation temperatures associated with NiTi are important parameters to control as they dictate the temperature range for shape-memory alloys to carry out their proper functions. The martensite transformation temperature is strongly dependent on composition. Varying the composition of NiTi is one of the most effective methods of changing transformation temperatures. In Ni-rich alloys, a composition change of less than 1 at.% can change the transformation temperature by more than 100°C.

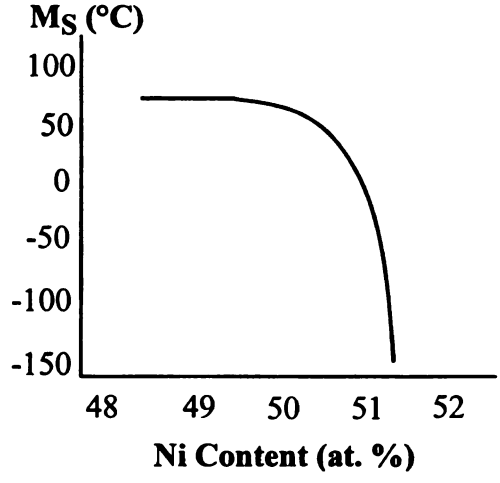

Figure 1.6 Effect of Ni composition in NiTi alloys on martensite start temperature.

Figure 1.6 shows that for Ti-rich to equi-atomic alloys, M_S remains rather constant at 60°C. However, M_S decreases rapidly from 60°C to -140°C when Ni composition increases from 50 to 51 at.%. [Melton 1990, Otsuka et al. 2005]. The insensitivity of M_S to composition changes when alloys are Ti-rich is believed to be associated with the almost vertical NiTi phase boundary on the Ti-rich side of the phase diagram (Figure 1.4) causing insignificant solubility of Ti in NiTi phase. Given that it is not possible to obtain Ti-rich NiTi solid solutions, Ti-rich alloys exhibit behaviors similar as equi-atomic NiTi [Otsuka et al. 2005].

The strong dependence of M_S on composition for Ni-rich alloys can be understood from a qualitative explanation. Recall that the microstructures of Ni-rich alloys consist of the metastable Ni_4Ti_3 phase in the NiTi matrix. Besides thermal aging, fine precipitates of the Ni_4Ti_3 phase can also form upon quenching from solution. These precipitates are coherent with the NiTi lattice and yield strain fields that will strengthen the *B2* matrix. Hence, a larger driving force or a lower M_S temperature is required to initiate martensite transformation [Miyazaki et al. 1982, Saburi et al. 1982].

1.2.5 Effects of Thermo-mechanical Treatment on Shape-Memory and Superelastic Characteristics

Recall in Section 1.2 that permanent deformation of NiTi will occur if the applied stress exceeds the critical stress for slip, M_d. Hence, significant efforts have been placed

to explore various approaches to improve M_d. Strengthening methods common in physical metallurgy, such as work hardening, precipitation hardening, and grain size refinement, have been studied for their applicability in NiTi.

It was found that cold work alone will improve yield stress but destroy the superelasticity of NiTi, resulting in low recoverable strains [Melton 1990]. It was believed that cold work introduces high densities of random dislocations, which hinder twin boundary mobility. Hence, the strengthening effect is attributed to the presence of these dislocations, but the constraint of twin boundary movements by dislocations also signifies a compromise of strain recovery performance. On the other hand, post cold-work annealing will improve strain recovery but reduces yield stress. The annealing process rearranges these dislocations to form cells or sub-grain boundaries, giving rise to relatively dislocation-free regions. Martensite twin boundaries will have relatively higher mobility in these regions. This translates into poorer strengthening effect but better strain recovery properties. Therefore, one can appreciate that the choice of degree of cold work and the annealing temperature will dictate the trade-off in the yield stress and recoverable strain.

Figure 1.7 shows the effect of annealing temperature on room-temperature yield strength and M_s after 40% cold work in the martensite phase of a 50.6 at.% Ni alloy [Melton 1990]. Annealing times are within the order of an hour. A rapid decrease in the yield strength is observed in the range from 350°C to 450°C, followed by a relatively gradual decrease from 450°C up to 850°C. On the other hand, M_s increases promptly

when annealing temperature increases from 350°C to 450°C, but becomes weakly dependent on temperature above 450°C.

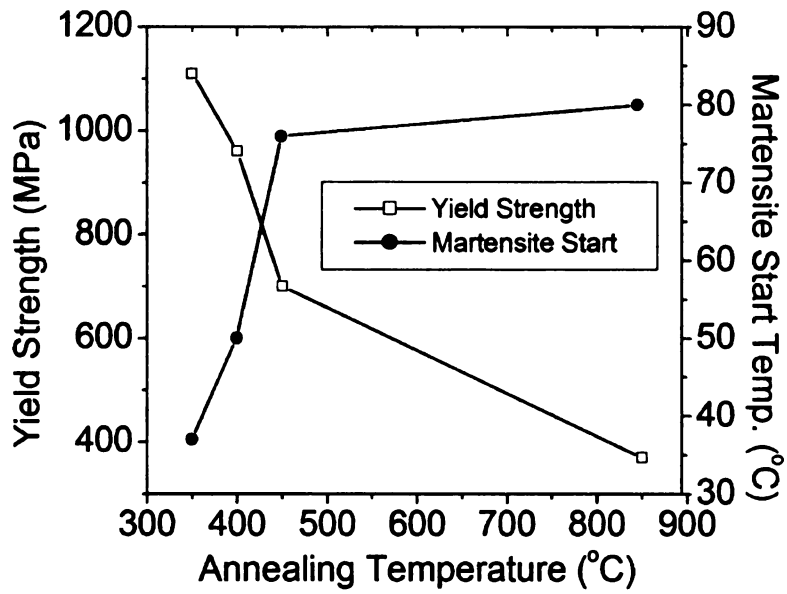

Figure 1.7 Effect of annealing temperature on room-temperature yield strength and martensite start temperature after 40% cold work in the martensite phase of a 50.6 at.% Ni alloy [Melton 1990].

Age hardening by precipitation of the Ni_4Ti_3 phase is also known to significantly affect shape-memory effect and superelasticity [Miyazaki et al. 1982, Saburi et al. 1982]. It was observed that a 1000°C solution-treated 50.6 at.% Ni alloy wire that was subsequently aged at 500°C exhibits poor strain recovery when mechanically-tested between -64°C and 51°C. Complete superelasticity can only be achieved within a limited temperature range from 31°C to 41°C, while permanent strains were introduced in the rest of the test temperatures. The solution treatment and aging durations were both fixed at 1 hour. When a similar solution-treated wire was aged at 400°C for 1 hour, superelasticity was observed over a significantly wider range from 4°C to 61°C. Furthermore, onset stresses of the upper-plateau in superelastic stress-strain curves tend

to be higher for the specimen aged at 400°C, which indicates strengthening of the *B2* phase [Miyazaki et al. 1982].

The strengthening of the *B2* phase can be understood from the physical metallurgy principles that the increase in critical stress for slip is most pronounced when high-density of fine, coherent precipitates are dispersed in the matrix. A lower annealing temperature may initiate extensive nucleation of Ni_4Ti_3 particles but does not encourage significant growth of these precipitates. On the other hand, higher annealing temperatures will enhance growth kinetics, resulting in coarser Ni_4Ti_3 precipitates. This deduction was supported by TEM experiments that revealed fine and densely-populated precipitates of Ni_4Ti_3 in the NiTi matrix when the specimen was annealed at 400°C, while the specimen that was annealed at 500°C contains fewer but larger Ni_4Ti_3 precipitates [Otsuka et al. 2005].

Grain size refinement has also been reported to be a viable approach to improve superelasticity of NiTi. Saburi et al. demonstrated the effect of grain size on superelastic performance of NiTi by employing single crystal and polycrystalline specimens of 50.5 at.% Ni alloy and subjected them to annealing at 800°C for 1 hour before tensile testing [Saburi et al. 1984]. Tests were performed at 40°C, which is 10°C higher than the A_f of these specimens. The authors found that single crystal specimens showed incomplete superelastic behavior, while polycrystalline specimens of 1 mm or smaller grain size revealed improvement in superelasticity. At a grain size of 50 μm, complete

superelasticity was observed. Therefore, the study clearly suggests that the reduction in grain size is also effective for improving superelastic performance of NiTi.

1.2.6 Effects of Ternary Alloying

There has been much effort to modify NiTi alloys by adding different elements to the binary system. It has been reported that transformation temperatures, hysteresis width, mechanical strength and corrosion properties of NiTi can be controlled by the addition of a third element [Melton 1990]. Alloying elements commonly-employed for study are Au, Cu, Co, Cr, Fe, Hf, Nb, Pd, Pt and Zr [Otsuka et al. 2005].

Some elements exhibit preference to substitute for a particular site in the NiTi lattice while others do not. For example, Nakata et al. found that Co, Fe and Pd have a strong preference for entering Ni sites, while there is no preference for Cr, Mn and V to occupy either Ni or Ti sites [Nakata et al. 1991]. From their findings, the authors deduced that electron configuration, chemical affinity and atomic size effect play important roles in governing the preferences for site occupancy of each alloying element.

The martensite start temperature, M_S, was observed to decrease monotonically with increasing V, Cr or Mn substitution for Ti sites [Honma 1987]. The suppression of M_S can also be effected by substituting Ni with Co or Fe [Eckelmeyer 1976, Honma 1987]. On the other hand, significant increase in transformation temperatures can be achieved by substitution of Ni with Pd or Pt [Lindquist et al. 1990, Winzek et al. 2001] or Ti with Hf or Zr [Johnson et al. 1995, Hsieh et al. 1998, Winzek et al. 2001, Firstov et al.

2004]. Lindquist et al. reported that M_S can be increased to about 500°C when more than 45 at.% Pd was alloyed, while 30 at.% Pt addition will increase M_S beyond 600°C [Lindquist et al. 1990]. Alloys of NiTiHf and NiTiZr were also observed to possess transformation temperatures between 300°C to 500°C [Hsieh et al. 1998, Firstov et al. 2004]. Hence, NiTiPd, NiTiPt, NiTiHf and NiTiZr alloys are considered as candidates for high-temperature shape-memory alloys. Grummon et al. have studied the effect of substituting Ni with Cu and observed a pronounced reduction in transformation hysteresis [Grummon et al. 1999]. Shape-memory alloys with narrow transformation hysteresis will be more sensitive and responsive to temperature changes, making them suitable for sensors and actuators applications.

Special attention will now be placed on the ternary addition of Nb in NiTi. Niobium is given particular emphasis in this review as it is the filler metal for the reactive eutectic braze process in this work. Ternary alloys of NiTiNb, particularly compositions close to 44Ti-47Ni-9Nb (at.%), are widely-studied because of their excellent constrained recovery properties that can be harnessed for use as pipe couplings and mechanical fastening devices [Duerig et al. 1990]. Details on constrained recovery can be found in [Proft 1990].

Another reason why NiTiNb alloys are excellent candidates for pipe coupling and mechanical fastening devices is because they exhibit wide transformation hysteresis behavior when subjected to cold-working [Duerig et al. 1990, Zhang et al. 1990, Zhao et al. 1990, Piao et al. 1992A, Siegert et al. 2003]. Specifically, NiTiNb alloys can have M_S

as low as -140°C and A_S about 50°C [Duerig et al. 1990]. By adjusting the transformation temperatures such that ambient temperature is located near the center of the wide hysteresis, these ternary alloys can (1) lower storage costs by eliminating the need to store the coupling components under impractically low temperatures after they have been expanded for future use; and (2) prolonged service life due to the ability to maintain the desired coupling strength at ambient (or moderately elevated) temperatures beyond a reasonably long period of time.

The transformation characteristics can be understood from the microstructures of these ternary alloys, which will consist of insoluble Nb precipitates in a matrix of martensitic NiTi phase when the alloys warm up to room temperature from storage temperature (i.e. less than -140°C) [Duerig et al. 1990, Zhao et al. 1990, Piao et al. 1993]. Given that the flow stress of the Nb precipitates is similar to that of the martensitic NiTi (approximately 150 – 200 MPa), Duerig et al. and Zhao et al. proposed that the NiTi and Nb phases undergo deformation simultaneously at relatively low stresses from cold-working. However, the martensite deforms reversibly by twin boundary motion, while the Nb phase deforms permanently via conventional slip. When the deformed alloy is heated above A_S of the NiTi, the martensite begins to recover but can only proceed significantly by first plastically re-deforming the Nb precipitates back to their original morphologies. Hence, the irreversible component of deformation delays recovery, causing an increase in apparent A_S. Such increase in apparent A_S is exclusively observed

in the first heat cycle of the NiTiNb alloy [Duerig et al. 1990, Piao et al. 1992A]. Subsequent heat cycles cause the apparent A_S to revert back to the original value.

1.2.7 Phase Equilibria of the Ni-Ti-Nb Ternary System

To date, the most widely-studied isothermal section of the Ni-Ti-Nb ternary system is at 900°C. Gupta [Gupta 1991] reported the presence of 4 intermediate ternary intermetallic phases (X_1, X_2, X_3 and X_4) in the Ni-rich region, with numerous two- and three-phase fields in the 900°C isothermal section; while the Ti-rich side has no known ternary intermediate phases. Piao et al. [Piao et al. 1992B] observed a eutectic microstructure in their 40Ni-40Ti-20Nb (at.%) specimens prepared by Vacuum Arc Re-melting (VAR). Based on their experimental findings, the authors proposed a NiTi-Nb quasibinary eutectic isopleth in the ternary system. They claimed that the eutectic point is 40Ni-40Ti-20Nb (at.%) at 1150°C. However, an extensive study of the solidus temperatures in the NiTi – Ni_6Nb_7 – Nb – Ti region by Prima et al. [Prima et al. 1995] revealed a quasibinary eutectic point close to 38Ni-36Ti-26Nb (at.%) at 1170°C (indicated on Figure 1.8). The findings of Gupta and Prima et al. on the 900°C isothermal section and liquidus projections are summarized in Figure 1.8. The NiTi + Nb(Ni,Ti) tie-line at 900°C, close to the quasibinary eutectic point [Prima et al. 1995], is also constructed in Figure 1.8.

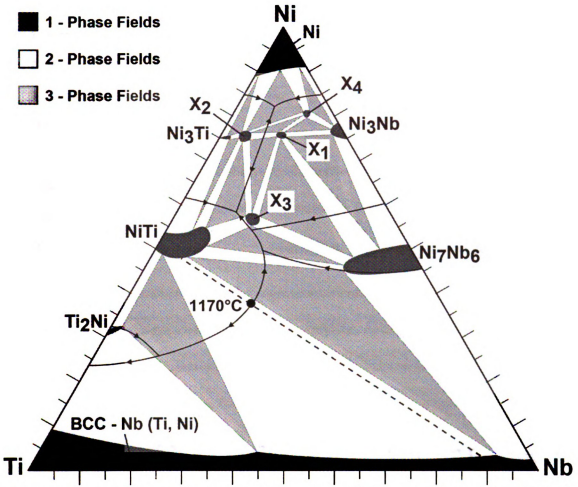

Figure 1.8 900°C – Isothermal section and liquidus projections of the Ni-Ti-Nb ternary system reported by [Gupta 1991] and [Prima et al. 1995]. (NiTi + Nb(Ni,Ti) tie-line at 900°C, close to the quasibinary eutectic point, is also indicated.)

More recently, a fifth ternary intermetallic phase (X_5) was discovered by Yang and coworkers in the Ni-rich region [Yang et al. 2000]. The liquidus projections of the ternary system were predicted by Matsumoto and coworkers using CALPHAD calculations [Matsumoto et al. 2005], taking into considerations all the reported phases, including the X_5 phase. However, the quasi-binary eutectic point was not accounted for. Figure 1.9 graphically summarizes the findings on the liquidus projections and 900°C isothermal section of the Ni-Ti-Nb system by Yang and Matsumoto groups.

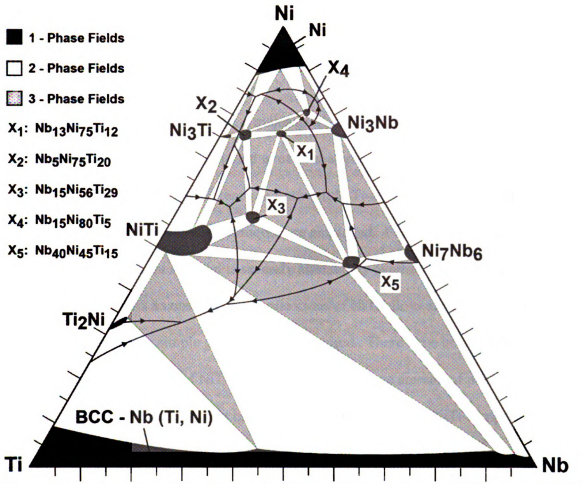

Figure 1.9 Summarized findings on the 900°C – isothermal section [Yang et al. 2000] and liquidus projection [Matsumoto et al. 2005] of the Ni-Ti-Nb ternary system.

Phase equilibria data for other temperatures are very limited. Specifically, little is known of the temperature-evolution of phase fields, such as those of NiTi + Nb(Ni,Ti) + $(Ti,Nb)_2Ni$ and the NiTi + Nb(Ni,Ti) + X_5. These may be presumed to degenerate to points at 0 K. The knowledge of the phase field evolution is critical for determining if $(Ti,Nb)_2Ni$ or X_5 phases will solidify in the eutectic matrix at lower temperatures.

1.3 Joining of NiTi Components

The ability to regulate the transformation and mechanical properties by adjusting its binary and ternary compositions makes NiTi alloys suitable for use over a broad range of operating temperatures. However, a major shortcoming of NiTi alloys is the difficulty of joining NiTi alloys to themselves and to other materials. The problem stems from either wettability issues or the tendency to form brittle Ti-rich intermetallic compounds in joints when conventional joining techniques are employed. Furthermore, shape memory performance of the parent material is severely affected by overheating from the various joining techniques. As a consequence, applications of NiTi alloys are currently restricted to situations where only simple geometries are required. There have been limited disclosed studies on joining of NiTi alloys. Within the scarce amount of published research, there are 5 techniques that have been explored for joining NiTi components. They are: (1) welding, (2) soldering, (3) mechanical joining, and (4) brazing, and (5) transient liquid phase (TLP) bonding.

1.3.1 Welding

Various types of welding, such as tungsten inert gas (TIG) welding [Ika 1996] and plasma welding [Van der Eijk et al. 2003] under Ar or He inert environment, have been employed for joining similar NiTi components, mostly yielding poor results. Common problems encountered were formations of Ti_2Ni and Ni_3Ti, which are brittle and have no shape-memory effect. However, laser welding appears to be a promising technique as there have been a few successful demonstrations showing reasonably strong NiTi joints

with their base alloys partially retaining their functional properties [Schlossmacher et al. 1995, Hsu et al. 2001, Schetky and Wu 2004].

Schlossmacher and coworkers [Schlossmacher et al. 1995] employed a Nd:YAG laser for joining a superelastic Ti-51.5Ni (at.%) alloy. Tensile tests on sheet metal of 0.5 mm thickness were performed at under martensitic and austenitic conditions. Their laser welded specimens exhibited an ultimate tensile strength of about 820 MPa and are independent of test temperature. This value corresponds to 80% of the ultimate tensile strength of their base material, which was also tested in both martensitic and austenitic conditions. Fractographic observations of ruptured specimens by scanning electron microscopy (SEM) revealed ductile characteristics of laser-welded joints. Schetky and Wu [Schetky and Wu 2004] also reported that Nd:YAG lasers are capable of producing welds with excellent strength retention, which they claimed to be 75% of the base metal strength. Their study showed only 0.2% permanent deformation after a 7% strain of a superelastic weld specimen.

In another case, Hsu and coworkers [Hsu et al. 2001] successfully demonstrated the ability to produce strong NiTi joints using laser welding. The authors welded an equi-atomic NiTi alloy using a CO_2 laser operated within 2200 to 2500 W at a travel speed of 1.5 m/min. Helium plasma was used during welding. Vickers micro-hardness tests showed that weldments possess similar hardness to the parent material. Tensile strengths as high as 740 MPa were observed when their laser welded joints were subjected to tensile tests, but strain at failure was only about 6%, which is poor.

Fractographic observations of the weldment showed brittle mode fracture. The authors attributed the poor fracture strain to segregation of impurity elements at the weldments during solidification, and increase in grain size.

Hirose and Akari [Akari et al. 1989, Hirose and Akari 1989] joined 3 mm-thick 50.7Ni-Ti (at.%) sheets using a 10 kW CO_2 laser, with a travel speed of 3.4 m/min. All welded specimens were subjected to post-weld heat-treatment at 400°C for 1 hour. Differential scanning calorimetry showed that the A_f, A_S, M_S and M_f of the base metal were 23°C, -22°C, -24°C and -79°C, respectively. There were no changes in A_f and M_S in the weldment, but A_S and M_f were each about 10°C lower in the weldment than the base metal. When subjected to tensile loading and unloading cycles at strains up to 4%, the welded specimen yielded room temperature superelastic recovery with about 0.3% unrecoverable strain. The authors also investigated the tensile strength of the welded joints at -40°C, 40°C and 120°C, which they found to be about 480 MPa, 670 MPa and 800 MPa, respectively.

Besides laser welding, friction stir welding is another promising technique that has attracted a lot of attention in the field of joining. Recently, London and coworkers [London et al. 2005] explored friction stir welding for joining NiTi alloys. Void-free friction stir processed zones were produced in 6.35 mm-thick NiTi plates using polycrystalline cubic boron nitride and tungsten-rhenium tools that were rotating from 400 to 600 rpm at a travel speed of 12.7 mm/min. Transformation temperatures of the

processed zones were measured using differential scanning calorimetry, which showed a lower A_f in the processed zones (-22.5°C) compared to the parent alloy (15.0°C). Optical and SEM revealed a slight reduction in grain diameter (33 μm) from the parent alloy (43 μm). Welded sheets were hot-rolled at 850°C to 76% total reduction and then subjected to tensile tests. Results showed that these friction stir welded NiTi alloys retained their superelastic responses with tensile strength approaching 700 MPa at a strain of about 16%.

Although some positive results were reported for welding NiTi alloys to itself, successful welding of dissimilar materials proves to be an even greater challenge. The main reason is the undesirable formation of hard and brittle intermetallic compounds, oxides or carbides at the weld zone. Van der Eijk and coworkers [Van der Eijk et al. 2003] had attempted to join NiTi alloys to stainless steel and Hastelloy C276 using plasma arc welding. The joining procedures were performed between 15 and 42 A of current under Ar plasma, and the shielding gas was also Ar. Working distance between the torch and the sample was approximately 6 mm. The authors observed significantly more melting of the NiTi as compared to the stainless steel, resulting in leaching of elements (predominantly Fe, Cr, Ni, Mn and Si) from the steel into the molten NiTi to form a mixed zone and TiC precipitates. Scanning electron microscopy revealed cracks within the mixed zone and the carbide precipitates, indicating that they are brittle. Welding of NiTi alloys to Hastelloy C276 also resulted in significant leaching of elements into the weldment, producing a mixed zone. Tensile tests could not be

performed on the NiTi-steel joint due to serious embrittlement, while tensile tests on the NiTi-Hastelloy joint revealed a tensile strength of only 70 MPa with negligible strain.

Chau and coworkers [Chau et al. 2006] investigated the possibility of using Nd:YAG laser for spot-welding 0.5 mm-thick NiTi sheets to 0.1 mm-thick commercially-pure Ti sheets. They found that welding at a beam voltage of 220V for 35 ms yielded the highest failure load of 193N, which translates to shear strength of 109 MPa. Such strength level does not meet the requirement of most applications.

1.3.2 Soldering

The predominant problem associated with soldering NiTi alloys is a lack of wettability, which is attributed to the presence of Ti-rich native oxide on NiTi. Given the chemically-inert nature of Ti-rich oxides, aggressive fluxes are usually required to remove them prior to soldering. In a U.S. patent by Hall [Hall 1993], it was claimed that an aluminum paste flux applied to NiTi surfaces will remove the Ti-rich native oxide layer when the flux is heated to its activation temperature. Consequently, Ti leaches from the surface of the base metal, forming a Ni-rich surface. The activated flux also coats the Ni-rich surface to prevent further oxidation. A bonding material, such as Sn – Ag solder is flowed onto the Ni-rich surface, which will then displace the flux. At this point, another NiTi member will be applied to the molten solder to form a joint. Ultrasonic soldering, developed for removing oxides from the aluminum to promote solder wettability, has also been employed successfully on NiTi alloys with a Sn-based solder [Schetky and Wu 2004].

Successful soldering of NiTi alloys was also claimed by Murai [Murai 1990]. The author reported in his U.S. patent that plating Ni onto NiTi creates a surface that will accept solder with mild flux can improve solderability. Other variants of this approach are plating Cu/Ni or Cu/Ni/Au onto NiTi surfaces.

1.3.3 Mechanical Joining

Various types of mechanical joints have been explored in industry. For example, threading and tapping can effectively couple NiTi components, but the machining process of NiTi is cost-ineffective. Joining by interference fit or interlocking components can be achieved by harnessing the SME and TSE properties of NiTi [Kapgan et al. 1990, Wu 2001]. However, precision machining of the joining part to ensure optimal fit poses a huge challenge in terms of reducing production time and cost.

1.3.4 Brazing

Problems associated with brazing NiTi alloys are analogous to those involved in welding. That is, the strong tendency to form intermetallic compounds, oxides or carbides result in serious embrittlement of braze joints. Brazing NiTi alloys to stainless steel and Ti-metal/alloys using industrial-standard braze fillers have been studied by a few groups. Seki and coworkers [Seki et al. 2000] employed a series of BAg-8 (American Welding Society standard brazing alloy with compositions of 72Ag-28Cu (at.%)) filler alloy with increasing Ni content for brazing NiTi alloys to 304-grade stainless steel. Brazing was performed above the flow point of the filler alloy of 790°C. The authors found that inter-diffusion of Fe, Ni and Ti during brazing resulted in the

formation of $(Fe,Ni)_2Ti$ at the bond line when the BAg-8 filler alloy did not contain Ni. Tensile tests on these NiTi-steel joints yielded fracture strength of only 275 MPa. Fracture occurred in the $(Fe,Ni)_2Ti$ phase. With the addition of Ni, Ni_3Ti phase formed in the joint instead of $(Fe,Ni)_2Ti$, and tensile strength of 400 MPa can be achieved. Fracture was observed to occur in the Ni_3Ti phase.

In a separate study, Kunimasa's group [Kunimasa et al. 2001] investigated brazing of NiTi to commercially-pure Ti using BAg-8 filler alloy at temperatures above 880°C. They reported that the predominant phase in the braze region is a Ti-Cu intermetallic compound, which solidified isothermally between the commercially-pure Ti and the BAg-8 filler during brazing. Mechanical tests revealed joint strength up to 350 MPa. Fracture was observed in the Ti-Cu intermetallic compound.

Other variants of brazing to join NiTi alloys to itself and to dissimilar materials have also been explored. Infrared brazing of NiTi was investigated by Yang's group [Yang et al. 2004]. Nitinol sheets of 1 mm thickness were brazed using using 25 μm-thick pure Cu and 50 μm-thick Ti-15Cu-15Ni (at.%) braze filler foils. Brazing was performed up to 1150°C. The authors observed CuNiTi and Ti(Ni,Cu) phases in the joints fabricated using pure Cu filler. Bend tests on these braze joints showed shape recovery. Extensive formation of $Ti_2(Ni,Cu)$ phase was observed in braze joints prepared using the Ti-15Cu-15Ni filler alloy. Bend tests could not be performed on these joints due to serious embrittlement from the Ti-rich phase.

An attempt to join NiTi alloys to Ti-6Al-4V (at.%) alloys using infrared brazing was reported by Shiue and Wu [Shiue and Wu 2005]. The authors employed BAg-8 as the filler alloy. Braze joints comprised mainly of hypo-eutectic Ag-Cu when brazing was performed below 850°C. It was found that Ag did not react with both base-alloys but Cu readily alloyed with Ti, forming various Ti-Cu intermetallic compounds. Mechanical tests on the 850°C-brazed joints revealed shear strength of about 200MPa. When brazed at 900°C, joint microstructure consisted mainly of Ti_2Ni phase. Due to serious embrittlement, shear tests could not be performed on the 900°C-brazed joints.

Chiu and coworkers [Chiu et al. 2005] adopted microwave-assisted brazing for cladding NiTi to 316L-grade stainless steel. The motivation of their work was to improve cavitation erosion resistance of stainless steel used in liquid handling systems with a NiTi surface layer. Brazing was performed in a commercial microwave oven operating at 2.45 GHz and a power of 1700 W for 150 seconds. The braze filler alloy used had a composition of 50Cu-33Zn-9Ag-8Cd (at.%). The authors found that the braze microstructure contained predominantly Fe and Ti elements, but did not specify the phases present. Indentation tests indicated that the brazed region had a Vickers hardness number of about 450, which was significantly higher than both NiTi and stainless steel. Nanoindentation performed on the post-braze NiTi surface showed superelastic recovery that is comparable to that of the as-received NiTi alloy. Shear strength of the braze joint was determined to be in the range of 100 to 150 MPa.

Li and coworkers [Li et al. 2006] employed a Nd:YAG laser for brazing NiTi wires to stainless steel wires. The braze filler alloy used had a composition of 52Ag-22Cu-18Zn-8Sn (wt.%). Laser power and brazing time were varied from 50 to 70 W and 10 to 20 seconds, respectively. The authors observed good wettability of the filler alloy on both NiTi and stainless steel. The braze microstructure consisted of α-Ag, α'-Cu and various types of intermetallic compounds. Braze joints were subjected to tensile loading and unloading cycles up to 4% strain. The 50 W/10 seconds braze joint incurred an unrecoverable strain of 0.37% after the loading/unloading cycle. Unrecoverable strain increased to 2.2% when laser power and braze duration increased to 70W and 20 seconds, respectively. Indentation tests indicated that the braze region possessed a Vickers hardness number of about 220, which is only 60% of the base NiTi alloy. However, the authors did not probe the tensile or shear strength of the braze joints.

1.3.5 Transient Liquid Phase Bonding

The transient liquid phase (TLP) bonding method had also been investigated for the possibility of joining NiTi alloys to other materials. Gale's group [Gale et al. 1997] applied TLP bonding to join NiAl and NiTi. Pure Cu interlayers were used as the melting point depressant. Melting at the bond interfaces were initiated at a temperature of 1150°C. The authors reported that complete isothermal solidification or removal of liquid phase was achievable within an hour at the process temperature, which resulted in the formation of Ni_2AlTi intermetallic compound at the bond line. Extending the processing duration to two hours caused significant leaching of Ti from the base NiTi

alloy to the joint region. No mechanical characterization was performed on these TLP-bonded joints.

The review on joining of NiTi alloys suggests that there are only limited reports on successful joining of NiTi alloy to itself, most of which involves laser welding. Despite claims that the functional properties of NiTi at the heat-affected zones can be reasonably retained, the high cost and low yield associated with laser welding tend to prevent the technique from being widely adopted in industries. Furthermore, welding of NiTi alloys to dissimilar materials, such as stainless steels, tend to produce brittle intermetallic compounds in the joints, resulting in mechanical strengths that are insignificant for most applications.

Although being a relatively low temperature process that will not adversely affect the functional properties of the base NiTi alloy, soldering NiTi alloys requires the use of aggressive fluxes to promote wetting and flow of typical solder materials on the mating surfaces. Most of these fluxes contain elements that are not biocompatible.

Brazing appears to be more suited for joining NiTi alloys to dissimilar materials, and it is an economical, high yield method that can be readily adopted by industries. But successful brazing tends to rely on the use of filler alloys with elements that are also not biocompatible. Most of the braze processes also produce undesirable intermetallic compounds in the braze region, causing embrittlement.

1.3.6 Preliminary Work on Reactive Eutectic Brazing of NiTi

Recognizing the ternary alloying ability of Nb in NiTi and the presence of a quasi-binary eutectic point in the ternary system, Grummon and Shaw [Grummon et al. 2006, Shaw et al. 2007] proposed using pure Nb filler metal to react and form a eutectic liquid for joining NiTi alloys. The authors prepared honeycomb structures from corrugated superelastic NiTi strips brazed together by Nb foils at 1175°C for less than 10 minutes under high-vacuum conditions. The honeycomb was thermally-aged at 450°C prior to mechanical tests.

Preliminary in-plane compression test results, summarized in Figure 1.10, show that the honeycomb joint integrity is not compromised despite a progressive compressive strain of up to 60%. Interestingly, the structure also exhibited very good transformational superelastic properties. The recoverable strain after each strain cycle is close to 95%. This strongly suggests that the structure possesses mechanically strong joints while the NiTi still retains its superelasticity. However, the NiTi and joints became weak and brittle when the braze duration was increased much beyond 10 minutes.

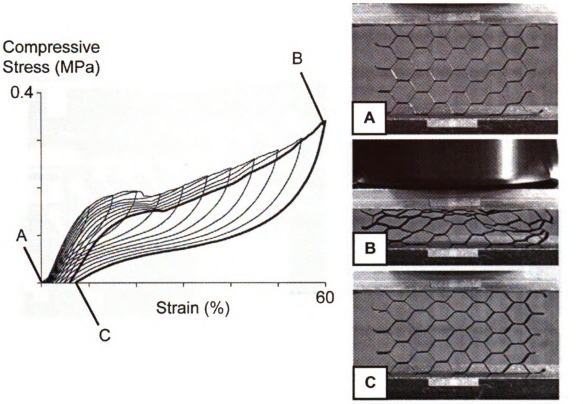

Figure 1.10 In-plane compression test results showing (a) Strain – Time and (b) Stress – Strain plots with (c) digital images at selected test stages [Grummon et al. 2006, Shaw et al. 2007].

Scanning electron microscopy (SEM) of a 'strong' lap joint area revealed coexistence of eutectic micro-constituents with a dendritic phase nucleating against the base-metal (Figure 1.11). Menisci were observed at the edges of the lap joint, suggesting that the braze liquid, once formed, readily wets and flows on the NiTi alloy surfaces. However, there is no compositional and crystallographic information on the brazed joints. Furthermore, the reactive eutectic brazing dynamics and mechanical properties (e.g. yield strength and failure strength, etc.) of the joints remains unclear.

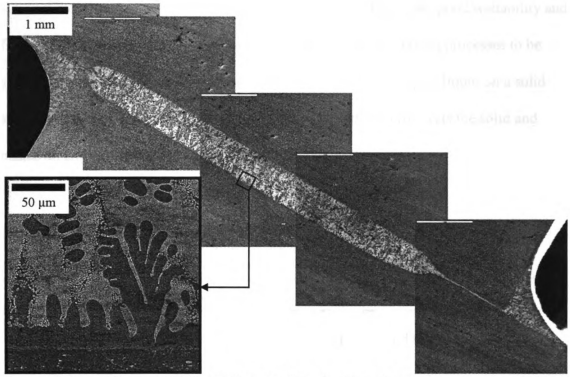

Figure 1.11 Collage of SEM micrographs showing the braze area of a room-temperature shape-memory lap joint (inset: Higher-magnification image of the braze microstructure).

1.4 Brazing

Brazing is a joining technique that is similar to soldering but done at much higher temperatures (typically above 450°C). It involves the use of ferrous or non-ferrous filler metal/alloy that melts and forms a liquid within the joint. In the case of reactive brazing, the filler metal will react with a thin layer of the base-metal of concern and form a molten filler alloy mixture. This liquid, being 'sandwiched' between the base-alloys, will be evenly distributed to the close-fitting regions of the joints by capillary action. Upon cooling, the brazed joint becomes metallurgically linked to the base material, hence, yielding a strong joint.

Given that brazing involves formation of liquid in the joints, good wettability and flow of braze liquid become the two critical requirements for brazing processes to be successful. For wettability, consider the scenario of a sessile drop of liquid on a solid surface, as shown in Figure 1.12. At equilibrium, the sessile drop wets the solid and makes an angle, σ, with the surface.

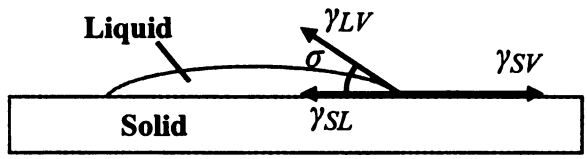

Figure 1.12 Sessile drop of liquid on a solid surface.

The forces acting at the solid-liquid-vapor triple-point at equilibrium are also indicated in Figure 1.12 and can be mathematically described by,

$$\gamma_{SL} = \gamma_{SV} - \gamma_{LV} \cos\sigma \qquad \text{Eq. (1.2)}$$

where γ_{SL} is the solid-liquid interface energy, γ_{SV} is the solid-vapor surface energy, and γ_{LV} is the liquid-vapor surface energy. Figure 1.12 and Equation (1.2) show that maximum wetting of $\sigma = 0°$ occurs when $\gamma_{SL} = \gamma_{SV} - \gamma_{LV}$. Wettability begins to decrease as σ increases. At $\sigma = 180°$, a system will experience complete non-wetting condition.

Flow is another important aspect of brazing. If the braze liquid wets but does not flow into joints, then the use of the filler metal or alloy will be greatly restricted. Figure

1.13 illustrates a schematic diagram of a simple flow scenario. Flow is driven by capillary attraction, which in turn, results from surface energy effects. If a braze liquid with viscosity, η, is confined in a narrow joint with a gap width, w, such as between two flat plates, the surface of the liquid must curve in order for its contact angle, σ, to form on both plates (recall contact angle in wettability). This curvature results in a pressure difference across the surface. The liquid flows into the gap until pressure caused by the surface energy, γ_{LV}, is equal to the hydrostatic pressure. By applying the principles of fluid flow under equilibrium conditions, it can be shown that the distance, $x(t)$, covered in time, t, by the braze liquid is given by Eq. (1.3) [Schwartz 1969].

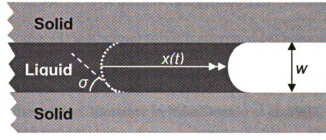

Figure 1.13 Schematic diagram showing a simple flow scenario.

$$x(t) = \frac{\sqrt{wt\gamma_{LV}\cos\sigma}}{3\eta} \qquad \text{Eq. (1.3)}$$

From Eq. (1.3), it becomes apparent that high liquid surface tension, low contact angle and low viscosity are desirable in brazing. Surface tensions of liquid metals are usually high [Iida et al. 1988], so it is usually not the deciding factor for choice of braze filler alloys. On the other hand, viscosity of liquid metals or alloys can vary significantly.

Alloys with narrow freezing ranges (i.e. temperature range between the solidus and liquidus) that are close to the eutectic composition generally have lower viscosity than those with wide freezing range [Schwartz 1969]. Hence, eutectic filler alloys are commonly used for brazing operations.

1.5 Transient Liquid Phase Bonding

Transient liquid phase (TLP) bonding is a form of brazing that involves solid-state diffusion. This joining method is known to produce strong and interface-free joints with no remnant of the bonding phase. Theoretical aspects of the TLP bonding process were extensively studied by Tuah-Poku et al. and MacDonald et al. [Tuah-Poku et al. 1988, MacDonald et al., 1992, 1998]. The authors categorized TLP bonding into 4 main stages: (1) melting, (2) widening, (3) isothermal solidification and (4) homogenization. Only qualitative description of their model will be reviewed. For detailed quantitative discussions, refer to the original literature in [MacDonald et al. 1992, 1998].

Most TLP bonding requires the use of interlayers, which can be provided by foils, electroplating or sputter coating. The interlayer is sandwiched between the parent materials to be joined. Upon heating to the bonding temperature, the interlayer and the parent material undergo inter-diffusion and form a liquid phase. In other words, the interlayer acts as a melting-point depressant to initiate melting at the interface. Melting continues, causing the liquid or joint gap to widen. The melting process typically takes minutes to complete, depending on thickness of the interlayer. Upon complete melting of the interlayer, isothermal solidification dominates, resulting in the narrowing of the joint

through solid-state diffusion of solute into the base-material. The isothermal solidification stage is the most critical stage in TLP bonding as it requires the greatest amount of time (typically hundreds of hours for interlayers that are about 100 μm thick) and is dependent on the width of the liquid and the rate of solute diffusion into the parent material. Finally, homogenization is achieved in the joints when isothermal solidification causes narrowing of the joint to the point where no liquid is left at the processing temperature. Microstructures of the joint will resemble closely to that of the parent material in this final stage, except for the effects of recrystallization and grain growth.

Tuah-Poku and coworkers [Tuah-Poku et al. 1988] developed a model to predict the solidification time required for homogenization and applied it to the Cu-Sn system. Their model was based on a stationary solid-liquid interface. The solidification time, t, is dependent on the diffusivity of the solute in the parent material, D, the initial concentration of solute in the interlayer, C_β, the solidus composition of the parent material, $C_{\alpha L}$, and the initial interlayer thickness, W_o. The mathematical relation among them is expressed as,

$$t = \frac{\pi}{D}\left(\frac{W_o C_\beta}{4C_{\alpha L}}\right)^2 \qquad \text{Eq. (1.4)}$$

The main advantages of TLP bonding are (1) no interface remains after bonding; (2) joints possess properties similar to those of the parent material; (3) large and complex geometries can be bonded simultaneously. On the other hand, TLP bonding also has its

shortcomings: (1) long bond durations and high temperatures are required; (2) the bonding process is only suitable for fast diffusers; (3) post-bonding heat treatments for age-hardenable alloys are required.

The high temperatures involved in TLP bonding (typically higher than 50% of the parent materials' melting points) makes it suitable for bonding high-temperature materials such as Ti-alloys and Ni-based superalloys [MacDonald et al. 1992, Yan et al. 1993, Gale et al. 1996, Bird et al. 1998, Su et al. 1999, Campbell et al. 2000]. Interlayers of pure Cu, Ni and Zn, eutectic Ag-Cu, Cu-Ni, Cu-Sn are commonly-used for joining Ti-alloys [MacDonald et al. 1992, Bird et al. 1998], while Ni-based interlayers containing Cr and Co are widely-employed for bonding Ni-based superalloys [Su et al. 1999].

For some material systems, joints solidified from the transient liquid may yield better mechanical properties as compared to those that had been homogenized. Hence, isothermal solidification and homogenization stages are deliberately avoided by premature termination of the bonding process. Examples of such TLP variants are reactive eutectic brazing of Zircaloy to stainless steel [Owczarski 1962], and Al-B composites to Al [Niemann et al. 1974]. In both cases, the liquids are not transient and are allowed to solidify into eutectic microstructures.

1.6 Liquid-Phase Diffusion

The reactive eutectic braze process discussed here involves liquid formation in the joint via contact melting between NiTi and Nb, so it is important to understand liquid-

phase diffusion, which plays a critical role in the dissolution kinetics. Although there has been no literature reporting on diffusion in liquid ternary alloys, it is still useful to review the basic characteristics of pure liquid metals, the fundamental principles of liquid-phase diffusion, and the key parameters affecting diffusion in these simple liquids.

The main observable difference between a solid and liquid is the inability of the latter to support a static shear force. Other differences include higher energy of liquids, higher compressibility, greater thermal expansion and higher diffusivity [Darken et al. 1953]. Many theories on the structure of a liquid metal have been proposed to account for the abovementioned physical differences, but the most widely-accepted general theory was proposed by Eyring [Eyring 1936]. The author stated that liquid metals can be considered analogous to their corresponding solids, except that some of the 'lattice sites' are empty, resulting in lattice distortion. Another perspective is to consider a case of a disordered close-packed crowd of atoms, with coordination numbers around 10 or 11 instead of 12. As a consequence, an atom can move into an adjacent 'hole' more frequently and easily, hence, its inability to support a static shear force. Since this hole-theory calls for only a relatively small number of vacancies in crystalline metals (~ 1 in 10^3 to 10^6 atoms even near melting point), whereas for liquids it requires one vacancy for about every 10 atoms, it predicted that the diffusivity of liquid metals should be 10^2 to 10^5 times greater than the corresponding solids ($10^{-11} - 10^{-14}$ m^2/s). In fact, most liquid metals are observed to possess diffusivities of the order of 10^{-9} m^2/s just above their melting temperatures [Iida et al. 1988B], which is grossly consistent with the prediction.

The fluidic characteristics of liquid metals also suggest that the ease of flow of atoms or the diffusive movement of atoms must be strongly dependent on the resistance to shearing among neighboring atomic layers, which is, related the viscosity of the liquid and is dependent on temperature. Equation (1.5) describes the Arrhenius type relation between viscosity, η, and temperature, T for liquid metals [Iida et al. 1988C].

$$\eta = A\exp(\frac{Q_{visc}}{RT}) \qquad \text{Eq. (1.5)}$$

where A is a pre-exponential constant, Q_{visc} is the viscosity activation energy required to overcome the resistance of shearing among neighboring atomic layers, and R is the universal gas constant.

In the hole-theory of Eyring [Eyring 1936], an attempt was made to develop a mathematical expression (Eq. (1.6)) that describes the relation between self-diffusivity, D, and η,

$$D\eta = \frac{kT}{2r} \qquad \text{Eq. (1.6)}$$

where r is the atomic radius, k is Boltzmann's constant and T is the temperature. However, self-diffusivity data predicted by Eq. (1.6) did not satisfactorily agree with many experimental values. Therefore, the Stokes-Einstein and Sutherland-Einstein relations [Iida et al. 1988B], given in Eq. (1.7) and (1.8), respectively, were formulated.

These two expressions take into account the hydrodynamics of fluids and are widely-accepted as one of the most robust empirical expressions for self-diffusivity in liquid metals and solute diffusivities in very dilute metallic solutions. Values predicted using Eq. (1.7) and (1.8) appears to agree reasonably well with experimental data, at least within the same order of magnitude (i.e. 10^{-9} m^2/s).

$D = \frac{kT}{6\pi\eta r}$	if diffusing particle is large compared with that of the medium.	Eq. (1.7)
$D = \frac{kT}{4\pi\eta r}$	if diffusing particle is approximately equal to that of the medium.	Eq. (1.8)

Little quantitative theoretical work has been performed on solute diffusion in liquid alloys because knowledge of the fundamental quantities, such as the pair potentials and the pair distribution functions of liquid alloys are insufficient. However, it still seems reasonable to extend the qualitative hole-theory of the liquid state to metallic solutions. For liquids originating from ordered alloys, such as β-brass [Darken et al. 1953], it is believed that short-range order may still persist despite absence of long-range ordering. The difference in either electronegativity or size factor is likely to still exert their influences in the liquid state but is expected to diminish as temperature increases.

While there are a few well-established methods for measuring self-diffusivities in pure liquid metals [Iida et al. 1988B], experimental work on solute diffusivities in liquid alloys, especially eutectic systems, are very limited. Getazheev's group [Getazheev et al. 1970] attempted to address this issue by developing an experimental approach that

involves contact melting between two pure metals that will ultimately produce a eutectic mixture. The authors assumed a diffusion-controlled melting process where the rate of diffusive removal of solute from the liquid at the solid-liquid interface is slower than the jump rate of particles from the solid into the liquid. They further assumed steady-state diffusion in the liquid and neglected hydrodynamic flow. The concentration profile in the liquid, $C_L(x)$, and melting interface velocities of A and B, v_A and v_B, were described by,

$$C_L(x) = -\frac{C_L^A - C_L^B}{w}x + C_L^B \qquad \text{Eq. (1.9)}$$

$$v_A(C_L^A - C_S^A) = \frac{\rho_L}{\rho_A}\left(D_L \frac{dC_L}{dx}\right) \qquad \text{Eq. (1.10)}$$

$$v_B(C_L^B - C_S^B) = \frac{\rho_L}{\rho_B}\left(D_L \frac{dC_L}{dx}\right) \qquad \text{Eq. (1.11)}$$

where C_L^A and C_L^B are the liquidus compositions of metal A and B, respectively, C_S^A and C_S^B are the solid compositions of metal A and B, respectively, ρ_A, ρ_B and ρ_L are the densities of A, B and the liquid phase, respectively, x is the distance in the liquid, w is the width of the liquid, D_L is the mutual diffusivity in the liquid. According to Darken's equation, partial-diffusivities of A and B in the liquid, D_A and D_B, are related to D_L by,

$$D_L = C_L D_A + (1 - C_L) D_B \qquad \text{Eq. (1.12)}$$

Using the above numerical model, Getazheev et al. predicted the contact melting rates between pure Bi and Sn at 200°C [Getazheev et al. 1970], which consequently allowed them to derive solute diffusivities of Bi and Sn in the eutectic mixture at this temperature. Their model was also applied to predict diffusivities in the Ga-In system [Savintsev et al. 1971]. All predicted results produced reasonable diffusivity values within the order of 10^{-9} m^2/s, thus demonstrating great potential in measuring solute diffusivities in eutectic systems. However, there is limited literature available to verify their findings. Furthermore, their approach has only been applied to binary eutectic systems. The ability to extend their model to quasibinary eutectic in ternary systems has not yet been tested.

1.7 Interpretation of Ternary Phase Diagrams

1.7.1 Basic Characteristics and Rules

Ternary systems are materials that are made up by three elements. The phases present in a ternary alloy and their relative fractions at a particular temperature and pressure can be described by a 4-dimensional phase diagram. However, it is visually impossible to illustrate such a phase diagram. Hence, it is common to assume constant pressure (atmospheric pressure in most cases) so that composition and temperature can be adequately described using just three-dimensional space. The composition of a ternary alloy is represented on a two-dimensional scale that takes on an equilateral triangular

geometry, also known as the Gibbs Triangle (see Figure 1.14), while the third dimension (out of the page) describes temperature.

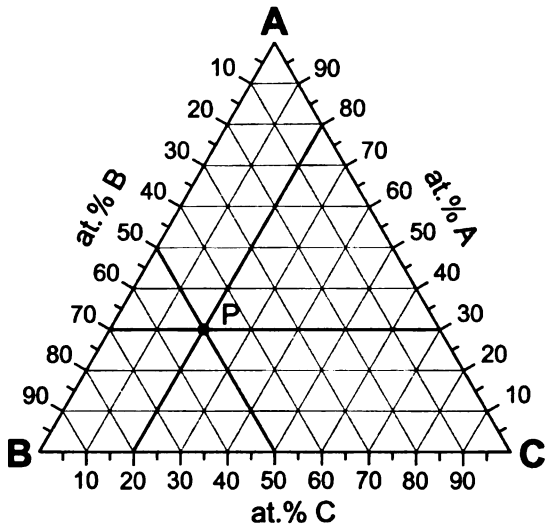

Figure 1.14 Gibbs triangle and a ternary alloy with an overall composition *P*.

The Gibbs triangle provides the simplest means for plotting compositions, where the three pure components are represented at the corners, A, B and C. Binary compositions are represented along the edges AB, AC and BC. Ternary alloys are represented within the Gibbs triangle. The composition scales are usually ruled with lines parallel to the edges for ease of reading. For example, the overall composition of a ternary alloy, *P*, in Figure 1.14 can easily be determined to be 30 at.% A, 50 at.% B and 20 at.% C.

Equilibria in phase diagrams are governed by the Gibbs phase rule, which is mathematically expressed as,

$$P + F = C + 2 \qquad \text{Eq. (1.13)}$$

where P is the number of phases, F is the degrees of freedom and C is the number of components in the system.

Given that most phase diagrams are drawn with pressure being held constant, Eq. (1.13) becomes,

$$P + F = C + 1 \qquad \text{Eq. (1.14)}$$

Therefore, in a ternary system where C is 3, equilibrium between two phases possesses two degrees of freedom, which can either be temperature and composition of one phase, or compositions of two phases. In other words, the knowledge of the temperature and composition of one phase allows one to determine the composition of the other phase, or the knowledge of the compositions of both phases will allow one to determine the temperature at which they occur. For equilibrium involving three phases, there is only one degree of freedom, where the equilibrium compositions of the three phases will be fixed for a particular temperature. For four phases to coexist at equilibrium, there are no degrees of freedom. This implies that such equilibrium can only occur at a single point in the ternary phase diagram. Ternary 4-phase equilibrium will be discussed in detail later.

Equilibrium compositions of two phases are described by tie-lines in the phase field. Tie-lines are construction lines that join the composition points of the two conjugate phases that exist at a particular temperature and pressure. Equilibrium

compositions of three phases are described by tie-triangles, whose edges are defined by tie-lines among the three phases. It is important to note that no phases can have compositions that fall along the tie-lines or within tie-triangles. Phases can assume compositions only at the end-points of tie-lines (i.e. corners of tie-triangles). Examples of tie-lines and tie-triangles of two- and three-phase fields are illustrated in Figure 1.15, respectively.

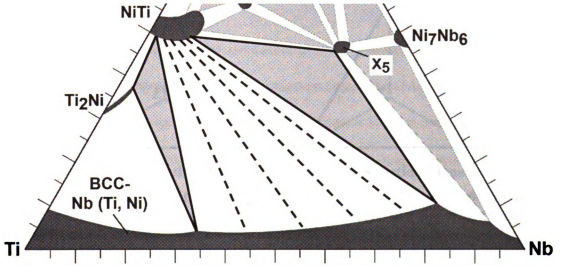

Figure 1.15 Examples of tie-lines and tie-triangles in a ternary phase diagram.

1.7.2 Classes of Ternary Four-Phase Equilibrium

As mentioned previously, a ternary system can have up to four phases coexisting in equilibrium at a single point in the composition-temperature space diagram. There are three possible classes of four-phase equilibria in a ternary system, namely the Class-I, Class-II and Class-III equilibria. Class-I equilibrium occurs at a particular composition when a single liquid (L) phase freezes isothermally into three different solid phases (α, β and γ) [Rhines 1956A]. It can be considered a ternary eutectic reaction, which is mathematically expressed in Eq. (1.15).

$$L \xrightarrow{Cooling} \alpha + \beta + \gamma \; ; \; L \xleftarrow{Heating} \alpha + \beta + \gamma \qquad \text{Eq. (1.15)}$$

Class-I equilibrium is represented in a phase diagram by a reaction plane that exists at a particular temperature. Figure 1.16 illustrates the plan-view of the reaction plane involving α, β, γ and L.

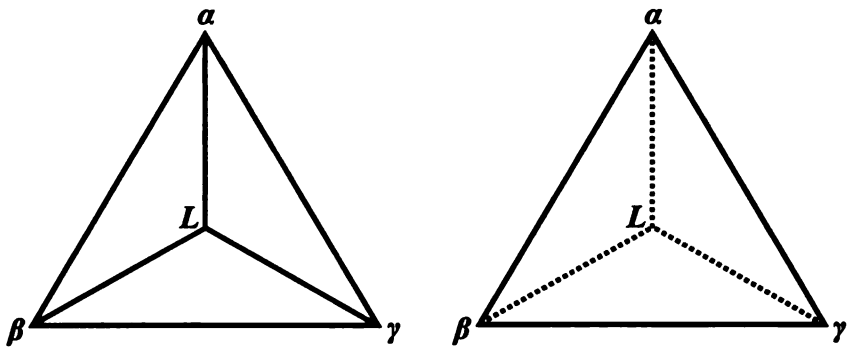

Above Reaction Plane **Below Reaction Plane**

Figure 1.16 Schematic of a ternary 4-phase Class-I reaction plane. ($\alpha + \beta + L$), ($\alpha + \gamma + L$) and ($\beta + \gamma + L$) tie-triangles are above the reaction plane. ($\alpha + \beta + \gamma$) tie-triangle is below the reaction plane.

The temperature axis is pointing out of the plane of the page. Just above the reaction temperature, the reaction plane consists of three tie-triangles, namely the ($\alpha + \beta + L$), ($\alpha + \gamma + L$) and ($\beta + \gamma + L$). Below the reaction temperature, the reaction plane consists only of a single tie-triangle of ($\alpha + \beta + \gamma$). Any initial liquid composition that falls within this reaction plane will eventually produce a ($\alpha + \beta + \gamma$) – ternary eutectic solid when cooled below the reaction temperature. An example of the four-phase Class-I reaction is the equilibrium among NiTi, X_3, X_5 and liquid phases in the Ni-Ti-Nb system, which is illustrated in Figure 1.17.

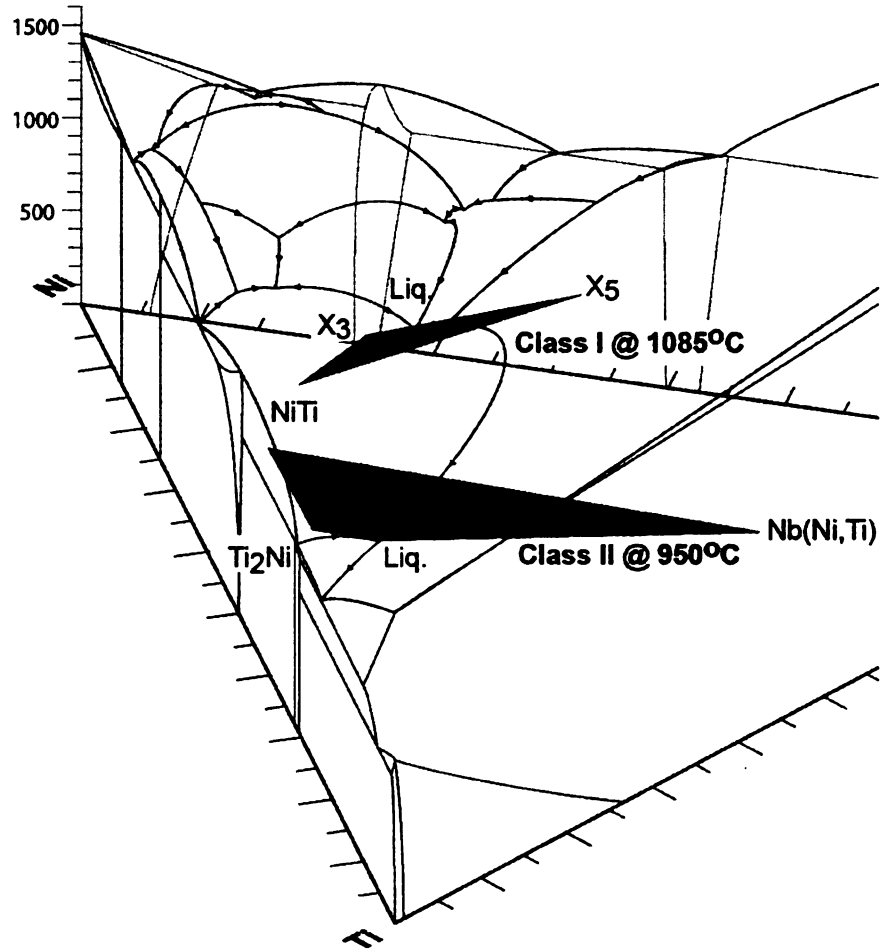

Figure 1.17 Four-phase Class-I (NiTi, X_3, X_5 and Liquid) and Class-II (NiTi, Ti_2Ni, Nb(Ni,Ti) and Liquid) reaction planes in the Ni-Ti-Nb ternary phase diagram illustrated in 3D.

Ternary four-phase Class-II equilibrium is one that may be thought of as being intermediate between eutectic and peritectic reaction [Rhines 1956B], which does not exist in binary systems. The reaction, which is also represented by a plane in the ternary phase diagram (see Figure 1.17), can be expressed as,

$$L + \alpha \xrightarrow{Cooling} \beta + \gamma \; ; \; L + \alpha \xleftarrow{Heating} \beta + \gamma \qquad \text{Eq. (1.16)}$$

During heating or cooling, two phases react to form two new phases. Figure 1.18 shows that just above the reaction temperature, the reaction plane consists of two tie-triangles, namely the ($\alpha + \beta + L$) and ($\alpha + \gamma + L$). Below the reaction temperature, the reaction plane consists of two different tie-triangles, namely the ($\alpha + \beta + \gamma$) and ($\beta + \gamma + L$). For the case of cooling, four scenarios are possible depending on the overall composition of the system. Consider alloys of 4 different compositions, *A*, *B*, *C* and *D* that will be cooled through the Class-II reaction plane (Figure 1.18). Due to the difference in initial compositions, each alloy will undergo different reaction pathways that are summarized as follow:

$$\text{A: } \alpha + \beta + L \longrightarrow \alpha + \beta + \gamma \qquad \text{Eq. (1.17)}$$

$$\text{B: } \alpha + \gamma + L \longrightarrow \alpha + \beta + \gamma \qquad \text{Eq. (1.18)}$$

$$\text{C: } \alpha + \beta + L \longrightarrow \beta + \gamma + L \qquad \text{Eq. (1.19)}$$

$$\text{D: } \alpha + \gamma + L \longrightarrow \beta + \gamma + L \qquad \text{Eq. (1.20)}$$

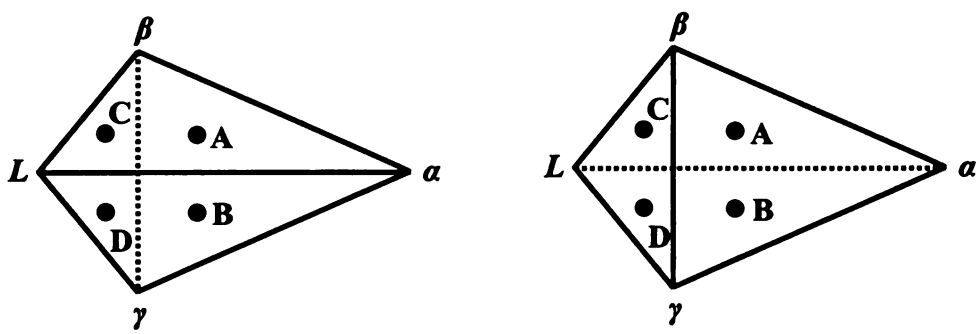

Above Reaction Plane **Below Reaction Plane**

Figure 1.18 Schematic of a ternary 4-phase Class-II reaction plane. ($\alpha + \beta + L$) and ($\alpha + \gamma + L$) are above the reaction plane. ($\alpha + \beta + \gamma$) and ($\beta + \gamma + L$) are below the reaction plane.

Ternary four-phase Class-III equilibrium is analogous to a peritectic reaction in the binary system [Rhines 1956C]. It can also be thought of as an inverse of the Class-I equilibrium, where upon cooling, three phases react isothermally to form a single new phase (Figure 1.19). The reaction pathway is described as follows:

$$L + \alpha + \beta \xrightarrow{Cooling} \gamma \; ; \; L + \alpha + \beta \xleftarrow{Heating} \gamma \qquad \text{Eq. (1.21)}$$

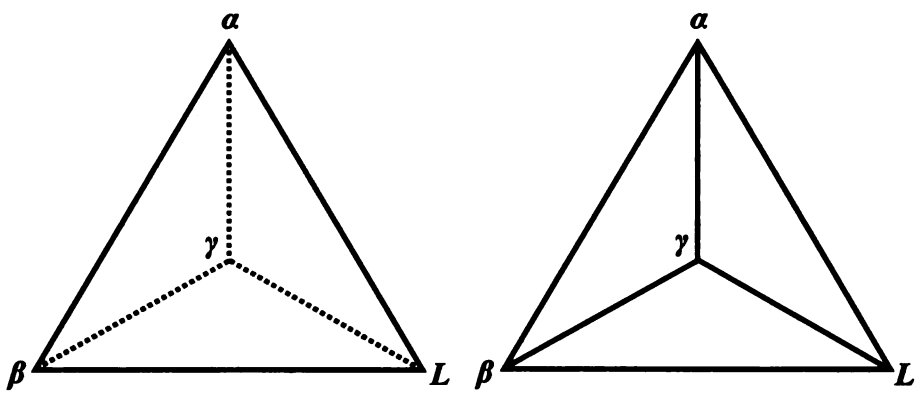

Above Reaction Plane **Below Reaction Plane**

Figure 1.19 Schematic of a ternary 4-phase Class-III reaction plane. $(\alpha + \beta + L)$ tie-triangle is above reaction plane. $(\alpha + \gamma + L)$, $(\beta + \gamma + L)$ and $(\alpha + \beta + \gamma)$ tie-triangles are below the reaction plane.

1.7.3 Isothermal Sections and Isopleths

The illustrations of three-dimensional ternary phase diagrams are often simplified further through constructions of two-dimensional horizontal and vertical sections. The former is known as an isothermal section, while the latter is termed an isopleth. Both forms will be widely-used in this dissertation. An isothermal section, which is illustrated in 3D in Figure 1.20, allows the location of phase fields at a particular temperature to be visualized more easily.

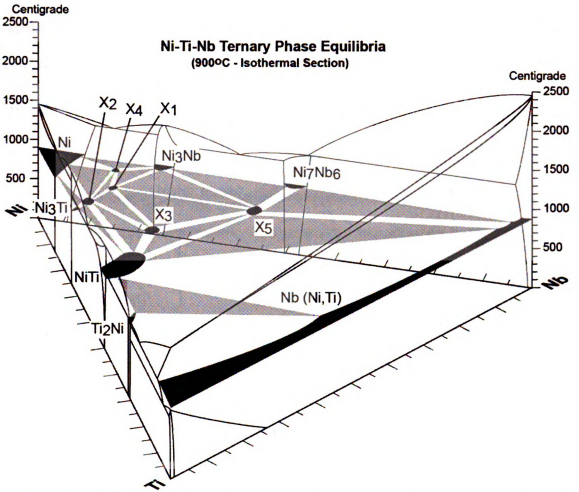

Figure 1.20 Three-dimensional view of a 900°C – isothermal section in a Ni-Ti-Nb ternary phase diagram.

Because of their resemblance to binary phase diagrams, isopleths are also widely-used to illustrate phase evolution at a particular composition as a function of temperature. Liquidus and solidus temperatures for any alloys represented can also be read from these vertical sections. However, it is not usually possible to represent tie-lines in an isopleth because tie-lines will not generally lie in the plane of the isopleth, with the exception of quasibinary sections. Isopleths selected for study are usually (1) those that originate from one corner of the Gibbs triangle and end at mid-point of the opposite edge, therefore representing a fixed ratio of two of the components (Figure 1.21), or (2) those that are

parallel to one edge of the phase diagram, representing a constant fraction of one of the components, or (3) those that extend from one binary line compound to another (e.g. Ni_3Ti to Ni_3Nb).

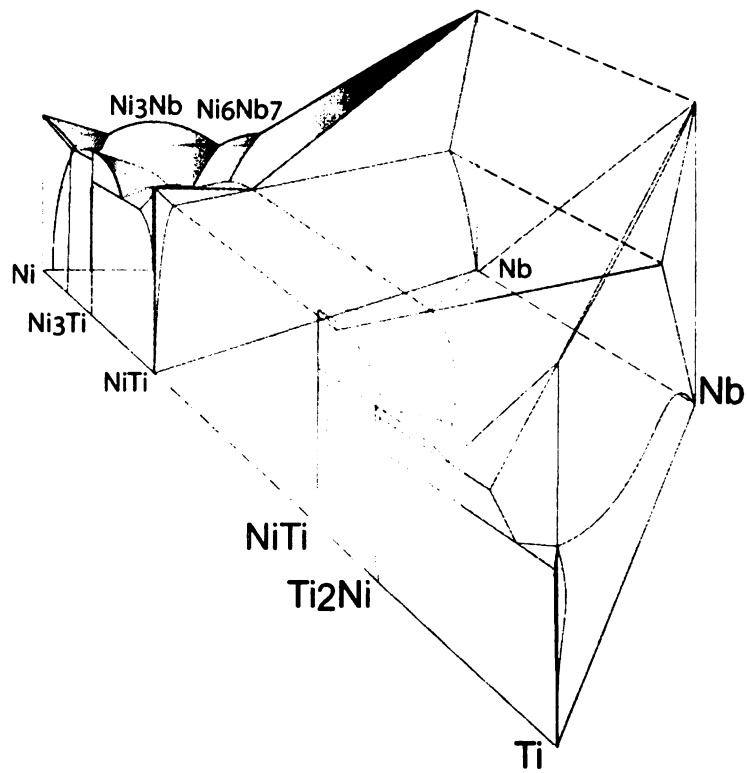

Figure 1.21 Three-dimensional view of a split Ni-Ti-Nb ternary phase diagram, exposing the NiTi-Nb quasibinary section or isopleth.

When a congruently-melting intermediate phase occurs in a ternary system, it sometimes happens that this phase forms a quasibinary system with one of the other phases. An example is shown in Figure 1.21, where a quasibinary system exists between the intermediate NiTi phase of the binary system Ni-Ti and the Nb component of the ternary system. A vertical section taken along the line joining these two phases will be, in all respects, equivalent to a binary phase diagram. The line that joins these two phases is also known as the Alkemades line (see below) [Hillert 1998]. All tie-lines in two-phase fields will lie in the plane of the section, while three-phase equilibrium will be

represented by a single horizontal line. No four-phase equilibrium can occur in the quasibinary section. All alloys behave as though binary in their structural response to temperature changes.

1.7.4 Alkemades Theorem

Another important feature of ternary phase diagram is its liquidus projections. It provides information on the change in liquid composition and the type of reaction involved (e.g. eutectic or peritectic, class-I, II or III) as an alloy is freezing. The directions of decreasing temperature of liquidus lines can be predicted using the Alkemades theorem [Hillert 1998], which states that the intersection of a liquidus line (or extrapolated liquidus line) with its corresponding Alkemades line (or extrapolated Alkemades line) is a temperature-maximum on the liquidus line and a temperature-minimum on the Alkemades line [Hillert 1998]. Alkemades lines are those that serve to connect two solid phases that share a common liquidus boundary.

An example is shown in Figure 1.22a. It shows a ternary system with a congruently-melting binary intermediate phase, *D*, and three other primary phases, *A*, *B* and *C*. The liquidus projection of the ternary system is also illustrated. In order to know the direction of decreasing temperature for the liquidus line separating *C* and *D*, an Alkemades line *CD* is drawn to connect *C* and *D*. Figure 1.22a shows that the liquidus line intersections the Alkemades line. Hence, a temperature-maximum exists on the liquidus line at the intersection and temperature decreases on either side as illustrated in Figure 1.22a. On the other hand, temperature decreases from either end of the

Alkemades line and a temperature-minimum occurs at the intersection with the liquidus line. Based on the Alkemade's theorem, directions can be assigned to the rest of the liquidus projections (Figure 1.22b).

Another example shown in Figure 1.23 describes a ternary system with an incongruently-melting binary intermediate phase, *E*, and the same primary phases, *A*, *B* and *C*. Given that the liquidus line between *C* and *E* does not intersect the corresponding Alkemades line, the liquidus line is extrapolated to facilitate the intersection (dotted-line in Figure 1.23). Therefore, direction can now be assigned to the liquidus line as shown in Figure 1.23.

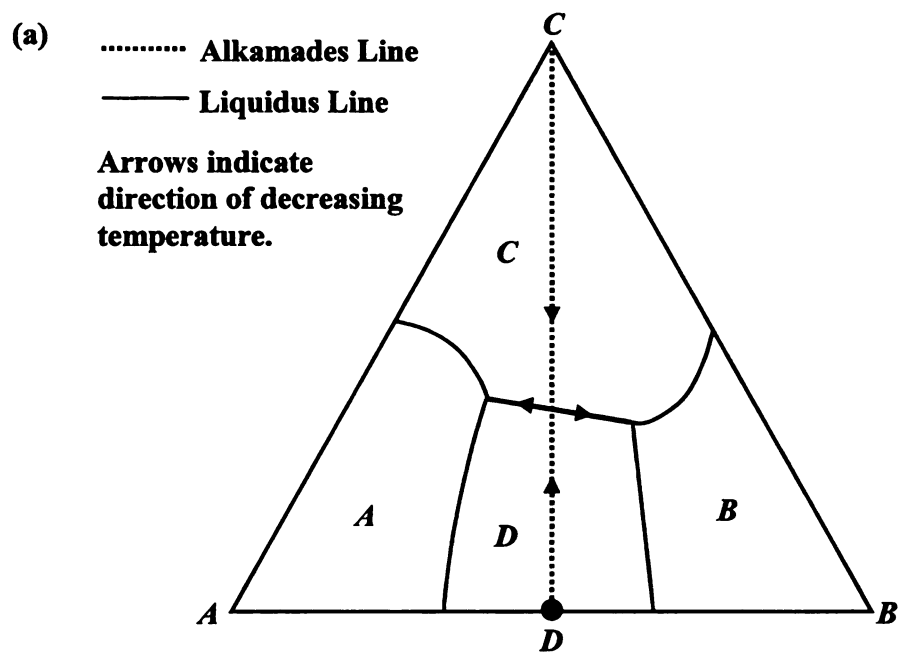

Figure 1.22 Schematic diagram of a ternary system with a congruently-melting phase, *D*, showing (a) the construction of Alkamades line *CD* and the directions of decreasing temperatures on the liquidus and Alkamades lines of concern; (b) the directions of decreasing temperatures on the rest of the liquidus projection, based on the Alkamades theorem.

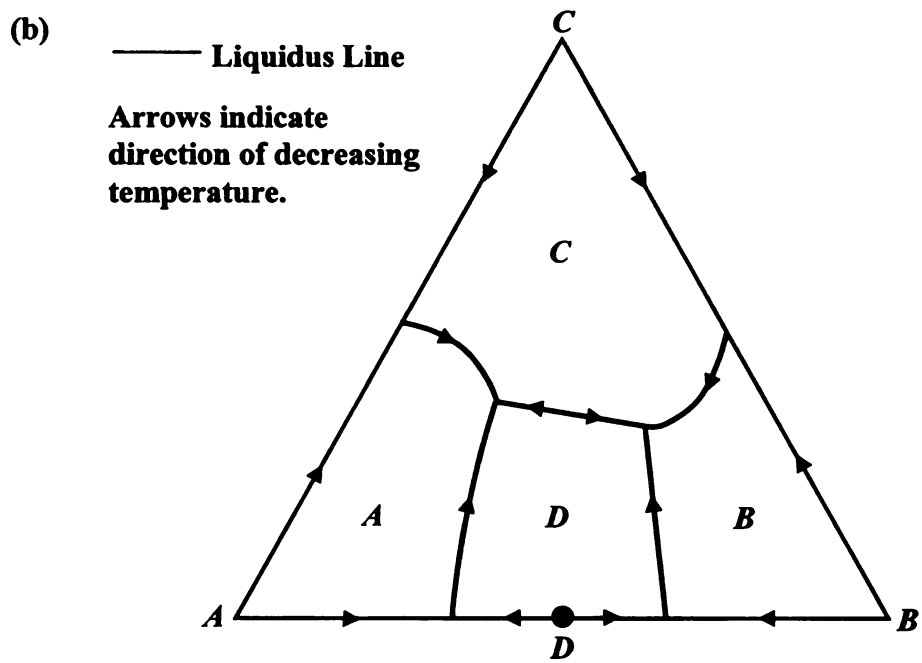

Figure 1.22 (Continued).

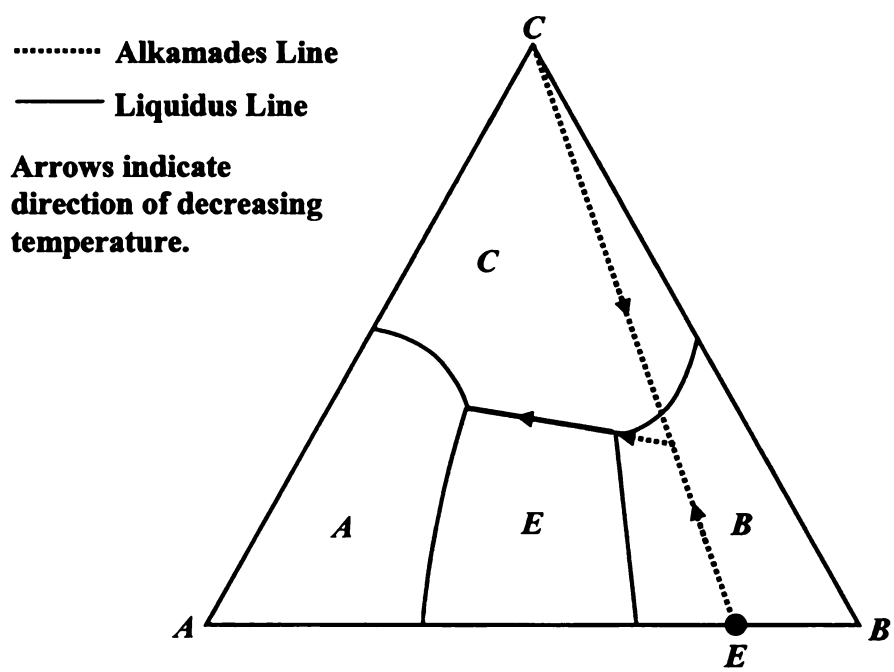

Figure 1.23 Schematic diagram of a ternary system with an incongruently-melting phase, *E*, showing the construction of Alkamades line *CE* and the directions of decreasing temperatures on the liquidus and Alkamades lines of concern.

CHAPTER 2: EXPERIMENTAL METHODOLOGY

2.1 Introduction

Details on experimental procedures are discussed in this chapter. Specifically, methodologies for specimen cleaning, brazing, annealing and alloying are provided, followed by details of sample preparation for electron microscopy. Mechanical testing procedures will be covered at the end of the chapter.

2.2 Surface Cleaning

Two types of base-NiTi alloys were employed in this work. They were room-temperature shape-memory (50 at.%Ni-Ti) and superelastic (51 at.%Ni-Ti) alloys with nominal thicknesses of 3.175 mm and 1.588 mm, respectively. Both alloys were supplied by Nitinol Devices and Components Inc. The room-temperature shape-memory alloy was mainly used for microstructural and indentation studies, while the superelastic form was extensively employed for preparing single-lap and butt-joints. The lateral dimensions for each purpose will be discussed in subsequent sections.

Prior to braze processing, native oxides on NiTi surfaces were chemically-removed. Surface cleaning was similar for both NiTi alloys used. The base-alloys were immersed in a pickling solution, consisting of $1HF:20HNO_3:10H_2O$ (by volume), for about 5 minutes. The oxide-removal process was then terminated by rinsing the NiTi sections in water. Base-NiTi and Nb braze foils were ultrasonically-cleaned in acetone, followed by methanol in order to remove organic contaminants.

2.3 Braze and Post-braze Processing

All braze processes were performed in a Centorr M60 vacuum annealing furnace. The specimen chamber is evacuated by a Varian VHS-4 diffusion pump and is capable of maintaining a base pressure better than 4×10^{-6} Torr. The hot zone is cylindrical, 2.5" in diameter and 6" in length. Specimens and an Omega Type-K thermocouple probe were positioned close to the center of the hot zone to ensure uniformity and accuracy in temperature measurements.

Braze specimens were in the form of an NiTi/Nb/NiTi stacking configuration. The Nb foils, which were acquired from ESPI Metals Inc., were held between the base-NiTi via spot-welding at their corners. No external pressure was applied to the samples during brazing. The fabrication of butt-joint specimens will be elaborated in the *Tensile Testing* section.

After loading of specimens into the vacuum chamber, degassing was performed at 250°C for at least 3 hours. Brazing was allowed to commence when base pressure was in the range of 10^{-6} Torr. Approximately 2800W of power was consistently applied to the heating elements to achieve a constant temperature ramp-up profile for all braze processes. Upon attaining the desired braze temperature, power to the heating elements was manually controlled to maintain the desired braze temperature, which in most cases were 1185°C. The manual control of braze temperature involves an error of +/- 5°C. During brazing, chamber pressure occasionally crept up to about 2×10^{-5} Torr. However,

pressure remained in the range of 10^{-6} Torr throughout most stages of the braze process. Termination of brazing was effected by shutting off power to the heating elements. Specimens were cooled naturally in the vacuum furnace before removing them from the chamber. Representative temperature-time and pressure-time profiles for the braze process are shown in Figure 2.1.

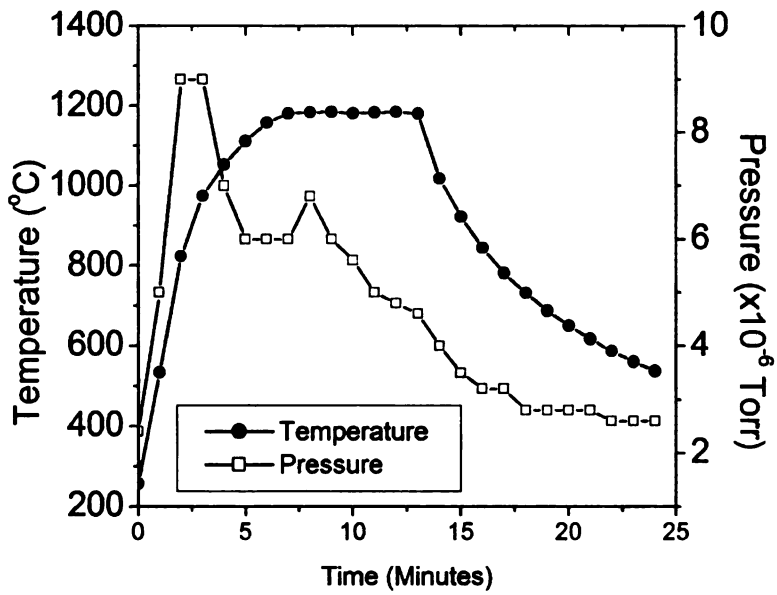

Figure 2.1 Typical temperature-time and pressure-time profiles of a braze process.

Post-braze heat treatments of braze joints were performed in air, using a Lindberg resistance-heated furnace. Temperature in the furnace was monitored by a K-type thermocouple. Heat-treated specimens were cooled by quenching in room-temperature water promptly upon removal from the furnace.

2.4 Micro-alloying with Tungsten in Nb-based Braze Joints

Tungsten was alloyed into Nb-based braze joints by coating Nb braze foils. Films of tungsten were deposited on Nb foils by DC magnetron sputtering at room-temperature

under a base vacuum of 2 x 10^{-6} Torr using a 3"-diameter Kurt J. Lesker Torus gun and MDX1K power supply. Argon working pressure during sputtering was 5 mTorr. Power applied to the cathode was maintained at 200W, while working distance from the tungsten sputter target to the substrate was 50 mm. The deposition rate was first determined before the actual film deposition runs. Tungsten films were deposited on glass microscope slides separately with increasing sputtering durations. The thicknesses of the films were measured using a Wyko optical profilometer. A plot of thickness vs. deposition time is provided in Figure 2.2. Linear regression of the data points estimated the deposition rate to be 0.1 μm per minute.

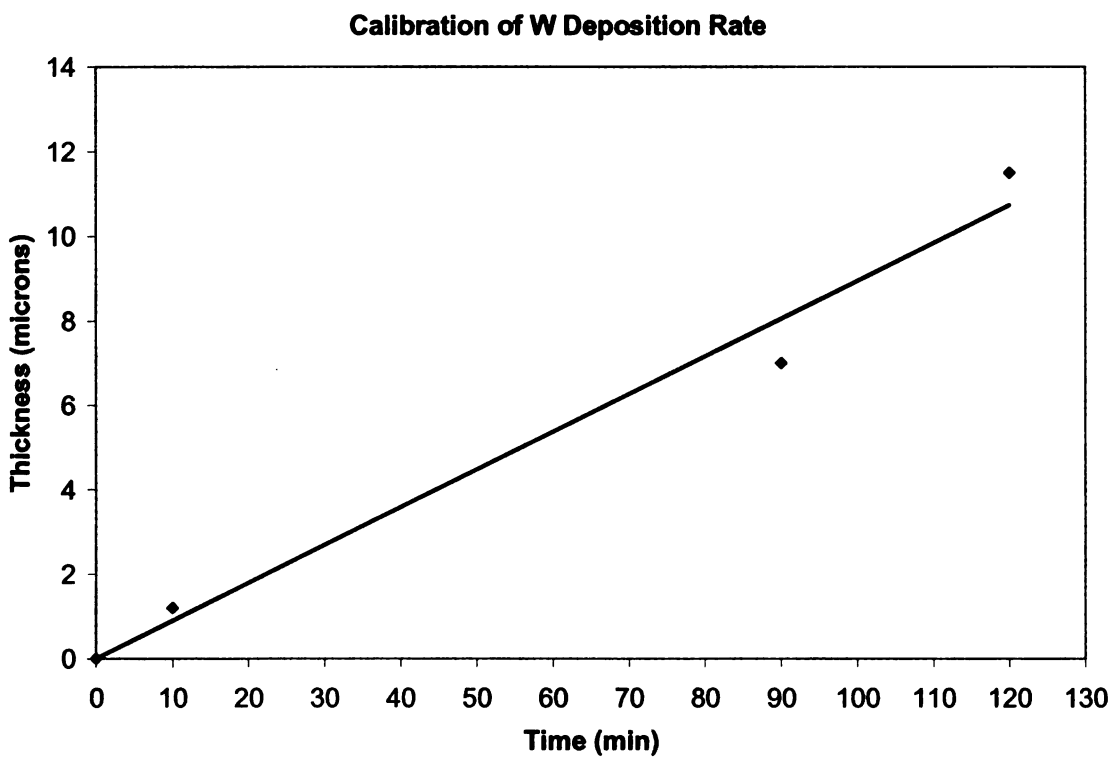

Figure 2.2 Plot of thickness vs. deposition time of tungsten at a cathode power of 200W, argon working pressure of 5 mTorr and working distance of 50 mm.

For the W-alloying studies discussed in Chapter 5, 1 μm of tungsten was deposited on 51 μm-thick Nb foils, which yield a composition of approximately 2 vol.%. Assuming theoretical density, this thickness will coincidentally also produce an overall braze foil composition of about 2 at.% tungsten.

The procedures and experimental conditions for the Nb film depositions on NiTi alloys were similar to those described for tungsten deposition. Niobium film depositions were required in an experiment that studied the effects of braze width on isothermal solidification time, which is discussed in Chapter 3. Niobium films of approximately 6 μm thick were deposited onto 300 μm thick superelastic NiTi strips as the braze filler for the experiment. The deposition rate for Nb was also found to be about 0.1 μm per minute.

2.5 Sample Preparation and Setup for SEM and TEM Studies

For scanning electron microscopy (SEM) studies, cross-sections of as-brazed specimens were first ground using progressively finer grit SiC abrasive papers (from 240-grit to 600-grit), followed by polishing with progressively finer Al_2O_3 powders (from 5 μm to 0.05 μm). Polishing was terminated only after mirror-like finishes of specimen surfaces were achieved. Finally, specimen surfaces were chemically-etched prior to SEM observations using a solution of $1HF:2HNO_3:10H_2O$ (by volume). Etching time was restricted to less than 10 seconds to limit formation of etch pits.

Most SEM observations were performed using a Hitachi S2500 SEM under an accelerating voltage of 25 KV at a working distance of 10 mm. All images shown were

taken in secondary electron (SE) mode, unless otherwise specified. X-ray fluorescence experiments were conducted using an Oxford Instruments detector in the SEM under an accelerating voltage of 20KV. All energy spectra were collected under the same acquisition duration of 120 seconds with spectrometer dead-time less than 30%. Calibration was performed on Ni, Ti and Nb standards and the *ZAF* correction was applied to all XRF quantitative results. The *ZAF* scheme corrects for matrix effects from the specimen, which are affected by atomic number, absorption and fluorescence. Details on *ZAF* corrections are described in [Flegler et al. 1993].

For Transmission Electron Microscopy (TEM) studies on the eutectic joints, approximately 500 μm-thick cross-sectional slices of the joint area were cut (see Figure 2.3). These bulk slices were mechanically-thinned down to less than 20 μm using SiC abrasive papers before being mounted onto open-aperture copper grids of 3 mm in diameter using vacuum-compatible Gatan *G1* epoxy. Excess material outside the copper grid was carefully trimmed away using fine surgical scissors. Next, eutectic joint areas of the samples were ion-milled down to electron transparency using the Gatan Precision Ion Polishing instrument. A milling angle of 4° and Ar ion energy of 4.0 KeV were employed throughout the thinning process. Penetration of light through the thinned area would indicate perforation and possible electron transparency along the perimeter of the hole(s), which were achieved within 4 to 6 hours of milling time. All samples were plasma-cleaned for 2 minutes before loading into the TEM specimen airlock.

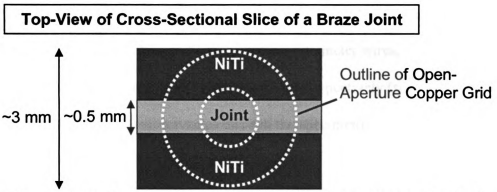

Figure 2.3 Schematic diagram showing top-view of the cross-sectional slice of a eutectic joint that would eventually be prepared as a TEM specimen. (The dotted circle indicates the outline of the open-aperture copper grid that will be attached to the specimen.)

Transmission electron microscopy studies were mainly conducted using a JEOL 2200FS field-emission TEM, which is also equipped with a similar XRF system to the SEM. Imaging was performed under bright-field conditions under an accelerating voltage of 200KV, while diffraction patterns were obtained using selected-area diffraction apertures. Quantitative results from XRF experiments in the TEM were corrected by the Cliff-Lorimer approach for thin-foils, which is described in [Flegler et al. 1993]. This correction scheme requires knowledge of the mass-density and thickness of the specimen foil. In this case, mass-density of NiTi is 6.45 g/cm^3, while the thickness was assumed to be 100 nm. Spectrum acquisition duration was 120 seconds and dead-time never exceeded 30%.

2.6 Tensile Testing

Butt-joint specimens were prepared using 50.8 mm (L) x 25.4 mm (W) NiTi coupons with slits cut almost across the widths (see Figure 2.4). The nominal coupon thickness for room-temperature shape-memory NiTi was 3.175 mm, while thickness for

room-temperature superelastic NiTi was 1.588 mm. The slits were electro-discharge machine (EDM)-cut with either 254 μm- or 356 μm -diameter wires, resulting in initial joint clearances of approximately 300 μm or 400 μm, respectively (some material loss occurred close to the wire as it traverses through the specimen).

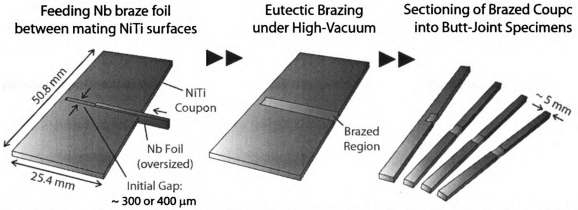

Figure 2.4 Schematic diagrams showing the procedures for fabricating NiTi butt-joint specimens.

After removing native oxides from the NiTi coupons, sufficient Nb braze foils were fed into the slits until they fit snugly between the mating NiTi surfaces. The Nb foils were deliberately oversized (i.e. wider than the thicknesses of the NiTi coupons) by about 50% so that sufficient braze liquid would form to completely fill up the gap. The Nb-filled NiTi coupons were individually loaded into the vacuum furnace for braze processing. Finally, brazed coupons were EDM-sectioned into approximately 5 mm-wide butt-joined bars for tensile testing. End pieces from each coupon were discarded. Tensile tests were performed using an Instron screw-driven universal testing instrument at room temperature. The gage length of butt-joints was fixed at 30 mm and tests were conducted at an elongation rate of 0.1 mm/s (measured at cross-head).

2.7 Micro- and Nanoindentation

Nanoindentation was carried out using the MTS Nanoindenter XP with a diamond Berkovich indenter. Hardness and elastic modulus were calculated from the basis of Oliver and Pharr's model [Oliver et al. 1992]. This model states that as the indenter tip is pressed into the specimen, elastic and plastic deformations occur, forming an impression related to the geometry of the indenter and to the plastic deformation mechanisms that occurred in the material. Figure 2.5 shows a typical load vs. displacement curve associated with loading and unloading during nanoindentation experiments.

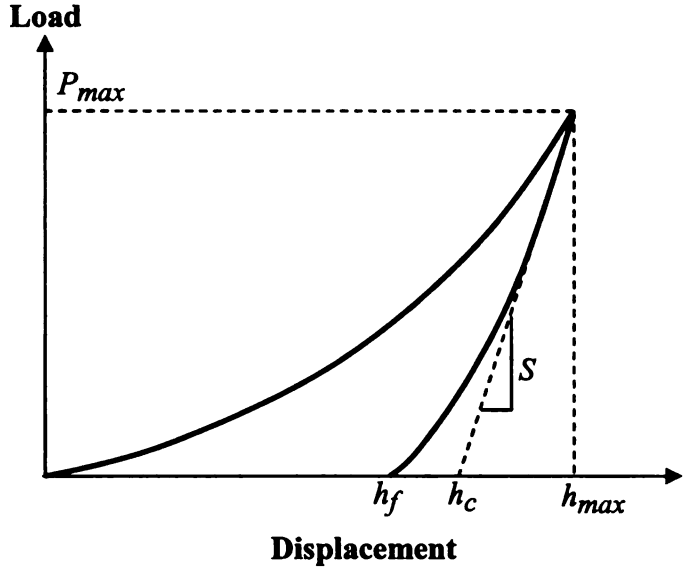

Figure 2.5 A typical load vs. displacement curve associated with loading and unloading during nanoindentation experiments.

In Figure 2.5, h_{max} represents the displacement at peak load, P_{max}, while h_c is the indenter displacement projected from the tangent of the initial unloading slope and h_f is the final displacement upon complete unloading. Given that only the elastic component of the displacement is recovered upon retracting the indenter from the specimen (see

Figure 2.5), elastic modulus of the specimen can be calculated from the initial unloading contact stiffness, S. The unloading curve in Figure 2.5 can be described as a power law function [Oliver et al. 1992]. Its mathematical form is shown in Eq. (2.1),

$$P = B(h - h_f)^m \qquad \text{Eq. (2.1)}$$

where B and m are empirically-determined fitting parameters. By differentiating Eq. (2.1) at h_{max}, S can be determined.

$$S = \left(\frac{dP}{dh}\right)_{h=h\max} = Bm(h - h_f)^{m-1} \qquad \text{Eq. (2.2)}$$

An expression was established by Sneddon [Sneddon 1965] involving contact stiffness, S, contact area, A_c, and reduced modulus, E_r, which is shown in Eq. (2.3),

$$S = 2\beta E_r \sqrt{\frac{A_c}{\pi}} \qquad \text{Eq. (2.3)}$$

where β is a constant that depends on the geometry of the indenter (β = 1.034 for a Berkovich indenter). E_r is a modulus that accounts for elastic deformations in both specimen and indenter.

The mathematical form of E_r is given in Eq. (2.4),

$$E_r = \frac{1-\upsilon^2}{E} + \frac{1-\upsilon_{indenter}}{E_{indenter}} \qquad \text{Eq. (2.4)}$$

where E and υ are the elastic modulus and Poisson's ratio for the specimen, respectively. In this study, a diamond Berkovich indenter was used where $E_{indenter} = 1141$ GPa and $\upsilon_{indenter} = 0.07$.

The contact area, A_c, can be obtained from the tip area function, as shown in Eq. (2.5). The first term corresponds to a perfect Berkovich indenter, while the last 2 terms were attributed to tip imperfections and were determined from calibrations performed on fused silica.

$$A_c = 24.56h_c^2 + 243.05h_c - 176.15\sqrt{h_c} \qquad \text{Eq. (2.5)}$$

The contact depth, h_c, can be approximated using the following relation,

$$h_c = h_{\max} - \varepsilon\frac{P_{\max}}{S} \qquad \text{Eq. (2.6)}$$

where ε is a indenter geometry-dependent parameter. In this case, ε = 0.75 for a Berkovich indenter.

The indentation strain rate, ζ, is defined as the descent rate of the indenter, $\frac{dh}{dt}$, divided by its current depth, h. That is,

$$\zeta = \left(\frac{dh}{dt}\right)\left(\frac{1}{h}\right) \qquad \text{Eq. (2.7)}$$

The nanoindentation hardness, H, is defined as the indentation load at maximum displacement divided by the corresponding contact area. Given that P_{max} and A_c are known, hardness can easily be calculated from Eq. (2.8).

$$H = \frac{P_{\max}}{A_c} \qquad \text{Eq. (2.8)}$$

Prior to conducting actual experiments, indentations on polished Al_2O_3 (99% density) were performed at holding depths of 50 nm, 100 nm and 200 nm with a strain rate of 0.001 per second. This was to verify accuracy of the indenter tip shape function described in Eq. (2.5). At least 10 indents were made at each depth. Using a Poisson's ratio of 0.18 for Al_2O_3, the Oliver and Pharr [Oliver et al. 1992] model was employed for calculating the hardness and elastic modulus of Al_2O_3. Results are shown in Figure 2.6.

The calculated hardnesses and elastic moduli were found to be reasonably constant across these indentation holding depths. The average hardness and modulus were determined to be 27.3 GPa and 402 GPa, respectively, which are consistent with values reported by [Munro 1997, Krell et al. 2001].

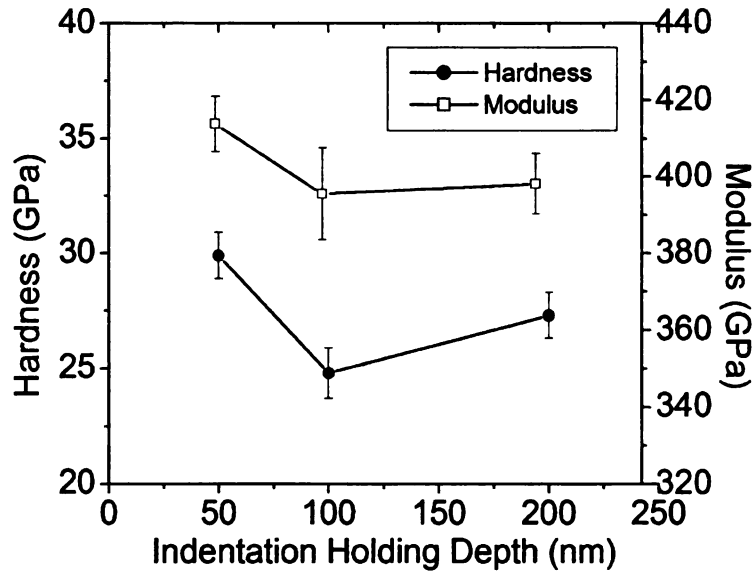

Figure 2.6 Hardness and elastic modulus of alumina derived from various indentation holding depths.

The indenter was then tested against pure Nb at various indentation holding depths. The strain rate was similar to that for Al_2O_3. At least 10 indents were made at each depth. Hardness and elastic modulus were calculated based on a Poisson's ratio of 0.38. Again, the mechanical properties remained reasonably consistent across the studied range of indentation depths (Figure 2.7). Mean hardness and modulus were 1.2 GPa and 99 GPa, respectively, which agree reasonably well with values reported by [Myneni et al. 2003, Wang et al. 2005, Alkorta et al. 2006]. The indents on pure Nb were observed in

SEM (Figure 2.8). No significant pile-up or sink-in behaviors were associated with these indents.

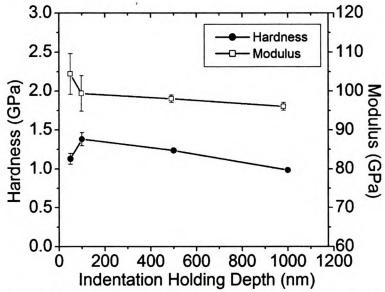

Figure 2.7 Hardness and elastic modulus of Nb derived from various indentation holding depths.

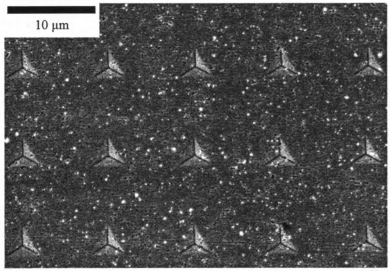

Figure 2.8 SEM micrograph showing an array of indents on pure Nb. (Indent depth of 500 nm.)

The verification studies on Al_2O_3 and pure Nb showed that reasonably accurate results can still be achieved with indentation depths as low as 50 nm. Hence, most of the nanoindentation work on pre-polished eutectic phase in braze joints and the base-NiTi alloy were conducted at holding depths of 50 nm. The reason for using a low indentation depth was to minimize the probability of probing any pro-eutectic NiTi phase that could be present beneath the exposed eutectic phase. Poisson's ratios of 0.30 were used for calculating indentation results derived from pure NiTi. Since there are no reported Poisson's ratio of the NiTi-Nb eutectic micro-constituent, a value of 0.35, intermediate of pure NiTi and Nb, was chosen for the indentation calculations.

Microindentations were employed to determine microscopic hardness. Experiments were conducted using Vickers indenter with a load of 300 grams. This load was selected as it produced indents that were almost as wide as the field-of-view of the microscope's eye-piece, hence minimizing measurement errors. Joint specimens were polished based on procedures described previously. The widths of indents were measured using the built-in microscope with a magnification of 50X. Only measurements of symmetrical indents were used for calculating hardness values.

CHAPTER 3: MICROSTRUCTURAL EVOLUTION IN REACTIVE EUTECTIC BRAZING

3.1 Introduction

In this chapter, results of experiments on the initial contact melting between base-NiTi and pure Nb filler metal, the propagation of the liquid, and termination stages (solidification) of the braze process will be presented. A diffusion-based numerical model is subsequently established to simulate the melting kinetics. Solidification products associated with the braze process will also be discussed. In particular, the effects of braze duration, post-braze anneal, surface preparation and vacuum conditions on microstructures and morphologies of the joints were extensively studied. In order to understand the origin of the NiTi quasibinary eutectic isopleth in the ternary system, the phase equilibria of Ni-Ti-Nb will be revisited. Finally, a section has been included that addresses the crystallography and phase equilibria of Ti_2Ni and $(Ti,Nb)_4Ni_2O$.

3.2 Nomenclature

The nomenclature adopted for most discussions in this chapter is introduced. Figure 3.1 shows the 'perfect' NiTi-Nb quasibinary eutectic isopleth that will be extensively used for discussions in terms of both thermodynamic and kinetic aspects of contact melting. The isopleth is analogous to a typical binary eutectic phase diagram with a quasibinary eutectic point at 26 at.% Nb occurring at 1170°C. Solidus compositions of NiTi and Nb at 1170°C were estimated from the literature [Gupta 1991, Prima et. al. 1995, Yang et. al. 2000, Matsumoto et. al. 2005] to be 7 at.% Nb and 91 at.% Nb, respectively. The origin of the perfect quasibinary eutectic isopleth in the

ternary system will be discussed in a later section. Two solid phases exist in Figure 3.1, which are the NiTi and Nb phases. Pure NiTi melts congruently at 1310°C, while pure Nb melts at 2469°C. Any liquid composition beyond the solubility limits of both solid phases will result in eutectic NiTi + Nb solidification.

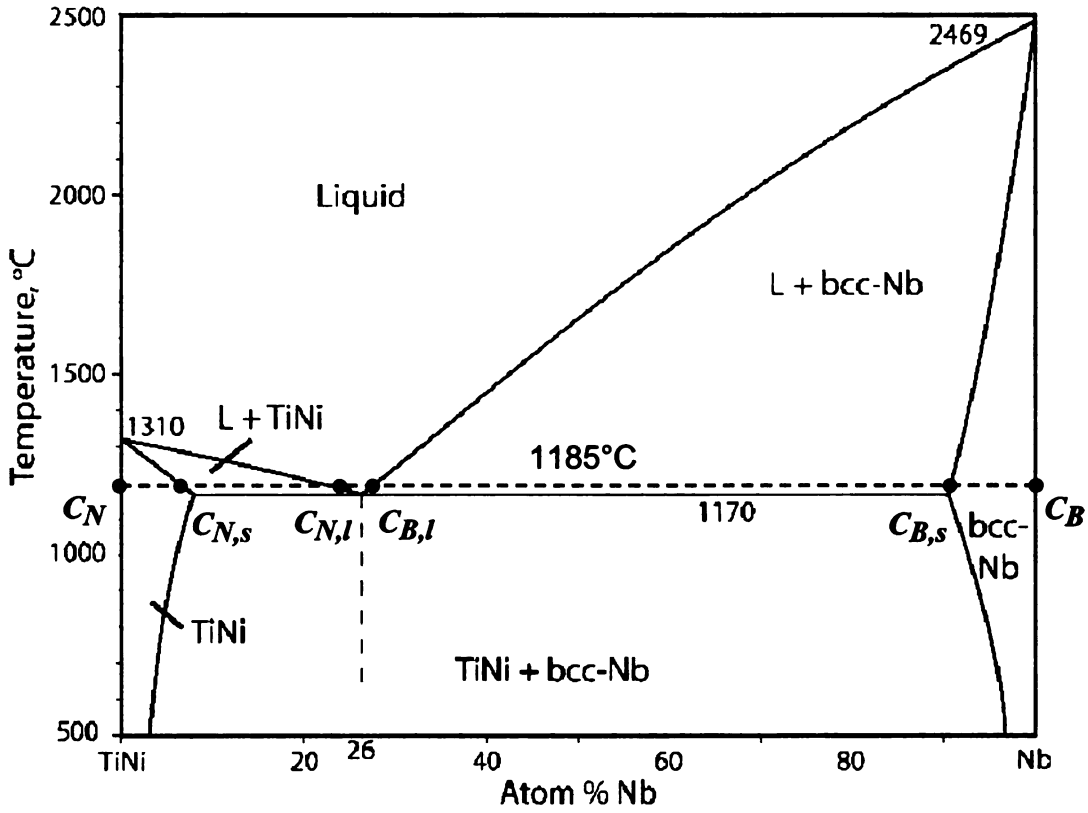

Figure 3.1 The 'perfect' NiTi-Nb quasibinary eutectic isopleth with key compositions labeled for 1185°C.

Given that most contact melting experiments were performed at 1185°C, the key compositions associated with NiTi and Nb phases at this temperature are represented by the symbols listed below. Values associated with the compositions (indicated by parentheses) were derived based on the assumption that the liquidus and solidus lines of Figure 3.1 are linear.

C_N: Pure NiTi (0.0 at.% Nb)

$C_{N,s}$: NiTi Solidus Composition (7.0 at.% Nb)

$C_{N,l}$: NiTi Liquidus Composition (23.2 at.% Nb)

$C_{B,l}$: Nb Liquidus Composition (26.9 at.% Nb)

$C_{B,s}$: Nb Solidus Composition (91.0 at.% Nb)

C_B: Pure Nb (100.0 at.% Nb)

C_E: Quasibinary Eutectic Composition (26.0 at.% Nb)

C_L: Instantaneous Average Liquid Composition = $(C_{N,l} + C_{B,l})/2$

All numerical modeling and related mathematical expressions were based on half-joint configuration as illustrated in Figure 3.2. Vector quantities abide by the convention that right-to-left direction is positive. The following lists the terms frequently used for discussion in this chapter and have also been labeled accordingly in Figure 3.2. Note that $J_{Ni} = J_{Ti}$ and $J_{NiTi} = J_{Ni} + J_{Ti}$ were assumed. Fluxes are in unit of $m^{-2}s^{-1}$, velocities in ms^{-1} and positions in m.

$J_{NiTi \rightarrow L}$: Flux of Ni plus Ti from solid NiTi into liquid

$J_{Nb \rightarrow L}$: Flux of Nb from solid Nb into liquid

$J_{NiTi \rightarrow Nb}$: Flux of Ni and Ti from liquid into solid Nb

$J_{Nb \rightarrow NiTi}$: Flux of Nb from liquid into solid NiTi

v_{NiTi}: NiTi-Liquid interface velocity

v_{Nb}: Nb-Liquid interface velocity

x_{NiTi}: NiTi-Liquid interface position (wrt to initial NiTi-Nb contact position)

x_{Nb}: Nb-Liquid interface position (wrt to initial NiTi-Nb contact position)

w: Liquid width of the half-joint configuration = $x_{NiTi} - x_{Nb}$

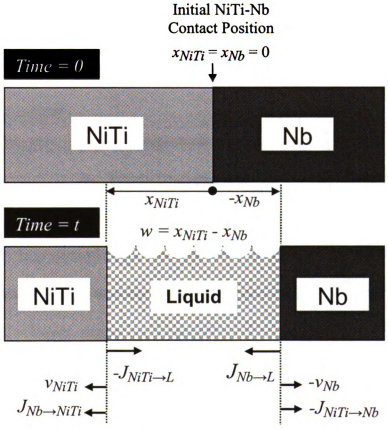

Figure 3.2 Schematic diagram of a half-joint configuration with frequently used terms indicated.

3.3 Contact Melting Mechanisms

In order to study the reactive brazing process, room-temperature shape-memory NiTi sheets (10.2 mm (L) x 7.6 mm (W) x 3.175 mm (T)) and 51 μm-thick Nb foils were stacked in a NiTi/Nb/NiTi configuration and brazed at 1185°C. Details on brazing procedures have been documented in Chapter 2, and will not be repeated here. Contact melting between the base-NiTi and Nb filler metal was found to occur at the braze temperature, resulting in liquid formation in the joint. The contact melting process can be classified into 3 stages. They are (1) *initial melting*, (2) *braze liquid propagation*, and (3) *termination*. Experimental observations pertaining to each of these stages of contact melting will be presented and discussed separately.

3.3.1 Initial Melting

Joint specimens were separately brazed at 1185°C for durations ranging from 5 seconds to 20 seconds. The braze temperature-time profiles were similar to that shown in Figure 2.1. A timer was initialized when temperature reached 1185°C and braze was terminated at progressively longer durations for each specimen with intervals of 5 seconds between them. It was found that braze liquid formed consistently only after a duration of 15 seconds, suggesting the presence of an 'incubation' period for contact melting to commence.

The incubation period might be attributed to the thermal inertia of the specimen requiring a finite amount of time for the joint area to approach braze temperature. A simple computation model was established to determine if thermal inertia is responsible

for the incubation time. The model is illustrated in Figure 3.3, which shows a half-joint configuration. The NiTi alloy and the Nb filler metal have thicknesses of 3.175 mm and 25.5 μm, respectively. The initial NiTi-Nb interface temperature, T_{int}, was 300°C (degassing temperature), while the specimen surface temperature, T_{surf}, was held indefinitely at 1185°C (brazing temperature). This give rise to an initial temperature difference, $\Delta T = T_{surf} - T_{int}$, of 885°C. The model assumed that heat can only flow to the NiTi-Nb interface through the NiTi surface.

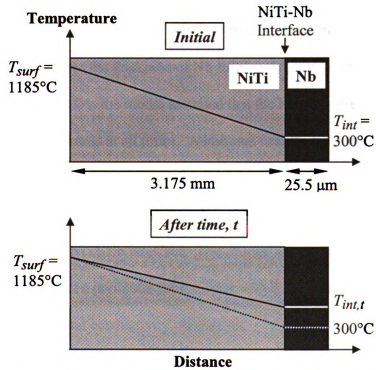

Figure 3.3 Schematic diagram showing the temperature profile across a half-joint as a function of time during the incubation period.

These initial conditions present an extremum situation that should provide an upper-bound to the time required for the NiTi-Nb interface temperature to reach 1170°C

(believed to be the onset temperature for contact melting) after the NiTi surface attains a temperature of 1185°C. But in actual experiments, ΔT should be smaller than 885°C because the NiTi surface and NiTi-Nb interface temperatures were both increasing dynamically over a finite amount of time during ramp-up such that T_{int} will be higher than 300°C when T_{surf} reaches 1185°C. Furthermore, besides the NiTi surfaces, heat can also enter through the edges. Hence, the actual duration for the NiTi-Nb interface to reach 1170°C (i.e. for melting to start) after the NiTi surface attains a temperature of 1185°C should be less than that predicted in the model.

Given the temperature setup, heat will flow from the specimen surface towards the NiTi-Nb interface. Since the thickness of Nb filler metal is significantly smaller than the thickness of the NiTi alloy, the model assumed that the Nb filler metal has a uniform temperature across its thickness at all times. Additional heat flowing across the NiTi-Nb interface will result in uniform temperature increment in the Nb filler metal. The model also assumed steady-state heat flow whereby a linear thermal gradient exists between the NiTi alloy surface and the NiTi-Nb interface. The change in heat flowing across the NiTi-Nb interface, $\Delta Q(t)$, at a particular time, t, over a finite time interval, Δt, can be determined using the thermal conductivity expression,

$$\Delta Q(t) = kA\left(\frac{\Delta T(t)}{x}\right)\Delta t \qquad \text{Eq. (3.1)}$$

where k is the thermal conductivity of NiTi, A is the NiTi-Nb interfacial area, which is conveniently chosen as unity, and x is the thickness of NiTi.

The heat input from $\Delta Q(t)$ caused $T(t)_{int}$ to increase to $T(t+1)_{int}$, hence decreasing the temperature difference between the surface and NiTi-Nb interface, $\Delta T(t+1)$, at time $t+1$. The change in $\Delta T(t+1)$ due to $\Delta Q(t)$ are mathematically expressed as,

$$T(t+1)_{\text{int}} = T(t)_{\text{int}} + \frac{\Delta Q(t)}{mC_p} \qquad \text{Eq. (3.2)}$$

$$\Delta T(t+1) = T_{surf} - T(t+1)_{\text{int}} \qquad \text{Eq. (3.3)}$$

where m is the mass of the Nb filler metal and C_p is the specific heat capacity of Nb.

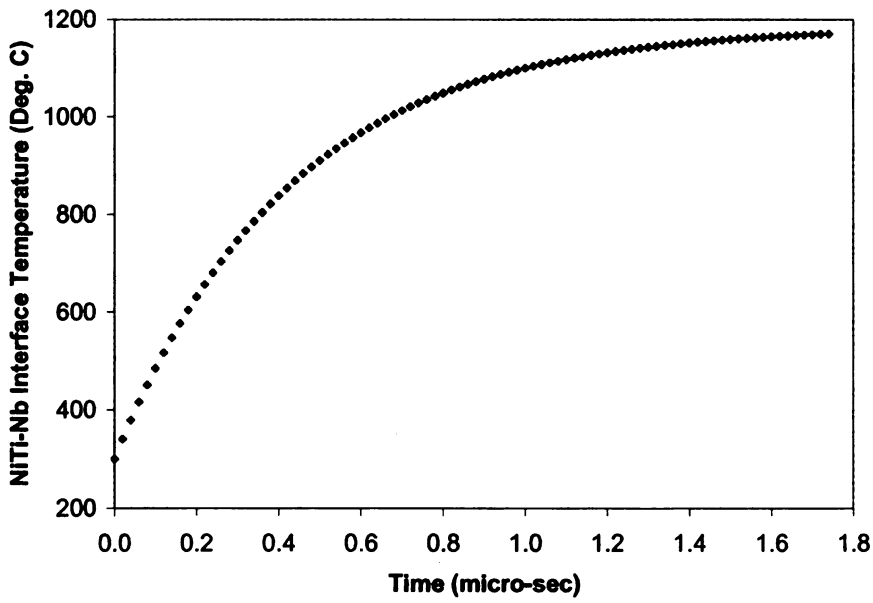

Figure 3.4 Predicted NiTi-Nb interface temperature as a function of time during the incubation period.

Using thermal conductivity of NiTi, $k = 41$ W/m-K [Yung et al. 2005], specific heat capacity of Nb, $C_p = 0.265$ J/g.K, and a time interval, $\Delta t = 20$ ns, the temperature at the NiTi-Nb interface, T_{int}, was predicted as a function of time using an explicit finite-difference scheme (2^{nd} order Runge-Kutta method) applied to Eq. (3.1) and (3.3). The simulation was terminated when T_{int} reached 1170°C. The program code was written in FORTRAN 77 and is provided in Appendix A.

Results from the numerical calculations shows that T_{int} increases rapidly from 300°C to 900°C, but the rate of increase retards significantly beyond 900°C (Figure 3.4). The simulation predicted that the time taken for the NiTi-Nb interface to start melting is about 1.7 μs from the time the NiTi surface reaches 1185°C. This predicted duration is almost 7 orders of magnitude smaller than the experimentally-observed incubation time, which strongly suggests that the incubation time for contact melting is not attributable to thermal inertia.

Alternatively, the incubation time might be due to the presence of thin surface oxide layers on NiTi and Nb serving as a temporary physical barrier for contact melting. These oxide layers would have formed during the short atmospheric exposure between cleaning and loading of samples into the vacuum chamber. Given that the braze chamber was only under moderate or high-vacuum, further oxidation of the specimens might also have occurred during the few minutes of ramping up to braze temperature. Hence, contact melting could only have occurred after Nb or Ni and Ti diffuses across this oxide

barrier in a finite amount of time, which manifests as the incubation period. To test the hypothesis of an oxide diffusion barrier, the characteristic diffusion lengths of Ni, Ti and Nb at 1170°C within a time frame of 15 seconds were estimated using Eq. (3.4).

$$L = \sqrt{4Dt} \qquad \text{Eq. (3.4)}$$

where L is the characteristic diffusion length, D is the diffusion coefficient and t is time.

Given that the intrinsic diffusion coefficients of NiTi and Nb at 1170°C are in the order of 10^{-12} [Bastin et al. 1974] and 10^{-15} m^2/s [Einziger et al. 1978], respectively, Eq. (3.4) shows that the characteristic diffusion lengths of these elements after an incubation time of 15 seconds range from about 200 nm to 7700 nm. Although oxide thickness measurements were not performed on the NiTi and Nb, it is reasonable to believe that tens to hundreds of nanometer thick oxides can form on these alloy/metal surfaces during the ramp-up stage, where the specimens were subjected to high temperatures under moderate or high vacuum conditions. The extent of oxidation is supported by the observation that alloy surfaces always have a yellowish-gold tint after brazing, indicating an oxide thickness about one-half the wavelength responsible for the color. Given that yellow and gold colors possess wavelengths within 570 – 620 nm, the approximate oxide thickness is about 300 nm. Since the calculated characteristic diffusion lengths fall within similar orders of magnitude with the predicted range of oxide thicknesses, it is reasonable to deduce that the incubation time for contact melting is attributed to the presence of oxide barriers on the NiTi and Nb mating surfaces.

It is crucial to highlight that superheating is not required for onset of melting (i.e. nucleation of liquid phase) [Porter et. al. 2001]. This can be understood from the relative free energies of the solid-liquid (γ_{SL}), liquid-vapor (γ_{LV}) and solid-vapor (γ_{SV}) interfaces, which are given by:

$$\gamma_{SL} + \gamma_{LV} < \gamma_{SV} \qquad \text{Eq. (3.5)}$$

Equation (3.5) implies that the wetting angle is zero, hence the absence of a nucleation barrier for melting. This is in contrast with solidification, where undercooling is required to overcome a nucleation barrier.

After Nb or Ni and Ti diffuse across the oxide layer, liquid forms and dissolves the oxide. In the following discussion, however, the presence of the oxide layer will be ignored. Experimental evidence, which will be provided in the next section, shows that melting commenced at the mating interface (hence, the term 'contact melting'). The driving force can be understood through analysis of the local concentration at the mating interface. First, surface atomic concentrations of NiTi and Nb of various low-index planes were calculated and summarized in Table 3.1. Since the base-alloy and filler metals used in this study were polycrystalline in nature, permutations of pairs of NiTi-Nb surface planes were performed to simulate some possible 'ideal interface' scenarios. The interface concentration, confined to the first-monolayers of NiTi and Nb, was then determined for each case. The purpose is to develop a general sense of the local concentrations at various NiTi-Nb interfaces. Calculations, shown in the matrix in Table

3.2, revealed that the NiTi-Nb interface generally have concentrations above 40 at.% Nb (average concentration is 61.5 at% Nb). These compositions fall between $C_{B,l}$ and $C_{B,s}$ or within the Nb + Liquid phase field of Figure 3.1, which are unstable against melting. Hence, contact melting occurred at the mating interface, producing the braze liquid.

Table 3.1 Surface atomic concentrations of NiTi and Nb on low-index planes.

Planes	**Surface Concentration of NiTi ($\times 10^{14}$ cm^{-2})**	**Surface Concentration of Nb ($\times 10^{14}$ cm^{-2})**
(100)	5.56	9.14
(110)	7.87	12.9
(111)	3.21	5.28

Table 3.2 Localized concentration at diffusion couple interface of various low-index plane combinations (First monolayer approximation).

Localized Concentration at Diffusion Couple Interface (at% Nb)				
		Contact Surface of Nb		
		(100)	(110)	(111)
Contact Surface of NiTi	(100)	62.2	69.9	48.7
	(110)	53.7	62.1	40.2
	(111)	74.0	80.1	62.2
Average			61.5	

3.3.2 Braze Liquid Propagation

After initial melting at the NiTi-Nb mating interface, propagation of the liquid phase occurred in the joint. A series of *ex-situ* SEM micrographs, capturing changes in the width of the liquid at 1, 8, 21 and 31 seconds of the NiTi-Nb contact melting process, are shown in Figure 3.5a – d, respectively. The braze durations stated in Figure 3.5 are actually resultant durations obtained by subtracting the incubation time from the total. Gray features at the top and bottom of the micrographs are the unmelted base-NiTi, while the bright feature in the center of each micrograph is the unmelted Nb filler metal. The

predominantly planar (but occasionally bulbous) layers against the unmelted NiTi are pro-eutectic NiTi. Both pro-eutectic NiTi and the eutectic micro-constituents are solidification products of the braze liquid. These microstructural features will be discussed in a later section.

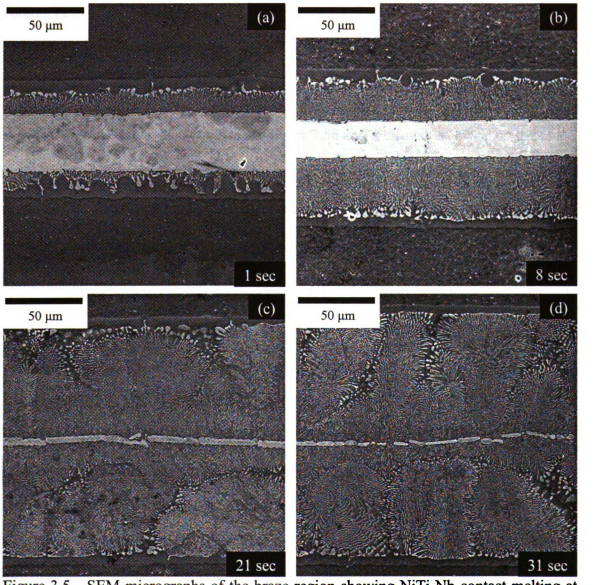

Figure 3.5 SEM micrographs of the braze region showing NiTi-Nb contact melting at braze duration of (a) 1 second; (b) 8 seconds; (c) 21 seconds; (d) 31 seconds.

It can be seen in Figure 3.5a that within the first second of contact melting (after the 15 seconds incubation time), the braze liquid had already propagated to an approximate thickness of 30 μm on each half of the braze joint. The half-thickness of Nb foil that had melted was measured to be 8 μm. Hence, approximately 22 μm of base-NiTi must have melted on each half of the joint. This suggests an almost 3:1 NiTi-to-Nb volume ratio or 1.4:1 molar ratio that contributed to braze liquid formation. This ratio corresponds to an approximate composition of 37Ni-37Ti-26Ni (at.%), which matches the composition, C_E. As contact melting proceeded from 1 to 21 seconds, wider liquid zones were formed, which are evident in Figure 3.5b and c. However, based on the time rate of change of remaining Nb thickness, the rate of melting appeared to decrease with increasing time. Significant attenuation of melting rates of NiTi and Nb was observed between 21 and 31 seconds (Figure 3.5c and d), resulting only in subtle widening of the braze liquid.

3.3.3 Termination

When specimens were subjected to braze durations beyond 31 seconds, complete melting of Nb braze foil occurred (Figure 3.6b). After Nb exhaustion, the pro-eutectic NiTi phase fraction increased substantially and a transition from a predominantly planar morphology to a dendritic form was observed. The pro-eutectic Nb phase was absent after Nb exhaustion. (Figure 3.6a is a lower-magnification duplicate of Figure 3.5d that serves as a basis for comparison with Figures 3.6b – d.) Liquid width continued to increase slightly between 31 and 120 seconds (Figure 3.6a and b), which can be attributed to continued melting of base-NiTi. The melting rate was significantly slower than those

observed in Figure 3.5. Figures 3.6c – d show that the liquid width maintained rather constant total width of 250 μm from 1200 seconds up to the maximum studied braze duration of 3600 seconds. Pronounced thickening of the pro-eutectic NiTi was not observed. These observations indicate the negligible rate of isothermal solidification (to be discussed in detail below).

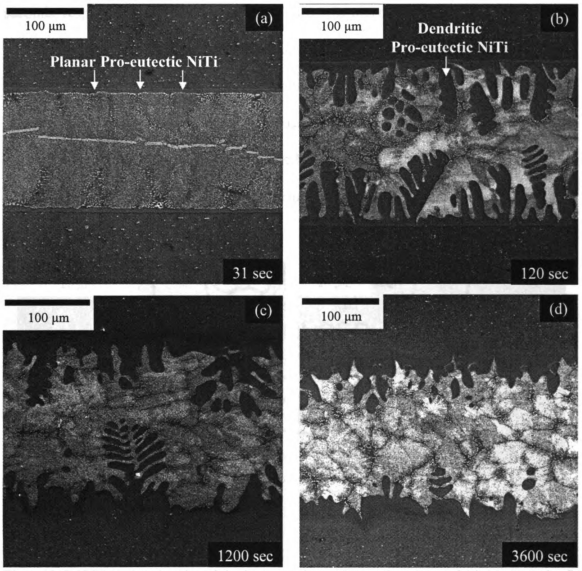

Figure 3.6 SEM micrographs of the braze region at braze durations of (a) 31 seconds; (b) 120 seconds; (c) 1200 seconds; (d) 3600 seconds.

Isothermal solidification is controlled by solute diffusion in the base-material. Once the solid Nb has been depleted, Nb diffusing from the liquid into the solid NiTi upsets the interface equilibrium, which can only be restored by freezing out NiTi, consequently rejecting Nb back into the liquid. Therefore, attention was focused on the diffusion of Nb across the NiTi-Liquid interface. Figures 3.7a and b show the Nb *Lα* XRF intensity profiles across NiTi-Liquid interfaces of specimens brazed for 31 and 3600 seconds, respectively. The line profile in Figure 3.7b was deliberately defined well within the bulk of the pro-eutectic NiTi phase as the micrograph suggests the presence of *coring* (to be discussed later) around the edges of the pro-eutectic NiTi phase, which will also yield a change in Nb-concentration across the cored structure. Both profiles revealed constant Nb compositions in the pro-eutectic NiTi phase (originated from the liquid). Approximately 4 and 12 at.% Nb were determined in Figure 3.7a and b, respectively.

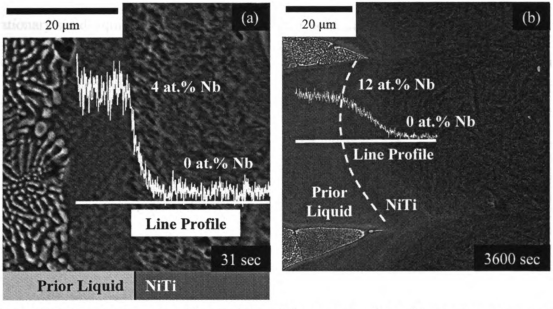

Figure 3.7 X-ray fluorescence line profiles of Nb *Lα* x-ray intensities across pro-eutectic NiTi/pure NiTi interfaces of specimens subjected to braze durations of (a) 31 seconds; (b) 3600 seconds.

However, Nb concentration decreased promptly across the NiTi-Liquid interface. The Nb composition in Figure 3.7a was observed to attenuate from 4 at.% to zero across a distance of approximately 5 μm from the NiTi-Liquid interface. It should be noted that the large excitation volume inherent in XRF (a few μm) is believed to generate an overestimation of the spatial measurement. Hence, it is reasonable to assume that Nb diffusion in NiTi is negligible at least within a braze duration of 31 seconds. For a braze duration of 3600 seconds, the Nb composition attenuated from 12 at.% to zero over a larger thickness of 20 μm (Figure 3.7b), thus implying that solid-state diffusion of Nb had become more pronounced.

For the case of Figure 3.7b, if one assumes that the solid NiTi adjacent to the NiTi-Liquid interface has a constant concentration of Nb, $C_{N,s}$, throughout the braze duration, t, and Nb diffusion in the semi-infinite base-NiTi alloy occurs across a stationary solid-liquid interface over a distance, x, then the diffusion problem can be expressed mathematically as shown in Eq. (3.6). Note that the concentration of Nb in the base-NiTi alloy far away from the NiTi-Liquid interface, C_N, is zero.

$$\frac{C - C_N}{C_{N,s} - C_N} = erfc\left(\frac{x}{2\sqrt{D_{Nb}t}}\right) \qquad \text{Eq. (3.6)}$$

The term $2\sqrt{D_{Nb}t}$ is the characteristic diffusion length, L, at which the diffuser concentration has decayed to about 15 % of $C_{N,s}$ at time t. Given the limited spatial

resolution of XRF, the attenuation length, instead of L, will be considered in the calculation of Nb diffusivity. With an attenuation length of 20 μm and time of 3600 seconds, the diffusion coefficient of Nb in NiTi, D_{Nb}, was estimated to be 2.8×10^{-14} m^2/s. This value is about an order of magnitude higher than the self-diffusion coefficient of Nb at 1185°C [Einziger et al. 1978]. As a means for comparison, the intrinsic diffusion coefficient of NiTi at the same temperature is about 2.0×10^{-12} m^2/s [Bastin et al. 1974], which is almost two orders of magnitude higher. From the calculated diffusivity, it is safe to deduce that low diffusivity of Nb in NiTi is responsible for the sluggish isothermal solidification after the complete melting of Nb filler. Given that the liquid layer was significantly thick as compared the diffusion distance of Nb in Figure 3.7b, homogenization of the joint through isothermal solidification was not observed, at least within the studied time frame. That is, braze processes involving thick liquid layers can be considered to have entered a 'termination' phase upon the exhaustion of Nb filler.

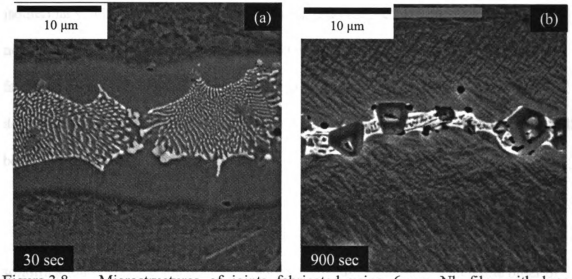

Figure 3.8 Microstructures of joints fabricated using 6 μm Nb film with braze durations of (a) 30 seconds; and (b) 900 seconds.

Effects of isothermal solidification can only be observed if thin Nb films of 3 μm thick were employed as braze filler instead of the 51 μm foils. Pure Nb films were deposited onto each mating NiTi surface at room-temperature using DC-magnetron sputtering, hence, yielding a total Nb thickness of 6 μm. Figures 3.8a and b show the microstructures of joints processed at 1185°C for 30 and 900 seconds, respectively. At 30 seconds, complete melting of the Nb film was observed (Figure 3.8a), resulting in pro-eutectic NiTi and eutectic micro-constituents. The total liquid width (pro-eutectic NiTi + eutectic) was measured to be about 20 μm.

In contrast, Figure 3.8b revealed near-homogenization of the joint due to isothermal solidification when braze time was increased to 900 seconds. This is evident from the significantly narrower eutectic width as compared to that observed in Figure 3.8a. Based on the calculated diffusion coefficient of Nb in NiTi, the characteristic diffusion length is approximately 10 μm for each half of the joint, which is in good agreement with the extent of narrowing of the joint in Figure 3.8b. As a result of isothermal solidification, the interfaces between pro-eutectic NiTi and base-NiTi were not physically distinguishable. In addition, new solidification products, in the form of facetted precipitates, were observed to formed in the liquid phase and extensively decorate the centerline of the joint. These precipitates are presumed to be oxides and will be discussed in a later section.

The results in Figure 3.8 suggest that homogenization of joint through isothermal solidification is viable if the maximum width of the liquid phase is in the same order of

magnitude as the Nb diffusion distance associated with the desired braze time. However, the process of homogenization, which is a desirable step in typical TLP processing, resulted in the precipitation of facetted phase along the centerline of the joint. Termination of braze process in the homogenization stage will be undesirable if these precipitates possesses brittle characteristics.

To summarize, the contact melting process can be categorized into 3 stages: (1) initial melting; (2) liquid propagation; and (3) termination of melting. The initial melting stage involves an incubation period, which is the time taken for Ni, Ti and Nb to inter-diffuse across the native oxide barriers before melting commences at the interface. The liquid phase widens or propagates as further melting of NiTi and Nb occurs, and is rate-controlled by diffusion in the liquid (to be discussed further below). When the liquid width is significantly larger than the diffusion length of Nb in NiTi associated with the braze duration, the effect of isothermal solidification is insignificant. Hence, narrowing of liquid width will not be observed after complete melting of Nb filler and the contact melting process is considered to have terminated. However, if the braze liquid thickness is within the same order of magnitude as the diffusion length of Nb, isothermal solidification will dominate after the complete melting of Nb, resulting in narrowing of liquid width.

3.4 Contact Melting Kinetics

In this section, a theoretical model of the contact melting process will be proposed to account for the experimental observations in section 3.3. The model assumes a half-space scenario where a NiTi-Nb couple was subjected to brazing at 1185°C. A thickness of 25.5 μm was chosen for the Nb filler, which corresponds to the thickness of those specimens employed in Section 3.3 in full-space. For ease of calculation, unit areas were assumed for both NiTi and Nb. The establishment of this model will also form the basis for numerical calculations of the contact melting kinetics, where the aim is to determine the diffusivities of Ni, Ti and Nb in the liquid. The contact melting kinetics will be presented later in the section.

Recall that contact melting originates from the NiTi-Nb mating interface. Contact melting occurs because the local concentration at the NiTi-Nb solid mating interface falls between $C_{B,l}$ and $C_{B,s}$, which is thermodynamically-forbidden at 1185°C. Upon the first instance of melting, it is postulated that braze liquids close to the solid NiTi and Nb immediately attempts to maintain equilibrium solid-liquid interface compositions at $C_{N,l}$ and $C_{B,l}$, respectively. The liquid close to the base-NiTi can establish equilibrium only if the base-NiTi adjacent to the liquid builds up a thin solid layer with composition, $C_{N,s}$. Likewise, the liquid next to the unmelted Nb will build up a thin layer of solid of composition, $C_{B,s}$. These layers are perhaps within the order of a few monolayers and their formation should, therefore, not control the rate of melting.

The discrepancy (ΔC) of composition between $C_{N,l}$ and $C_{B,l}$ across the liquid ($w(t)$) at a particular time (t) sets up a concentration gradient ($\Delta C/w(t)$) in the liquid phase. Flux exchanges between Ni, Ti and Nb must therefore occur in the presence of this concentration gradient, whereby Ni and Ti atoms in the liquid diffuse towards solid Nb, while Nb atoms in the liquid diffuse towards solid NiTi. These fluxes in turn upset the local interface equilibria at both solid-liquid interfaces. The system can re-establish local equilibrium only by further melting of the respective solids. Therefore, it is the deviation from local equilibrium at the NiTi-Liquid and Nb-Liquid interfaces that forms the driving force for continuous melting. Melting is thus hypothesized to be rate-controlled by solute diffusion in the liquid.

Assuming steady-state liquid diffusion conditions (linear concentration gradient), and given that the local concentrations of liquids at the two solid-liquid interfaces are fixed at $C_{N,l}$ and $C_{B,l}$ for all liquid widths, continued melting flattens the concentration gradient in the liquid as w increases with time. Fluxes of Ni, Ti and Nb, which are directly proportional to concentration gradient (Fick's first law), will therefore also decrease. The reduction in flux associated with increasing liquid width slows down subsequent melting of the base-NiTi and Nb filler. A schematic diagram showing the establishment and change of a liquid concentration gradient across the two solid-liquid interfaces as a function of time before exhaustion of Nb filler is illustrated in Figure 3.9.

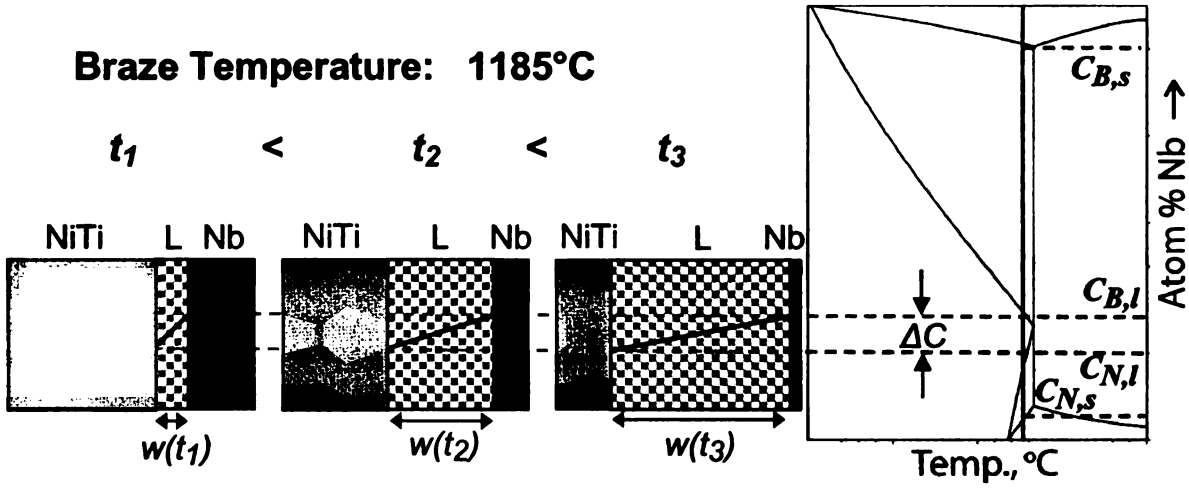

Figure 3.9 Schematic diagram illustrating the establishment and evolution of a concentration gradient in the braze liquid as a function of time, based on the assumed perfect NiTi-Nb quasibinary eutectic isopleth.

Based on the proposed model, the diffusion-controlled process of melting can be represented by the mass-balance equation, shown in Eq. (3.7) and (3.8).

$$v_{NiTi}(C_{N,l} - C_{N,s}) = -J_{NiTi \to L} + J_{Nb \to NiTi} \qquad \text{Eq. (3.7)}$$

$$v_{Nb}(C_{B,s} - C_{B,l}) = J_{Nb \to L} - J_{NiTi \to Nb} \qquad \text{Eq. (3.8)}$$

Since solid-state diffusion is slow compared to liquid-phase diffusion, Eq. (3.7) and (3.8) can be simplified into:

$$v(t)_{NiTi} C_{N,s} \approx D^{L}_{Ni,Ti} \left(\frac{\Delta C}{w(t)} \right)_{L} \qquad \text{Eq. (3.9)}$$

$$v(t)_{Nb} C_{B,s} \approx -D_{Nb}^{L}\left(\frac{\Delta C}{w(t)}\right)_{L} \qquad \text{Eq. (3.10)}$$

where D_{Nb}^{L} is the diffusion coefficient of Nb in the braze liquid. $D_{Ni,Ti}^{L}$ is the collective diffusion coefficient of Ni and Ti, or the sum of the diffusivities of Ni (D_{Ni}^{L}) and Ti (D_{Ti}^{L}). Note that Ni and Ti are assumed to possess similar transport behavior in this model in order to facilitate the use of a common concentration gradient, ($\Delta C/w(t)$). The mathematical relation among D_{Ni}^{L}, D_{Ti}^{L} and $D_{Ni,Ti}^{L}$ are summarized in Eq. (3.11) and (3.12).

$$D_{Ni}^{L} = D_{Ti}^{L} \qquad \text{Eq. (3.11)}$$

and,

$$D_{Ni,Ti}^{L} = D_{Ni}^{L} + D_{Ti}^{L} \qquad \text{Eq. (3.12)}$$

An explicit finite-difference scheme (2nd order Runge-Kutta method) was applied to Eq. (3.13) – (3.17) in order to numerically-model the contact melting as a function of time prior to the complete melting of Nb filler. The program code was written in FORTRAN 77 and the input parameters are provided in the Appendix B.

$$\delta x(t)_{NiTi} = v(t)_{NiTi}\,\Delta t = \frac{D_{Ni,Ti}^{L}}{C_{N,s}}\left(\frac{\Delta C}{w(t)}\right)_{L}\Delta t \qquad \text{Eq. (3.13)}$$

$$\delta x(t)_{Nb} = v(t)_{Nb}\Delta t = -\frac{D_{Nb}^{L}}{C_{B,s}}\left(\frac{\Delta C}{w(t)}\right)_{L}\Delta t \qquad \text{Eq. (3.14)}$$

$$x(t+1)_{NiTi} = x(t)_{NiTi} + \delta x(t)_{NiTi} \qquad \text{Eq. (3.15)}$$

$$x(t+1)_{Nb} = -x(t)_{Nb} - \delta x(t)_{Nb} \qquad \text{Eq. (3.16)}$$

$$w(t+1) = x(t+1)_{NiTi} - x(t+1)_{Nb} \qquad \text{Eq. (3.17)}$$

Due to the nature of the mathematical expressions, an initial braze liquid width of zero cannot be used for the numerical calculations. Hence, a finite braze liquid width of 10 nm, a legitimately small value, was employed to serve as the initial condition. The braze temperature for calculation was set at 1185°C and the initial half Nb braze foil thickness of 25.5 μm was used, both consistent with the experimental setup employed for the time-evolution studies in section 3.3. The calculation employed values of $C_{N,s}$, $C_{N,l}$, $C_{B,l}$ and $C_{B,s}$ described in section 3.2. Given the high rate of change of interface velocities during initial melting, small time steps had to be used to reduce computation error. It was found that a computation time interval, Δt, of 0.002 seconds is suitable for the nature of this numerical work. While the abovementioned parameters were fixed, diffusion coefficients $D_{Ni,Ti}^{L}$ and D_{Nb}^{L} were adjusted to obtain an optimum fit between predicted and experimental data. Hence, diffusivities of Ni, Ti and Nb can be inferred from the numerical simulation.

Figure 3.10 illustrates the experimental and predicted solid-liquid interface positions, x_{NiTi} and x_{Nb}, as a function of braze time prior to complete melting of Nb filler.

When $D^{L}_{Ni,Ti}$ and D^{L}_{Nb} were assigned values of 4.10 x 10^{-9} m^2/s and 1.55 x 10^{-9} m^2/s, respectively, simulation results were able to correctly replicate the trends of experimental data. The predicted duration for complete melting of a 25.5 μm-thick Nb foil is about 34 seconds, which is in excellent agreement with experimental observations. It is worth mentioning that such similar contact melting model has been successfully utilized in the past by [Getazheev et al. 1970] to predict the liquid diffusion coefficients in the Bi-Sn binary eutectic system (see Chapter 1). The predicted diffusivities for Bi-Sn in [Getazheev et al. 1970] and NiTi-Nb in this work are consistent with many pure liquid metals studied close to their respective melting points [Vadovic et al. 1970, Roy et al. 1988, Mei et al. 1990, Alemany et al. 1998] in terms of order of magnitude.

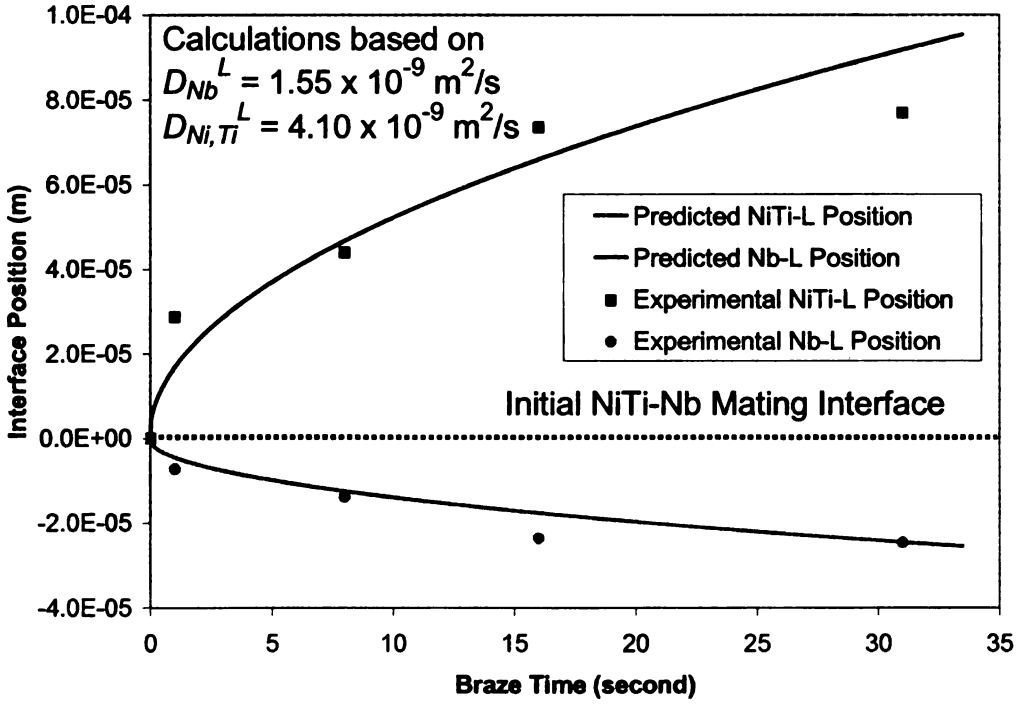

Figure 3.10 Experimental and predicted solid/liquid interface positions during dissolution at 1185°C. (Experimental interface positions were measured and defined with respect to the initial NiTi-Nb mating interface.)

Although the simulation is able to determine $D^L_{Ni,Ti}$, it is unable to quantify the individual contributions of Ni and Ti diffusivities to $D^L_{Ni,Ti}$. Recall that the calculation assumed $D^L_{Ni} = D^L_{Ti}$ (see Eq. (3.11)). In such an ideal scenario, Ni and Ti will be transported away from the unmelted NiTi at the same rate. Hence, the composition across the liquid can be described by Line 1 in the 1185°C – isothermal section of the NiTi-Ni_6Nb_7-Nb-Ti phase diagram (Figure 3.11). Note that Line 1 lies in the plane of the NiTi-Nb isopleth (indicated by the dotted lines in Figure 3.11 and the inset), which implies that the ratio of Ni to Ti will always be unity in the liquid at any position and time.

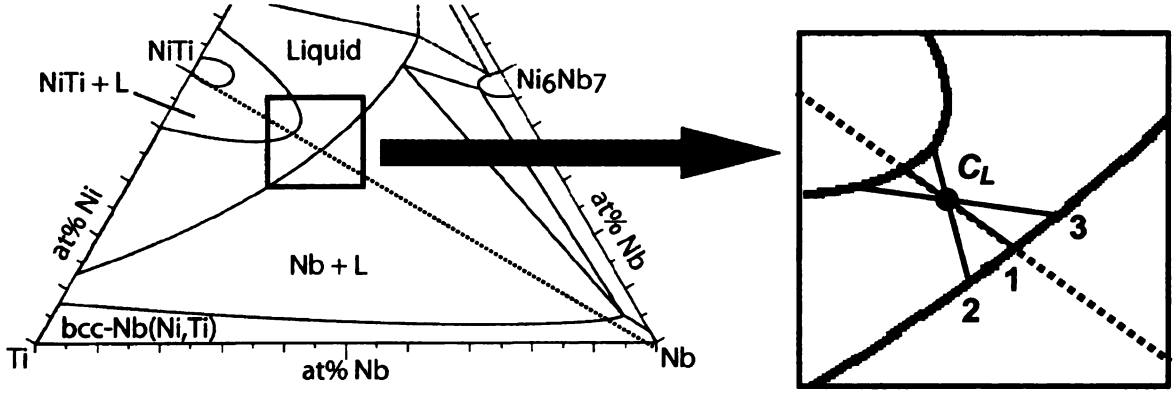

Figure 3.11 Estimated isothermal section of the NiTi-Ni_6Nb_7-Nb-Ti phase diagram at 1185°C. Inset: Magnified view of the liquid phase at the NiTi-Nb isopleth revealing compositions across the liquid when Ni and Ti possess similar diffusivity (Line 1); Ni diffuses slower than Ti (Line 2); and Ti diffuses slower than Ni (Line 3). The average liquid composition is indicated by C_L.

If $D^L_{Ni} \neq D^L_{Ti}$, the flux of the slow-diffuser will be smaller than that of the fast-diffuser and a build-up of the slower-diffusing solute near the NiTi-Liquid interface will happen momentarily when contact melting first occurs. Assume a case where Ni is

diffusing more slowly than Ti. The liquid adjacent to the unmelted NiTi will build up more Ni than Ti initially, while the liquid close to the unmelted Nb possesses less Ni. Consequently, the composition across the liquid during this transient stage can be described by Line 2 in Figure 3.11. The build-up of Ni near the unmelted NiTi end results in an increase in Ni concentration gradient across the liquid. This, in turn, increases the Ni flux, J_{Ni}^{L}, towards the unmelted Nb. In other words, increase in J_{Ni}^{L} will compensate for its lower diffusivity. Concurrently, the faster diffusing Ti will responsd in an antagonistic manner by reducing its concentration gradient and flux, J_{Ti}^{L}, across the liquid. Assuming the solid NiTi to be perfectly equi-atomic, steady-state occurs when $J_{Ni}^{L} = J_{Ti}^{L}$ and the composition across the liquid will be driven back to Line 1 in Figure 3.11 (this statement additionally assumes negligible solid-state diffusion of Ni and Ti).

In contrast, if Ti is diffusing slower than Ni, the situation reverses and the composition across the liquid during the transient stage can be described by Line 3 in Figure 3.11. The system will then drive the liquid composition back to Line 1 by simultaneously decreasing J_{Ni}^{L} and increasing J_{Ti}^{L} to the point when $J_{Ni}^{L} = J_{Ti}^{L}$. Therefore, a self-moderating mechanism exists in the contact melting process, which prevents deviation of liquid composition from the NiTi-Nb isopleth even if $D_{Ni}^{L} \neq D_{Ti}^{L}$. Furthermore, mass-conservation dictates that the average liquid composition, C_L, in the joint (indicated by the black dot in the inset of Figure 3.11) is invariant whether discrepancies between Ni and Ti diffusivities exist or not.

The melting kinetics simulation also predicted the interface velocities (the rate of melting) for NiTi and Nb, which are shown in Figure 3.12. The predicted trends in Figure 3.12 show that melting proceeds rapidly for both NiTi (> 20 μm/s) and Nb (> 5 μm/s) during initial melting. However, the velocities attenuate rapidly to less than 5 μm/s within first 5 seconds of contact melting (or as the braze width increases).

Simulation results suggest that Nb possesses a lower rate of melting compared to NiTi, which is attributed to its lower diffusivity with respect to the NiTi counterpart. The discrepancy in diffusivities can be qualitatively explained by the Einstein theory on self-diffusivity of liquid metals, which was discussed in Chapter 1. Equations (1.6) and (1.7) state that diffusion coefficient is dependent on temperature, viscosity and atomic radius of the diffusing species. Since diffusion of Ni, Ti and Nb occurred in the same liquid at the same temperature, the viscosity and temperature terms in Eq. (1.6) and (1.7) should be constant. Therefore, atomic radius is the only parameter that should affect diffusivity. Given that diffusivity is inversely proportional to atomic radius and Nb possesses larger atomic radius than Ni or Ti [Hume-Rothery et al. 1954], $D^{L}_{Ni,Ti}$ will be greater than D^{L}_{Nb}. Furthermore, the Einstein theory also predicts Ni as a faster diffuser than Ti in the liquid. Therefore, it is believed that the transient stage indicated by Line 2 in Figure 3.11 is the likely scenario that precedes steady-state. Given that Nb is the slowest diffuser in the liquid, it should be the rate-limiting parameter for the contact melting process.

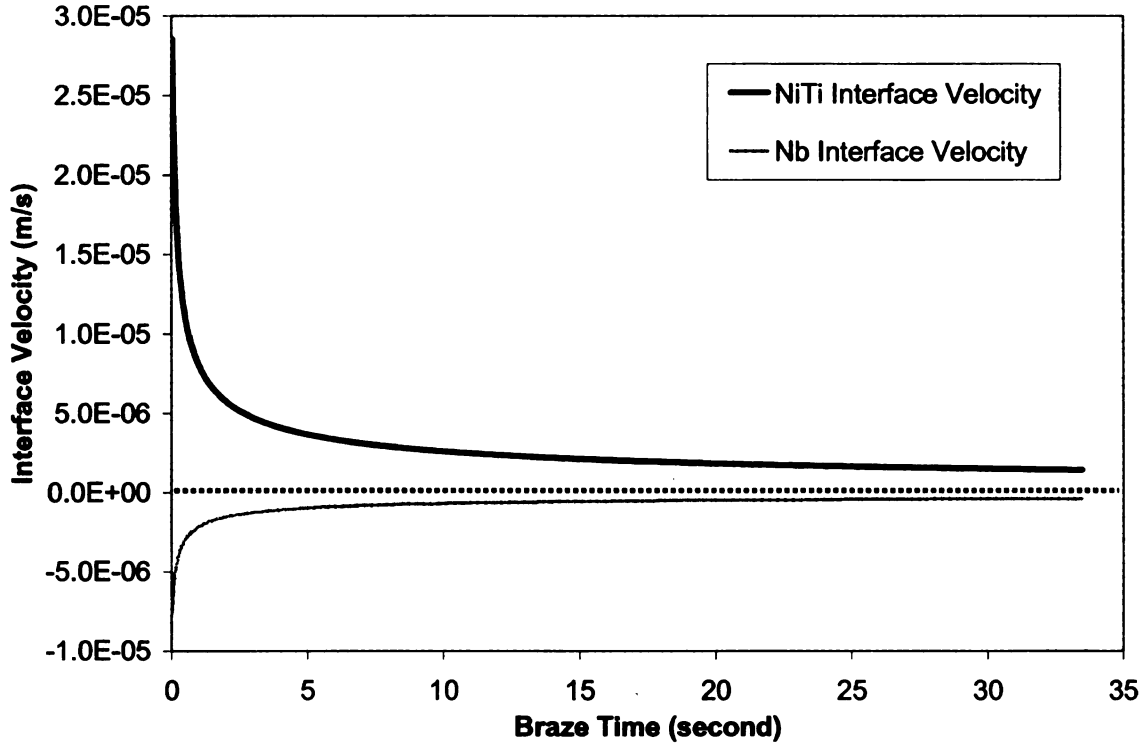

Figure 3.12 Predicted melt interface velocities for NiTi and Nb at 1185°C.

Upon complete melting of solid Nb, additional Nb flux will no longer be supplied into the liquid phase and the liquid does not need to establish local equilibrium composition at $C_{B,l}$. All liquid in the joint will now attempt to establish a uniform equilibrium composition only at $C_{N,l}$. In other words, the liquid will attempt to achieve zero concentration gradient. A final liquid composition of $C_{N,l}$, or zero concentration gradient, can only be attained by continued melting of the base-NiTi, which will cease only when the overall liquid composition reaches $C_{N,l}$. Figure 3.13 illustrates the proposed time-evolution of the concentration profile in the liquid after the exhaustion of Nb filler, where linear concentration gradients are also assumed.

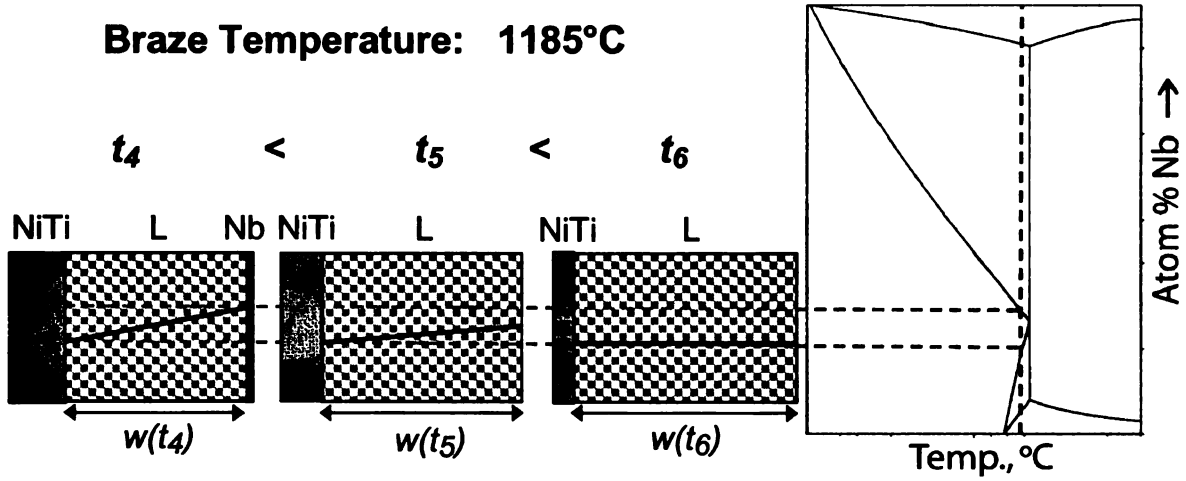

Figure 3.13 Schematic diagram illustrating the evolution of a concentration gradient in the braze liquid as a function of time after Nb exhaustion.

The numerical scheme was allowed to continue upon the complete melting of Nb filler. Since the liquid can no longer support a local composition at $C_{B,l}$, Eq. (3.13) has to be replaced by Eq. (3.18) and (3.19) to allow the liquid to eventually achieve a uniform composition $C_{N,l}$. Equations (3.18) and (3.19) describe the enrichment of liquid with Ni and Ti through further melting of NiTi, which causes an attenuation of the concentration gradient as a function of time. When the concentration gradient approaches zero (that is, the overall liquid attains $C_{N,l}$ composition), there is no driving force for melting of NiTi. Hence, the numerical scheme would be terminated at this point. The program code is provided in Appendix C.

$$C(t+1) = D^{L}_{Ni,Ti}\left(\frac{\Delta C - C(t)}{w(t)}\right)_{L}\Delta t\left(\frac{1}{w(t)}\right) \qquad \text{Eq. (3.18)}$$

$$\delta x(t+1)_{NiTi} = \frac{D^{L}_{Ni,Ti}}{C_{N,s}}\left(\frac{\Delta C - C(t+1)}{w(t+1)}\right)_{L}\Delta t \qquad \text{Eq. (3.19)}$$

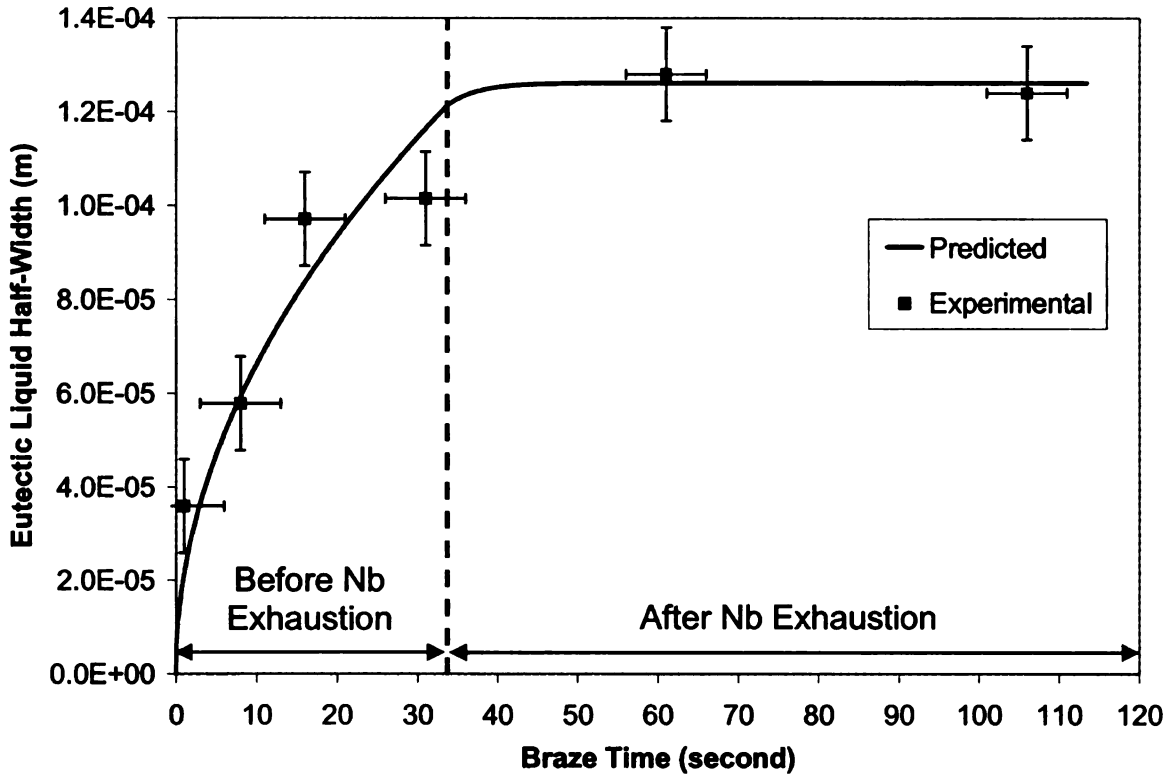

Figure 3.14 Experimental and predicted liquid half-width as a function of time at braze temperature of 1185°C.

Figure 3.14 shows the experimental and predicted evolution of liquid half-width from 0 to 115 seconds. The predicted trend in Figure 3.14 suggests that the liquid continued to widen by approximately 5 μm after complete melting of Nb filler in order for the liquid to achieve uniform composition at $C_{N,l}$. According to the numerical scheme, this process took less than 15 seconds to complete, which is reasonably consistent with experimental results. The final liquid half-width of 126 μm was achieved within 50 seconds from the point of initial melting.

Recall that the contact melting model hypothesized that melting is rate-controlled only by solute diffusion in the liquid. The model did not address possible contributions

of latent heat effects to the melting rate. Hence, heat conduction calculations, based on the half-space specimen configuration, were performed to determine if heat transfer plays a rate-limiting role in contact melting. Initial conditions for the calculations were such that the NiTi surface is constantly at 1185°C, while the NiTi-Nb interface had attained a temperature of 1170°C and the system had just passed the incubation period for melting. That is, any additional heat flux across the NiTi-Nb interface will initiate and cause subsequent melting without raising the liquid and the solid Nb temperature. The calculations assumed steady-state heat flow where a linear thermal gradient existed in the NiTi and perfect mixing of solutes in the liquid at all times. Figure 3.15 illustrates the temperature profile across the half-space configuration of a braze joint at initial condition and after some time, *t*.

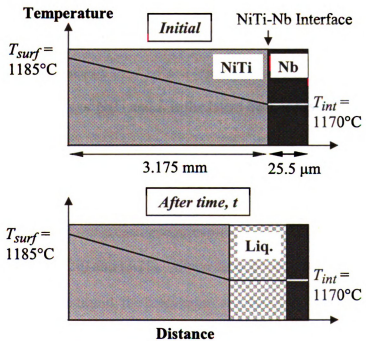

Figure 3.15 Schematic diagram showing the temperature profile across a half-joint at initial condition and after some time, *t*, if melting is rate-controlled by heat transfer.

The heat conduction problem can be mathematically expressed by Eq. (3.20),

$$\Delta Q(t) = kA\left(\frac{\Delta T}{x(t)}\right)\Delta t \qquad \text{Eq. (3.20)}$$

where k is the thermal conductivity of NiTi, $\Delta Q(t)$ is the change in heat at time t, Δt is the time interval, $x(t)$ is the remaining thickness of base-NiTi alloy at time t, A is the NiTi-Liquid interfacial area and ΔT is the temperature difference between exposed surface of the base-NiTi alloy and the NiTi-Nb interface.

The remaining thickness of NiTi after Δt can be determined by Eq. (3.21),

$$x(t+1) = x(t) - \frac{\Delta Q(t)}{\rho AL} \qquad \text{Eq. (3.21)}$$

where ρ is the mass density of NiTi and L is the latent heat of fusion of the braze liquid.

The thickness of melted NiTi was predicted as a function of time (after the incubation period) using an explicit finite-difference scheme (2^{nd} order Runge-Kutta method) applied to Eq. (3.20) and (3.21). Since there are no data available on the latent heat of fusion for the braze liquid, the calculation was based on the latent heat of fusion of NiTi, L = 357 J/g [Yung et al. 2005]. Results derived from the latent heats of fusion of 500 J/g and 1000 J/g were also presented as reference. The latter value represents an exceptionally high latent heat of fusion. Therefore, results predicted from such a high

latent heat of fusion will serve as a lower-bound to the NiTi melting rates. The simulation was terminated when approximately 96 μm of NiTi had melted. This thickness was deliberately chosen because it corresponds to the calculated thickness of melted NiTi in the diffusion-controlled model upon complete melting of a 25.5 μm thick Nb foil, and is also reasonably consistent with experimental observation. Time interval, $\Delta t = 2$ μs, was used. The program code was written in FORTRAN 77 and is provided in Appendix D.

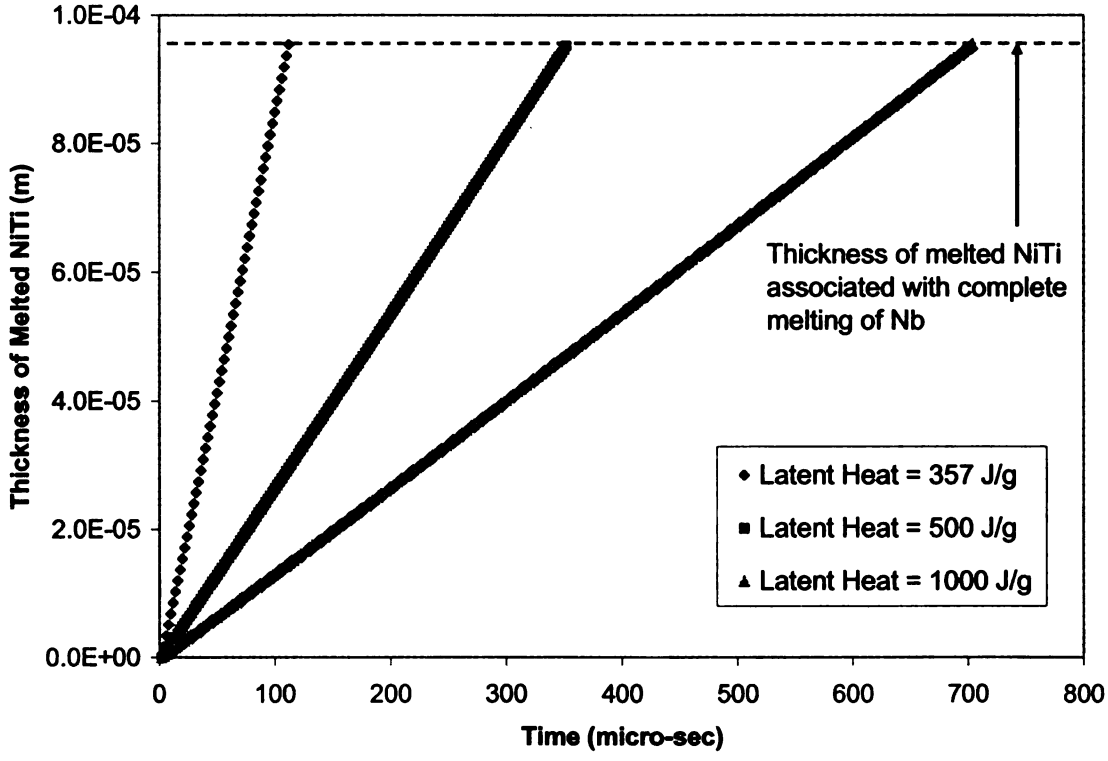

Figure 3.16 Predicted thickness of melted NiTi alloy as a function of time after the incubation period.

Figure 3.16 shows the thickness of melted NiTi alloy as a function of time after incubation period. The predicted results revealed that NiTi melts at an almost linear rate for all latent heats of fusion. When the latent heat of fusion of NiTi was employed for

calculations, the time taken to melt 96 μm of NiTi was predicted to be 112 μs. Figure 3.16 shows that despite a longer required duration when a high latent heat of fusion of 1000 J/g was assumed, the time taken to melt 96 μm of NiTi is still less than 1 ms, which is about 5 orders of magnitude smaller than what was experimentally observed. It can safely be concluded therefore, that latent heat effects are negligible in the present context.

3.5 Solidification

The discussion will now focus on the solidification products originating from the braze process. Specifically, the as-brazed and annealed microstructure of braze joints will be discussed in detail. Before the end of this section, the effects of surface preparation and vacuum conditions on joint morphology will also be considered.

3.5.1 As-Brazed Microstructures

A higher-magnification SEM micrograph of Figure 3.5a is shown in Figure 3.17. It revealed microstructural details of a typical joint that was solidified before complete melting of the Nb filler. Figure 3.17 reveals the presence of pro-eutectic Nb, which has nucleated against the unmelted Nb foil during cooling. The pro-eutectic Nb phase possessed a nearly planar solidification morphology. Likewise, the pro-eutectic NiTi phase was also observed to nucleate against the base-NiTi, and also possessed a predominantly planar solidification front (Figures 3.5b – d). However, it occasionally assumed a cellular morphology similar to those observed in Figure 3.17. The eutectic mixture forms the main constituent in the joint and well-defined eutectic impingement

boundaries only developed beyond 8 seconds from initial melting (Figures 3.5c – d). The average eutectic grain size is approximately 60 μm.

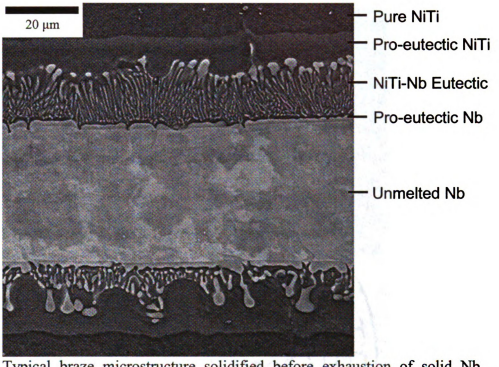

Figure 3.17 Typical braze microstructure solidified before exhaustion of solid Nb (contact melting at 1185°C).

X-ray fluorescence studies revealed that the pro-eutectic NiTi phase contains about 4 at.% Nb with a corresponding decrease in Ti composition (Table 3.3). This suggests that Nb tends to substitute for Ti in the NiTi phase. Elemental XRF mapping of the braze area, shown in Figure 3.18, indicates presence of Nb and reduced Ti $K\alpha$ intensity in the pro-eutectic NiTi while Ni $K\alpha$ intensity remains constant across the base-NiTi and pro-eutectic NiTi. This reinforces the previous deduction that solutionizing of Nb in pro-eutectic NiTi occurs by preferential substitution for Ti lattice sites in NiTi.

Due to spatial resolution limits of XRF, the composition of pro-eutectic Nb could not be determined.

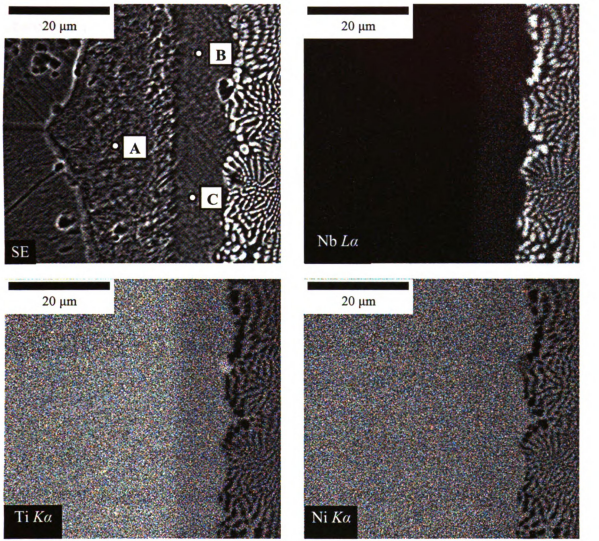

Figure 3.18 Elemental XRF maps showing (a) secondary-electron, (b) Nb *Lα*, (c) Ti *Kα* and (d) Ni *Kα* intensities originating from base-NiTi, pro-eutectic NiTi and eutectic phases.

Table 3.3 X-ray fluorescence analysis on selected spots in Figure 3.18.

Spot	Nb (at%)	Ni (at%)	Ti (at%)
A	0	51	49
B	5	52	43
C	4	51	45

Upon the complete melting of Nb filler, the pro-eutectic NiTi phase appeared to change from a planar/cellular to a dendritic morphology (Figure 3.6). Occasional facetted precipitates, later identified as the Ti_2Ni-type phase (or its oxide, Ti_4Ni_2O), were observed within the eutectic micro-constituents in experiments involving complete melting of the Nb filler. Their grain size ranged from 5 to 20 μm, although there were noticeably more grains near 20 μm in size when joints were subjected to longer braze durations. Figure 3.19a shows the typical morphology and size of these facetted precipitates in joints brazed for 3600 seconds.

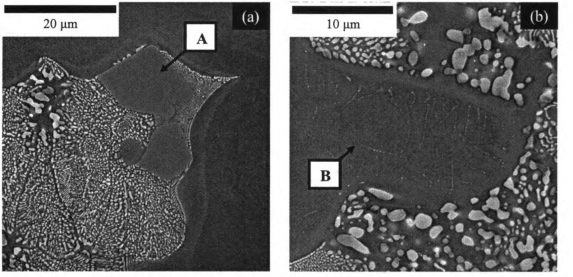

Figure 3.19 SEM micrographs showing (a) facetted Ti_2Ni-type precipitates (indicated by 'A'), (b) fine Nb-rich precipitates decorating sub-grain boundaries of a pro-eutectic NiTi dendrite (indicated by 'B').

Bright, spheroidal precipitates can also be occasionally observed forming networks within the pro-eutectic NiTi dendrites (Figure 3.19b). Given that their SE intensities closely resemble those of the eutectic-Nb phase, these fine precipitates are likely to be Nb-rich and appear to have formed along sub-grain boundaries in the pro-

eutectic NiTi dendrites during cool-down from braze temperature. Figure 3.20a and b shows SE and back-scatter electron (BSE) micrographs of sub-grain boundaries of the same pro-eutectic NiTi dendrite. The sub-grain boundaries are visible possibly due to etching effects. These sub-grain boundaries appeared dark in both micrographs either because the Nb-rich precipitates may be too fine to be resolved by SEM, or because these sub-grain boundaries were not decorated with Nb precipitates. The preferential precipitation of Nb-rich phase along the sub-grain boundaries of the dendrites can be attributed to Nb supersaturation in the pro-eutectic NiTi phase at lower temperatures. Figure 3.19b and Figure 3.20 show abrupt changes in SE intensities near the dendrite borders (bright near the perimeter, but dark in the bulk), suggesting higher Nb-concentrations at the boundaries of these dendrites. Such phenomenon is termed *coring*, which is due to slow solid-state diffusion associated with non-equilibrium solidification.

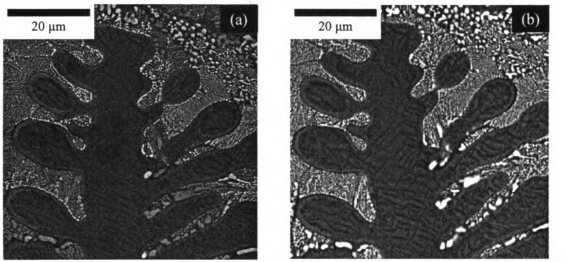

Figure 3.20 SEM micrographs of a pro-eutectic NiTi dendrite observed under (b) SE and (c) BSE modes.

However, the XRF line profile in Figure 3.21 revealed that the change in Nb composition across a perceived cored dendrite is rather gradual. The perceived cored

region possessed a maximum Nb concentration of 13 at.% Nb, which is comparable to the Nb content in the bulk of the dendrite in Figure 3.7b. The prominent decrease in Nb content actually occurred away from the perceived coring. Hence, the abrupt change in SE intensities may, in fact, also be an artifact of the etching process.

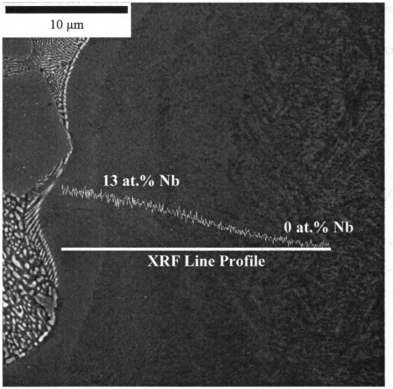

Figure 3.21 X-ray fluorescence line profile of Nb *La* across the perceived cored pro-eutectic NiTi phase and the base-NiTi alloy.

The transition of the character of the pro-eutectic NiTi solidification front from planar to dendritic can be explained qualitatively with the aid of Figure 3.22. During the melting process, the liquid possesses an average composition, C_L, of 25 at.% Nb. If the braze joint was cooled from 1185°C at this juncture, the pro-eutectic NiTi would solidify against the base-NiTi, rejecting excess Nb into the liquid immediately ahead. The liquid ahead of the solid-liquid interface may build up sufficient Nb to yield a composition C_E,

while liquid far away from the solid-liquid interface will have composition of 25 at.% Nb. Consequently, the liquid must have a composition-distance profile indicated as C_{before} in Figure 3.22. The corresponding liquidus temperature-distance profile is shown as T_{before} in Figure 3.22. The reason for the planar solidification morphology may be attributed to a thermal gradient in the liquid phase being tangential to the slope of T_{before} at the solid-liquid interface. Hence, the liquid does not experience constitutional supercooling and solidification can proceed in a planar fashion.

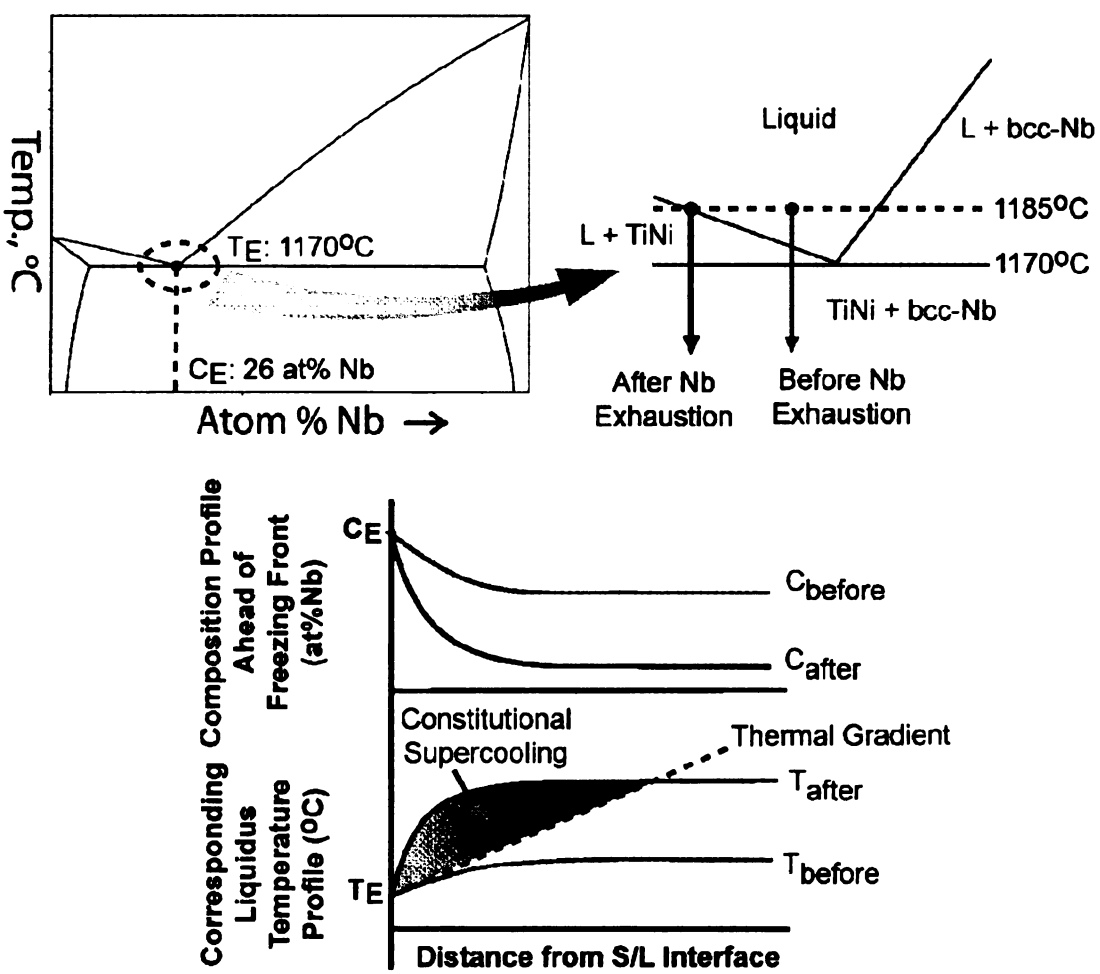

Figure 3.22 Qualitative model accounting for the pro-eutectic NiTi solidification morphology at different stages of brazing.

Upon complete melting of the Nb filler, the liquid now maintains equilibrium composition at $C_{N,l}$ of Figure 3.1, which is leaner in Nb content than the previous case. When the liquid is allowed to cool, the liquid ahead of the solidified pro-eutectic NiTi will also build up Nb. Again, the liquid ahead of the solid-liquid interface may have as high of a Nb concentration as C_E, while liquid far away from the solid-liquid interface will have composition of $C_{N,l}$. The resulting composition- and liquidus temperature-distance profiles are indicated by C_{after} and T_{after} in Figure 3.22, respectively. Comparison between T_{before} and T_{after} shows that the latter has a steeper slope at the solid-liquid interface. If the thermal gradient in T_{before} is also imposed on T_{after} (similar cooling regime in both cases), a finite distance of the liquid ahead of the solid-liquid interface will have lower temperature than the liquidus temperature of those corresponding liquid. Hence, constitutional supercooling occurs, causing instability in the pro-eutectic NiTi solidification front and eventual dendrite formation [Porter et. al. 2001].

The eutectic-Nb phase (appears bright in Figure 3.23) was observed to possess a predominantly lamellar morphology. However, rod-like eutectic-Nb was also occasionally encountered. The average eutectic spacings of lamellae and rods were determined to be about 0.4 and 0.6 μm, respectively. Stereology performed on Figure 3.23 and other similar micrographs indicates an approximate 30 vol.% occupancy by eutectic-Nb in the eutectic micro-constituents. If one assumes the solubility limits of

NiTi and Nb at eutectic solidification temperature are approximately $C_{N,S}$ and $C_{B,S}$, respectively, Lever-rule suggests that this volume fraction of eutectic-Nb should correspond to a quasibinary eutectic point at 23 at.% Nb. This value puts it close to the literature-reported value of 26 at.% Nb [Prima et al. 1995]. The morphology of the eutectic micro-constituents will be discussed in a later section.

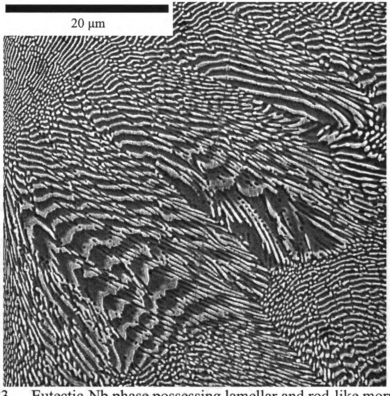

Figure 3.23 Eutectic-Nb phase possessing lamellar and rod-like morphologies.

Braze joints prepared at 1185°C for 360 seconds were investigated by TEM and results are shown in Figure 3.24 and 3.25. In-plane eutectic-Nb rods (darker contrast) in the matrix of eutectic-NiTi (lighter contrast) can be clearly seen in Figure 3.24. Selected-area diffraction of the eutectic-NiTi showed diffraction spots with a diffuse ring as background. The ring indicates amorphous or low crystallinity of the eutectic-NiTi from

ion-milling. Indexing the diffraction spots revealed *BCC*-type crystal structure with two zone-axes, possibly due to sampling of adjacent grains simultaneously by the aperture. The first zone-axis was determined to be [011] with weak ordered-*B2* superlattice reflections, while the second zone-axis was identified to be $[\bar{1}33]$. Again, the weak superlattice reflections are indications of poor ordering, attributed to the moderately fast cooling upon termination of the braze process. No martensite phase was observed in the eutectic-NiTi. Note that these joint specimens were never subjected to temperatures lower than room temperature after they were cooled from 1185°C. Hence, the absence of martensite suggests that the martensite start temperature may be lower than room temperature.

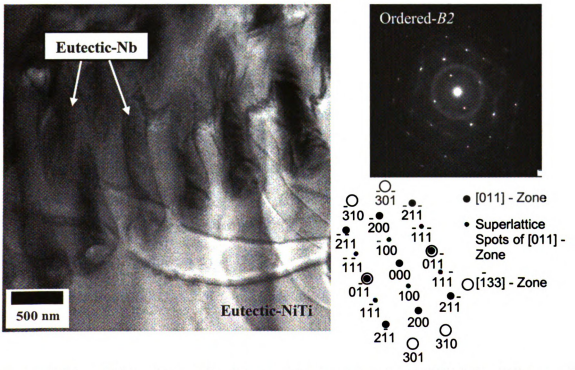

Figure 3.24 TEM micrograph of braze joints processed at 1185°C for 360 seconds showing in-plane eutectic-Nb rods and SAD pattern of the eutectic-NiTi. (Diffraction originating from bottom-right of micrograph.)

The selected-area diffraction from the out-of-plane eutectic-Nb rod in Figure 3.25 showed strong diffraction spots that are associated with disordered-*BCC* [012]-zone axis. No amorphous ring was observed. Hence, the degree of crystallinity in the eutectic-Nb phase was high despite fast cooling, which is consistent with its purity and disordered-*BCC* equilibrium state.

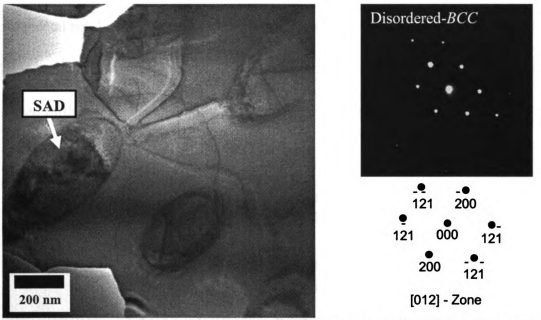

Figure 3.25 TEM micrograph of braze joints processed at 1185°C for 360 seconds showing eutectic phase and SAD pattern of the out-of-plane eutectic-Nb rod. (Diffraction originating from indicated eutectic-Nb rod.)

3.5.2 Annealed Microstructures

Brazed joints processed at 1185°C for 1200 seconds were subjected to annealing temperatures from 300°C to 920°C in air followed by water-quench. At lower temperatures, SEM did not reveal any distinctive changes in joint microstructures. Notable changes only occurred when annealing temperatures were increased to 800°C and beyond. When annealed at 800°C for 29 hours, Nb-rich precipitate networks in pro-

eutectic NiTi dendrites became bigger and more extensive than those observed in the as-brazed specimens (not shown in Figure 3.26a but are similar to those in Figure 3.26b). However, there were no morphological changes to the eutectic micro-constituents and facetted grains (Figure 3.26a). The eutectic mixture still remains morphologically stable when subjected to annealing at 800°C for 104 hours, but the Ti_2Ni-type precipitates appeared to be in the process of coalescence to form larger grains (Figure 3.26b). Experimental results suggest that the coalescence has to be a thermally-activated process and one can expect to observe larger Ti_2Ni-type grains if either annealing duration was increased further or higher annealing temperatures were implemented.

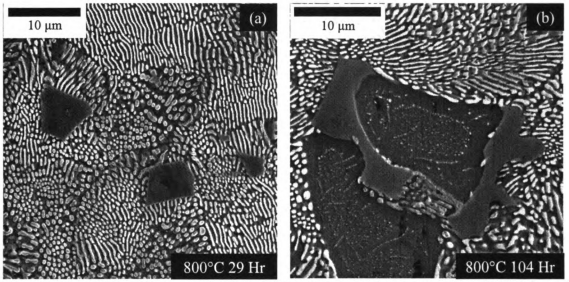

Figure 3.26 Microstructures of joints subjected to post-braze anneal at 800°C for (a) 29 hours; and (b) 104 hours.

Figures 3.27a and b show the microstructures of a braze joint subjected to annealing at 920°C for 20 hours. Significant morphological change was evident in the eutectic micro-constituents. The eutectic-Nb phase now appears to transit from lamellar

and rod-like morphology (Figure 3.27a) into final spheroidal form (Figure 3.27b). Recall that in as-brazed joints that the eutectic-Nb lamellae and rods had average spacings of 0.4 and 0.6 μm, respectively. However, the spheroidized eutectic has an average spacing of 0.9 μm. Similar to the coalescence of Ti_2Ni-type grains at 800°C, the spheroidization of the eutectic phase has to be a thermally-activated process and the driving force for such morphological transition is the reduction of eutectic-NiTi/eutectic-Nb interfacial boundary energy (assuming isotropic surface energies for both phases in the eutectic) [Flemings 1974].

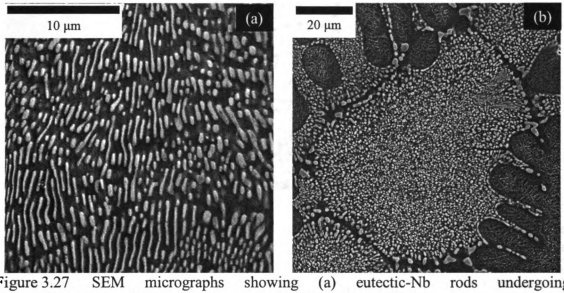

Figure 3.27 SEM micrographs showing (a) eutectic-Nb rods undergoing spheroidization and (b) completely spheroidized eutectic-Nb in braze joints subjected to post-braze anneal at 920°C for 20 hours.

Besides morphological changes in the eutectic micro-constituents, bigger and more extensive networks of Nb-rich precipitates were also observed in the pro-eutectic NiTi dendrites in Figure 3.27b than those seen in Figure 3.26b. This is not surprising as the microstructure approaches equilibrium from the annealing process. The Ti_2Ni-type

grains, originally seen in prolonged braze specimens, were no longer present when annealed at 900°C and water-quenched. This may be attributed to thermal decomposition and solutionizing of the Ti_2Ni-type precipitates into the eutectic matrix.

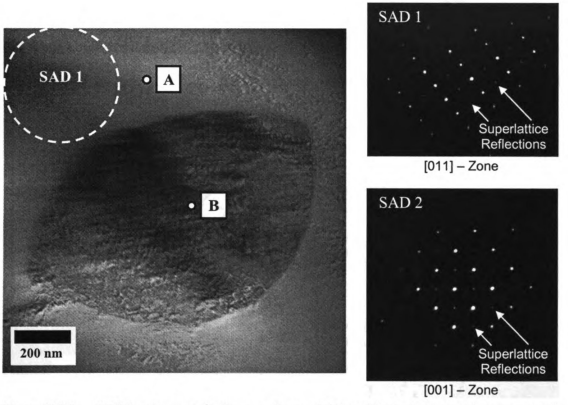

Figure 3.28 TEM micrograph from a braze joint subjected to post-braze anneal at 920°C for 20 hours and water-quenched showing a spheroidized eutectic-Nb particle in the eutectic-NiTi matrix, together with two SAD patterns from the eutectic-NiTi. (SAD 2 was taken from eutectic-NiTi at another location within the same specimen.) Positions A and B were sites for XRF analysis.

Table 3.4 X-ray fluorescence analysis on selected spots in Figure 3.28.

Spot	Nb (at%)	Ni (at%)	Ti (at%)
A	9	49	42
B	76	11	13

Selected-area diffraction obtained from the 920°C-annealed eutectic-NiTi phase in the TEM micrograph (SAD 1 of Figure 3.28) showed strong diffraction spots and

ordered-*B2* superlattice reflections from the [011]-zone. Diffraction obtained from eutectic-NiTi at a different location (SAD 2) also revealed strong superlattice ordering in the [001]-zone. Furthermore, distinct lattice fringes were observed in the high-resolution TEM micrograph of the eutectic-NiTi in the same specimen (Figure 3.29). Fast-Fourier Transform analysis shows that the grain was oriented along the *B2* [$\bar{1}22$]-zone axis. Martensite was again not observed in the eutectic-NiTi phase. From Figure 3.28 and 3.29, it can be deduced that post-braze annealing is necessary to fully restore *B2* ordering in the eutectic-NiTi phase in braze joints.

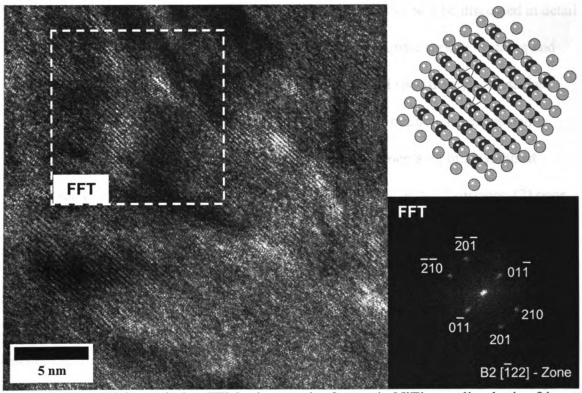

Figure 3.29 High-resolution TEM micrograph of eutectic-NiTi revealing lattice fringes oriented on the B2 [$\bar{1}22$]-zone axis. Top-right image schematically shows the real-space lattice arrangement (bright spheres: Ni atoms; dark spheres: Ti atoms). Bottom-right image is the FFT pattern of the selected area showing periodicity in reciprocal space. (FFT pattern originated from the indicated area of the micrograph.)

X-ray fluorescence was also performed on the phases in Figure 3.28 and results were summarized in Table 3.4. The higher spatial resolution associated with XRF in TEM allows the composition of eutectic-Nb to be determined and was found to possess approximately 10 at. % Ni and Ti solutionized in Nb. The TEM-XRF revealed eutectic-NiTi compositions in close agreement with the SEM-XRF results in Table 3.3.

3.5.3 Effects of Surface Preparation and Vacuum Contaminants on Joint Microstructures

Besides post-braze anneal temperatures, contamination is also a critical factor that is known to affect braze joint properties (mechanical properties will be discussed in detail in Chapter 4). Contaminations usually originate from inadequate surface cleaning and non-ideal braze ambient conditions. Hence, this section will specifically address the effects of surface preparations and vacuum conditions on joint microstructures and morphology. This study involved 3 controlled scenarios: Processing braze joints at 1185°C for 120 seconds under (1) good vacuum and using clean NiTi surfaces; (2) poor vacuum and using clean NiTi surfaces; and (3) poor vacuum and oxidized NiTi surfaces. Niobium foils were identically cleaned in each case. The definition of 'good vacuum' in this study implies vacuum in the range of 10^{-6} Torr, while 'poor vacuum' implies vacuum in the range of 10^{-4} Torr. These selected states of vacuum will provide distinctively different oxygen partial pressures in the braze chamber. The oxidized NiTi surfaces were obtained by first chemically removing native oxides from the NiTi specimens as described in Chapter 2, followed by heating them in air at 350°C for 1 hour. In this way, the mating surfaces were oxidized in a consistent and controlled fashion.

Figures 3.30a – c shows the SEM micrographs of braze joints processed under the 3 described scenarios, respectively.

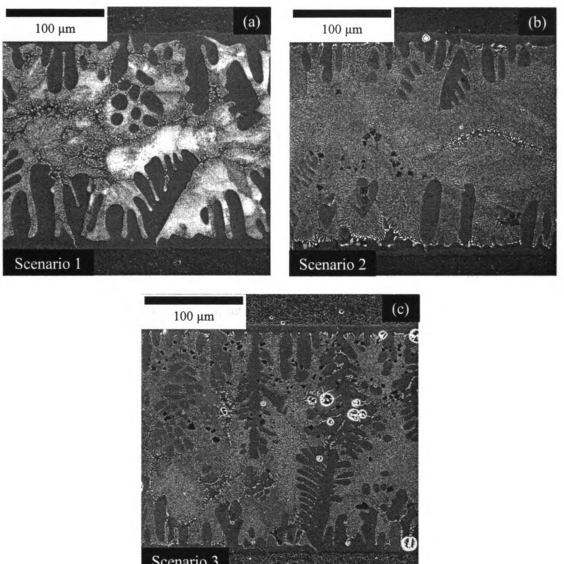

Figure 3.30 SEM micrographs of braze joints processed at 1185°C for 120 seconds under (a) scenario 1; (b) scenario 2; and (c) scenario 3. (Scenario 1: Good vacuum, Clean NiTi; Scenario 2: Poor vacuum, Clean NiTi; Scenario 3: Poor vacuum, Oxidized NiTi)

Experimental results show that brazing under good vacuum with clean mating NiTi surfaces produce joints with no Ti_2Ni-type precipitates and porosity (Figure 3.30a).

Despite clean surfaces, the number density of Ti_2Ni-type precipitates appears to increase when poor vacuum conditions were employed (Figure 3.30b). When brazing under poor vacuum with oxidized NiTi surfaces (Figure 3.30c), Ti_2Ni-type grains and pores form even more extensively in the joint. The significant increase in number density of Ti_2Ni-type precipitates as oxygen contamination worsens is consistent with the known ability of oxygen to stabilize their formation [Nevitt 1960, Melton 1990]. This comparative study highlights the importance of performing reactive eutectic brazing of NiTi alloys using clean mating surfaces under reasonably high vacuum conditions.

3.6 The Origin of the Perfect NiTi-Nb Quasibinary Eutectic Isopleth

At the beginning of this chapter, discussions on contact melting between NiTi and Nb were based on the assumption of a perfect NiTi-Nb quasibinary eutectic isopleth in the ternary system. However, the perfect quasibinary eutectic isopleth may not be an exact representation of the NiTi-Nb pseudobinary section. The literature suggests that the actual NiTi-Nb isopleth is more complex and may contain three-phase fields. Therefore, this section aims to address the origins of both possibilities for the isopleth through a qualitative analysis of the ternary phase equilibria. The literature strongly indicates that the Ni-Ti-Nb ternary phase diagram contains a NiTi-Nb quasibinary eutectic point close to 38Ni-36Ti-26Nb (at.%) at 1170°C and a NiTi + Nb(Ni,Ti) tie-line at 900°C has also been proposed [Prima et al. 1995] (see Figure 3.31). Although majority of the liquidus projections recently calculated by Matsumoto and coworkers [Matsumoto et al. 2005] is consistent with existing work, they did not take into account

the existence of the quasibinary eutectic point. In fact, Matsumoto's calculated liquidus projection at the quasibinary eutectic point violates the Alkamade's principle [Hillert 1998], which states that a temperature-maximum should occur in the liquidus line that demarcates two congruently-melting phases. In this case, the two congruently-melting phases are NiTi and Nb. Hence, a new liquidus projection of the ternary system is proposed to accommodate the existence of the quasibinary eutectic point as well as the Alkamade's principle (Figure 3.31). Therefore, the quasibinary eutectic point, which should lie close to the tie-line in Figure 3.31, will be at the temperature-maximum of the liquidus line.

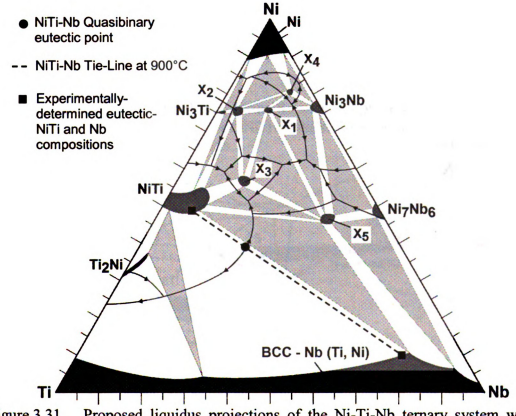

Figure 3.31 Proposed liquidus projections of the Ni-Ti-Nb ternary system with the reported 900°C isothermal section. (The literature-reported NiTi-Nb quasibinary eutectic point and NiTi + Nb(Ni,Ti) tie-line at 900°C (close to the quasibinary eutectic point) [Prima et al. 1995]; and experimentally-determined pro-eutectic NiTi and Nb compositions (Table 3.4) are indicated.)

Compositions of eutectic NiTi and Nb equilibrated at 920°C, as determined by TEM-XRF (summarized in Table 3.2), are also indicated in Figure 3.31. The TEM-XRF results are in fairly good agreement with the literature-reported NiTi + Nb(Ni,Ti) tie-line at 900°C [Prima et al. 1995], which confirms the validity of phase field positions close to the NiTi-Nb isopleth and will, later, aid in the determination of the true NiTi-Nb isopleth. Data from [Prima et al. 1995, Yang et al. 2000, Matsumoto et al. 2005] suggest that there are two four-phase Class-II reaction planes, U_1 and U_2, close to the NiTi-Nb quasibinary eutectic point (Figure 3.32). U_1 exist at about 950°C and involves the reaction:

$NiTi + Liq. \xrightarrow{cooling} Nb(Ni,Ti) + Ti_2Ni$; while U_2 occurs close to 1140°C, and involves the reaction: $Nb(Ni,Ti) + Liq. \xrightarrow{cooling} NiTi + X_5$.

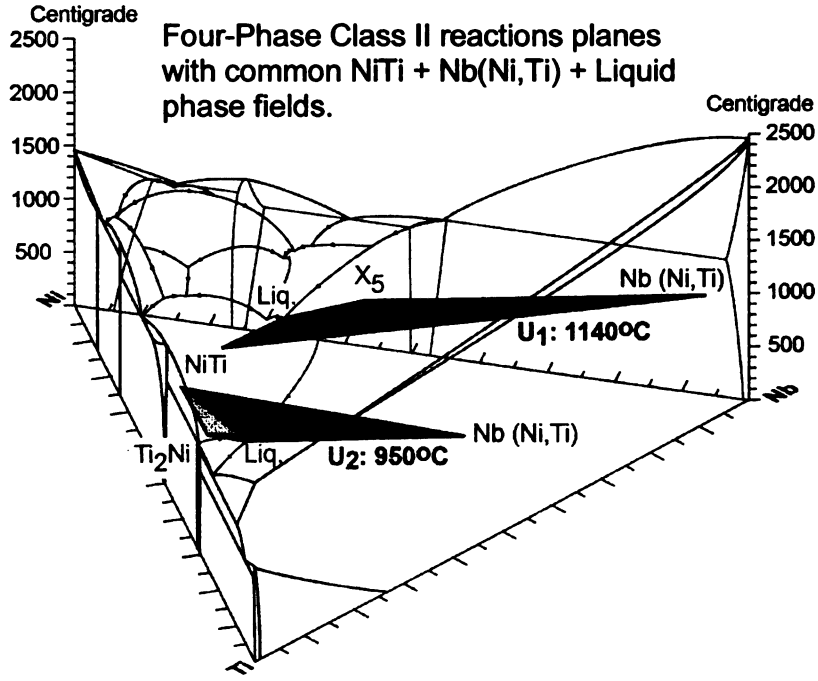

Figure 3.32 Four-phase Class-II reaction planes (U_1 and U_2) in close proximity to the NiTi-Nb quasibinary eutectic point.

There are NiTi + Nb(Ni,Ti) + Liquid phase fields in each reaction plane. These will converge and degenerate into the NiTi + Nb(Ni,Ti) tie-line as the temperature approaches 1170°C. For clarity, Figure 3.33 only illustrates how the NiTi + Nb(Ni,Ti) + Liquid phase triangle of the Ti-rich reaction plane degenerates into the NiTi + Nb(Ni,Ti) tie-line. The Ni-rich counterpart follows likewise. The NiTi + Nb(Ni,Ti) tie-line at 1170°C forms the reaction horizontal for the perfect quasibinary eutectic isopleth.

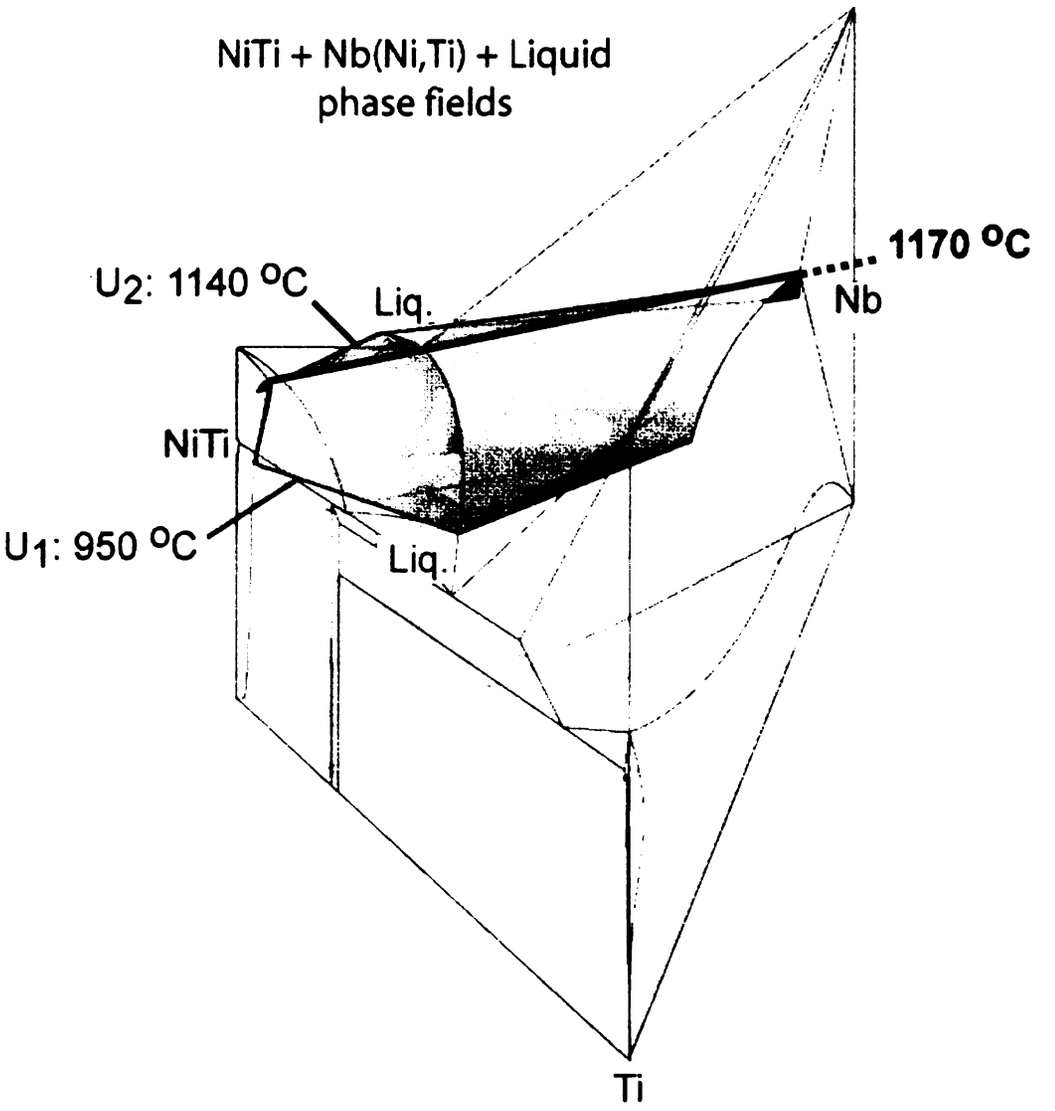

Figure 3.33 NiTi + Nb(Ni,Ti) + Liquid phase fields from U_1 and U_2 degenerating into a single NiTi + Nb(Ni,Ti) tie-line at 1170°C, forming the reaction horizontal for the perfect NiTi-Nb quasibinary isopleth.

The NiTi + Nb(Ni,Ti) tie-line at 900°C has been reported by Prima and coworkers [Prima et al. 1995] to be off the plane of the NiTi-Nb isopleth (see Figure 3.31). If this is the case, a perfect quasibinary eutectic diagram would not be a true representation of the NiTi-Nb isopleth. Furthermore, the NiTi + Nb(Ni,Ti) + X_5 phase field appears to intersect the NiTi-Nb isopleth. Therefore, the NiTi-Nb isopleth, after taking past work into consideration, is proposed to take on the form shown in Figure 3.34. Note that the X_5 + Ni_7Nb_6 + Nb(Ni,Ti) phase field was assumed not to cross the isopleth.

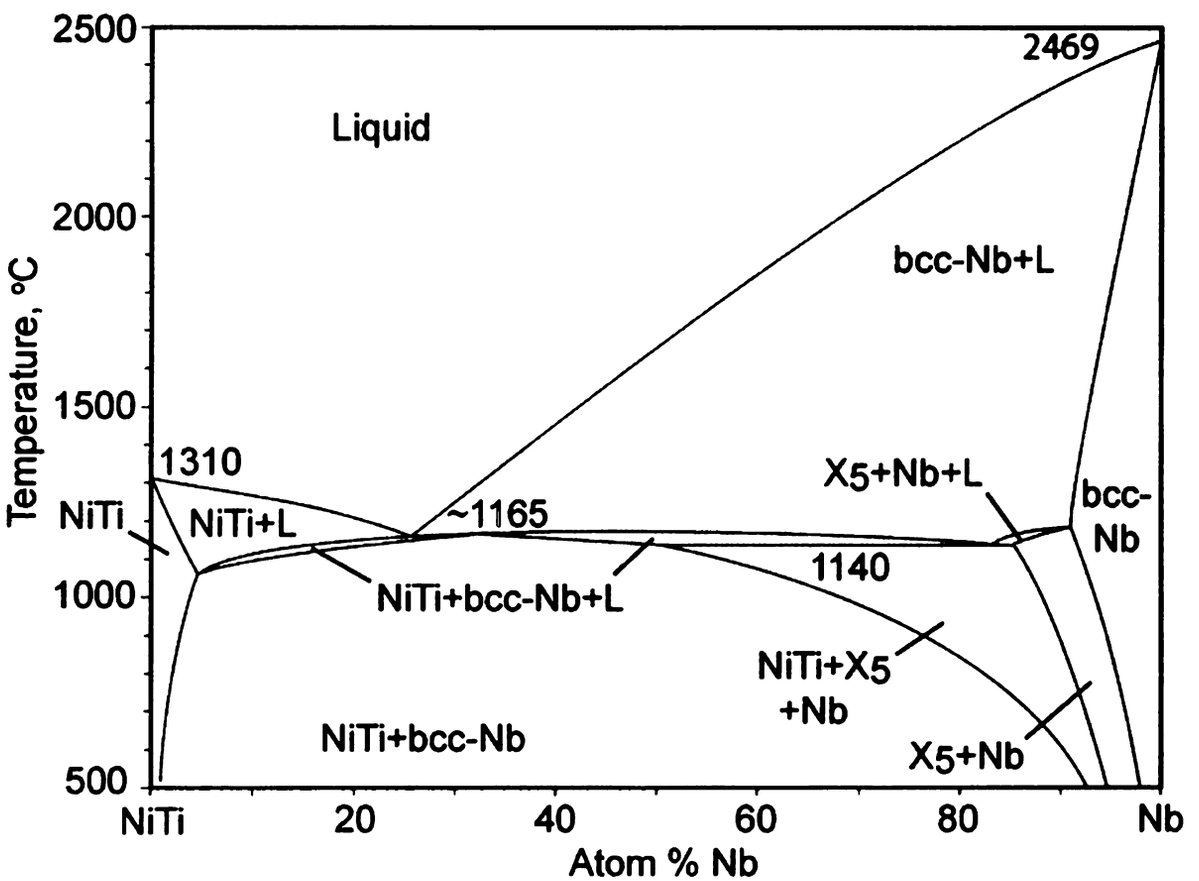

Figure 3.34 The proposed NiTi-Nb isopleth of the Ni-Ti-Nb ternary system.

Given its close proximity with the NiTi + Nb(Ni,Ti) tie-line, the NiTi-Nb isopleth possesses a high degree of similarity with the perfect quasibinary eutectic isopleth with

exceptions at the Nb-rich end. It is because of its similarity with the true isopleth and its simplicity that the perfect quasibinary eutectic isopleth was selected as the basis for previous contact melting discussions. A noteworthy feature to highlight in Figure 3.34 is the presence of a narrow NiTi + Nb(Ni,Ti) + Liquid phase field between the NiTi + Liquid and NiTi + Nb(Ni,Ti) phase fields, and it is expected to exist within an estimated range from 1130°C to 1170°C. If this is true, the presence of this NiTi + Nb(Ni,Ti) + Liquid phase field on the true NiTi-Nb isopleth suggests that contact melting between NiTi and Nb can actually occur between 1130°C to 1170°C.

Indeed, contact melting has been observed in this study at temperatures as low as 1155°C. Figure 3.35 shows the microstructure of a joint processed at 1155°C for 120 seconds, revealing pro-eutectic NiTi, eutectic and a high number density of Ti_2Ni-type precipitates. Some of these precipitates (Sites A, B and C in Figure 3.35) were analyzed by XRF and their compositions are tabulated in Table 3.5. The reason for the precipitation of these Ti_2Ni-type grains will be discussed in the next section.

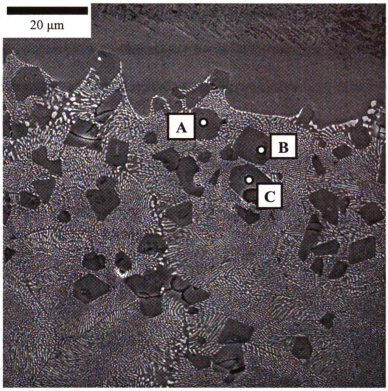

Figure 3.35 SEM micrographs of joints brazed at 1155°C showing coexistence of pro-eutectic NiTi, eutectic micro-constituents and Ti_2Ni-type phase.

Table 3.5 X-ray fluorescence analysis on selected spots in Figure 3.35.

Spot	Nb (at%)	Ni (at%)	Ti (at%)
A	11	37	52
B	13	36	51
C	12	36	52

3.7 Crystallography and Phase Equilibria of Ti_2Ni

Throughout the chapter, facetted precipitates were frequently observed in joints subjected to (1) prolong braze durations; (2) high degree of oxygen contamination; and (3) low braze temperature (1155°C). In section 3.4, these grains were shown to coarsen at 800°C, but dissolved at 920°C. Hence, this section is dedicated to discussion on the crystallography and phase equilibria of these facetted precipitates.

X-ray fluorescence was performed on the facetted precipitates in Figure 3.35. Results revealed that they contain almost 50 at.% Ti, but only have about 35 at.% Ni while the remaining composition is made up of Nb (Table 3.5). Since it has been demonstrated (Table 3.3) that Nb tends to substitute for Ti, the facetted precipitates should be of the Ti_2Ni-type phase with a more precise chemical formula of $(Ti,Nb)_2Ni$. The $(Ti,Nb)_2Ni$ precipitates were also studied by TEM. A micrograph and selected-area diffraction of a Ti-rich grain are given in Figure 3.36, which revealed the *FCC*-type crystal structure and the diffraction spots were associated with the [011]-zone. The chemical composition of the $(Ti,Nb)_2Ni$ precipitate was determined by TEM-XRF to be 39Ni-58Ti-3Nb, which is in reasonably close agreement with results from SEM-XRF (Table 3.5).

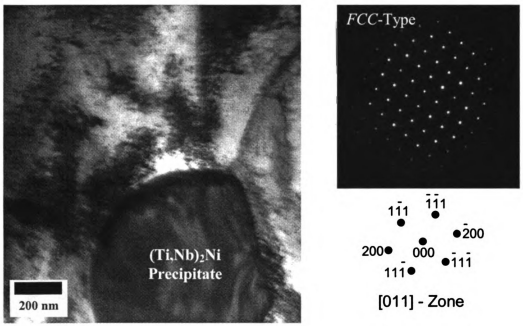

Figure 3.36 TEM micrograph of braze joints processed at 1185°C for 360 seconds showing a $(Ti,Nb)_2Ni$ precipitate and its SAD pattern.

Recall that oxygen contamination tends to encourage precipitation of the Ti_2Ni-type phase (see Figure 3.30). The catalyzing role of oxygen can be attributed to the solubility of oxygen in $(Ti,Nb)_2Ni$. According to data from [Nevitt 1960, Gupta 1991, Prima et al. 1995, Yang et al. 2000, Chuprina et al. 2002], the 900°C isothermal tetrahedron of the quaternary Ni-Ti-Nb-O system was constructed (Figure 3.37) and it indicates that up to approximately 15 at.% oxygen should be soluble in $(Ti,Nb)_2Ni$, giving rise to $(Ti,Nb)_4Ni_2O$ formation.

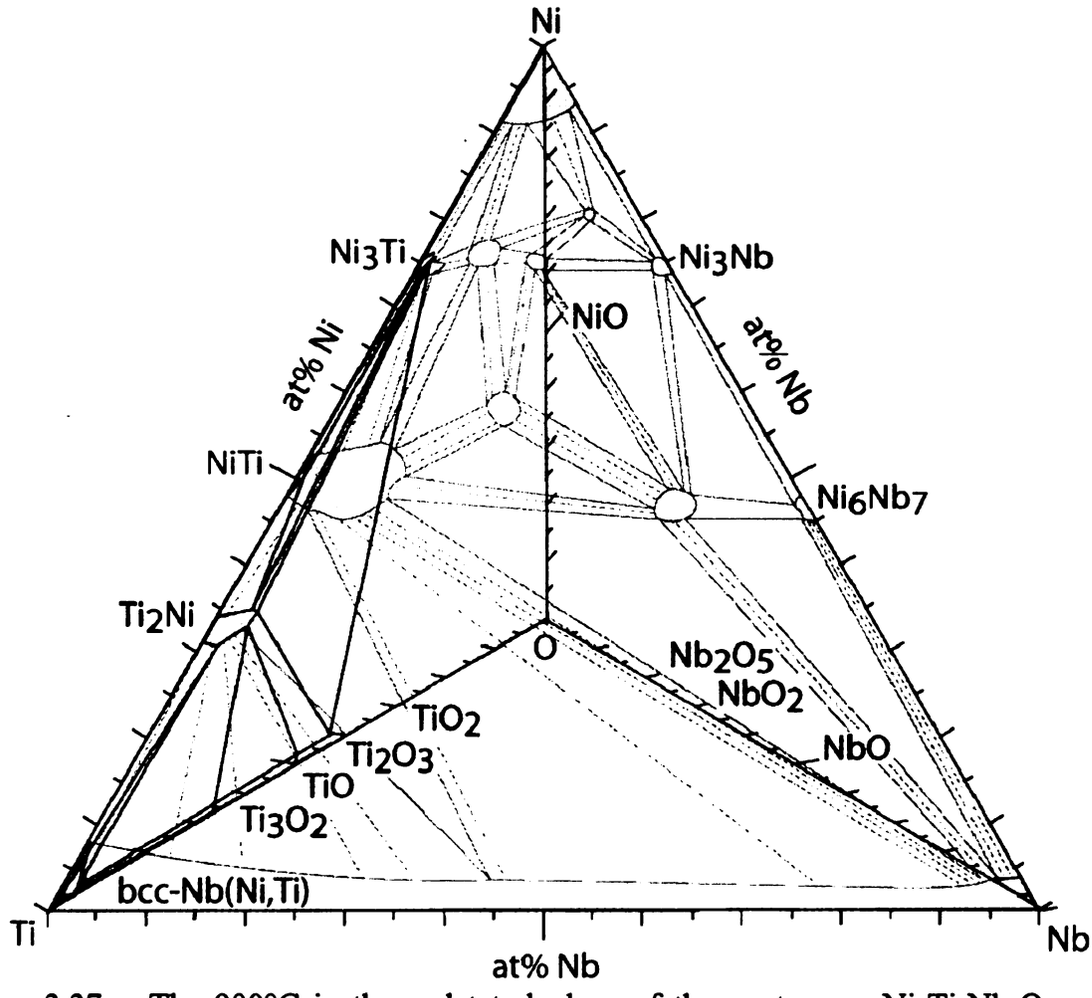

Figure 3.37 The 900°C isothermal tetrahedron of the quaternary Ni-Ti-Nb-O system [Nevitt 1960, Gupta 1991, Prima et al. 1995, Yang et al. 2000, Chuprina et al. 2002].

The ability of oxygen to be incorporated into the Ti_2Ni lattice can also be appreciated through the crystal structures of Ti_2Ni and Ti_4Ni_2O. Figure 3.38 illustrates the unit cells of Ti_2Ni and Ti_4Ni_2O. The former has 96 atoms per unit cell, while the latter has 112 atoms per unit cell. Both phases have cubic structures and share the same space group of Fd3m [Mueller et al. 1963], making them crystallographically very similar, and almost indistinguishable by diffraction techniques. The calculated powder diffraction spectra of both species in Figure 3.38 revealed that the three strongest reflections of both phases are identical. Ti_2Ni can be transformed into Ti_4Ni_2O by addition of 16 oxygen atoms to all of its unoccupied tetrahedral interstitial sites of alternate sub-cells. However, non-stoichiometric Ti_4Ni_2O or sub-oxides can also form. In other words, it is not necessary for each unit cell to have full occupancy of 16 oxygen atoms.

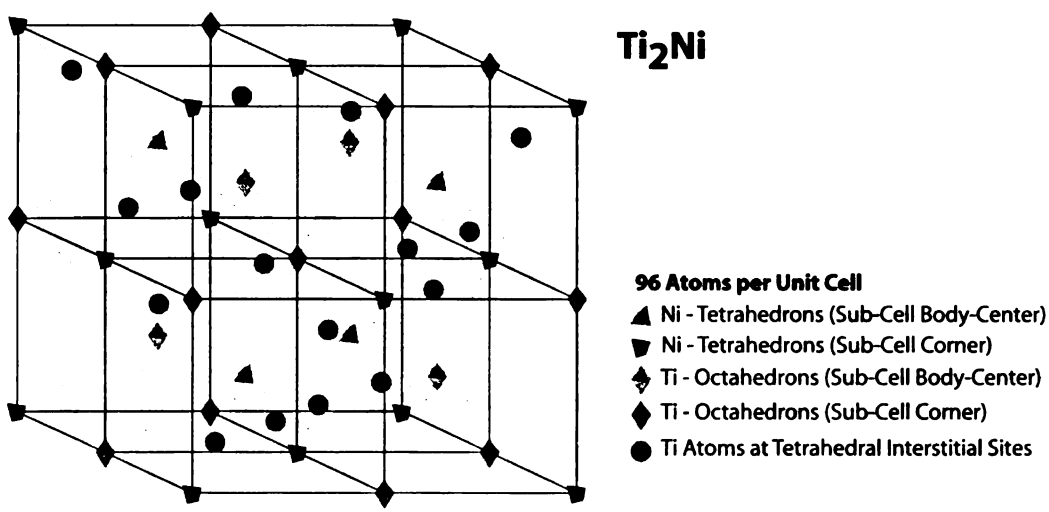

Figure 3.38 Unit cells of Ti_2Ni and Ti_4Ni_2O [Mueller et al. 1963], and their respective calculated power diffraction spectra. (Both phases share similar strongest peaks, which are labeled according to their *hkl* planes.)

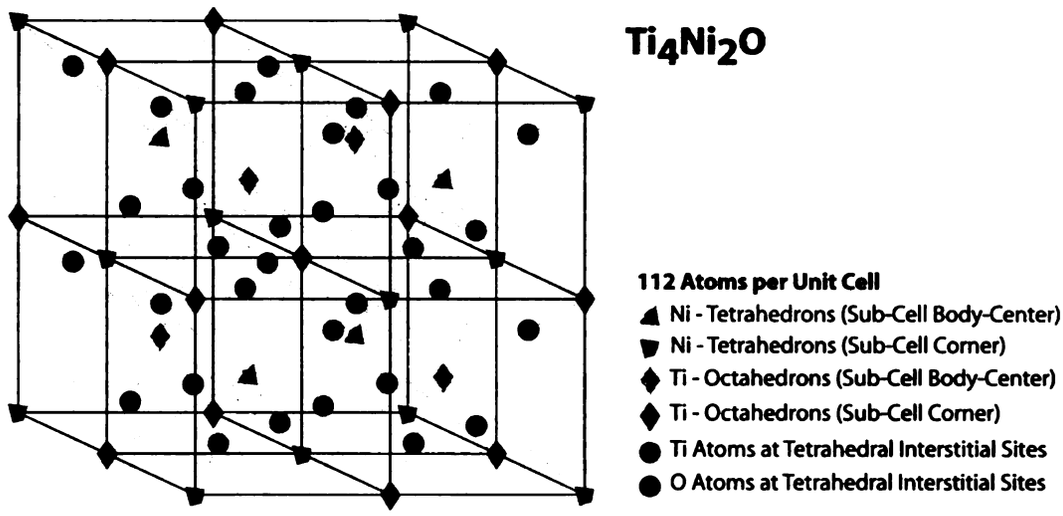

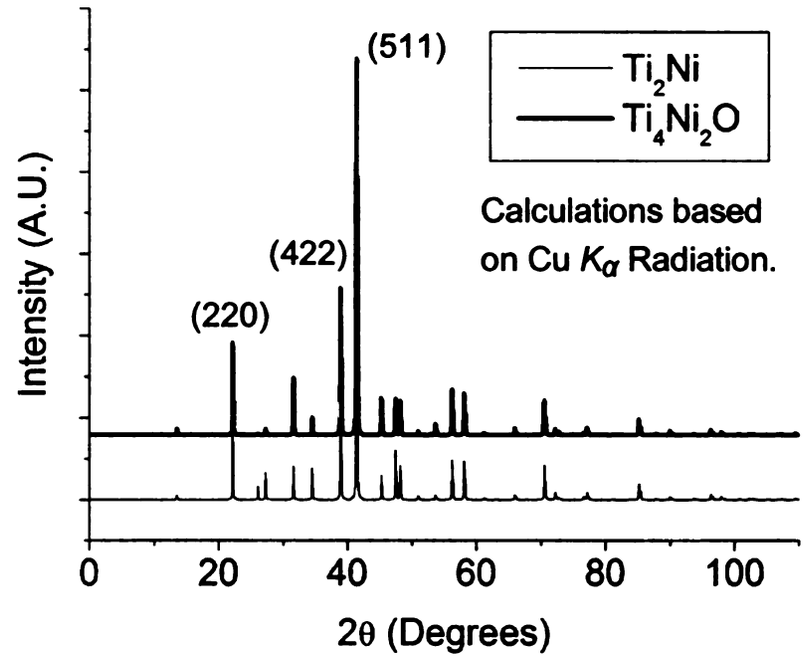

Figure 3.38 (Continued).

Apparently, an oxygen-contaminated braze liquid (originating either from high oxygen partial pressures or from dissolution of native oxides) will attempt to incorporate the oxygen chemically into the joint by precipitating sub-oxides of $(Ti,Nb)_4Ni_2O$ during cooling. The reason stems from the fact that $(Ti,Nb)_2Ni$ has a moderately high oxygen solubility limit, perhaps much higher than eutectic-NiTi or eutectic Nb. This deduction is

also consistent with the frequent observation of Ti_2Ni-type precipitates in joints subjected to prolonged braze durations, where there is higher tendency for braze liquid to absorb oxygen from vacuum contamination. Note that SEM-XRF and TEM-XRF study did not reveal any oxygen in the Ti_2Ni-type precipitates because the O *Kα* x-ray line (0.5249 KeV) is close to the Ti *Lα* line (0.4522 KeV) and the energy resolution of XRF (approximately 100 eV) is not good enough to resolve the two peaks.

Besides oxygen contamination, brazing at 1155°C for short durations (< 120 seconds) was also observed to result in extensive precipitation of the Ti_2Ni-type phase. Their formation at a braze temperature of 1155°C can be explained with the aid of Figure 3.39, which illustrates the NiTi + Nb(Ni,Ti) + Liquid phase field evolution as temperature decreases from 1165°C to 1155°C. Note that liquid compositions are governed by the liquidus projection. At 1155°C, the braze liquid establishes equilibrium at composition $C_{T,2}$, making it higher in Ti content than those at $C_{T,1}$ and C_E.

For $(Ti,Nb)_2Ni$ to precipitate from liquid composition $C_{T,2}$, the temperature-evolution of the NiTi + Nb(Ni,Ti) + $(Ti,Nb)_2Ni$ phase field should take on the form as shown in Figure 3.40, where the phase field is shown to swing rapidly towards the NiTi-Nb isopleth as temperature decreases from 950°C. At 20°C, the isothermal section is estimated to resemble the one shown in Figure 3.41. If the hypothesized phase field evolution is true, liquid composition $C_{T,2}$ will first enter the NiTi + Nb(Ni,Ti) phase field

during initial cooling, but abruptly falls into the NiTi + Nb(Ni,Ti) + $(Ti,Nb)_2Ni$ three-phase field below 950°C. Because of the gentle-sloping solidus boundary of the NiTi + Nb(Ni,Ti) + $(Ti,Nb)_2Ni$ phase field, the hypothesized phase field evolution predicts the ability to re-solutionize $(Ti,Nb)_2Ni$ phase at temperatures around 950°C. This prediction agrees well with experimental observations of the Ti_2Ni – type precipitates re-solutionizing into the eutectic phase at 920°C (Figure 3.27).

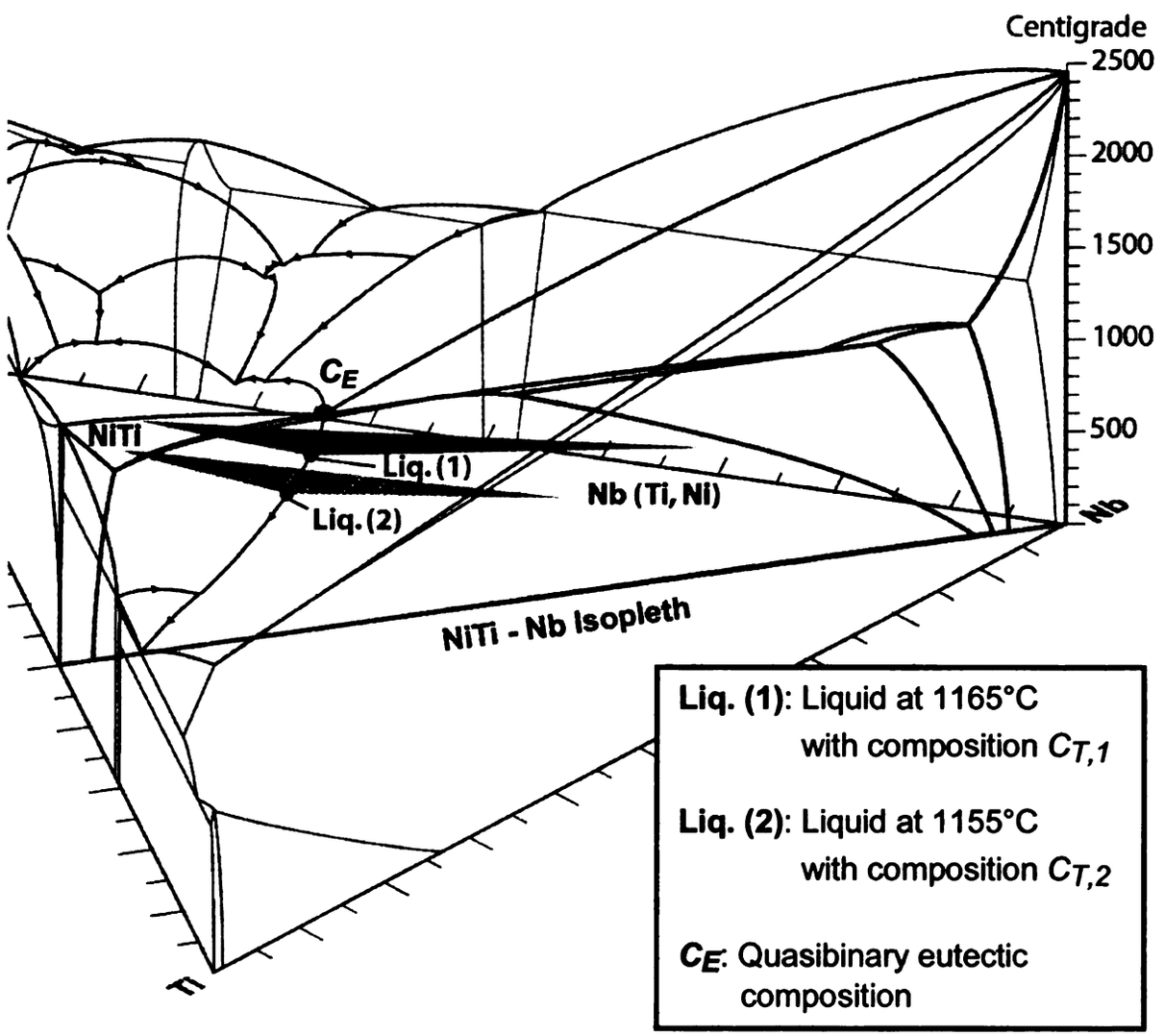

Figure 3.39 NiTi + Nb(Ni,Ti) + Liquid phase field evolution as temperature decreases from 1165°C to 1155°C, resulting in Ti-enrichment in the liquid phase.

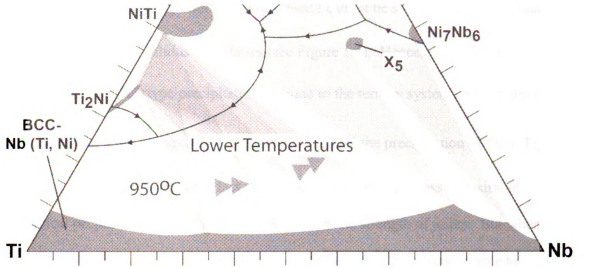

Figure 3.40 Hypothesized NiTi + Nb(Ni,Ti) + $(Ti,Nb)_2Ni$ phase field evolution as temperature decreases from 950°C. Gently-sloping NiTi + Nb(Ni,Ti) + $(Ti,Nb)_2Ni$ / NiTi + Nb(Ni,Ti) phase boundary providing re-solutionizing possibility for $(Ti,Nb)_2Ni$. (Color tone of phase fields corresponds to temperatures: Darker – Higher temperature; Lighter – Lower temperature.)

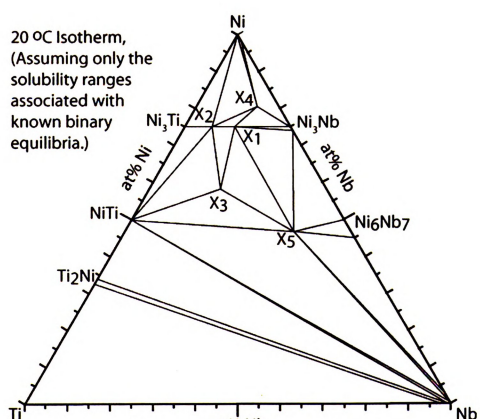

Figure 3.41 The proposed 20°C isothermal section of the Ni-Ti-Nb system.

It is important to highlight that Ti_2Ni phase cannot be solutionized in the binary system due to its steep solidus boundaries (see Figure 1.4). Hence, the ability to re-solutionize the Ti_2Ni – type precipitates is unique to the ternary system and can serve as a means to control their precipitation. The need to control the precipitation of these Ti_2Ni – type precipitates stems from the fact that, when coarse, they possess undesirable mechanical properties that will compromise the ultimate strength of joints. But when developed as fine, coherent precipitates, or even as GP zones, they may be able to strengthen the NiTi phase substantially. (Details on their mechanical properties will be discussed in Chapter 4.)

3.8 Summary

Experimental and simulation results show that the driving force for NiTi-Nb contact melting stems from the deviation from local equilibria at the respective melt interfaces, while the melting process is rate-controlled by liquid diffusion rates. For a Nb foil thickness of 51 μm, melting was found to occur rapidly during the first few seconds. However, the rate of melting decreased as the liquid width increased at longer braze times. Due to sluggish solid-state diffusion of Nb, isothermal solidification plays an insignificant role in the reactive eutectic braze process. On the other hand, isothermal solidification was feasible only when thin Nb films were employed as the braze filler.

Owing to the presence of a NiTi-Nb quasibinary eutectic isopleth in the ternary system, braze liquid solidifies with predominantly eutectic micro-constituents. However,

oxygen contamination arising from poor surface preparations, poor vacuum conditions or prolonged braze durations tends to encourage the precipitation of $(Ti,Nb)_4Ni_2O$ sub-oxides. Phase equilibria considerations and experimental evidence have shown that these Ti_2Ni – type precipitates can be re-solutionized at 920°C. The re-solutionizing treatment will concurrently spheroidize the eutectic-Nb phase.

CHAPTER 4: MECHANICAL PROPERTIES OF NIOBIUM-EUTECTIC BRAZE JOINTS

4.1 Introduction

Results of experiments on the mechanical performance of Nb-eutectic braze joints will be presented in this chapter. In particular, experimental techniques, such as nano- and microindentation, shear and tensile tests, were employed to probe the mechanical properties of the eutectic and its constitutive phases. Fractography will also be discussed. Besides NiTi-NiTi homo-joints, the reactive eutectic braze process was also applied to hetero-joints of NiTi-Ta and NiTi-Al_2O_3, whose mechanical properties will be presented at the end of this chapter.

4.2 Nanoindentation Studies

Nanoindentation experiments were performed on near-equiatomic NiTi joint specimens that were brazed using 51 μm-thick Nb foils. Braze temperature and duration used in this series of experiments were 1185°C and 120 seconds, respectively. The details of the nanoindentation setup, calibration and experimental procedures were described in Chapter 2 and will not be reiterated here. Most of the results were derived from indentation holding depth of 50 nm and a strain rate of 0.001 per second unless otherwise specified.

For the purpose of comparison, a control experiment was first performed on pure Nb and on the base-NiTi material. At least 10 indents were made on each material in

order to obtain meaningful average values of hardness and elastic modulus from the results. The typical load vs. displacement curves of pure Nb and base-NiTi at an indentation depth of 100 nm are given in Figure 4.1. Using the Oliver-Pharr model [Oliver et al. 1992], the mean hardness and elastic modulus of pure Nb derived at this indentation depth were found to be 1.1 GPa and 104 GPa, respectively. As mentioned in Chapter 2, these values are reasonably consistent with those reported in literature [Myneni et al. 2003, Wang et al. 2005, Alkorta et al. 2006]. For the base-NiTi, the mean hardness and elastic modulus are 4.3 GPa and 101 GPa, respectively.

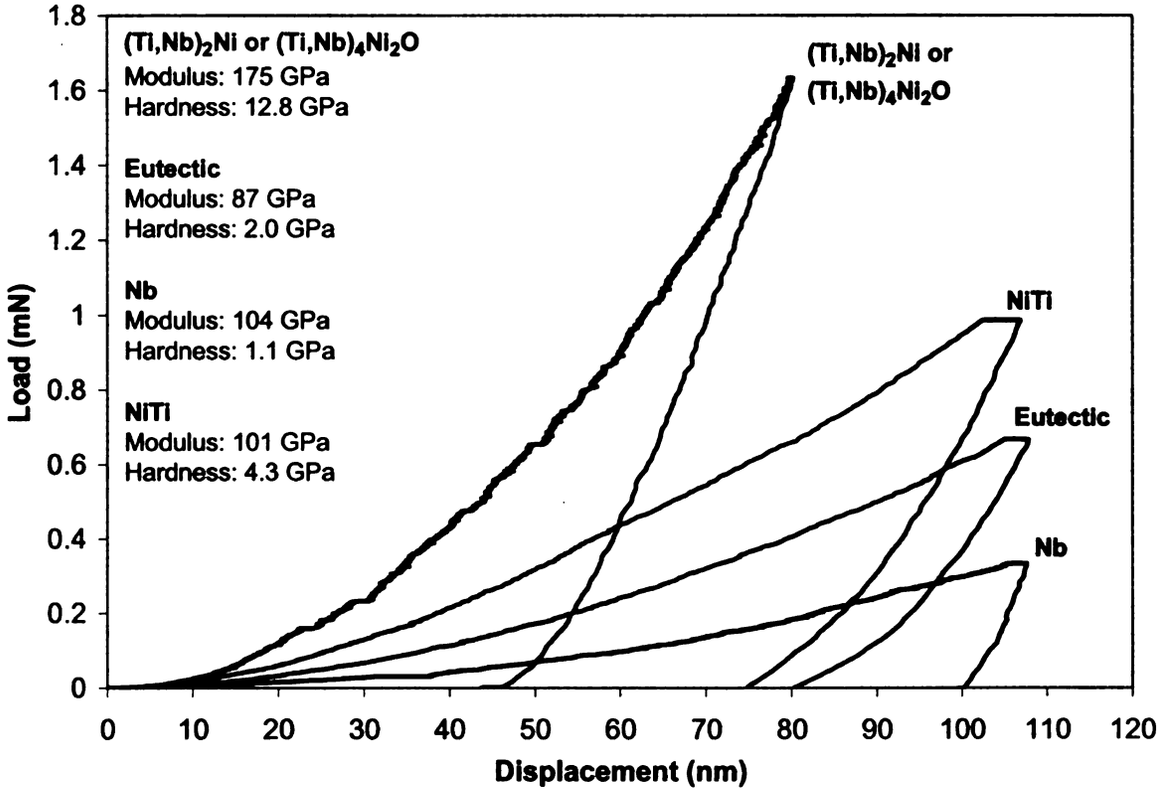

Figure 4.1 Load vs. Displacement curves of various phases. Indentation holding depth: 100 nm. Strain rate: 0.001 per second.)

Next, the effect of post-braze anneals on mechanical properties of the eutectic joint and base-NiTi were investigated. Specifically, separate specimens were subjected

to post-braze annealing regimes of 350°C (1.5 hours), 800°C (104 hours) and 920°C (29 hours). All specimens were annealed in air followed by a water-quench. For this series of experiments, at least 50 indents were made on each studied area. Statistical data for measured hardness and elastic modulus, of an as-brazed eutectic joint, is plotted in the form of histograms in Figure 4.2a and b to illustrate the typical sampling distributions.

Since the joint consists mainly of eutectic-NiTi and eutectic-Nb phases, which are expected to have differing mechanical properties[1], one would expect the hardness and/or the modulus distribution to have bi-modal characteristic. However, the histograms in Figure 4.2a and b are single-mode distributions. The mean indentation hardness and elastic modulus were calculated to be 2.0 GPa and 87 GPa, respectively.

Recall that the typical spacing in the eutectic phase is about 0.5 μm, while the indentation holding depth employed for this experiment is 50 nm, which yield a projected indentation width of about 0.3 μm. Given the similarity in eutectic spacing and indenter lateral probing resolution, there is strong tendency that the indenter was actually probing both phases simultaneously during each indentation. It is important to stress that although the indentation holding depth can be further reduced to improve the lateral probing resolution, it will increase measurement noise by doing so and hence compromise measurement resolution.

---

[1] At least in terms of hardness as the control tests showed that pure Nb and the base NiTi alloy have rather similar elastic modulus.

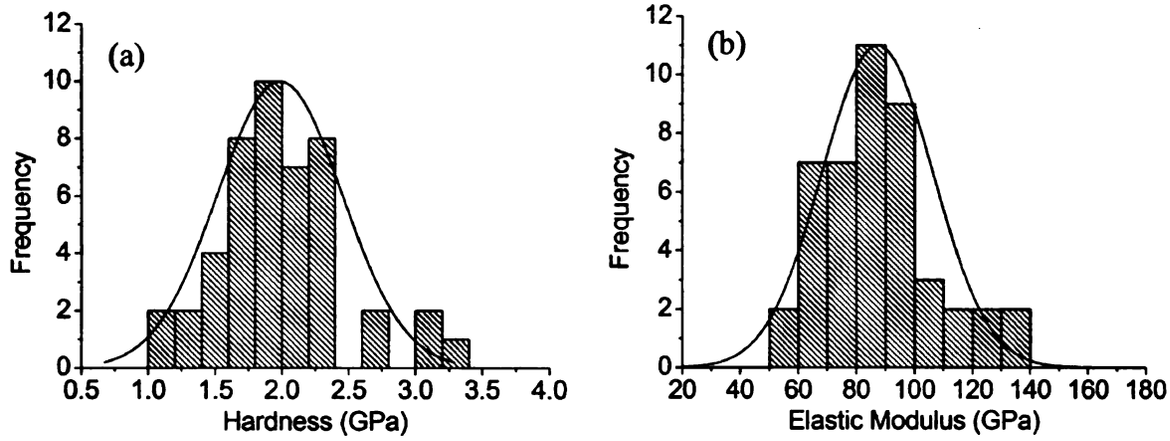

Figure 4.2 Histograms of (a) hardness and (b) elastic modulus of as-brazed eutectic joints showing the typical sampling distributions. Continuous lines are Gaussian distribution curves fitted over the histograms. (Data derived from indentation holding depth of 50nm.)

The typical load vs. displacement curve of the eutectic micro-constituents at an indentation depth of 100 nm is illustrated in Figure 4.1, which clearly shows that the eutectic micro-constituents required an indentation load that is intermediate of those required for pure NiTi and Nb in order to achieve similar indentation displacement. This is consistent with the calculated hardness of pure NiTi, Nb and the eutectic mixture. Recall in Chapter 3 that stereology suggested an estimated 30 vol.% occupancy by the eutectic-Nb phase. By applying the rule of mixture to the indentation hardness of pure NiTi and Nb, the eutectic micro-constituents was expected to possess a hardness of about 2.7 GPa, which is in fair agreement with the experimentally-determined hardness of 2.0 GPa.

The mean hardness and elastic modulus, for both eutectic joints and base-NiTi, at various annealing temperatures are summarized and plotted in Figure 4.3a and b, respectively. The as-brazed eutectic joint was found to possess an average hardness of 2.0 GPa, which is about half of the as-brazed base-NiTi's hardness. A mean elastic

modulus of 87 GPa for the as-brazed eutectic joint is also lower than those of the base-NiTi and the pure Nb. The joint hardness increases from as-brazed condition to a value comparable to the base-NiTi's hardness when subjected to annealing temperature of 350°C, but hardness decreases gradually to as-brazed state when the annealing temperature was increased to 920°C. Annealing at 350°C seems to lower joint stiffness while annealing beyond 800°C leads to a slightly higher modulus than as-brazed joints.

The base-NiTi hardness appears constant from the as-brazed state to an annealing temperature of 350°C, but increases significantly after annealing at 920°C. Elastic modulus of base-NiTi was observed to decrease gradually as the annealing temperature was increased. To summarize, temperature studies on the joints and base-NiTi, annealing at 350°C yields the maximum joint hardness, which becomes comparable to the hardness of the base-NiTi.

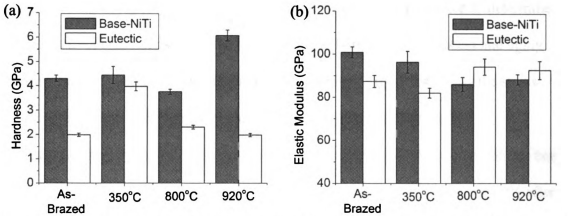

Figure 4.3 Plots of (a) hardness and (b) elastic modulus versus post-braze anneal temperatures of 350°C, 800°C and 920°C of eutectic joints and base-NiTi. As-brazed data included. (Data derived from indentation holding depth of 50nm.)

By performing nanoindentation in areas with high number-density of the facetted $(Ti,Nb)_2Ni$ or $(Ti,Nb)_4Ni_2O$ precipitates, their mechanical properties can also be determined. Figure 4.1 shows the load vs. displacement curve of a Ti_2Ni-type precipitate at an indentation depth of 100 nm. Given that poisson's ratio of the Ti-rich phase is unknown, an arbitrary poisson's ratio has to be assigned in order to calculate the hardness and elastic modulus. Since most metallic and intermetallic materials have values that fall between 0.3 and 0.4, a value of 0.35 was assumed. Calculations yield hardness of 12.8 GPa and an elastic modulus of 175 GPa, which are significantly higher than those of the base-NiTi alloy and the eutectic micro-constituents. The indentation characteristics of Ti_2Ni-type precipitate suggest that it is likely to be brittle in nature.

4.3 Base-NiTi Properties and Annealing Response

Before commencing mechanical tests on these joints, control specimens of room-temperature superelastic NiTi alloy with no joints were first tensile-tested to determine the stress-strain characteristics of the base-NiTi, and how the braze process and aging treatments affect the base-alloy's mechanical properties. Figure 4.4 shows the stress-strain curve of an as-received superelastic NiTi alloy subjected to tensile loading/unloading cycles (with progressively larger strains from 6% to 12%) before being strained to failure. The material suffered an unrecoverable strain of more than 2% after the first strain cycle of 6%, with each subsequent cycle only producing about 0.5% permanent strain. The last cycle yielded a recoverable strain of about 8%. Despite superelastic recovery, no distinct plateau stresses were observed in the stress-strain plot.

Fracture occurred at about 1.10 GPa at a strain of 37%. Elastic modulus measured from the second unloading slope revealed a value of about 17 GPa, which appears to be significantly lower than values obtained from nanoindentation experiments. Given that extensometers were not used in the tensile experiments, substantial errors in strain measurements can be expected, which in turn, will affect all modulus measurements. In order for the elastic modulus of NiTi alloys measured from tensile experiments to agree with the widely reported range between 50 GPa to 70 GPa, the strain scale can be re-calibrated by dividing the current strain magnitudes by a factor of 3 to 4. However, the main goal of this work is to compare the relative tensile strengths of the braze joints, rather than to accurately determine the strains and elastic moduli, no corrections will be applied to the rest of the stress-strain plots.

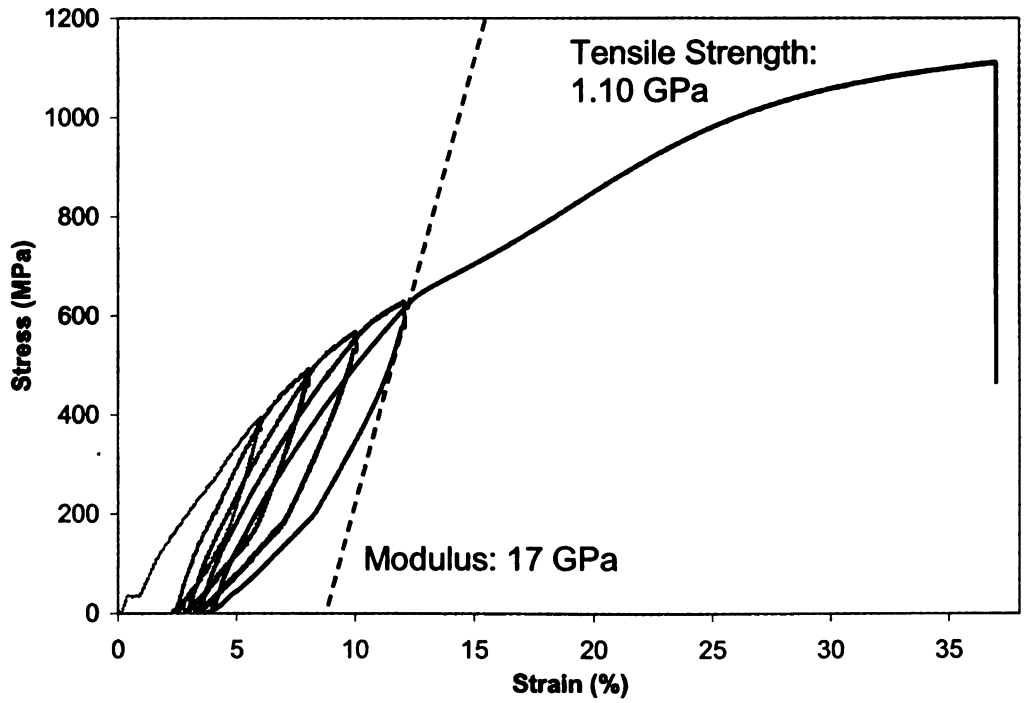

Figure 4.4 Stress vs. strain plot of as-received room-temperature superelastic base-NiTi control specimen.

Next, an as-received superelastic control specimen was subjected to annealing at 350°C for 1.5 hours before undergoing similar tensile testing. The mechanical behavior is shown in Figure 4.5. Again, initial loading up to 6% strain yielded an unrecoverable 2% strain upon unloading, and subsequent loading/unloading cycles each produces less than 1% permanent strain. Mean elastic modulus derived from the unloading curves of these subsequent cycles was 24 GPa. Maximum superelastic recovery of about 9% was observed in the final cycle. Tensile stress and strain at fracture were approximately 1.35 GPa and 28%, respectively. A relatively more defined upper- and lower-plateau stresses close to 300 MPa and 100 MPa, respectively, could now be seen in the initial cycle in Figure 4.5. However, these plateau stresses decreases gradually as the strains associated with each cycle increases.

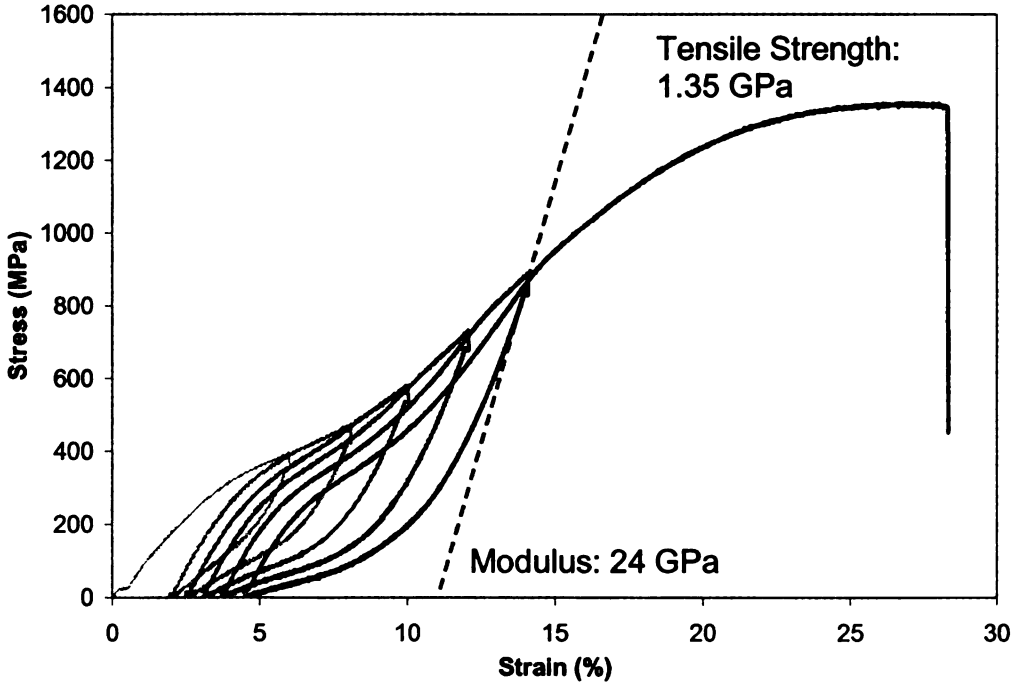

Figure 4.5 Stress vs. strain plot of as-received room-temperature superelastic base-NiTi control specimen that had been subjected to aging treatment at 350°C for 1.5 hours (then water-quenched) prior to testing.

Monolithic NiTi sections that had undergone the typical braze regime were tested under tensile loading/unloading conditions to evaluate the effects of brazing on base-NiTi mechanical properties. Figure 4.6 shows permanent strains of 1% associated with each progressive loading/unloading cycle. Recoverable strains of about 7.8% can be achieved in the second cycle. No distinct plateau stresses were observed and the specimen fractured at a stress and strain of about 800 MPa and 26%, respectively.

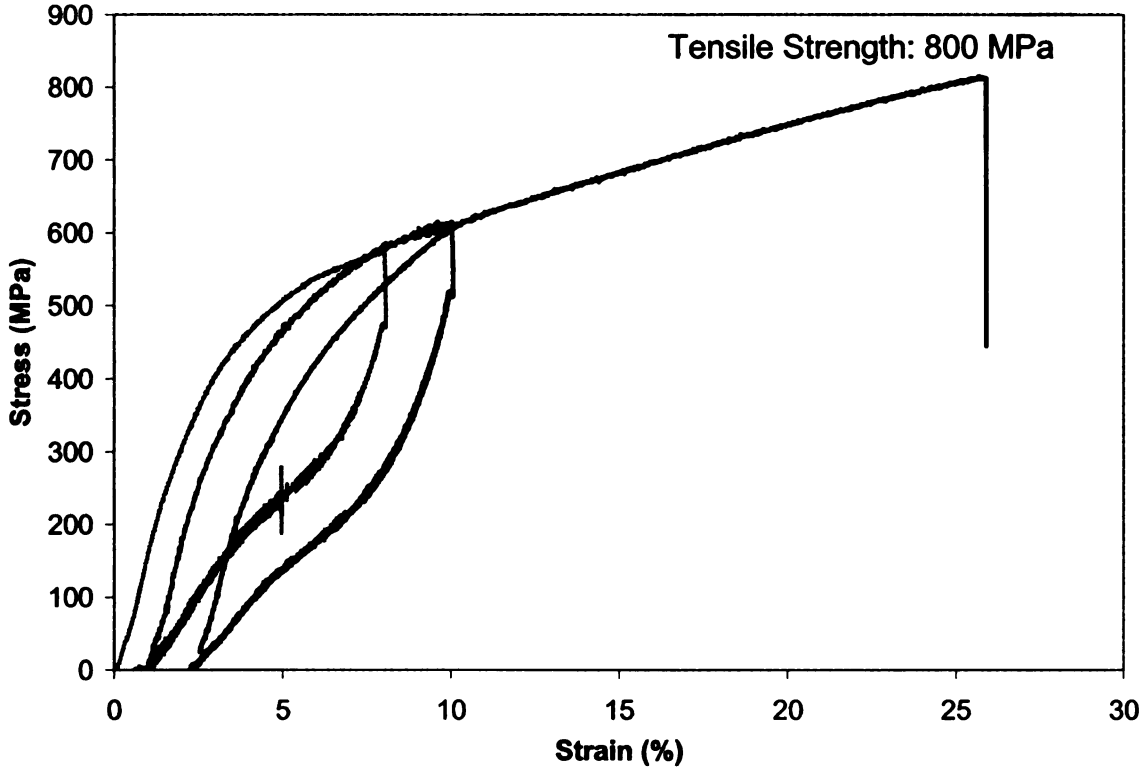

Figure 4.6 Stress vs. strain plot of as-received room-temperature superelastic base-NiTi control specimen that had been subjected to the typical braze process conditions prior to testing.

Figure 4.7 shows the stress-strain behavior of a control specimen subjected to the braze process and subsequently aged at 350°C for 1.5 hours prior to testing. Initial loading/unloading cycle produces an unrecoverable strain of more than 1%. A

recoverable strain of about 7% could be achieved if total strain did not exceed 8%. The stress-strain plot now shows flatter, well-defined upper- and lower-plateau stresses at about 350 MPa and 150 MPa, respectively, in the first cycle. They were observed to decrease gradually as the strain associated with each loading/unloading cycle increases. The control specimen failed at about 900 MPa at a strain of 23%.

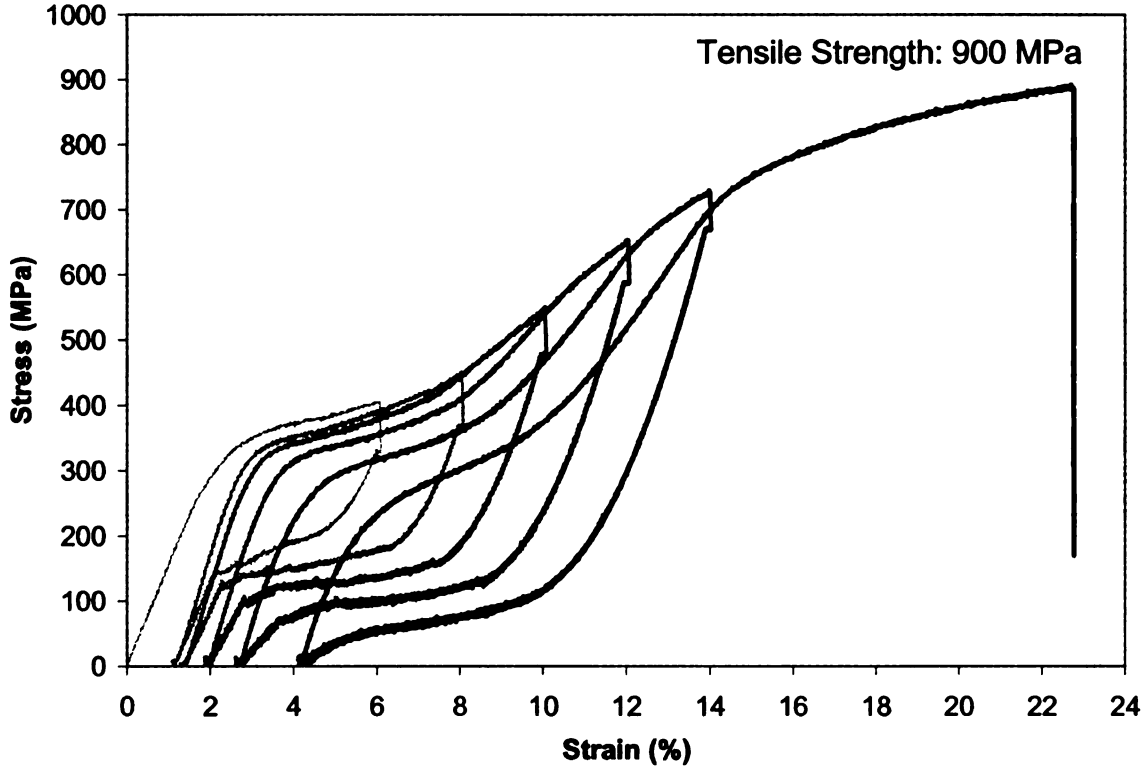

Figure 4.7 Stress vs. strain plot of as-received room-temperature superelastic base-NiTi control specimen that had been subjected to the typical braze process followed by aging at 350°C for 1.5 hours (then water-quenched) prior to testing.

From Figure 4.4 to Figure 4.7, it can be deduced that the braze process did result in mechanical degradation in terms of strength and ductility, but typical superelastic response can be restored in the base-NiTi after post-braze aging treatments. Note that this alloy is designed for superelasticity at 37°C, while all the above tensile tests were run

at 20°C. It is believed that superelastic response would have been superior if tests were performed at 37°C.

4.4 Tensile Tests on Eutectic Braze Butt-Joints

The reactive eutectic braze process was next employed to prepare butt-joint specimens. Most of the specimens made for this series of the study were the room-temperature superelastic NiTi used for the base-line tests described in Section 4.3. The initial joint clearance was approximately 400 μm (unless otherwise specified). Sufficient Nb foils were used to fill in the gap. Figure 4.8 shows the representative stress-strain behavior of a typical as-brazed superelastic butt-joint. The butt-joint specimen failed consistently within the eutectic joint, which will give a good measure of the joint mechanical properties. Based on the loading curve, the superelastic butt-joint specimen possessed an elastic modulus of 22 GPa. This value is fairly consistent with the modulus obtained from the control specimen in Figure 4.4. The superelastic butt-joint failed at a stress and strain of 680 MPa and 21%, respectively.

Comparison between stress-strain characteristics of as-brazed superelastic butt-joint (Figure 4.8) and that of the monolithic control (Figure 4.6) shows high degree of similarity, with the exception that the former only have 85% of the base-NiTi's strength and ductility. This indicates that the eutectic joint possesses mechanical properties that are comparable, but still inferior to that of the base-NiTi alloy. Given that pure Nb is weaker than pure NiTi, with a room-temperature tensile strength of about 170 MPa

[Gupta and Suri 1994], it is expected that the strength-limiting phase in the joint is the eutectic-Nb.

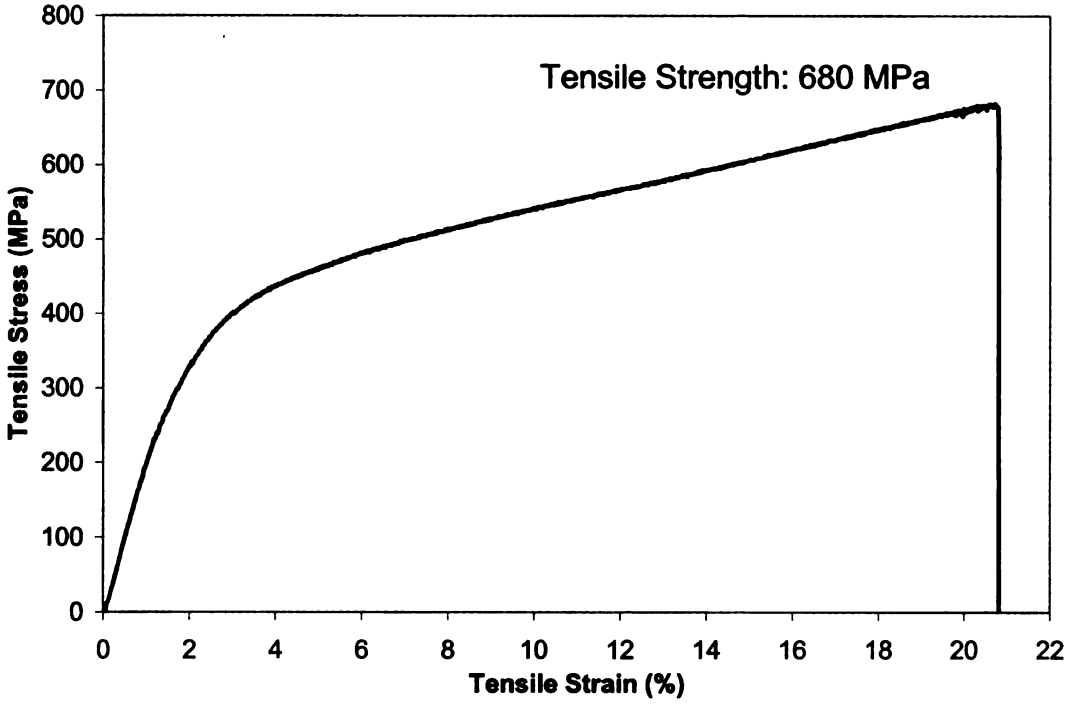

Figure 4.8 Stress vs. strain plot of as-brazed room-temperature superelastic butt-joint specimen. (Initial joint clearance: Approximately 400 μm.)

However, it is also possible that the embrittling nature of Ti_2Ni-type precipitates that are randomly distributed in the joint may also form crack initiation sites that will result in premature joint failure during tensile loading. Figure 4.9 shows the micrograph of a pre-polished section of a lap-joint that had undergone shear-loading but not to the point of failure. The joint was deliberately fabricated under conditions that favor precipitation of Ti_2Ni-type grains. Distinct cracks were evident in the facetted precipitates even before joint failure occurred. Composition mapping at site 'B' and 'C' by XRF (see Table 4.1) confirmed that these facetted grains are of Ti_2Ni-type.

Fracture surface of Ti_2Ni-free butt-joint specimens typically revealed two distinct fracture surface morphologies, which are shown in Figure 4.10a and b. In Figure 4.10a, the fracture mode is primarily ductile cleavage, whereas in Figure 4.10b, highly-dimpled surface and micro-void coalescence indicates a fracture mode with extensive ductile tearing. The former was determined by XRF to be attributed to failure predominantly within the pro-eutectic NiTi phase, while the latter was identified with the eutectic micro-constituents.

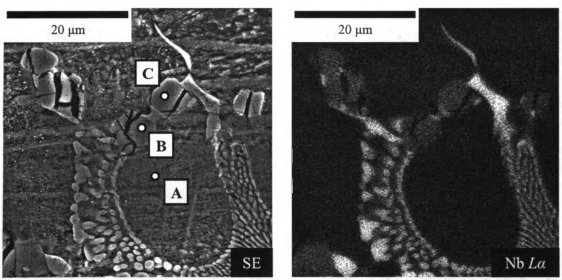

Figure 4.9 Photograph of a room-temperature shape-memory single-lap joint that had experienced onset of failure under shear loading. SEM micrograph of cracks traversing facetted Ti-rich precipitates in the joint region. Elemental XRF maps of the same area are also included.

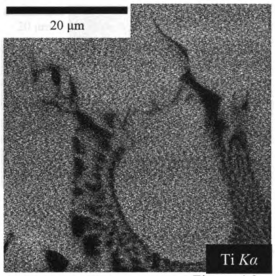

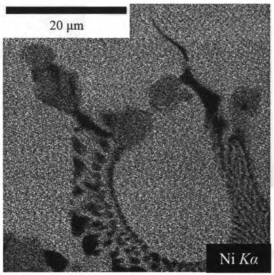

Figure 4.9 (Continued).

Table 4.1 X-ray fluorescence analysis on selected spots in Figure 4.9.

Spot	Nb (at%)	Ni (at%)	Ti (at%)
A	3	51	46
B	13	36	51
C	12	36	52

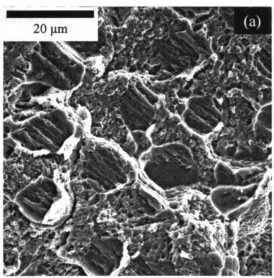

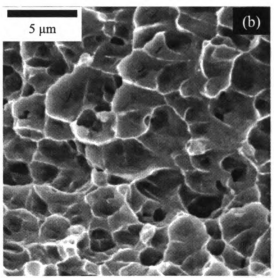

Figure 4.10 Fracture surfaces of the (a) pro-eutectic NiTi; and (b) eutectic micro-constituents in a typical superelastic butt-joint specimen that failed under tension. Elemental XRF maps of (a) are also shown.

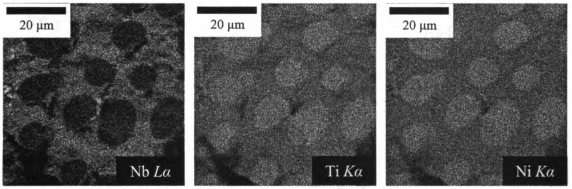

Figure 4.10 (Continued).

Butt-joint specimens were also tested after thermal annealing. The aging regimes employed are as follow: (1) 350°C for 1.5 hours; (2) 500°C for 20 minutes; and (3) 750°C for 10 minutes, water-quenched, followed by 350°C for 1.5 hours. All specimens are annealed in air and water-quenched. Figure 4.11 shows the representative tensile behaviors of as-brazed and the aged butt-joints. As mentioned previously, the typical plateau stress, found in room-temperature superelastic NiTi, were not observed in as-brazed butt-joint specimens. In contrast, stress-plateau was observed in each of the annealed butt-joints, with lower aging temperature yielding a better-defined plateau. All aged specimens appear to fracture at a strain of about 13%. The highest plateau and failure stresses of about 380 and 770 MPa, respectively, were attained by specimens aged at 350°C. Higher annealing temperatures of 500°C and 750°C resulted in degradation of both the plateau stress and ultimate strength.

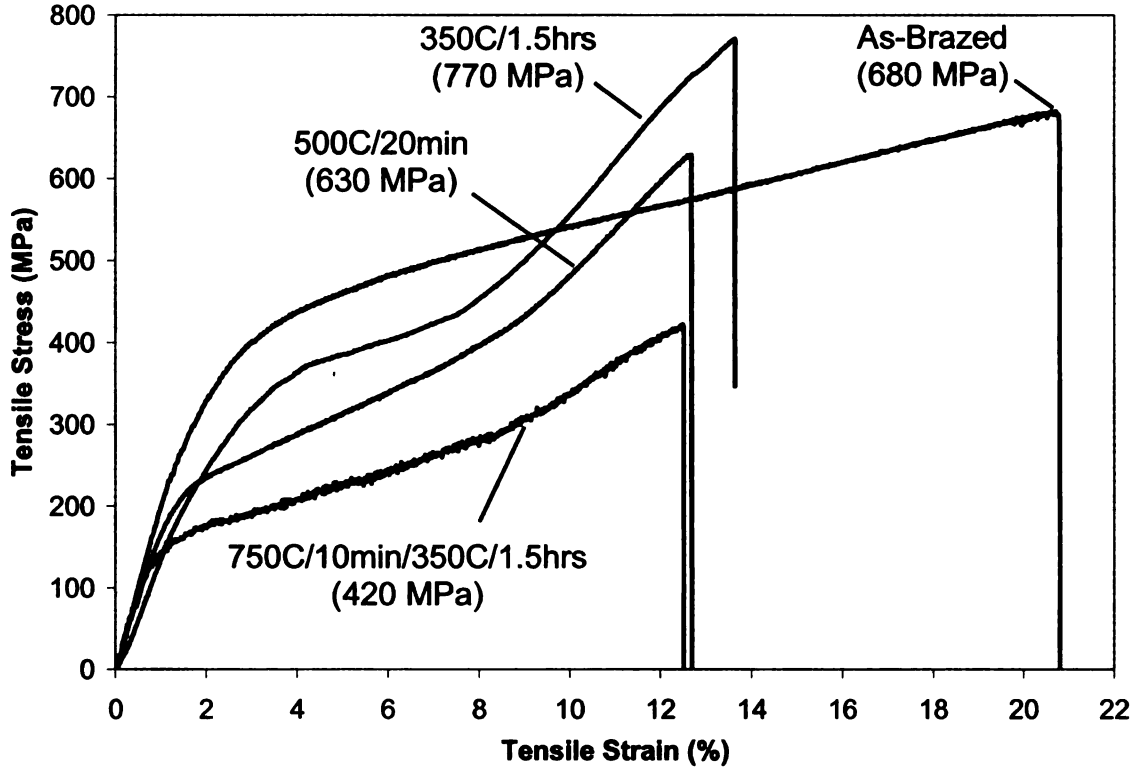

Figure 4.11 Stress vs. strain plots of as-brazed and aged superelastic butt-joint specimens. (Aging regime: 350°C for 1.5 hours; 500°C for 20 minutes; 750°C for 10 minutes, followed by 350°C for 1.5 hours. All anneals performed in air and water-quenched. Initial joint clearance: Approximately 400 μm.)

The degradation of mechanical properties in the 750°C solution treatment-then-350°C aging specimen was unexpected because aging after a solution treatment should yield mechanical results comparable to a specimen annealed solely at 350°C. There are two possible explanations: (1) the duration for solution treatment may not be sufficiently long to solutionize the Ni_4Ti_3 phase. Hence, subsequent aging actually resulted in growth of pre-existing Ni_4Ti_3 phase; (2) significant oxidation might have occurred in the joint, causing embrittlement.

Since superior plateau and failure stresses seem to be associated with lower aging temperatures, butt-joint specimens were aged at 300°C for 8 hours and then tested in tension. On the contrary, the initial cycle stress-strain characteristics of the 300°C-aged joint, given in Figure 4.12, reveal upper- and lower-plateau stresses of less than 300 MPa and 50 MPa, respectively. After the first loading/unloading cycle, the specimen incurred about 1.5% unrecoverable strain. Subsequent 8 cycles yielded a consistent strain recovery of about 6.5%. The upper-plateau stress decreased gradually as cycle increases, while lower-plateau stress remained rather constant throughout the 8 cycles. On the 10th cycle, the specimen was tensile-loaded to failure at a stress of 660 MPa at a strain of 10.6%.

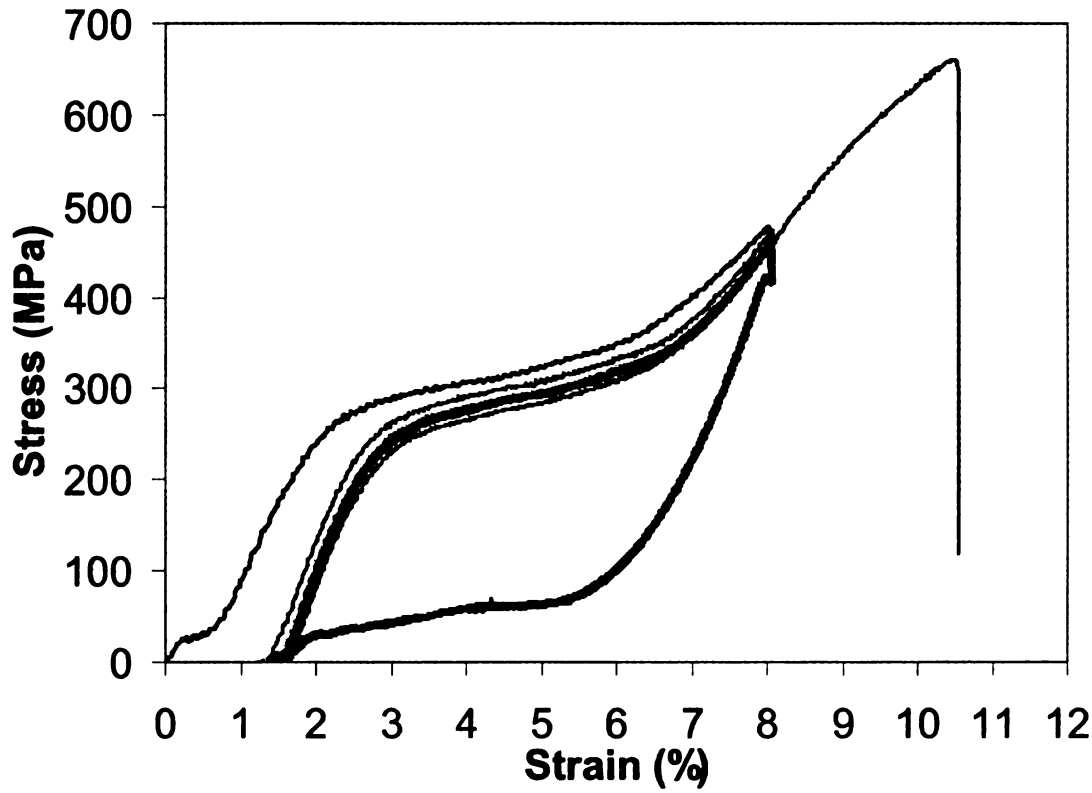

Figure 4.12 Stress vs. strain plots of an aged superelastic butt-joint undergoing 10 tensile loading/unloading cycles. (Aging regime: 300°C in air for 8 hours followed by a water-quench. Initial joint clearance: Approximately 400 μm.)

The mechanical properties of room-temperature superelastic butt-joints with narrower initial joint clearance of approximately 300 μm were also investigated. The stress-strain plots of as-brazed and 350°C-aged butt-joints are shown in Figure 4.13. For comparison, results from the wider (~ 400 μm) joint clearance specimens are also plotted in Figure 4.13. The narrow as-brazed joint fails slightly above 500 MPa, while the aged narrow joint fractures at about 680 MPa. On the other hand, the wider counterparts have higher fracture strengths. The plateau stress of the narrow butt-joint was observed to be lower (less than 300 MPa) than the wider joint (about 380 MPa). No significant difference in fracture strain was observed.

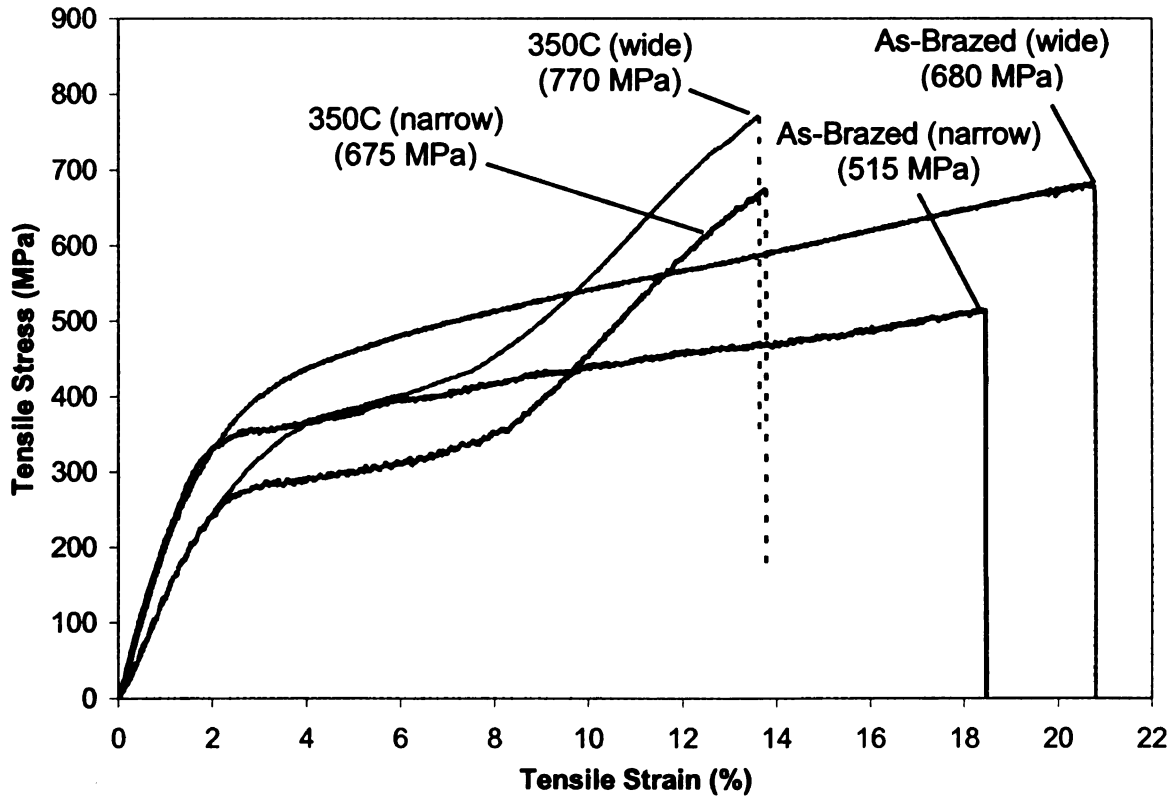

Figure 4.13 Stress vs. strain plots of as-brazed and aged superelastic butt-joints with initial joint clearances of approximately 300 μm (narrow) and 400 μm (wide). (Aging regime: 350°C for 1.5 hours in air, followed by a water-quench.)

4.5 Tensile Tests on Tungsten Inert Gas-Welded Butt-Joints

As discussed previously, the braze process involved heating entire test specimens to braze temperature in order to initiate contact melting between NiTi and Nb at the joint area, which inevitably degrades the base-NiTi's mechnical properties. Hence, an attempt was made to explore joining techniques that only involve localized heating at the joint region. The Tungsten-Inert-Gas (TIG) welding method was employed and adapted for this purpose, where 0.51 mm-diameter Nb wires were manually-fed into the joint by the welder during welding for eutectic liquid formation. The disadvantage of this approach is that there is no direct control over welding temperature, while welding speed is solely dependent on experience and dexterity of the welder. Furthermore, the argon gas shield of the TIG welding process was not sufficient to suppress oxidation of NiTi, especially in the joint regions.

The general microstructure and a higher-magnification of an as-welded room-temperature superelastic butt-joint are shown in Figure 4.14a and b, respectively. Typical pro-eutectic NiTi dendrites and eutectic phase were observed in the welded joint. However, a second dendritic phase also coexisted randomly with the two common microstructures. The fact that this phase was dendritic indicated that it formed before general eutectic freezing occurred. Stereology performed on these micrographs provided an estimated 5% volume fraction of this anomalous phase in the joint.

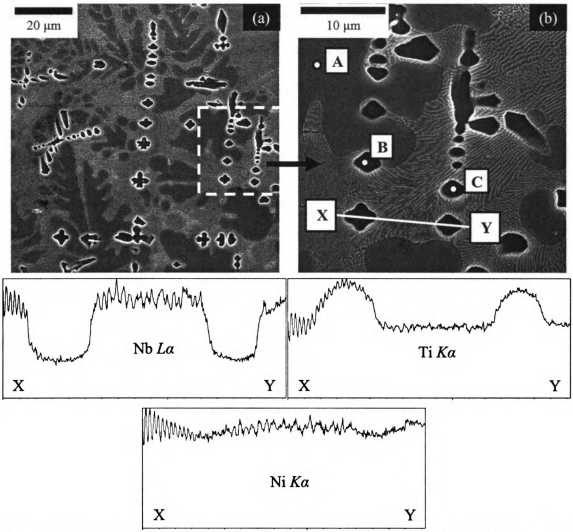

Figure 4.14 SEM micrographs of (a) general as-welded joint microstructure, and (b) high-magnification of the indicated area of (a). (XRF line profiles showing composition variations across X-Y are also provided.)

Table 4.2 X-ray fluorescence analysis on selected spots in Figure 4.14.

Spot	Nb (at%)	Ni (at%)	Ti (at%)
A	4	52	44
B	7	39	54
C	5	38	57

Line profiles from XRF analysis, indicated by 'X-Y' in Figure 4.23b, revealed higher Ti content, but lower Nb concentration in this unknown phase as compared with the eutectic micro-constituents, while XRF spot analysis (Table 4.2) shows that this phase

also has higher Ti concentration but comparable Nb content with the pro-eutectic NiTi phase. However, these dendritic precipitates do not share similar chemical compositions with those Ti-rich phases discussed in Chapter 3. It is, hence, suspected that the argon gas shielding from the TIG welding process was unable to prevent extensive oxidation from occurring in the joint. The significantly high oxygen contamination might have resulted in formation of a complex quaternary oxide that differs from the $(Ti,Nb)_2Ni$ or $(Ti,Nb)_4Ni_2O$ stoichiometry.

Room-temperature superelastic butt-joints were prepared using the TIG welding technique. Initial joint clearance was approximately 400 μm, which is similar to most of the brazed butt-joints. Niobium filler wires of 0.51 mm-diameter were used instead of Nb foils. Some welded joints were subjected to thermal aging at 350°C for 1.5 hours and 500°C for 20 minutes in air, followed by water-quench before tensile testing. Figure 4.15 shows that the as-welded butt-joint had failure strength of only 590 MPa and had limited ductility (< 9% strain at failure). This may be attributed to presence of residual stresses in the welded joint due to large thermal gradients associated with localized heating and the presence of oxides in the joint. Aging welded joints at 350°C resulted in distinct improvement in tensile strength (~ 750 MPa) but not in ductility. In addition, a plateau stress of about 350 MPa could be achieved. However, joint strength and ductility deteriorated to only 310 MPa and 6%, respectively, when welded joints were annealed at 500°C. Its plateau stress (less than 250 MPa) was also lower than the 350°C-aged joint. The degradation of joint mechanical properties at aging temperatures above 350°C in Figure 4.15 is consistent with those observed for brazed joints in Figure 4.11.

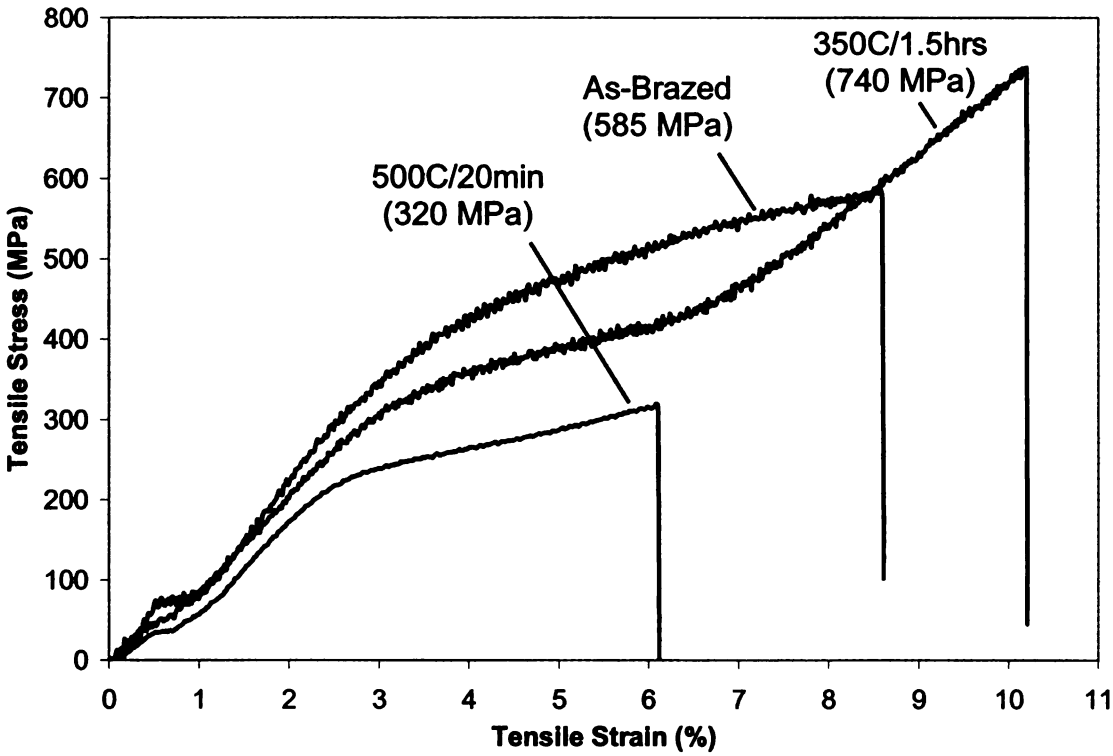

Figure 4.15 Stress vs. strain plots of as-welded and aged superelastic butt-joints. (Aging regimes: 350°C for 1.5 hours; 500°C for 20 minutes. All anneals performed in air and cooling by water-quench. Initial joint clearance: Approximately 400 μm.)

Fractography of the welded joint, given in Figure 4.16, reveals micro-void coalescence in most areas, which suggests that the failure mode is predominantly ductile tearing. However, 'caterpillar track' features (indicated by 'A' in Figure 4.16) can also be seen on the fracture surface and some of them have brittle-mode cracks in close proximity (indicated by 'B' in Figure 4.16). Based on the morphology, this failure mode is probably associated with the Ti-rich complex oxides that were previously observed (Figure 4.14). Therefore, it is highly probable that this dendritic phase initiates failure by either inter- or trans-granular fracture. The former gives rise to the 'caterpillar track' features, while the latter manifests as cracks. In either case, it can be deduced that this anomalous phase possesses brittle characteristics.

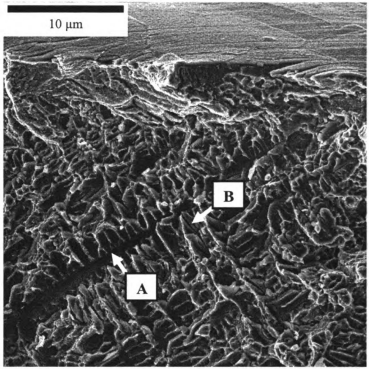

Figure 4.16 SEM micrographs of the fracture surface of a welded room-temperature superelastic butt-joint that failed under tension. ('A' indicates 'caterpillar track' features; 'B' indicates brittle-mode cracks associated with the presence of 'A'.)

4.6 Eutectic Braze Joints of Dissimilar Materials

In this section, a preliminary attempt is made to extend the reactive eutectic braze process to join NiTi to dissimilar materials. In particular, the mechanical properties of NiTi-Ta and NiTi-Al_2O_3 hetero-joints will be briefly discussed. There are two reasons for the choice of materials for investigation. Firstly, Ta and Al_2O_3 are both bio-compatible and commonly used as part of medical implants that also contain NiTi alloys. For example, high-atomic number elements, such as Ta, coated onto NiTi stents, can improve radiopacity [Schetky et al. 2004], while Al_2O_3 coating on NiTi bone implants can inhibit release of Ni into human bodies [Ozeki et al. 2003]. Secondly, they represent two classes of materials of vastly different mechanical properties, so it will be interesting

to evaluate the mechanical responses when these two types of materials are joined to NiTi alloys. Furthermore, Al_2O_3 is an insulator that could be integrated with NiTi electrically-excited actuators.

4.6.1 NiTi-Tantalum Joints

Tantalum coupons with nominal thickness of 1.588 mm was brazed to room-temperature superelastic NiTi of similar thickness using 127 μm-thick Nb foil as the braze filler metal. The two base-metals were placed 'edge-on' against each other with the braze foil between them. Braze temperature and duration were 1185°C and 5 minutes, respectively. Butt-joints of NiTi-Ta were prepared and then tested under tensile loading to evaluate the joint mechanical properties. Figure 4.17 shows the stress-strain behavior of an as-brazed NiTi-Ta butt-joint. The ultimate tensile strength of the joint is approximately 210 MPa, which coincides with the reported tensile strength of high-purity Ta (~ 210 MPa) [Sisco et al. 1963]. Necking was observed in the Ta section of the specimen around 20% strain (see inset of Figure 4.17). The strain at failure was close to 30%. Results and observations in Figure 4.17 clearly imply that the eutectic joint is mechanically superior to the base-Ta metal.

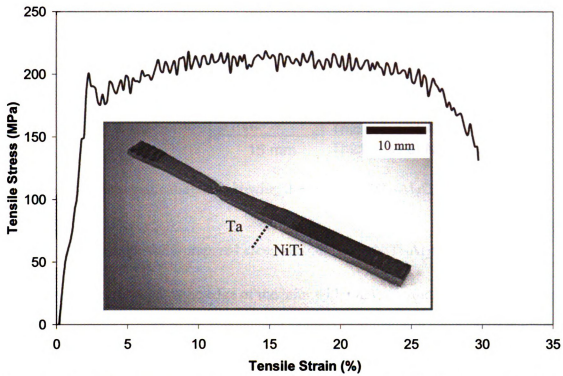

Figure 4.17 Stress vs. strain plot of as-brazed superelastic NiTi-Ta butt-joint. (Inset shows necking occurred in the Ta section of the specimen.)

4.6.2 NiTi-Alumina Joints

For this study, 99%-density Al_2O_3 plates and room-temperature superelastic NiTi strips were employed. The former has dimensions of 15 x 10 x 3.175 mm, while the latter has dimensions of 30 x 4.7 x 0.2 mm. Instead of the conventional butt-joint or single-lap joint configurations, the NiTi-Al_2O_3 joint was fabricated according to Figure 4.18. The overlap distance was 5 mm and the gage length on each NiTi strip was 15 mm. Niobium foil with a thickness of 51 μm was used for brazing, while braze temperature and duration were set at 1185°C and 3 minutes, respectively. The specimen was cooled naturally in the vacuum furnace before removing them from the chamber (see Figure 2.1 for the temperature-time profile of the braze process).

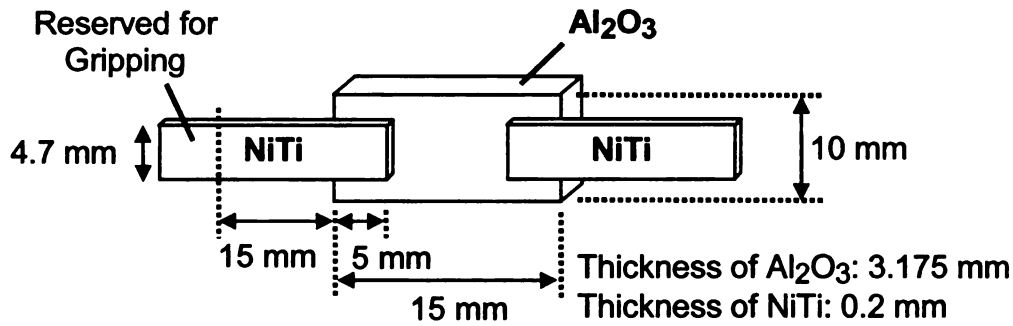

Figure 4.18 Schematic diagram showing the setup of NiTi-Al_2O_3 lap shear specimen.

A metallographically-prepared cross-section of the NiTi-Al_2O_3 joint (Figure 4.19) reveals meniscus forming at the edge of the joint with minimal voids forming in the braze area. Figure 4.19b is a duplicate of Figure 4.19a that had undergone contrast enhancement to reveal the eutectic micro-constituents. These observations indicate good wetting and flow of the eutectic liquid on Al_2O_3. The joint consists mainly of eutectic mixture and pro-eutectic NiTi dendrites, where the latter can be seen to solidify against the base-NiTi. The Al_2O_3-liquid interface does not appear to recede like the NiTi counterpart and only the eutectic micro-constituents was observed to solidify against the base-Al_2O_3, which indicates that Al_2O_3 does not participate strongly in braze liquid formation. Some discrete facetted precipitates, believed to be either $(Ti,Nb)_2Ni$ or $(Ti,Nb)_4Ni_2O$, were also present in the joint. Cracks in the base-Al_2O_3 can be seen extending from the meniscus (indicated in Figure 4.19), which might have formed as a result of thermal shock due to low toughness ($2 - 3$ MPa.m$^{1/2}$), low thermal conductivity

(8 – 10 W/m.K) and a moderately high coefficient of thermal expansion (~ 8 x 10^{-6} K^{-1}) [Munro, 1997] of Al_2O_3.

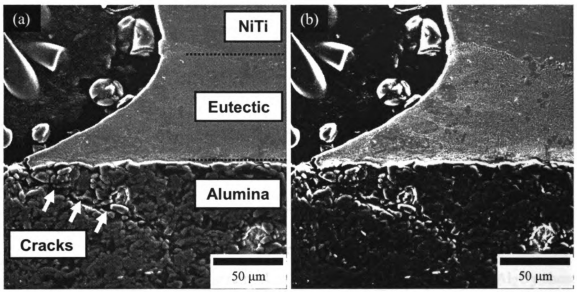

Figure 4.19 SEM micrograph showing (a) the typical cross-section of a NiTi-Al_2O_3 braze joint. (b) is the contrast-enhanced duplicate of (a).

The stress-strain plots of the NiTi-Al_2O_3 shear specimen are shown in Figure 4.20. It should be highlighted that tensile stress and strain in Figure 4.20 were calculated based on the assumption that elongation was entirely concentrated in the NiTi sections. This is reasonable given that the thickness of Al_2O_3 is significantly larger than the NiTi strips. The specimen failed at a tensile stress of slightly less than 160 MPa, while fracture strain was less than 1%. Fracture was observed to occur in the base-Al_2O_3 but close to the joint. The poor mechanical properties and fracture site suggest probable weakening near the joint interface due to thermal shock during cooling, which is consistent with the observations of cracks in Figure 4.19.

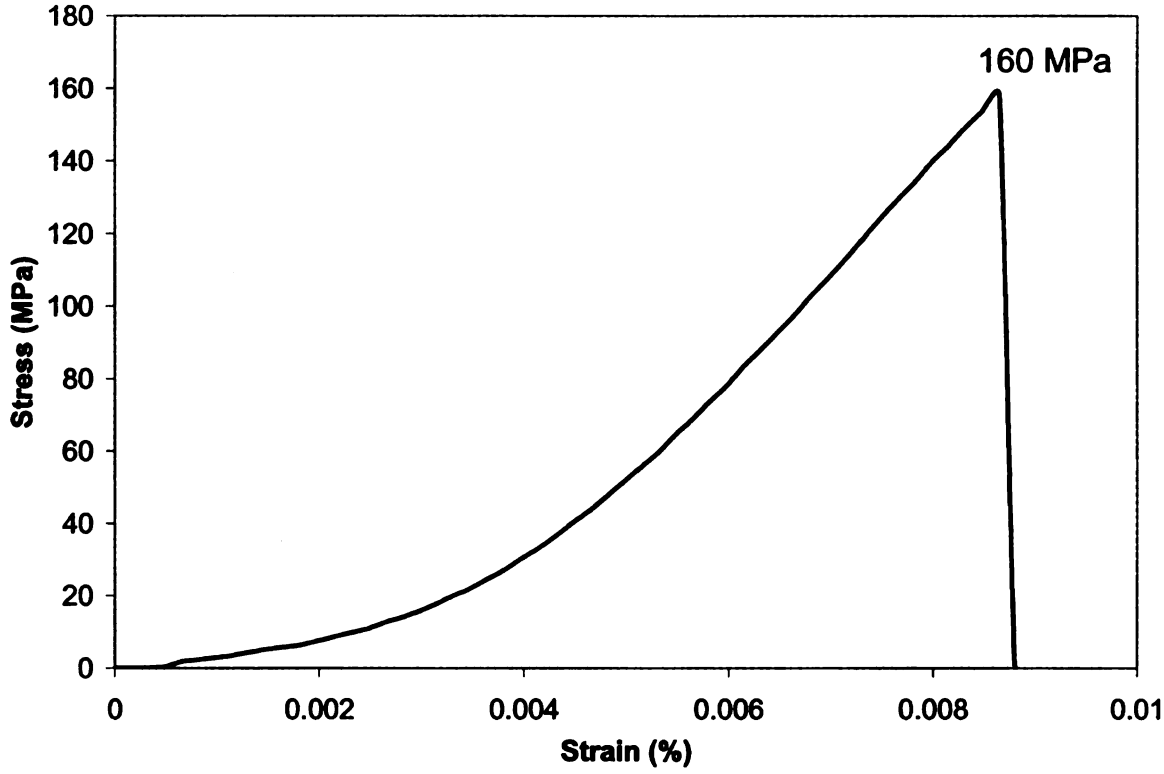

Figure 4.20 Tensile stress vs. strain plots of as-brazed superelastic NiTi-Al_2O_3 shear specimen.

Nanoindentation was performed at the NiTi-Al_2O_3 joint area (see Figure 4.21). The indentation holding depth for this study was set at 500 nm with a strain rate of 0.02 per second. Results in Figure 4.21 shows that the base-NiTi alloy and the eutectic micro-constituents possess indentation hardnesses of 4.5 GPa and 3.0 GPa, respectively, which are consistent with results in section 4.2. Hardness of the base-Al_2O_3 away from the joint area was measured to be 27.8 GPa, which also agrees well with literature-reported values [Krell et al. 2001]. However, Al_2O_3 in close proximity to the joint appears significantly weaker with a hardness of only 18.7 GPa. Therefore, localized mechanical properties obtained from this nanoindentation study further support the claim that poor

shear and tensile strengths of NiTi-Al_2O_3 joint is indeed attributed to weakening of the Al_2O_3 near the joint.

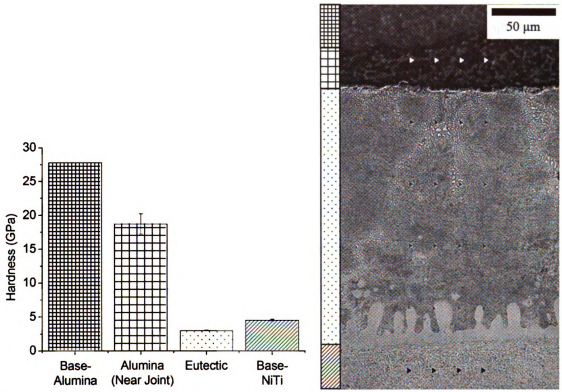

Figure 4.21 Bar-chart (left) illustrating the hardness of various phases in a NiTi-Al_2O_3 joint obtained from nanoindentations performed at the area shown in the optical micrograph (right). Array of indents across the joint can be seen (except the indents in the base-Al_2O_3).

4.7 Summary

The mechanical properties of eutectic joints were investigated at both micro- and macro-scales. Results show that the braze process will cause degradation in the base-NiTi's strength and ductility, but superelastic response can be restored in the base-NiTi through post-braze thermal aging. It was found that the optimum aging temperature is around 350°C, where highest tensile strength and plateau stresses were observed.

However, the eutectic joints are still mechanically-inferior to the base-NiTi alloy, which can be attributed to the strength-limiting eutectic-Nb phase or the presence of embrittling Ti_2Ni-type precipitates serving as crack initiation sites for premature joint failure.

The TIG welding approach was successfully adapted to form eutectic liquid in joint area. Despite the presence of a possible complex quaternary oxide phase, mechanical strengths of welded joints are equivalent to the brazed counterparts, except for a reduction in ductility.

The reactive eutectic braze process has also been successfully extended to joining NiTi to Ta. Joint strength was observed to be well in excess of the ultimate tensile strength of pure Ta. For joining NiTi to Al_2O_3, it was found that the eutectic liquid does wet and flow on Al_2O_3. Weakening of the Al_2O_3 near the joint interface was observed, which consequently results in poor shear and tensile strengths.

CHAPTER 5: MICRO-ALLOYING OF NIOBIUM-EUTECTIC BRAZE FOILS AND AN ALTERNATIVE EUTECTIC BRAZE SYSTEM

5.1 Introduction

The study on mechanical properties of braze joints in Chapter 4 shows that the joints possess strengths that are comparable but still inferior to that of the base-NiTi alloy. Two phases in the joints were believed to limit mechanical strength. They are (1) the Ti_2Ni-type precipitates within the eutectic phase that can act as crack initiation sites; and (2) the eutectic-Nb phase, which is mechanically-weaker than the eutectic-NiTi phase. Therefore, work reported in this chapter was undertaken to explore micro-alloying strategies in an effort to improve mechanical properties. Towards the end of this chapter, the NiTi-V eutectic system, which is qualitatively similar to the NiTi-Nb system, will also be explored for its potential as an alternative braze material.

5.2 Micro-Alloying of the Niobium-Eutectic Micro-constituents with Zirconium and Tungsten

Since eutectic-Nb is believed to be the strength-limiting phase in the eutectic micro-constituents, it is logical to devise a strengthening approach to improve its mechanical properties. In particular, solution-strengthening was selected for this study, where Zr and tungsten were separately micro-alloyed into eutectic braze joints. For micro-alloying with Zr, Nb-1Zr (at.%) foils (from ATI-Wah Chang) were employed as the braze filler metal, while tungsten micro-alloying was carried out via thin-film

sputtering of tungsten on pure Nb braze foils in order to obtain an approximate Nb-2W (at.%) composition. Details on the sputtering procedures are highlighted in Chapter 2.

Zirconium and tungsten were selected as alloying candidates for the following reasons: (1) they are both soluble in Nb; (2) the atomic radius of Zr and tungsten are about 10% larger and smaller, respectively, than that of Nb, which lead to a solution-strengthening effect; (3) they have been reported to produce solution-strengthening in Nb alloys [Wilcox et al. 1967, Jax 1971, Davidson et al. 1992]; and (4) they are both bio-compatible metals, which make the strengthening approach compatible with bio-medical applications. In addition, Zr has been reported to have the ability to suppress brittle $(Ti,Nb)_2Ni$ phase formation in Ni-Ti-Nb alloys [Jia et al. 2000].

5.2.1 Effects on Microstructures

Reactive eutectic brazing of near-equiatomic NiTi (nominal thickness of 3.175mm) were performed using the Zr- and W-alloyed Nb foils (nominal thickness of 51μm), separately, using braze temperature and duration of 1185°C and 120 seconds, respectively. Scanning electron microscopy revealed only pro-eutectic NiTi and eutectic phases present in the Zr-alloyed joints (see Figure 5.1). Similar to the pure Nb-based eutectic system, the Zr-alloyed eutectic possesses primarily lamallar and rod-like morphologies. The average eutectic spacing was approximately 0.6 μm, which is also similar to those observed in the pure Nb counterpart. No Ti_2Ni-type precipitates were observed in any of the Zr-alloyed eutectic joints studied, strongly suggesting that the presence of Zr can suppress Ti_2Ni-type phase formation.

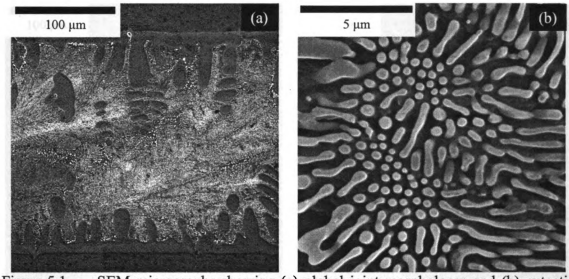

Figure 5.1 SEM micrographs showing (a) global joint morphology; and (b) eutectic microstructure of a Zr-alloyed eutectic joint.

In order to confirm this observation, Zr-alloyed braze specimens, with deliberately pre-oxidized NiTi surfaces, were prepared with prolonged braze duration of 1200 seconds under 'poor' vacuum conditions (similar to those described in Chapter 3). The aim was to create a favorable condition for the precipitation of Ti_2Ni-type grains. Microstructures of the Zr-alloyed joint were then compared against the pure Nb braze foil counterpart of similar process conditions. As discussed in Chapter 3, the pre-oxidized NiTi surface had resulted in significant amounts of Ti_2Ni-type precipitates and voids in the pure Nb braze joint (Figure 5.2a). In contrast, no Ti_2Ni-type compounds were observed in the Zr-alloyed joint and voids were rarely encountered (Figure 5.2b). Therefore, it is safe to deduce that addition of Zr in the eutectic phase does indeed suppress Ti_2Ni-type phase and void formation.

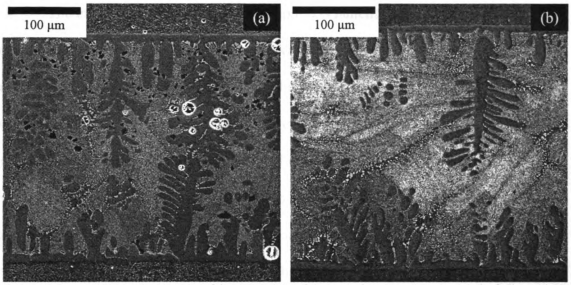

Figure 5.2 Microstructures of braze joints fabricated using (a) pure Nb foil; and (b) Nb-1Zr foil. (Mating surfaces were deliberately pre-oxidized before brazing under 'poor' vacuum conditions.)

The general joint morphology and eutectic micro-constituents of W-alloyed joints are shown in Figure 5.3a and b, respectively. Again, the joint consists mainly of pro-eutectic NiTi and eutectic phases. In this case, the joints were prepared with chemically-cleaned NiTi under high vacuum conditions, so proliferation of Ti_2Ni-type precipitates and voids should not be expected under such brazing conditions. However, Figure 5.3a shows that despite careful specimen preparation and good vacuum conditions, facetted Ti_2Ni-type phase and voids were observed in the W-alloyed joint. Such phase formation might be attributed to a reduction in oxygen solubility in the eutectic micro-constituents when tungsten was present. Precipitation of Ti_2Ni-type phase would occur in an effort to incorporate excess oxygen.

The eutectic micro-constituents also possess lamellar and rod-like morphologies (Figure 5.3b), but average eutectic spacing was determined to be about 1.3 μm. This average spacing is distinctively wider than those of Zr-alloyed and pure Nb-eutectic (inset of Figure 5.3b), which are approximately 0.6 μm. Eutectic spacing is known to be governed by growth velocities and degree of undercooling in the liquid ahead of solidification fronts [Flemings 1974]. Given that the rate of cooling was consistent across all types of braze joint (cooled in the same vacuum braze chamber), it is proposed that the larger eutectic spacing observed in the W-alloyed braze joint may be due to a decrease in undercooling that is somehow associated with the addition of tungsten.

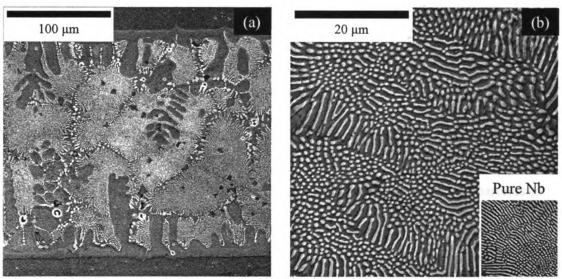

Figure 5.3 SEM micrographs showing (a) global joint morphology; and (b) eutectic micro-constituents of a W-alloyed eutectic joint. (Inset of (b) shows the eutectic micro-constituents of a pure Nb-eutectic joint under similar magnification as (b).)

5.2.2 Effects on Mechanical Properties

Nanoindentation experiments were carried out on Zr- and W-alloyed eutectic joints prepared in section 5.2.1 in the as-brazed condition. At least 40 indents were performed on each specimen in order to obtain meaningful statistics. The

representative load vs. displacement plots for pure Nb-eutectic, Zr-alloyed eutectic and W-alloyed eutectic are shown in Figure 5.4.

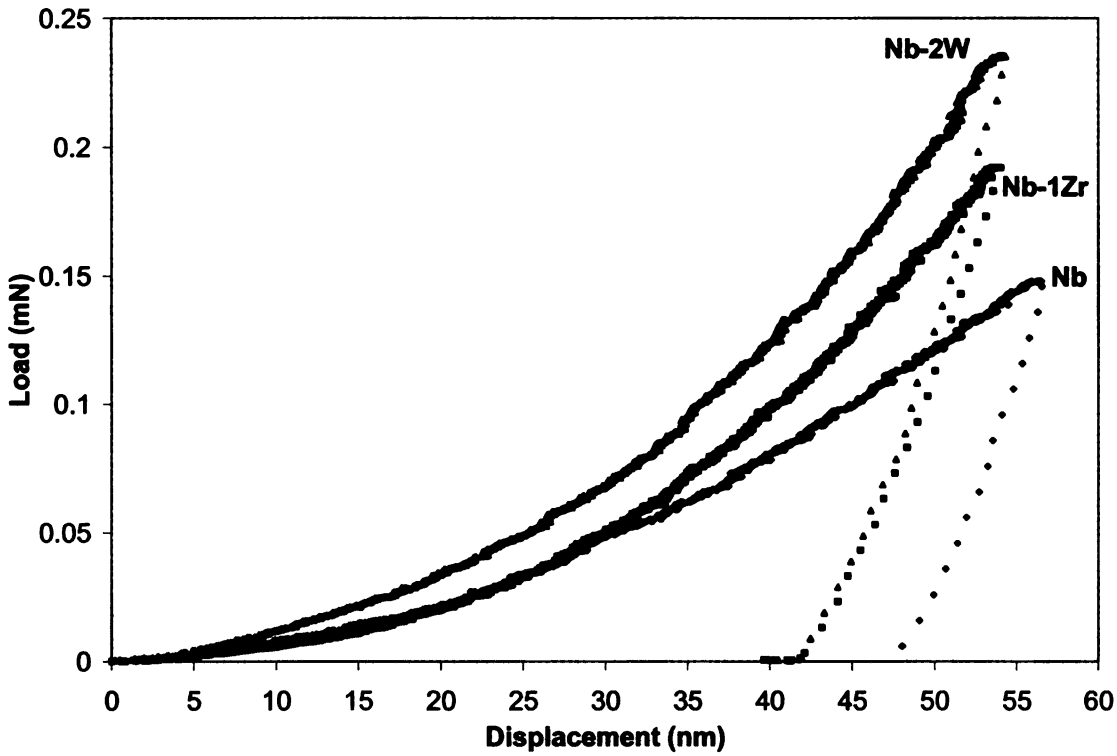

Figure 5.4 Load vs. displacement plots of pure Nb-eutectic, Zr-alloyed eutectic and W-alloyed eutectic. (Indentation holding depth: 50 nm. Strain rate: 0.001 per second.)

Figure 5.5a and b illustrate the histograms of calculated indentation hardnesses and elastic moduli of Zr- and W-alloyed eutectic joints, respectively. For comparison, results from pure Nb-eutectic joints are also plotted with existing data. The histograms in Figure 5.5a show that alloying eutectic joints with Zr yielded an increase in average hardness from 2.0 GPa to 2.6 GPa, while W-alloyed eutectic joints possess hardness of 2.9 GPa, which is almost 50% increase over the pure Nb counterpart. Only subtle increases in elastic moduli, from 87 GPa to about 99 GPa, were observed in both types of alloyed joints.

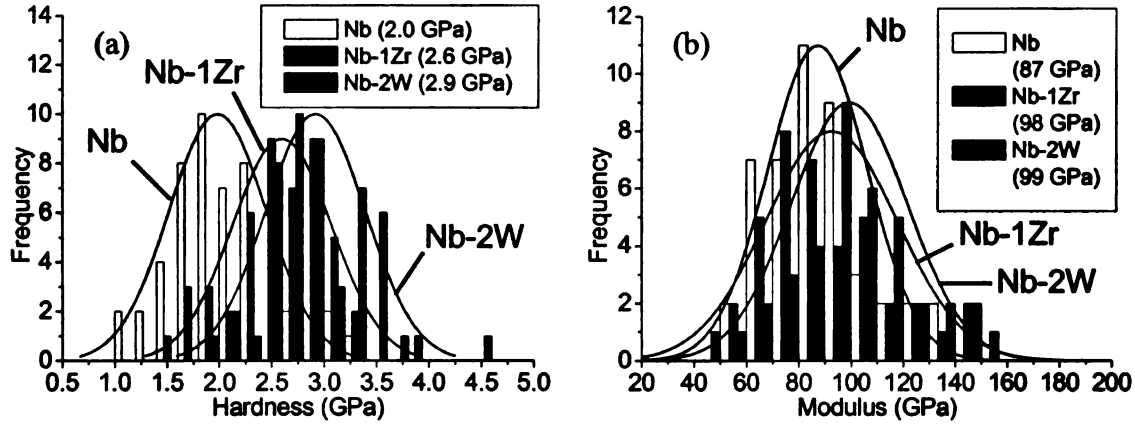

Figure 5.5 Histograms of (a) hardness; and (b) elastic modulus of pure Nb, Zr- and W-alloyed eutectic braze joints. Continuous lines are Gaussian distribution curves fitted over the histograms of the three eutectic braze joints. (All tests performed on as-brazed joints. Data derived from indentation holding depth of 50nm.)

Alloyed joint specimens were then subjected to Vickers micro-hardness testing using indentation load of 300 grams to assess the effect of micro-alloying on overall eutectic properties. Approximately 10 indents were made on each type of joints. In order to minimize sampling errors, indents were performed on areas solely of eutectic phase. Optical and electron micrographs showing typical Vickers indents on ideal test areas (i.e. fully eutectic) are provided in Figure 5.6a and b, respectively. However, given that these indents had depth of approximately 10 μm, there is still the possibility that the indenter might have probed pro-eutectic NiTi phase underneath the test area, causing erratic results. Indentations were also performed on the near-equiatomic base-NiTi alloy.

Vickers indentation results are summarized in Figure 5.7. At a load of 300 grams, the Vickers hardness number (VHN) of base-NiTi was determined to be 250. The pure Nb-eutectic has a VHN of about 205, while Zr- and W-alloyed eutectic possess VHNs of 215 and 226, respectively. The micro-hardness analysis is consistent with the nanoindentation results.

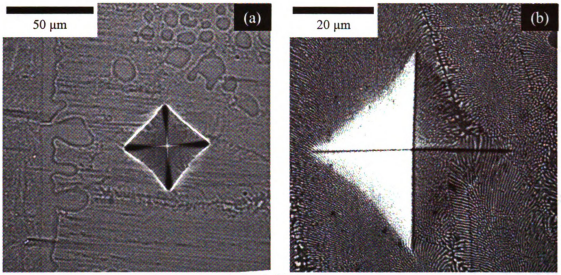

Figure 5.6 (a) Optical micrograph; and (b) SEM micrograph showing Vickers indents within the eutectic micro-constituents.

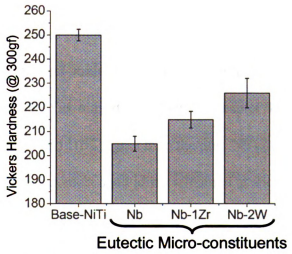

Figure 5.7 Bar chart showing the Vickers hardness of pure Nb, Zr- and W-alloyed eutectic braze joints. (All tests performed on as-brazed joints at 300 grams.)

Hence, it can be deduced that alloying Zr and tungsten will yield improvements in the mechanical properties of eutectic joints, and based on indentation studies, tungsten may be a more effective solution-strengthening candidate than Zr. However, the indentation experiments only probed mechanical characteristics of the eutectic micro-constituents, where effects of those Ti_2Ni-type precipitates on overall joint mechanical

properties did not come into play. Therefore, tensile tests on butt-joints, fabricated from the alloyed Nb braze foils, were also conducted in order to determine how improvements in the nano- and micro-mechanical properties of these eutectic joints were manifested in mechanical tests on bulk sections.

Zirconium-alloyed eutectic butt-joints were brazed at 1185°C for 6 minutes using room-temperature superelastic NiTi (nominal thickness of 1.588 mm). Initial joint clearance was approximately 400 μm. Their tensile properties were studied in as-brazed and thermally-aged conditions, where the latter range from 300°C to 500°C for 1 to 4 hours. All aging regimes were performed in air, followed by water-quench. Figure 5.8 shows that as-brazed Zr-alloyed joints exhibit tensile strength close to 840 MPa at a failure strain of 30%. The stress-strain plot did not exhibit any stress-plateau, which is consistent with observations of as-brazed butt-joints in Chapter 4. The fracture strength and strain is about 100 MPa and 10% higher than the pure Nb counterpart, respectively. However, the strain at failure in most aged joints remained at about 13%, which is similar to the pure Nb-eutectic joints.

Room-temperature superelastic behavior was observed in the base-NiTi of all thermally-aged Zr-alloyed joints. Consistent with results in Chapter 4, aging temperatures from 300°C to 350°C tend to produce higher and flatter upper-plateau stresses, while stress-plateau become lower and less pronounced at higher aging temperatures. However, fracture strengths of Zr-alloyed joints did not seem to be affected by any of the aging regimes and remained close to 800 MPa even when annealed

at 500°C. In contrast, pure Nb-eutectic joints experienced a marked decrease in tensile strength when they were subjected to annealing at 500°C prior to tensile testing.

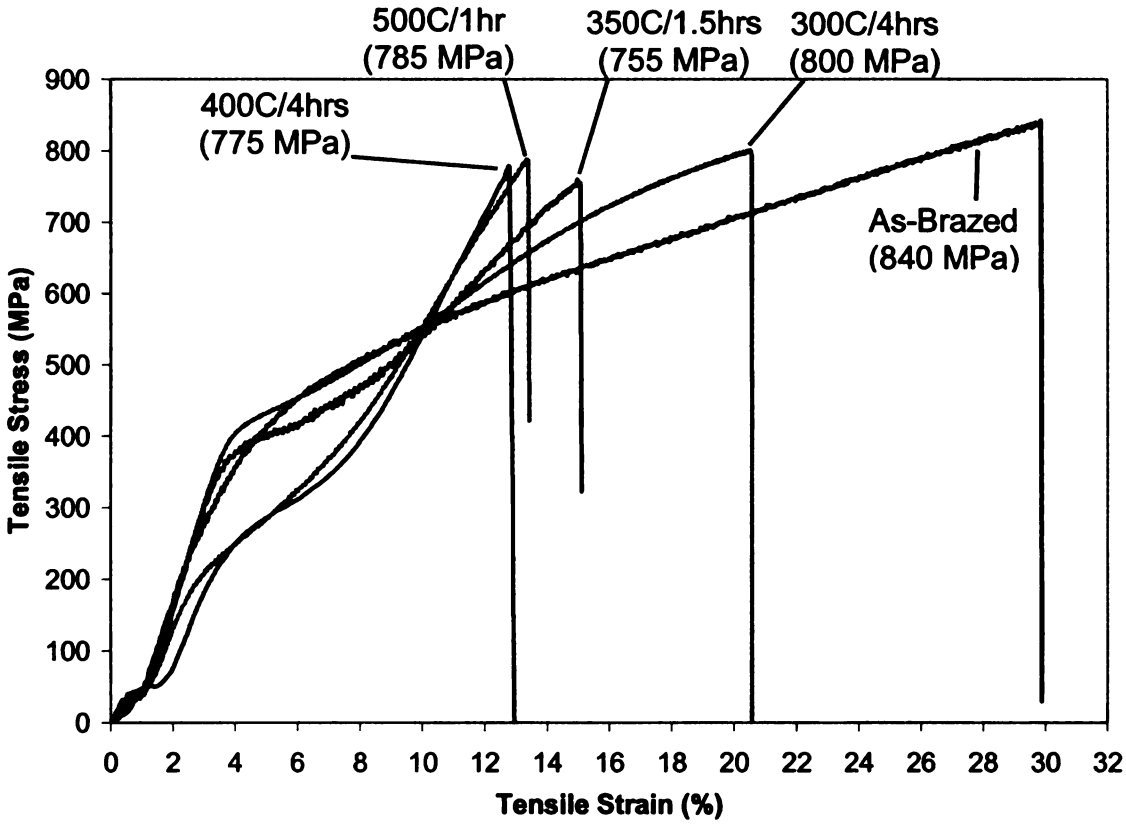

Figure 5.8 Stress vs. strain plots of Zr-alloyed as-brazed and aged superelastic butt-joint specimens. (Aging regime: 300°C for 4 hours; 350°C for 1.5 hours; 400°C for 4 hours; 500°C for 1 hour. All anneals performed in air and cooling by water-quench. Initial joint clearance: Approximately 400 μm.)

Fracture surface of Zr-alloyed eutectic joints that failed under tensile loading were examined. The rough global fracture morphology in Figure 5.9a indicates ductile-mode failure. Higher-magnification of the fracture surface (Figure 5.9b) reveals extensive dimpling from micro-void coalescence, which is consistent with the ductile-tearing behavior observed in the pure Nb-eutectic joints discussed in Chapter 4. No brittle-mode fracture was detected in any of the Zr-alloyed eutectic joints. This was expected since the joint microstructures did not reveal any presence of Ti_2Ni-type grains.

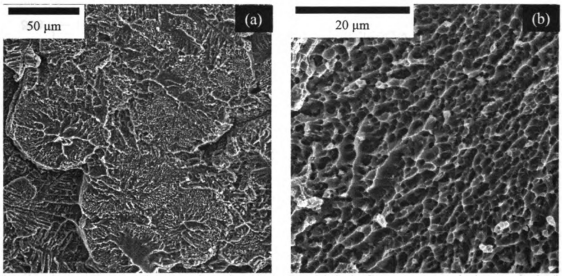

Figure 5.9 SEM micrographs showing (a) global fracture morphology; and (b) highly-dimpled fracture surface of a Zr-alloyed eutectic butt-joint that failed under tensile loading.

Tungsten-alloyed eutectic butt-joints, prepared under similar braze conditions as those described for the Zr counterpart, were also tested under tensile loading. Results are shown in Figure 5.10. The stress-strain plot of as-brazed butt-joint revealed the tensile strength to be 680 MPa and a failure strain of about 15%. The aged specimen failed at tensile stress and strain close to 800 MPa and 13%, respectively. Hence, W-alloyed joints share rather similar mechanical characteristics with pure Nb-eutectic butt-joints with no distinct improvement in fracture strength. This is surprising since nanoindentations and micro-Vickers hardness test results unanimously suggested pronounced improvement in hardness of eutectic micro-constituents from micro-alloying with tungsten.

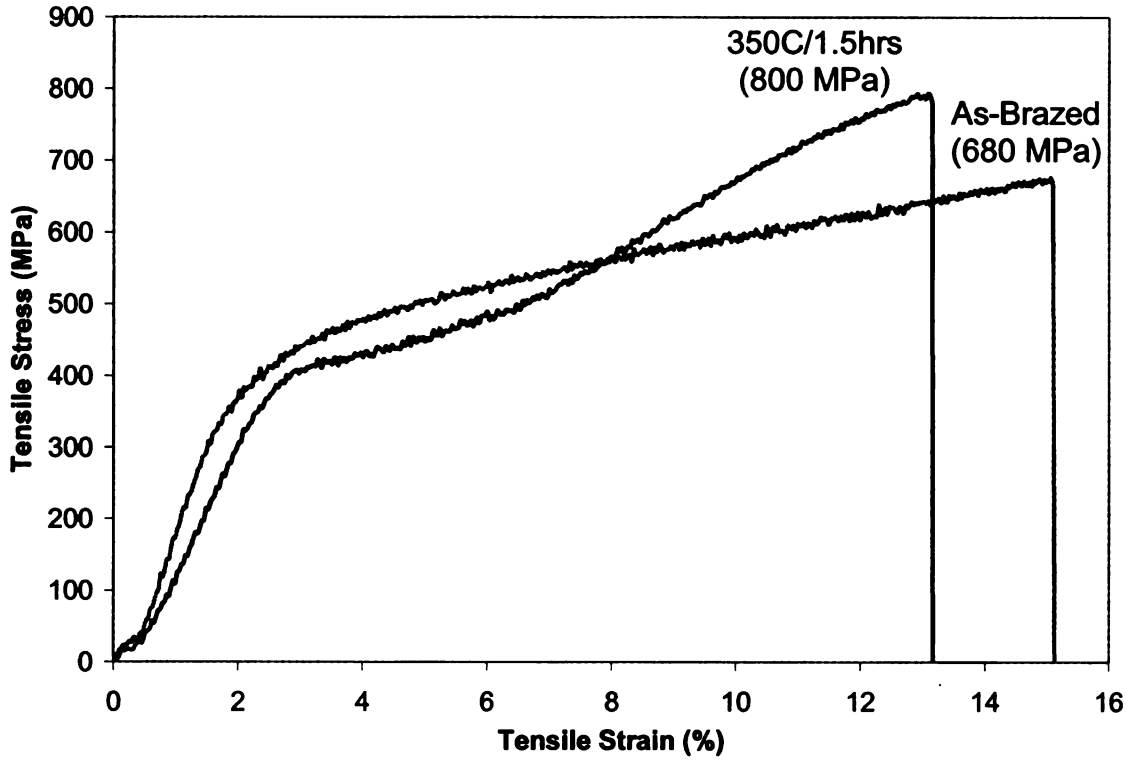

Figure 5.10 Stress vs. strain plots of W-alloyed as-brazed and aged superelastic butt-joint specimens. (Aging regime: 350°C for 1.5 hours. Anneal performed in air and cooling by water-quench. Initial joint clearance: Approximately 400 μm.)

Fractography of the failed W-alloyed eutectic butt-joints revealed a highly-undulating surface (Figure 5.11a), which is a common observation among all eutectic joints. Detailed study of the fracture morphology shows discontinuous regions with flat and smooth topographies among the predominantly dimpled surface. Trans-granular cracks were also observed within these flat regions (indicated by 'A' in Figure 5.11b), which are believed to be associated with initiation of fracture across the Ti_2Ni-type precipitates. Therefore, it can be deduced that despite pronounced strengthening of the eutectic micro-constituents, presence of Ti_2Ni-type precipitates in W-alloyed joints could have acted as crack initiation sites, consequently causing premature joint failure to occur.

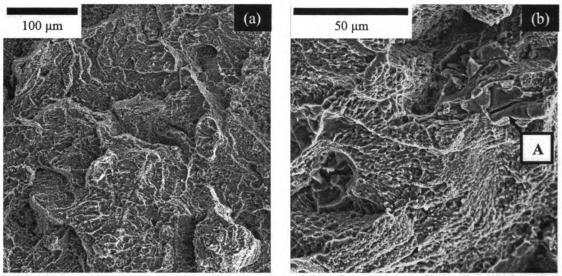

Figure 5.11 SEM micrographs showing (a) global fracture morphology; and (b) brittle cracks (indicated by 'A') among dimpled fracture surface of a W-alloyed eutectic butt-joint that failed under tensile loading.

5.3 Vanadium-Based Eutectic: An Alternative Braze System

It now seems apparent that solution-strengthening Nb-based eutectic braze joints via micro-alloying is a promising approach to improve their mechanical properties. Concurrently, there is also motivation to explore alternative braze filler metals that will react and produce braze liquid in an analogous fashion with respect to Nb, but yield superior joint strength and ductility. Since vanadium and Nb belong to the same group in the periodic table, and literature [Prima 1992] suggests that many phase features in the 900°C isothermal section of the Ni-Ti-V ternary system are in common with those of the Ni-Ti-Nb system, vanadium was selected as an alternative braze metal to be investigated. Furthermore, vanadium possesses a room-temperature tensile strength of 350 MPa [Maksimovich et al. 1982], which is higher than that of Nb (170 MPa) [Gupta and Suri 1994]. In the following sub-section, the microstructural and mechanical properties of braze joints, prepared using pure vanadium filler metal, will be discussed.

5.3.1 Joint Microstructural and Mechanical Properties

Braze joint specimens were prepared using room-temerature shape-memory NiTi (nominal thickness of 3.175mm) as the base-alloy. Brazing procedures were similar to those employed for Nb-eutectic joints, except that vanadium foils (nominal thickness of 51μm) were used instead. It was found that contact melting between NiTi and vanadium occurs between 1160°C to 1180°C. The typical joint microstructures fabricated from a braze temperature of 1185°C and duration of 120 seconds are shown in Figure 5.12. Complete exhaustion of the vanadium foil was observed, which resulted in a final joint width of about 240 μm. With a braze foil thickness of 51 μm, this implies that approximately 190 μm of NiTi was consumed for braze liquid formation.

The braze region consists mainly of dendritic phase and eutectic micro-constituents (Figure 5.12a). Elemental XRF mapping (Figure 5.13) and spot analysis (Table 5.1) indicated that the dendritic phase is pro-eutectic NiTi with approximately 1 at.% V. This possibly suggests that solubility of vanadium in NiTi is lower than that of Nb. Only trace amount of Ti_2Ni-type precipitates were observed in the V-eutectic joints, which were believed to be analogous with the Ti-rich phase observed in Nb-based eutectic joints. The NiTi-V eutectic micro-constituents was observed to possess a 'network'-type morphology (Figure 5.12b), with the brighter phase being eutectic-V and the gray phase being eutectic-NiTi. Average eutectic spacing within the grain boundaries was determined to be 0.4 μm. However, the eutectic phase tends to transit towards rod-like near some of the boundaries with average spacing increasing beyond 1 μm.

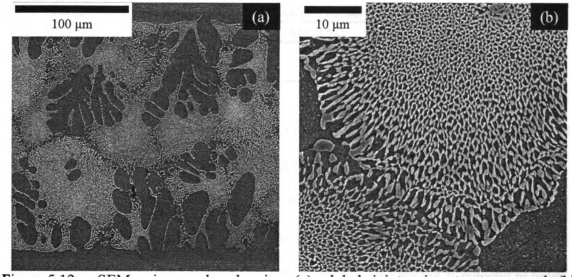

Figure 5.12 SEM micrographs showing (a) global joint microstructures; and (b) eutectic micro-constituents of a V-eutectic braze joint.

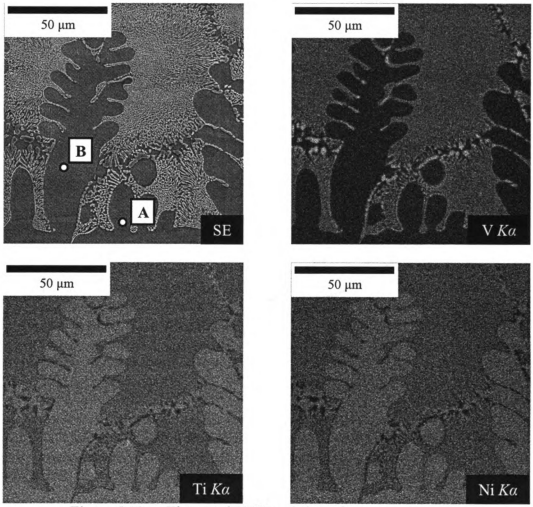

Figure 5.13 Elemental XRF mapping of a V-eutectic joint.

Table 5.1 X-ray fluorescence analysis on selected spots in Figure 5.13.

Spot	V (at%)	Ni (at%)	Ti (at%)
A	1	48	51
B	1	48	51

Nanoindentation was performed on as-brazed and thermally aged joint specimens, where the latter was annealed at 350°C in air for 1.5 hours, followed by water-quench. At least 20 indents were made on each specimen. The representative load vs. displacement plots associated with indentations on as-brazed V- and Nb-eutectic are given in Figure 5.14. It is clear that higher loads are required for the V-eutectic in order to achieve the same indentation holding depth as the Nb-eutectic.

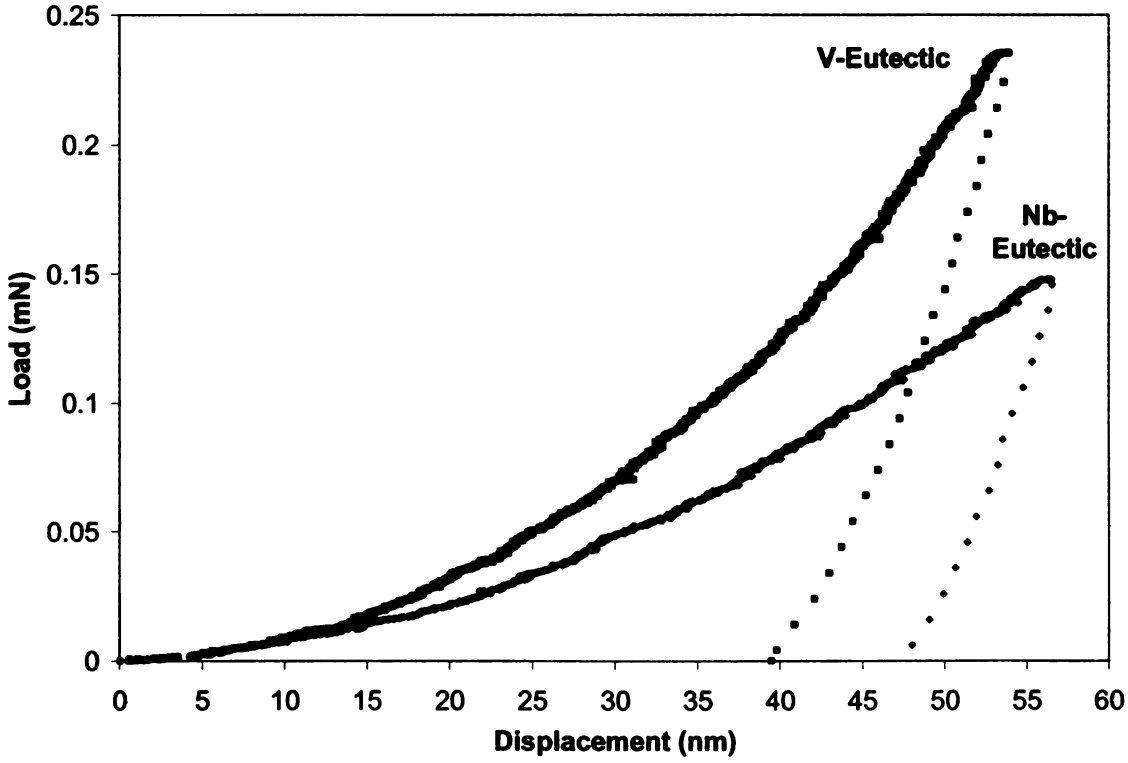

Figure 5.14 Load vs. displacement plots of pure Nb- and V-eutectic micro-constituents. (Indentation holding depth: 50 nm. Strain rate: 0.001 per second.)

Figure 5.15a and b illustrates the hardness and modulus of as-brazed joint in the form of histograms, respectively. Data from the pure Nb counterpart are also included for comparison. Calculations from the nanoindentation result showed that as-brazed V-eutectic micro-constituents possess an average hardness of 3.6 GPa, which is significantly higher than the mean hardness of Nb-eutectic micro-constituents. The elastic modulus of V-eutectic was determined to be 78 GPa, being slightly lower than the Nb counterpart. For the thermally-aged V-eutectic joint, no change in the hardness was observed (Figure 5.16a). In contrast, the Nb-eutectic joint experienced a significant improvement in hardness from the same aging regime. The calculated elastic modulus of both V- and Nb-eutectic joints appeared to decrease after annealing at 350°C.

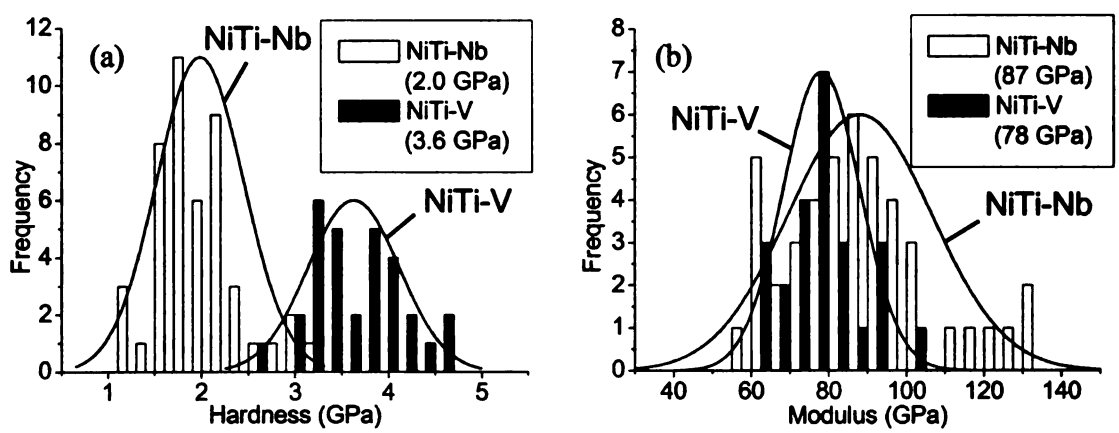

Figure 5.15 Histograms of (a) hardness; and (b) elastic modulus of as-brazed pure Nb- and V-eutectic braze joints. Continuous lines are Gaussian distribution curves fitted over the histograms of the two eutectic braze joints. (Data derived from indentation holding depth of 50nm.)

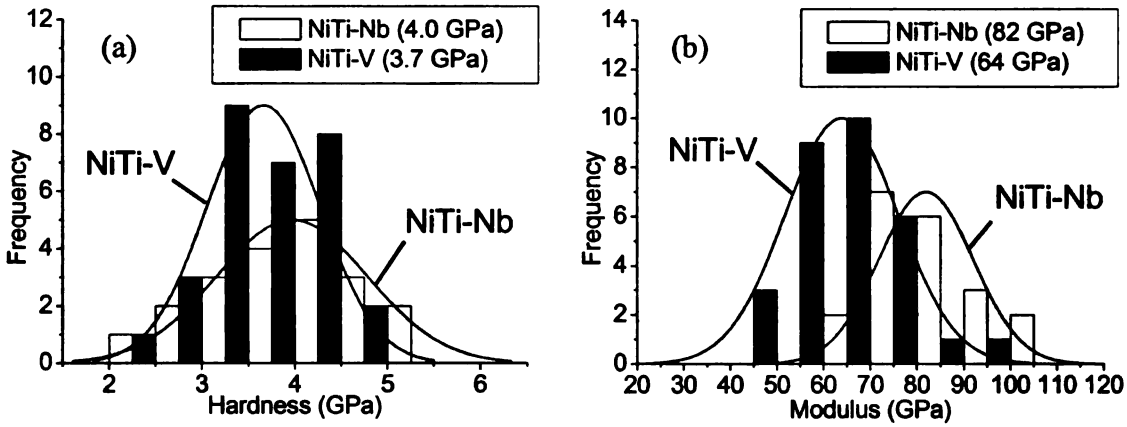

Figure 5.16 Histograms of (a) hardness; and (b) elastic modulus of thermally-aged pure Nb- and V-eutectic braze joints. Continuous lines are Gaussian distribution curves fitted over the histograms of the two eutectic braze joints. (Aging regime: 350°C in air for 1.5 hours, followed by water-quench. Data derived from indentation holding depth of 50nm.)

Next, butt-joint specimens were prepared for tensile testing. Room-temperature superelastic NiTi was employed as base-alloy. Joint clearance was kept at about 400 μm, which is consistent with most of the brazed butt-joints. Pure vanadium foils were used as the braze filler metal. Brazing was performed at 1185°C for 6 minutes. Eutectic joints were also subjected to aging at 350°C in air for 1.5 hours, followed by a water-quench. Figure 5.17 shows that the as-brazed V-eutectic joint failed at 780 MPa with fracture strain close to 20%, while aging the V-eutectic butt-joints at 350°C resulted in a tensile strength of 920 MPa and a fracture strain close to 18%.

Both as-brazed and aged joints exhibited failure strengths that are comparable to their respective control specimens (Figure 4.6 and 4.7, respectively). Hence, the tensile test results strongly suggest that the V-based eutectic system can serve as a braze alternative with the potential to have superior joint mechanical properties to the Nb counterpart. However, vanadium is a toxic element that is not biocompatible.

Fracture occurred in the joint region of the as-brazed V-eutectic joint and the facture surface was examined by SEM. Micrographs revealed undulating general fracture morphology (Figure 5.18a), which was a common observation among the Nb-based eutectic joints and indicates primarily ductile failure. No brittle cracks were detected in the as-brazed joint. However, higher-magnification of the fracture surface showed interesting 'web'-like features, which also suggests ductile cleavage (Figure 5.18b).

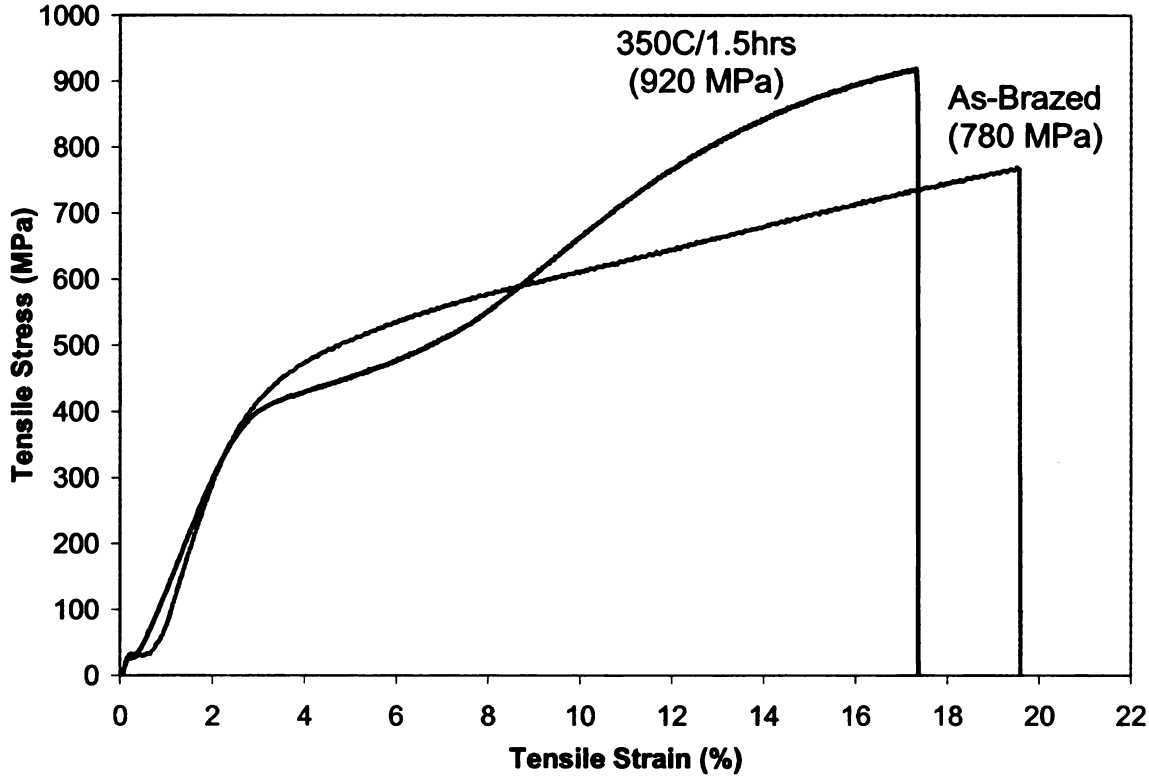

Figure 5.17 Stress vs. strain plots of as-brazed and aged room-temperature superelastic butt-joints fabricated using V-based eutectic. (Aging regime: 350°C for 1.5 hours. Anneal performed in air and cooling by water-quench. Initial joint clearance: Approximately 400 μm.)

Similar 'web'-like features were observed in both low- and high-magnification micrographs of the fracture surface originating from the 350°C-aged butt-joint (Figure 5.19a and b). This confirms that such features are not artifacts but truly pertain to failure

in the V-based eutectic system. Based on the dimensions and their resemblance with the morphology of the V-based eutectic, these features are likely associated with failure in the eutectic micro-constituents.

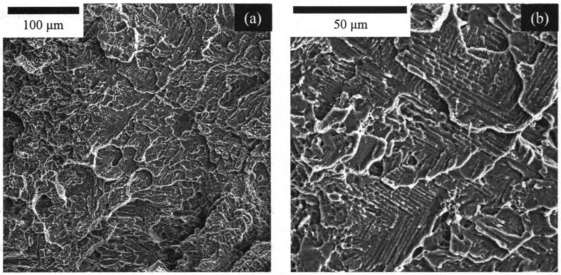

Figure 5.18 SEM micrographs showing (a) global fracture morphology; and (b) 'web'-like ductile tearing features associated with the eutectic micro-constituents of an as-brazed V-based eutectic butt-joint that failed under tensile loading.

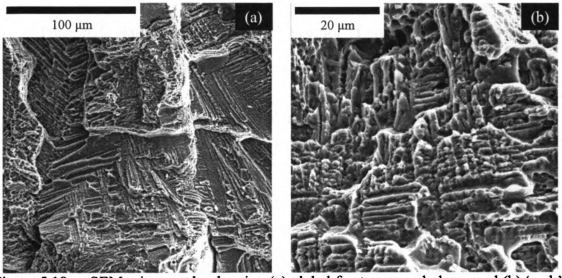

Figure 5.19 SEM micrographs showing (a) global fracture morphology; and (b) 'web'-like ductile tearing features associated with the eutectic micro-constituents of a 350°C-aged V-based eutectic butt-joint that failed under tensile loading.

5.3.2 *Ternary Phase Equilibria in the Ni-Ti-V System*

The Ni-Ti-V ternary system has received little attention and there is limited literature on phase equilibria in this system. Prima and coworkers [Prima 1992] made a preliminary attempt to study partial regions of the 900°C- and 1000°C- isothermal sections. Besides the known binary phases, no ternary intermediate compounds were reported. There is also no information on the liquidus projections or solidus boundaries in the phase diagram. Based on Prima's findings, the 920°C-isothermal section of the Ni-Ti-V system was constructed and is shown in Figure 5.20. Note that 920°C was selected for illustration because Ni_2V phase melts congruently at about 915°C and phase fields will appear unnecessarily complicated in the Ni-rich region if the 900°C-isothermal section was drawn instead. Furthermore, the Ni-rich region of the phase diagram serves no purpose in discussions pertaining to contact melting, which occurs close to the NiTi-V isopleth.

Phase field features in the NiTi-σ'-V-Ti section of Figure 5.20 appear to be analogous with the NiTi-Ni_7Nb_6-Nb-Ti region in Figure 3.31. Hence, it is reasonable to hypothesize the presence of a similar quasibinary eutectic point at compositions close to the NiTi-V isopleth. Indeed, experimental evidence had indicated that NiTi-V eutectic formation in braze joints, which confirms the validity of the hypothesis and suggests similarities in the driving force for contact melting and dissolution kinetics with the NiTi-Nb eutectic system.

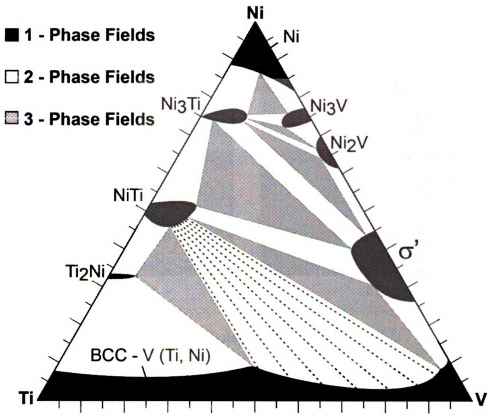

Figure 5.20 Estimated 920°C-isothermal section of the Ni-Ti-V ternary system [Prima 1992].

Stereology of the NiTi-V eutectic mixture revealed an estimated 57% volume fraction of eutectic-V (Figure 5.21), which, upon density considerations, places the quasibinary eutectic point approximately at 20Ni-20Ti-60V (at.%). However, the thicknesses of NiTi and vanadium consumed for braze liquid formation did not seem to agree with results obtained from stereology. Based on measurements of the receded thicknesses of base-NiTi alloy derived from Figure 5.12a and other similar micrographs, the quasibinary eutectic composition should approximately be 40Ni-40Ti-20V (at.%).

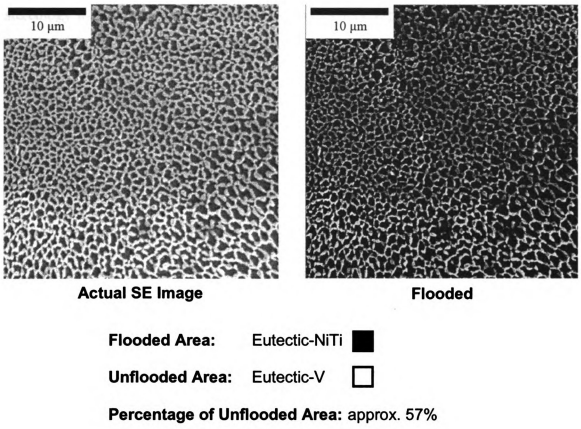

Figure 5.21 Stereology on NiTi-V eutectic micro-constituents (performed using WSXM software from Nanotec Electronica).

It is believed that measurement errors are larger in stereology than in the receding-thickness measurement method because the former approach relies on measuring the 2D projections of 3D features on a plane, which is known for its inaccuracy when complex and highly-anisotropic features are involved. An example is illustrated in Figure 5.22. Volume fraction estimations on the 3D network are highly-dependent on the exposed surface employed for stereology. Figure 5.22a shows that an under-estimation of volume fraction of the phase will occur if stereology was performed on a surface that exposes only the out-of-plane rods of the network. On the other hand, Figure 5.22b indicates that volume fraction of the phase will be over-estimated if

stereology was performed on a surface that exposes only in-plane rods. Given that the eutectic microstructural features in Figure 5.12 resemble more of those illustrated in Figure 5.22b, it is possibly a case of over-estimating the vanadium content of the eutectic micro-constituents.

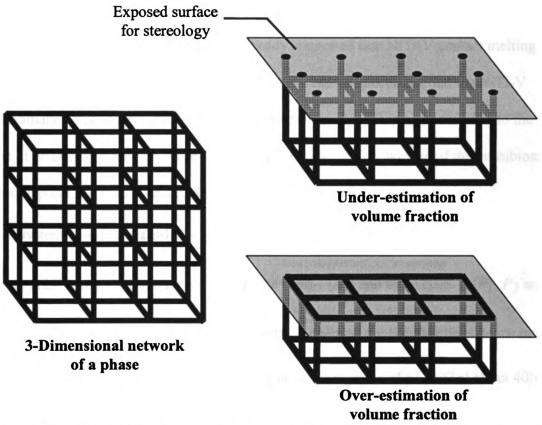

Figure 5.22 Schematic diagram showing a 3-dimensional network of a phase. (a) Under-estimation of volume fraction when stereology is performed on out-of-plane rods of the network. (b) Over-estimation of volume fraction when stereology is performed on in-plane rods of the network.

The receding-thickness measurements on joints that had experienced complete dissolution of vanadium will tend to under-estimate the vanadium content of the eutectic liquid. The reason is that part of the dissolved base-alloy was spent in enriching the liquid with Ni and Ti so as to drive the liquid composition against the NiTi liquidus

surface after the complete exhaustion of vanadium. However, melting kinetics simulations in Chapter 3 had shown that the thickness of base-NiTi alloy required for this purpose is only of the order of about 10 μm. Hence, the error incurred in receding-thickness measurement should not be significant, and the quasibinary eutectic composition predicted using this method will be employed for further discussion.

Experimental observations have already suggested that NiTi-V contact melting occurs between 1160°C and 1180°C. Therefore, it can be speculated that the NiTi-V quasibinary eutectic temperature lies approximately at 1170°C, which is similar to the case of NiTi-Nb. Based on Alkamade's principles and the knowledge of the quasibinary eutectic point, two possible liquidus projections are proposed. Figure 5.23a shows a Ni-Ti-V system with two class-I (E_1 and E_2) and two class-II (P_1 and P_2) reactions, while Figure 5.23b shows a ternary system with one class-I (E_1) and three class-II (P_1, P_2 and P_3) reactions. Despite the differences in reaction schemes, the liquidus lines demarcating NiTi and V(Ni,Ti) phases possess similar temperature maxima of 1170°C at about 40Ni-40Ti-20V (at.%) in both cases. In addition, both scenarios involve two four-phase class-II reaction planes on either sides of the NiTi-V isopleth (Figure 5.24) that are similar to those in the Ni-Ti-Nb system (Figure 3.32). The NiTi + V(Ni,Ti) + Liquid phase fields in both reaction planes will converge towards the NiTi-V isopleth and degenerate into a single NiTi + V(Ni,Ti) tie-line onto the plane of the said isopleth at approximately 1170°C, producing a perfect quasibinary eutectic isopleth (Figure 5.25).

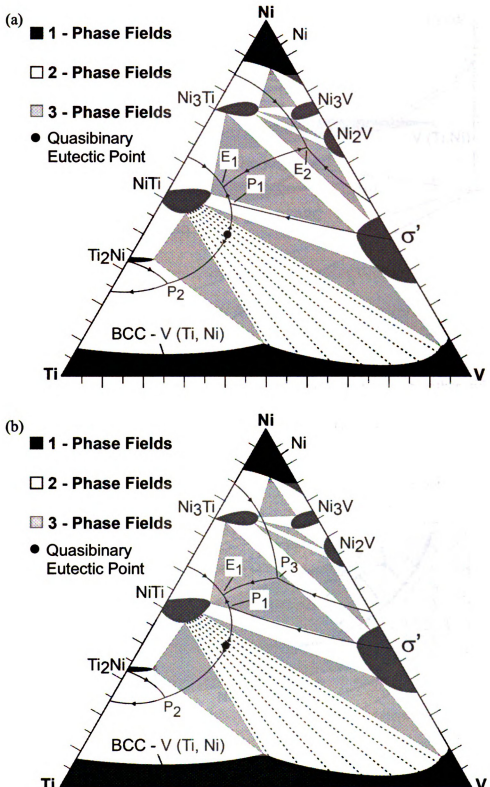

Figure 5.23 Two possible liquidus projections for the Ni-Ti-V system: (a) two class-I (E_1 and E_2), two class-II (P_1 and P_2) reactions; (b) one class-I (E_1), three class-II (P_1, P_2 and P_3) reactions. (Quasibinary eutectic points are also indicated.)

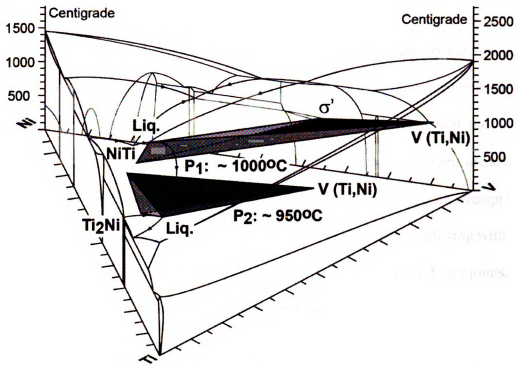

Figure 5.24 A four-phase class-II reaction plane (P_1 and P_2) on either sides of the NiTi-V isopleth in the ternary system. Both possess common NiTi + V(Ni,Ti) + Liquid phase fields. (The reaction plane temperatures are speculative.)

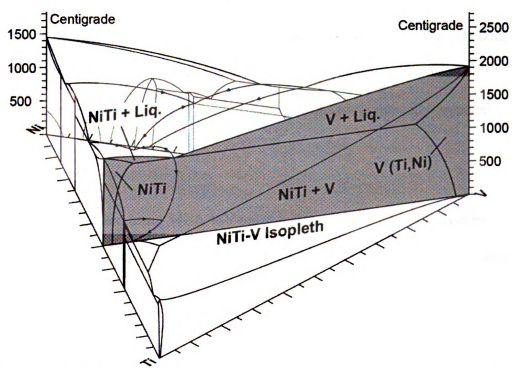

Figure 5.25 A perfect NiTi-V quasibinary eutectic isopleth in the ternary system.

5.4 Vanadium-Alloyed Niobium Braze System

It was demonstrated in section 5.3 that a pure V-based quasibinary eutectic, which yields promising joint mechanical characteristics, can be employed as an alternative braze system. Besides having analogous mechanisms for eutectic liquid formation, the coordinates of the quasibinary eutectic points in both ternary phase diagrams are also believed to be close. Given that vanadium and Nb are mutually soluble, an attempt was made to explore solution-strengthening of Nb-based eutectic joints by alloying with vanadium. The microstructural and mechanical properties of Nb-based braze joints, with different degrees of V-alloying, will be discussed in this section.

5.4.1 Joint Microstructural and Mechanical Properties

Room-temperature superelastic butt-joints, with initial joint clearance of about 400 μm, were fabricated using Nb and vanadium foils at the same time. Braze temperature and duration were 1185°C and 6 minutes, respectively. Prior to brazing, the filler metal foils were weighed and calculated to yield an approximate overall composition of 54Nb-46V (at.%). Braze joints were metallographically-prepared and studied by SEM.

Joints fabricated using 54Nb-46V braze foils possess predominantly eutectic micro-constituents (Figure 5.26a) and pro-eutectic NiTi phase. However, the eutectic did not possess attributes that are associated with either the NiTi-Nb or NiTi-V systems. Instead, it is a mixture of rod-like and labyrinth morphologies. The eutectic spacing was observed to be much wider than the two previously-discussed eutectic systems. The

darker phase in Figure 5.26 is believed to be pro-eutectic NiTi or eutectic-NiTi, while the lighter phase is unidentified. For ease of discussion, the latter will be termed 'χ' phase. Discontinuous colonies of NiTi-Nb eutectic micro-constituents (region 'B' in Figure 5.26b) also coexisted with the NiTi-χ eutectic micro-constituents (region 'A' in Figure 5.26b), but were not prolific. The microstructural transition from NiTi-Nb eutectic to χ phase in Figure 5.26b strongly implies that the latter might have formed subsequently from a peritectoid reaction between prior-solidified eutectic-NiTi and eutectic-Nb. That is, NiTi + Nb → χ phase during cooling.

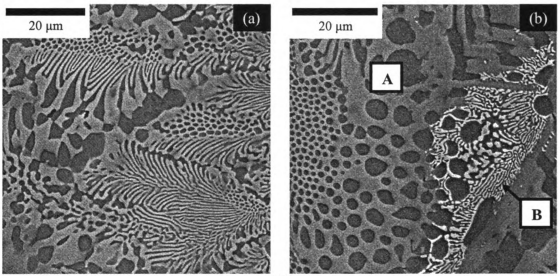

Figure 5.26 SEM micrographs showing (a) NiTi-χ eutectic micro-constituents; and (b) coexistence of NiTi-χ eutectic (indicated by 'A') and NiTi-Nb eutectic (indicated by 'B') micro-constituents in joints fabricated using 54Nb-46V braze foils.

The experiment was repeated using an overall braze foil composition of 77Nb-23V (at.%) and its joint microstructures are provided in Figure 5.27a and b. More colonies of NiTi-Nb eutectic micro-constituents were observed in the braze joint (Figure 5.27a), while majority of the χ phase (indicated by 'A' in Figure 5.27a) no longer form the eutectic micro-constituents previously observed in Figure 5.26a. Instead, the χ phase

manifested as elongated grains that are usually coupled with the pro-eutectic NiTi phase (Figure 5.27b).

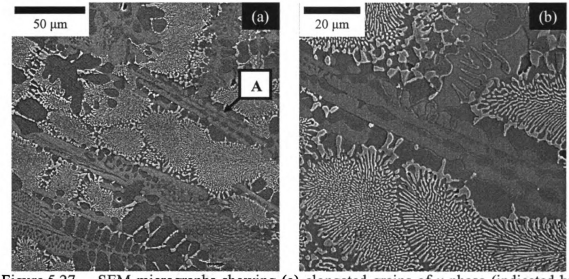

Figure 5.27 SEM micrographs showing (a) elongated grains of χ phase (indicated by 'A') among dense colonies of NiTi-Nb eutectic; and (b) higher-magnification of the elongated grains of χ phase in joints fabricated using 77Nb-23V braze foils.

Elemental mapping of the microstructures in Figure 5.27b are provided in Figure 5.28. Based on the fluorescence intensities, the χ phase possesses lower Ni and Ti concentrations than the pro-eutectic NiTi phase, but the former has higher Nb and vanadium concentration than the latter. When compared against the eutectic-Nb phase, the χ phase appears to have lower Nb concentration. The element maps for vanadium and Ti did not provide clear intensity distributions between χ phase and eutectic-Nb phase.

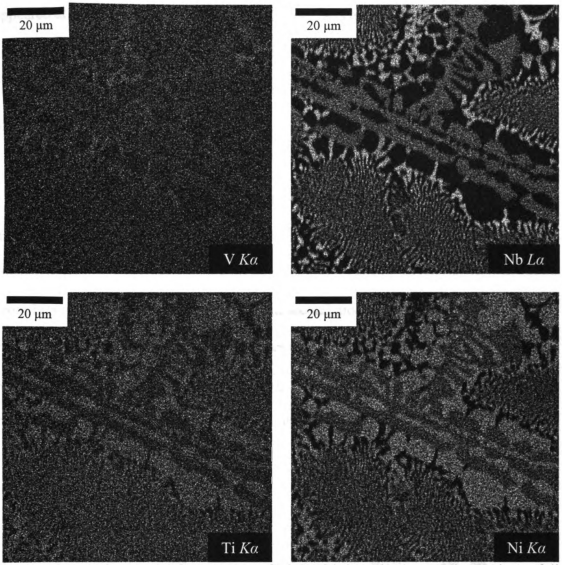

Figure 5.28 Elemental XRF mapping of a joint fabricated using 77Nb-23V braze foil.

Next, nanoindentations were performed on as-brazed 54Nb-46V joints. Indentation holding depth was kept at 100 nm with a strain rate of 0.001 per second. At least 50 indents were made on the specimen. For hardness and elastic modulus calculations, Poisson's ratio of 0.35 was assumed for all the phases. Results were illustrated in the form of histograms and shown in Figure 5.29a and b. A bi-modal distribution was observed in the calculated hardness of the 54Nb-46V joint (Figure 5.29a), suggesting that the nanoindenter was sampling two different phases. The first mode

appeared at about 4.5 GPa, while the second mode was estimated to be 9.5 GPa. Based on previous nanoindentation results, it is reasonable to assume that the first mode is associated with either pro-eutectic NiTi or eutectic-NiTi. Therefore, the second mode must be attributed to the χ phase.

In contrast, the histogram of calculated elastic modulus did not appear to be bi-modal, but rather manifested as one broad distribution (Figure 5.29b). This is likely attributed to closeness of elastic moduli of both phases causing an overlap of distributions. From Figure 5.29b, it seems that the first and second mode occurred around 90 GPa and 150 GPa, respectively. The first mode agrees reasonably well with the elastic moduli of NiTi-Nb eutectic mixture and base-NiTi alloy. Hence, it is provisionally concluded that the χ phase possesses an approximate modulus of 150 GPa.

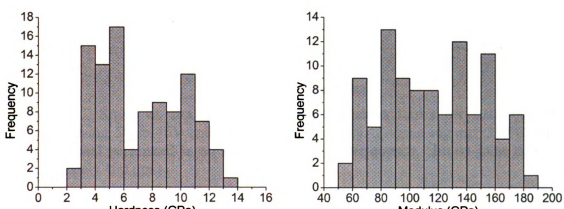

Figure 5.29 Histograms of (a) hardness; and (b) elastic modulus of as-brazed 54Nb-46V joints.

Tensile tests performed on aged butt-joints (350°C in air for 1.5 hours, followed by a water-quench) fabricated using 54Nb-46V and 77Nb-23V foils revealed poor fracture strength and ductility (Figure 5.30). The former failed at 200 MPa with a strain

of less than 3%, while the latter fractured at 390 MPa with a strain slightly beyond 3%. The decrease in tensile strength and ductility as volume fraction of χ phase increases strongly suggests that χ phase is hard and brittle. This deduction is consistent with the nanoindentation results.

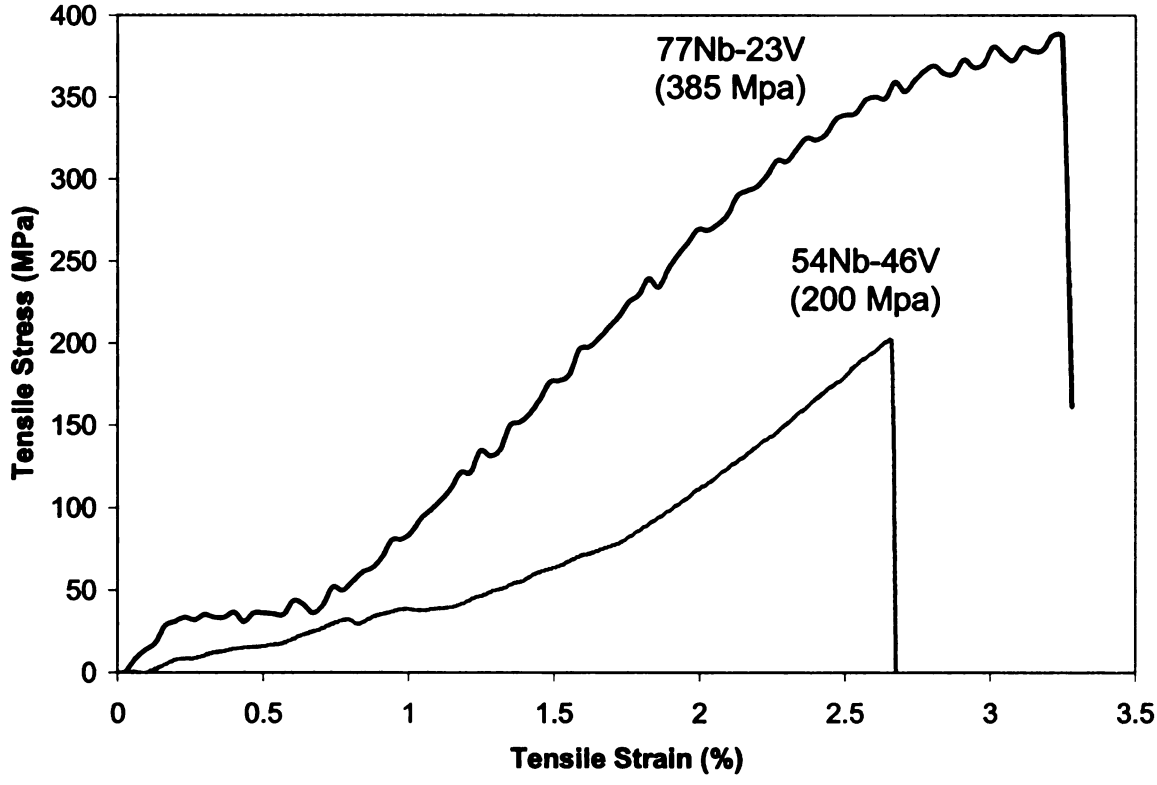

Figure 5.30 Stress vs. strain plots of aged room-temperature superelastic butt-joints fabricated using 54Nb-46V and 77Nb-23V braze foils. (Aging regime: 350°C for 1.5 hours. Anneal performed in air and cooling by water-quench. Initial joint clearance: Approximately 400 μm.)

Fractography performed on the aged 54Nb-46V butt-joint revealed more brittle-like general fracture morphology as compared to the typical eutectic joints. Flat and smooth topographies can be observed frequently in Figure 5.31a. A higher-magnification micrograph of the fracture surface shows discrete and sparse regions of ductile tearing embedded in a matrix of cleavage fracture (Figure 5.31b). Brittle cracks were also

observed close to the ductile-brittle interfaces. Given the similarity in the features between Figure 5.31b and 5.26a, it can be deduced that the ductile-mode fractures in Figure 5.31b were attributed to failure in the pro-eutectic NiTi or eutectic-NiTi phase, while the brittle cleavages were associated with the χ phase.

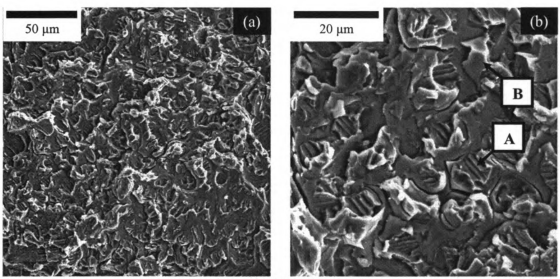

Figure 5.31 SEM micrographs showing (a) global fracture morphology; and (b) mixed ductile/brittle fracture features in a 350°C-aged room-temperature superelastic butt-joint, fabricated using 54Nb-46V foils, which failed under tensile loading. (Ductile features are indicated by 'A', while brittle features are indicated by 'B'.)

The ultimate tensile strengths of Nb braze joints were plotted as a function of vanadium composition. Figure 5.32 shows that the ultimate tensile strength of Nb braze joint decreases steadily from 770 MPa to 200 MPa when vanadium composition increases from 0 to 46 at.%. However, pure vanadium braze joint possesses an ultimate tensile strength of 920 MPa, which is superior to the pure Nb counterpart. The experimental data were fitted with a parabolic trend (solid line in Figure 5.32), which predicts that the weakest joint of 220 MPa will be produced at a vanadium composition of 47 at.% V. This prediction is reasonable because joints fabricated from 54Nb-46V foils possesses an

almost 100% volume fraction of NiTi-χ eutectic mixture, signifying that the brittle χ phase has a predominantly continuous microstructure in the joints. The consequence of a continuous brittle phase is a joint with lowest ductility and strength.

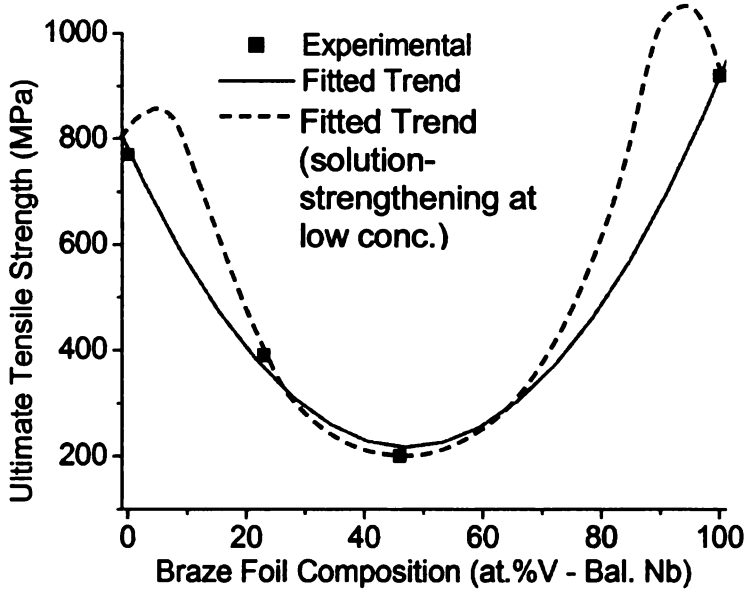

Figure 5.32 Ultimate tensile strength of Nb braze joints as a function of vanadium composition (experimental and fitted data shown).

Based on the solid trend line in Figure 5.32, increasing vanadium content beyond 47 at.% should improve the ultimate tensile strength. Such increase in ultimate tensile strength can be explained by the emergence of NiTi-V eutectic and their progressive substitution for the NiTi-χ eutectic as vanadium composition increases. This predicted trend, however, did not consider the possibility of solution-strengthening at very low concentrations of vanadium or Nb. If Nb braze joints can be solution-strengthened by low amounts of vanadium, vice versa, the dotted line in Figure 5.32 will be a more accurate representation than the solid trend as it contains a maximum close to each end of the composition scale.

5.4.2 Quaternary Phase Equilibria in the Ni-Ti-Nb-V System

Given the complete solubility of vanadium in Nb, presence of χ phase in the V-alloyed Nb braze system was unexpected. However, after analyzing quaternary phase equilibria of Ni-Ti-Nb-V, it became apparent that χ phase is actually a quaternary intermetallic compound. In this section, an attempt will be made to discuss phase equilibria in the quaternary system and the origin of χ phase. The understanding of the Ni-Ti-Nb-V system will serve as an important basis for future attempts to alloy Nb-based braze joints with other alloying elements of similar properties with vanadium.

With the addition of vanadium, Gibb's phase rule dictates that an extra degree-of-freedom will be introduced in the phase equilibria. Hence, up to five phases can be in mutual equilibrium. Phase fields in the quaternary system will be represented by the following (corresponding degrees-of-freedom indicated in parenthesis):

One-phase – Entire phase volume (four degrees-of-freedom);

Two-phase – Series of tie-lines (three degrees-of-freedom);

Three-phase – Series of tie-triangles (two degrees-of-freedom);

Four-phase – Single tie-tetrahedrons (one degree-of-freedom);

Five-phase – Single-point (no degree-of-freedom).

A tetrahedron representing the 920°C-isotherm of the Ni-Ti-Nb-V quaternary phase diagram is constructed and shown in Figure 5.33, with only essential phases illustrated. From Figure 5.33, it can be seen that it is impossible to construct four-phase tie-tetrahedrons among the NiTi, BCC-(Nb,V,Ti,Ni), Ti_2Ni, X_5 and σ' phases without

introducing a quaternary intermediate phase in the NiTi-Nb-Ti-V space of the phase diagram (Figure 5.34).

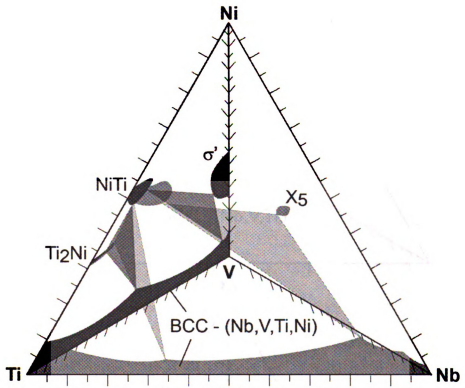

Figure 5.33 920°C-isotherm of the Ni-Ti-Nb-V quaternary phase diagram showing only the NiTi, BCC-(Nb,V,Ti,Ni), Ti_2Ni, X_5 and σ' phases and their tie-triangles.

This intermediate compound is, in fact, the χ phase observed in previous section. The position of χ phase in the quaternary space is consistent with the elemental mapping results in Figure 5.28. Figure 5.34 shows how χ phase establishes equilibrium and forms four tie-tetrahedrons with its surrounding phases. Given the complexity of illustration, two phase diagrams were constructed to show how χ phase establishes equilibrium with NiTi, BCC-(Nb,V,Ti,Ni), Ti_2Ni and σ' in the Ni-Ti-V system (Figure 5.34a), and NiTi, BCC-(Nb,V,Ti,Ni), Ti_2Ni and X_5 in the Ni-Ti-Nb system (Figure 5.34b).

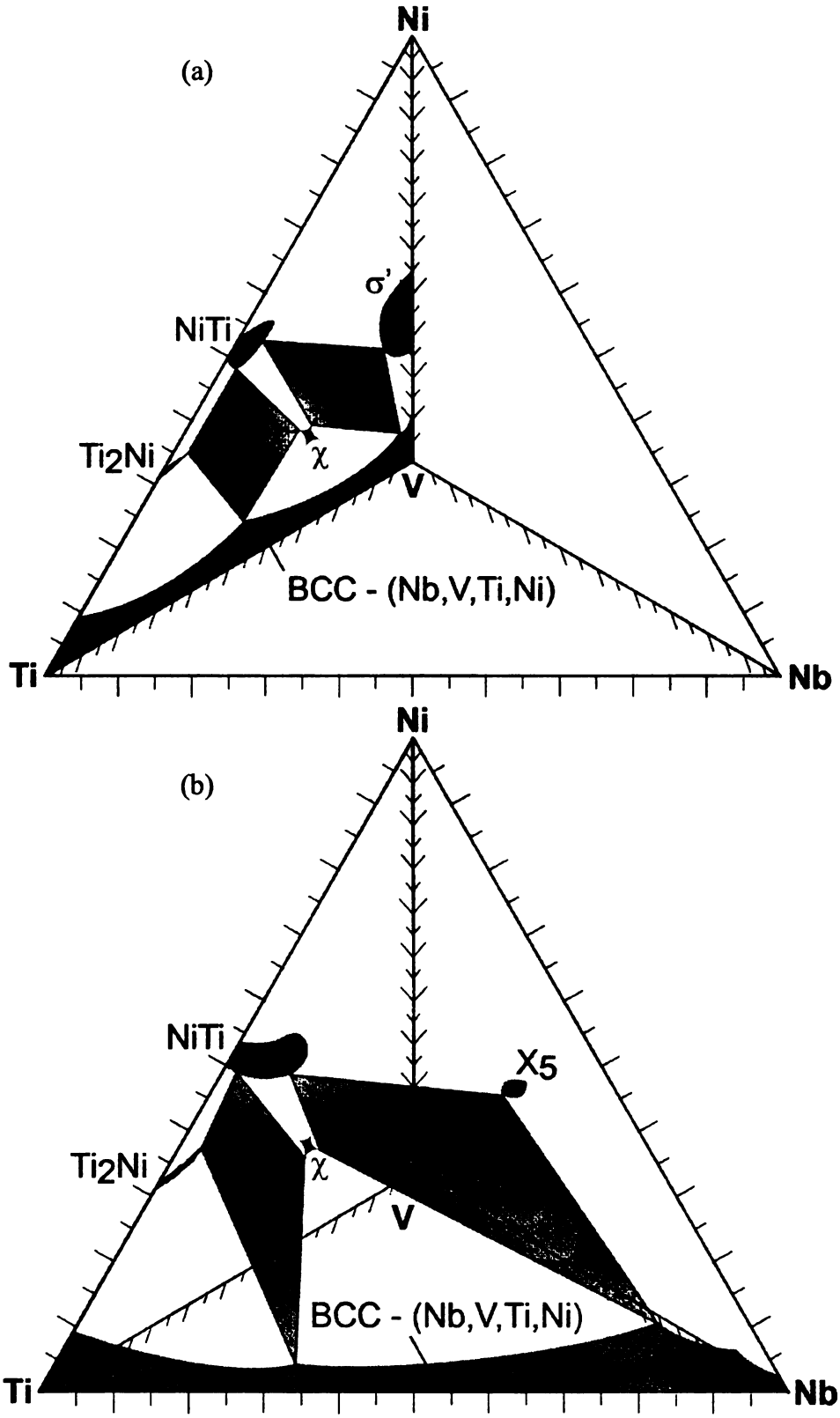

Figure 5.34 Possible 920°C-isotherm of the Ni-Ti-Nb-V quaternary phase diagram showing how the χ phase could establish equilibrium with (a) NiTi, BCC-(Nb,V,Ti,Ni), Ti_2Ni and σ' phases in the Ni-Ti-V system; or (b) NiTi, BCC-(Nb,V,Ti,Ni), Ti_2Ni and X_5 in the Ni-Ti-Nb system.

The two tie-tetrahedrons illustrated in Figure 5.34b each possess a tie-triangle of NiTi + BCC-(Nb,V,Ti,Ni) + χ as one of its faces. Since there are two degrees-of-freedom for three-phase equilibrium in a quaternary system, the NiTi + BCC-(Nb,V,Ti,Ni) + χ phase field will be made up by the volume shown in Figure 5.35b, while the NiTi + BCC-(Nb,V,Ti,Ni) phase field will be confined in a space between the NiTi + BCC-(Nb,V,Ti,Ni) + χ phase field and the Ni-Ti-Nb 'face' of the quaternary phase diagram (Figure 5.35a). The space configuration of the NiTi + BCC-(Nb,V,Ti,Ni) phase field is illustrated in Figure 5.35c.

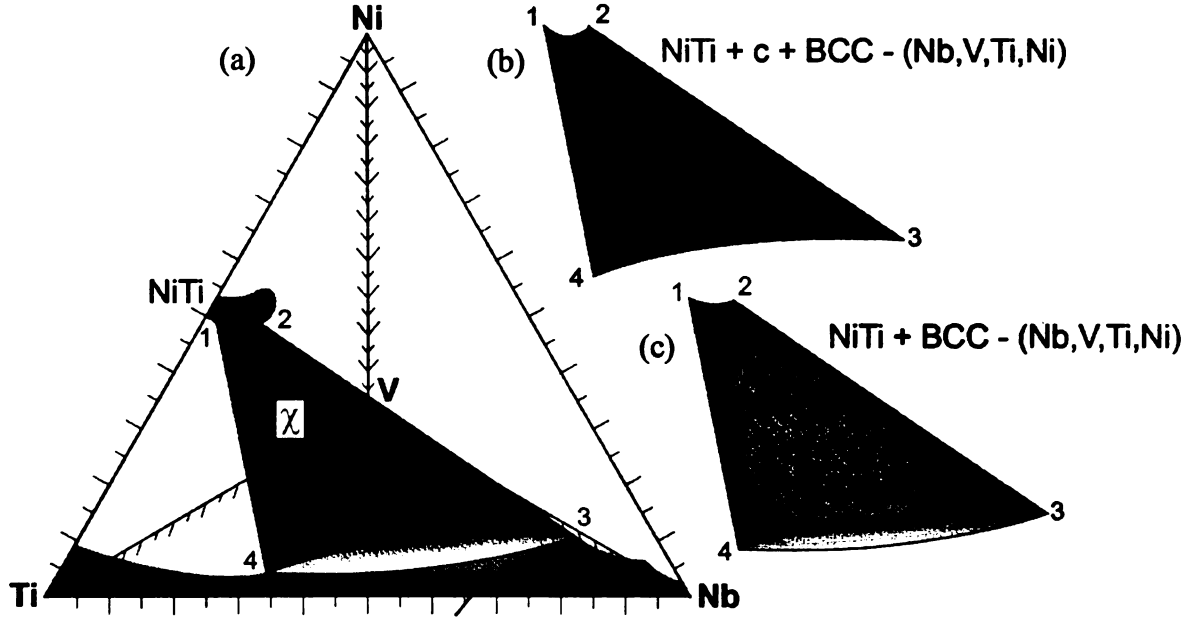

Figure 5.35 (a) Possible 920°C-isotherm of the Ni-Ti-Nb-V quaternary phase diagram showing common NiTi + BCC-(Nb,V,Ti,Ni) + χ tie-triangles as one of their faces of the tie-tetrahedrons illustrated in the bottom of the phase diagram in Figure 5.31. Space configurations of the (b) NiTi + BCC-(Nb,V,Ti,Ni) + χ - phase field; and (c) NiTi + BCC-(Nb,V,Ti,Ni) - phase field.

The confinement of the NiTi + BCC-(Nb,V,Ti,Ni) phase field to low vanadium compositions implies limited V-solubility. Since braze liquid compositions of V-alloyed Nb-based joints lies in the vertical NiTi-Nb-V section of the quaternary diagram and

should be in the vicinities of both quasibinary eutectic compositions, it is easy to see that excessive vanadium will result in liquid composition crossing into the NiTi + BCC-(Nb,V,Ti,Ni) + χ phase field, consequently producing joint microstructures observed in Figure 5.26 and 5.27. Stereology performed on the 54Nb-46V (Figure 5.26) and 77Nb-23V (Figure 5.27) braze joints revealed approximate χ phase volume occupancies of 60% and 20%, respectively. By linearly extrapolating χ phase volume fraction to zero, the composition of vanadium is calculated to be about 12 at.%. Therefore, the degree of V-alloying must be lowered below 12 at.% in order to produce predominantly Nb-based eutectic micro-constituents and, at the same time, possibly solution-strengthen the alloyed braze joints.

5.5 Summary

It is evident from indentation experiments that solution-strengthening of mechanical properties of Nb-based eutectic phase can be achieved through micro-alloying with Zr and tungsten, with the latter being a more effective strengthener. However, Ti_2Ni-type phase formation can be suppressed by addition of Zr but not with tungsten. Consequently, strengthening effect only manifested in tensile tests of Zr-alloyed joints. On the other hand, crack initiation by embrittling Ti_2Ni-type precipitates were believed to have occurred in W-alloyed joints, which caused the potentially-stronger eutectic joint to fail prematurely.

A vanadium braze foil was explored as an alternative braze material. Contact melting between NiTi and vanadium was observed, which also resulted in a

predominantly eutectic joint microstructure. Experimental evidence and phase equilibrium analysis showed that a NiTi-V quasibinary eutectic point exists at composition and temperature of approximately 40Ni-40Ti-20V (at.%) and 1170°C, respectively. Nanoindentation and tensile test indicated that mechanical properties of these joints are superior to the Nb-based counterpart. Given the toxic nature of vanadium, it will not be compatible with bio-medical applications, but may find use in aerospace, transportation or energy fields.

Alloying of Nb-based joints with substantial amounts of vanadium (23 at.% and 46 at.%) yielded joints with an unidentified quaternary intermetallic (termed 'χ' phase) and NiTi-Nb eutectic micro-constituents. The former was observed to increase in volume fraction with increasing vanadium content. Nanoindentation studies and fractography showed that the χ phase is hard and brittle, which seriously degraded tensile strength and ductility. Analysis of the Ni-Ti-Nb-V quaternary phase equilibria indicated that χ phase is a quaternary intermediate compound and its formation in V-alloyed Nb-based joints was attributed to excess vanadium. Hence, despite mutual solubility of Nb and vanadium, the degree of V-alloying should be reduced further in order to prevent χ phase formation, while effecting solution-strengthening.

CHAPTER 6: CONCLUSIONS AND FUTURE WORK

6.1 Conclusions

A novel reactive eutectic brazing technique has been successfully devised to form metallurgical bonds between NiTi alloys. The joining method relies on contact melting between pure Nb filler metal and the base-NiTi to form the braze liquid. Brazing was carried out under moderate high vacuum at temperatures above 1150°C. Contact melting between NiTi and Nb is governed by the NiTi-Nb isopleth in the ternary phase diagram, which closely resembles a perfect quasibinary eutectic isopleth.

When 51 μm-thick Nb foils were employed as the braze filler metal, the brazing process can be divided into 3 stages: (1) initial melting, (2) liquid propagation, and (3) termination. The driving force for initial melting is due to the presence of a thermodynamically-forbidden local concentration at the initial NiTi-Nb mating interface. The braze liquid formed from initial melting can dissolve any surface oxide present. Subsequent melting or liquid propagation is driven by the system's attempt to simultaneously maintain different NiTi and Nb equilibrium compositions at the NiTi-Liquid and Nb-Liquid interfaces, respectively. The rate of melting is not controlled by heat transfer kinetics, but by diffusion of Ni, Ti and Nb across the liquid. A diffusion-based model was established to predict the contact melting kinetics. Simulation suggests that rate of melting decreases rapidly as braze time and liquid width increases. The diffusion-based model also predicted the diffusivities of Ni (and Ti) and Nb in the liquid

to be 2.10 x 10^{-9} m^2/s and 1.55 x 10^{-9} m^2/s, respectively. Experimental results revealed that the NiTi and Nb melts at a constant molar ratio of about 1.4NiTi:1Nb (at.%).

Upon complete melting of Nb, the base-NiTi alloy continued to melt. Termination of contact melting occurred only when the liquid attained the NiTi liquidus composition. Hence, a 51 μm-thick Nb foil will ultimately produce a maximum liquid width that is approximately 200 μm. Due to the slow diffusivity of Nb in NiTi, isothermal solidification was insignificant within an hour of braze time when such filler foil thickness was used. On the other hand, isothermal solidification was observed after a braze duration of 15 minutes when 6 μm-thick Nb films were employed as the filler.

The presence of a quasibinary eutectic point at 38Ni-36Ti-26Nb (at.%) in the ternary system caused the braze liquid to solidify predominantly into eutectic NiTi-Nb micro-constituents and pro-eutectic NiTi phase upon cooling. The pro-eutectic NiTi phase assumed a planar solidification front if freezing occurred prior to Nb exhaustion, but promptly evolved into a dendritic morphology if the Nb were melted completely prior to solidification. The transition from a planar to a dendritic morphology is attributed to instability at the solidification front due to constitutional supercooling. Due to fast cooling rate associated with the termination of brazing, sub-grain boundaries appeared within the pro-eutectic NiTi dendrites. Some of the sub-grain boundaries may be decorated by fine Nb-rich precipitates.

The majority of the eutectic-Nb phase in the joint possessed lamellar morphology, although there were also regions that were rod-like. Trace amounts of facetted precipitates were observed within the eutectic phase in joints that were brazed for more than 120 seconds. Selected-area diffraction from TEM revealed that these precipitates have crystal structure that is related to the Ti_2Ni phase. Further experimental work suggests that they are $(Ti,Nb)_4Ni_2O$ sub-oxides, which formed due to stabilization of $(Ti,Nb)_2Ni$ phase by oxygen contamination.

No microstructural changes were observed in SEM when brazed joints were thermally aged below 800°C. But at 800°C, $(Ti,Nb)_4Ni_2O$ sub-oxides precipitates began coalescing to form larger grains. At 920°C, these sub-oxides appeared to be solutionized in the eutectic matrix at 920°C, while the eutectic-Nb phase evolved from rod-like into spheroidal morphology. Spheroidization of the eutectic-Nb phase can most likely be attributed to the minimization of interfacial energy between eutectic-NiTi and eutectic-Nb phases.

Nanoindentation studies revealed that as-brazed eutectic joints possess an average hardness of 2.0 GPa. When thermally aged at 350°C for 1.5 hours, joint hardness can be increased to 4.0 GPa, which is comparable to the base-NiTi alloy hardness. Elastic moduli of as-brazed and aged joints measured by the Oliver and Pharr method yield values in the range of 80 to 95 GPa, which are also comparable to the moduli of base-NiTi alloys of corresponding conditions. Nanoindentation experiments also revealed the

mechanical properties of $(Ti,Nb)_4Ni_2O$ precipitates. Average hardness and elastic modulus of these sub-oxides were estimated to be 12.8 GPa and 175 GPa, respectively.

Results from tensile tests performed on butt-joints show that the braze process caused degradation in the base-NiTi's strength and ductility, but superelastic response could be restored in the base-NiTi alloy through post-braze thermal aging. It was found that the optimum aging temperature is around 350°C for 1.5 hours, where the highest tensile strength and plateau stresses of 770 MPa and 380 MPa were observed, respectively. However, the eutectic joints are still mechanically weaker than the base-NiTi alloy, which has a ultimate tensile strength of about 900 MPa after being subjected to the braze and optimum aging temperatures. The lower eutectic braze strength may be attributed to either the strength-limiting eutectic-Nb phase or the presence of embrittling Ti_2Ni-type precipitates serving as crack initiation sites for premature joint failure. Fractography revealed extensive ductile tearing and micro-void coalescence, strongly suggesting that the joint is primarily ductile.

Tungsten-inert gas welding was successfully adapted for the formation of eutectic liquid at the joint area. The microstructure at the joint revealed pro-eutectic NiTi dendrites, eutectic micro-constituents and another anomalous dendritic phase that was believed to be a complex quaternary oxide. An ultimate tensile strength of 750 MPa was achieved using this approach, which is comparable to the brazed counterparts. However, TIG welded joints suffered poorer ductility, probably due to the presence of the complex quaternary oxide.

A preliminary attempt was also made to join NiTi alloys to Ta and alumina using the reactive eutectic braze process. Necking was observed in a NiTi-Ta butt joint and the stress-strain plot revealed an ultimate tensile strength of about 210 MPa, which strongly indicates that the joint possesses strength that exceeds that of the Ta base-metal. Wetting and flow of the braze liquid was observed on alumina substrates. However, thermal shock apparently caused weakening of the alumina near the joint interface. As a result, the NiTi-alumina lap-joint specimen suffered poor shear and tensile strengths.

Solution-strengthening of Nb-eutectic braze joints through micro-alloying with Zr and tungsten was studied. The addition of 1 at.% Zr to the Nb braze resulted in a microstructure free from the Ti-rich sub-oxide precipitates and porosity even when brazing was performed on oxidized samples under poor vacuum conditions. On the other hand, the addition of tungsten (~ 2 at.%) appeared to encourage precipitation of the Ti-rich sub-oxide and also increased the eutectic spacing. The latter is likely caused by the slow-diffusing nature of tungsten. Micro- and nanoindentation studies showed that hardness of the eutectic micro-constituents can be improved by micro-alloying with both Zr and tungsten. Distinct improvements in tensile strength were, however, only observed in Zr-alloyed eutectic joints, where an ultimate tensile strength of 850 MPa was achieved. Tungsten-alloyed joints did not produce an increase in strength, probably because the adverse effects of Ti_2Ni-type precipitates outweigh the improvement in strength of the eutectic-Nb phase.

An alternative braze material system was also explored. Pure vanadium was employed as the braze filler metal for the reactive eutectic braze process. Contact melting between NiTi and vanadium was observed to occur around 1170°C. The contact melting mechanism is believed to be similar to that of the NiTi-Nb system. Because of the likely presence of a perfect quasibinary eutectic isopleth in the Ni-Ti-V system, V-eutectic braze joints have a predominantly eutectic microstructure, which has a network-like morphology. Pro-eutectic NiTi dendrites were also observed to solidify against the unmelted base-NiTi alloy. The NiTi-V quasibinary eutectic point was estimated to be at 40Ni-40Ti-20V (at.%) at a temperature of 1170°C. Nanoindentation results revealed that as-brazed V-eutectic joints have higher hardness than the Nb counterparts, while no significant difference in hardness was observed in the 350°C-aged joints. However, tensile tests indicated that 350°C-aged V-eutectic butt-joints possess higher ultimate tensile strength as compared to as-brazed specimens. An ultimate tensile strength of 920 MPa was achieved in the aged V-eutectic joint, which is the highest reported in this work. Similar to the Nb-eutectic joints, fractography performed on the V-eutectic joint also revealed primarily ductile-tearing.

Alloying of Nb braze joints with vanadium was also explored in this work. Two alloying compositions were studied. They were 54Nb-46V and 77Nb-23V (at.%). The former produced predominantly NiTi-χ eutectic micro-constituents in the joint, while the latter resulted in elongated grains of χ phase in a mainly NiTi-Nb eutectic microstructure. Nanoindentation revealed that the χ phase have hardness and elastic modulus of 9.5 GPa and 150 GPa, respectively. Tensile tests on these V-alloyed Nb braze joints indicated

poor tensile strength and ductility for both alloying compositions. The 54Nb-46V joint has a tensile strength of 200 MPa, while the 77Nb-23V joint failed at 390 MPa. Fractography performed on the 54Nb-46V and 77Nb-23V joints revealed predominantly smooth and flat cleavage surfaces. Hence, nanoindentation, tensile tests and fractography all suggest that the χ phase is hard and brittle.

Phase equilibrium analysis of the Ni-Ti-Nb-V system indicated that χ phase is a quaternary intermediate compound that mediates equilibrium among the NiTi, BCC-(Nb,V,Ti,Ni), Ti_2Ni, X_5 and σ' phases. The χ phase was believed to have formed via a peritectoid reaction between the NiTi and BCC-(Nb,V,Ti,Ni) phases during cooling due to high V-composition in the braze joints.

6.2 Future Work

Given the fact that Nb is mutually soluble with many elements, solid-solution strengthening appears to be the promising choice to improve the mechanical properties of brazed joints. Indeed, nanoindentation and tensile results have demonstrated that micro-alloying Nb filler metal with Zr and tungsten have the potential to produce stronger braze joints. Furthermore, it was observed that $(Ti,Nb)_4Ni_2O$ formation can be suppressed by the addition of Zr. Positive results from both alloying candidates suggest that further improvements in the mechanical properties of eutectic braze joints may be achievable through simultaneous alloying of Nb with Zr and tungsten. Since vanadium can also be solution-hardened using Nb and tungsten [Maksimovich et al. 1982], strengthening of

vanadium-eutectic joints may also be achievable through micro-alloying using these elements. Tantalum and Zr are also potential candidates.

The ability to re-solutionize the Ti_2Ni-type precipitates in the Ni-Ti-Nb system opens up the possibility of strengthening Nb-eutectic joints by precipitation-hardening. The precipitation of Ti_2Ni-type phase after solution-treatment can be controlled by thermal aging. To maximize the strengthening effect, coherent Ti_2Ni-type precipitates should be finely-dispersed in the eutectic matrix as GP-zones. With a thorough knowledge of the quaternary phase equilibria and the ability to control χ phase formation in the Nb braze joints, it is believed that precipitation-hardening of Nb-eutectic joints can also be achieved with the χ phase using a similar approach for the Ti_2Ni-type precipitates. Therefore, it is critical to understand the physical metallurgy of χ phase in the joint.

Despite the poor mechanical properties of the NiTi-alumina joint, reasonably good wettability and flow of the braze liquid on alumina show that the braze process is still a promising approach for joining NiTi alloys to alumina and possibly other ceramic materials. Thermal shock, responsible for weakening of the alumina near the mating interface during cooling, may be minimized by employing a lower cooling rate. Also, recent preliminary work has also demonstrated wettability and flow of the braze liquid on hydroxyapatite (HAP), although there is no mechanical data from a joint between NiTi and HAP. Hence, it will be of great interest to investigate the tensile and shear properties of the NiTi-HAP joint, and melting reaction among NiTi, Nb and HAP.

APPENDIX A

Numerical calculations on heat transfer kinetics, involved in the 'incubation' period of initial melting, were written in FORTRAN 77. An explicit finite-difference scheme using the 2^{nd}-order Runge-Kutta method was applied to Eq. (3.1) – (3.3). The FORTRAN code, input parameters and summarized results are listed below.

```
      PROGRAM incubation time
*-----------------------------------------------------------------------
*     Program created by Kebin Low
*     CHEMS Department, MSU
*     March 10th, 2008
*
*     This program performs numerical iterations to calculate
*     the incubation time for initial melting.
*
*-----------------------------------------------------------------------
*
*     Declarations
      implicit none
      integer*4 t,k,numstep
      real*8 conduct,heatcap,cte_niti,tempext,tempint(300001)
      real*8 density,correctdensity,deltime,tottime
      real*8 delq(300001),nitithickness,tempdiff(300001)
      real*8 nbthickness,melttemp
*
*     Print on-screen menu
      write(*,*)""
      write(*,*)"-------------------------------------------------"
      write(*,*)"This program performs numerical iterations to"
      write(*,*)"calculate the incubation time for initial melting."
      write(*,*)"-------------------------------------------------"
      write(*,*)""
*
*     Prompt user inputs
      write(*,*)"Input desired time frame (sec):"
      read(*,*) tottime
      write(*,*)"Input desired total number of steps (0-300000):"
      read(*,*) numstep
      write(*,*)""
      write(*,*)"Please Wait . . . "
      write(*,*)""
*
*     Dividing the total time by the number of steps
      deltime=tottime/float(numstep)
*
*     Setting all time-variables to zero initially
      do 10 t=1,numstep
```

```
      tempdiff(t)=0
      delq(t)=0
 10   continue
*
*     Continue with user prompts
      write(*,*)"Input NiTi Plate Thickness (m):"
      read(*,*) nitithickness
      write(*,*)"Input Thickness of Nb Foil (m):"
      read(*,*) nbthickness
      write(*,*)"Input Thermal Conductivity of NiTi (W/m.K):"
      read(*,*) conduct
      write(*,*)"Input Specific Heat Capacity of Nb (J/g.K):"
      read(*,*) heatcap
      write(*,*)"Input External Temperature (Degrees Celsius):"
      read(*,*) tempext
      write(*,*)"Input Initial NiTi-Nb Int. Temp. (Degrees Celsius):"
      read(*,*) tempint(1)
      write(*,*)""
      write(*,*)"Calculation in Progress . . . "
      write(*,*)""
      write(*,*)"********************************************************"
      write(*,*)"'raw.dat', 'output.dat' and 'results.dat'"
      write(*,*)"will be generated at the end of calculations."
      write(*,*)""
      write(*,*)"See 'results.dat' for details."
      write(*,*)"********************************************************"
*
*     Opening output files
      open(unit=1,file='raw.dat',status='unknown')
      open(unit=2,file='output.dat',status='unknown')
      open(unit=3,file='results.dat',status='unknown')
*
*     Writing inputs into results.dat
      write(3,*)"Input Parameters"
      write(3,*)"~~~~~~~~~~~~~~~~~~~~~~~~~~~~~~~~~~~~~~~~~~~~~~~~~~~~~~~"
      write(3,*)"Time Frame:",tottime," seconds"
      write(3,*)"Total Number of Steps:",numstep
      write(3,*)"Nb Foil Thickness:",nbthickness," m"
      write(3,*)"Thermal Conductivity of NiTi:",conduct," W/m.K"
      write(3,*)"Specific Heat Capacity of Nb:",heatcap," J/g.K"
      write(3,*)"External Temperature:",tempext," C"
      write(3,*)"Initial NiTi-Nb Temperature:",tempint(1)," C"
      write(3,*)""
*
*     Density of NiTi (g/m3)
      density=8.57
*
*     Define melting temperature
      melttemp=1170.0
*
*     Calculating thermal expansion at braze temperature
      cte_niti=1+(7.1E-6*tempext)
*
*     Corrected density
      correctdensity=density/(cte_niti**3)
*
```

```
*     Calculating the temperature difference
      tempdiff(1)=tempext-tempint(1)
*
*     Print in-calculation message
      write(*,*)""
      write(*,*)"Please wait... Calculation in progress..."
*
*     Numerical iterations
      do 20 t=1,numstep
*
*     Check if NiTi thickness limit has been exceeded
      if(tempint(t).lt.melttemp) then
*
*     Calculating change in heat
      delq(t)=(conduct*tempdiff(t)*deltime)/nitithickness
*
*     Calculating new interface temperature
      tempint(t+1)=((delq(t)/heatcap)/(correctdensity*nbthickness*100))
     C+tempint(t)
      tempdiff(t+1)=tempext-tempint(t+1)
*
*     Write results to raw.dat
      write(1,*)t*deltime,delq(t),tempint(t),tempdiff(t)
*
      endif
*
      if(tempint(t).gt.melttemp) then
*
*        Write data points for plotting into output.dat
*         do 21 k=1,t,200
*         write(2,*)k*deltime,delq(k),meltthickness(k),vniti(k)
* 21      continue
*
*     Print important information with regards to Nb exhaustion
      write(3,*)"Information Associated With Incubation Time"
      write(3,*)"~~~~~~~~~~~~~~~~~~~~~~~~~~~~~~~~~~~~~~~~~~~~~~~~~~~~~~~~~~~~~~"
      write(3,*)"Time:",(t-1)*deltime," seconds"
      write(3,*)"NiTi-Nb Interface Temperature",tempint(t-1)," C"
*
*     Print End-of-Program message
      write(3,*)""
      write(3,*)"Files Generated"
      write(3,*)"*******************************************************"
      write(3,*)"'raw.dat', 'output.dat', and 'results.dat'"
      write(3,*)" have been generated."
      write(3,*)""
      write(3,*)"'raw.dat' contains all time-evolution data."
      write(3,*)"Data is in the following sequence:"
      write(3,*)"Time, Change in Heat, Interface Temp. and Temp. Diff."
      write(3,*)""
      write(3,*)"'results.dat' contains most-recent input parameters"
      write(3,*)"and calculated values."
      write(3,*)""
      write(3,*)"END OF PROGRAM"
      write(3,*)"*******************************************************"
      write(3,*)""
```

```
*
*   Close output files
    close(unit=1)
    close(unit=2)
    close(unit=3)
*
    stop
*
    endif
*
 20  continue
*
    end
```

Table A-1 Input parameters for calculating incubation time for initial melting.

Input Parameters	Values
Time Frame (secs)	1E-03
Total Number of Steps	50000
Nb Foil Thickness (m)	2.55E-05
Thermal Conductivity of NiTi (W/m-K)	41
Specific Heat Capacity of Nb (J/g-K)	0.265
External Temperature (°C)	1185
Initial NiTi-Nb Temperature (°C)	300

Table A-2 Results from the incubation time calculation.

Results	Values
Target NiTi-Nb Interface Temperature (°C)	1169.9
Time Taken to Attain Target Temperature (secs)	1.76E-06

APPENDIX B

Numerical calculations on melting kinetics before complete melting of the solid Nb, on the assumption that it is rate-limited by diffusion in the liquid, were written in FORTRAN 77. An explicit finite-difference scheme using the 2^{nd}-order Runge-Kutta method was applied to Eq. (3.13) – (3.17). The FORTRAN code, input parameters and summarized results are listed below.

```
      PROGRAM eutectic
*-----------------------------------------------------------------------
*     Program created by Kebin Low
*     CHEMS Department, MSU
*     July 27th, 2007
*
*     This program performs numerical iterations to simulate
*     the NiTi-Nb eutectic half-width evolution as a function of time
*     before exhaustion of the Nb interlayer.
*
*     The program assumes:
*     (1) Density of solid and liquid phases are the same;
*     (2) The NiTi/L and Nb/L interfaces attempt to maintain
*         their respective liquidus compositions;
*     (3) A linear concentration gradient hence exists across
*         the 2 solids;
*     (4) Fick's 1st law holds in the eutectic liquid;
*     (5) Dissolution process is diffusion-controlled;
*     (6) Heat transfer does not play a rate-limiting role;
*     (7) Solid-state diffusion is negligible within the simulation
*         time-frame.
*-----------------------------------------------------------------------
*
*     Declarations
      implicit none
      integer*4 t,k,numstep
      real*8 jnb(300001),jniti(300001),xnb(300001),xniti(300001)
      real*8 w(300001),vnb(300001),vniti(300001),cte_nb,cte_niti,temp
      real*8 nbconc,latticenb,latticeniti,deltime,tottime
      real*8 nbthickness,c1,c2,c3,c4,rho_nb,rho_niti,rho_nb1,rho_niti1
      real*8 diffusion_nb,diffusion_niti
*
*     Print on-screen menu
      write(*,*)""
      write(*,*)"-------------------------------------------------------"
      write(*,*)"This program performs numerical iterations to simulate"
      write(*,*)"the NiTi-Nb eutectic half-width evolution"
      write(*,*)"as a function of time before exhaustion of the"
      write(*,*)"Nb interlayer."
```

```
      write(*,*)"-------------------------------------------------"
      write(*,*)""
*
*     Prompt user inputs
      write(*,*)"Input desired time frame (sec):"
      read(*,*) tottime
      write(*,*)"Input desired total number of steps (0-300000):"
      read(*,*) numstep
      write(*,*)""
      write(*,*)"Please Wait . . . "
      write(*,*)""
*
*     Dividing the total time by the number of steps
      deltime=tottime/float(numstep)
*
*     Setting all time-variables to zero initially
      do 10 t=1,numstep
      jnb(t)=0
      jniti(t)=0
      vnb(t)=0
      vniti(t)=0
      xnb(t)=0
      xniti(t)=0
      w(t)=0
 10   continue
*
*     Continue with user prompts
      write(*,*)"Input Initial Nb Interlayer Half-Thickness (m):"
      read(*,*) nbthickness
      write(*,*)"Input Initial Liquid Half-Width (m):"
      read(*,*) w(1)
      write(*,*)"Input Lattice Parameter of Nb (angstrom):"
      read(*,*) latticenb
      write(*,*)"Input Lattice Parameter of NiTi (angstrom):"
      read(*,*) latticeniti
      write(*,*)"Input Braze Temperature (Degrees Celsius):"
      read(*,*) temp
      write(*,*)"Input NiTi Solidus Composition (atomic % Nb):"
      read(*,*) c1
      write(*,*)"Input Nb Solidus Composition (atomic % Nb):"
      read(*,*) c4
      write(*,*)"Input Self-Diffusion Coefficient of Nb (m^2/s):"
      read(*,*) diffusion_nb
      write(*,*)"Input Self-Diffusion Coefficient of NiTi (m^2/s):"
      read(*,*) diffusion_niti
      write(*,*)""
      write(*,*)"Calculation in Progress . . . "
      write(*,*)""
      write(*,*)"************************************************************"
      write(*,*)"'raw.dat', 'output.dat', and 'results.dat'"
      write(*,*)"will be generated at the end of calculations."
      write(*,*)""
      write(*,*)"See 'results.dat' for details."
      write(*,*)"************************************************************"
*
*     Calculating the liq. comp. of Nb and NiTi at selected temp.
```

```
      c2=(1310-temp)*(float(26)/float(140))
      c3=(temp-(2468-(float(1298)*100/float(74))))/
     C(float(1298)/float(74))
*
*     Opening output files
      open(unit=1,file='raw.dat',status='unknown')
      open(unit=2,file='output.dat',status='unknown')
      open(unit=3,file='results.dat',status='unknown')
*
*     Writing inputs into results.dat
      write(3,*)"Input Parameters"
      write(3,*)"~~~~~~~~~~~~~~~~~~~~~~~~~~~~~~~~~~~~~~~~~~~~~~~~~~~~~~~~~~~~"
      write(3,*)"Time Frame:",tottime," seconds"
      write(3,*)"Total Number of Steps:",numstep
      write(3,*)"Initial Nb Interlayer Half-Thickness:",nbthickness," m"
      write(3,*)"Initial Liquid Width:",w(1)," m"
      write(3,*)"Lattice Parameter of Nb:",latticenb," Angstroms"
      write(3,*)"Lattice Parameter of NiTi:",latticeniti," Angstroms"
      write(3,*)"Braze Temperature:",temp," Degrees Celsius"
      write(3,*)"NiTi Solidus Composition:",c1
      write(3,*)"Nb Solidus Composition:",c4
      write(3,*)"Nb Diffusion:",diffusion_nb," m^2/s"
      write(3,*)"NiTi Diffusion:",diffusion_niti," m^2/s"
      write(3,*)""
*
*     Calculating thermal expansion at braze temperature
      cte_nb=1+(7.3E-6*temp)
      cte_niti=1+(6.6E-6*temp)
*
*     Calculating the number density of Nb and NiTi
      rho_nb=2/(latticenb*1E-10*cte_nb)**3
      rho_niti=1/(latticeniti*1E-10*cte_niti)**3
*
      rho_nb1=((c4/100.0)*rho_nb)+(((100.0-c4)/100.0)*rho_niti)
      rho_niti1=((c1/100.0)*rho_nb)+(((100.0-c1)/100.0)*rho_niti)
*
*     Calculating the Nb concentration difference in #Nb/m^3
      nbconc=(c3/(((c3/2.0)*((latticenb*1E-10*cte_nb)**3))
     C+((100.0-c3)*((latticeniti*1E-10*cte_niti)**3))))
     C-(c2/(((c2/2.0)*((latticenb*1E-10*cte_nb)**3))
     C+((100.0-c2)*((latticeniti*1E-10*cte_niti)**3))))
*
*     Print in-calculation message
      write(*,*)""
      write(*,*)"Please wait... Calculation in progress..."
*
*     Numerical iterations
      do 20 t=1,numstep
*
*     Check if Nb interlayer thickness has been exceeded
      if(xnb(t).lt.nbthickness) then
*
*     Calculating the Nb and NiTi flux in the liquid
      jnb(t)=diffusion_nb*nbconc/w(t)
      jniti(t)=diffusion_niti*nbconc/w(t)
*
```

```
*     Calculating the Nb/L interface velocity
      vnb(t)=jnb(t)/rho_nb1
      vniti(t)=jniti(t)/rho_niti1
*
*     Calculating the position of Nb/L and NiTi/L interfaces
      xnb(t+1)=xnb(t)+(vnb(t)*deltime)
      xniti(t+1)=xniti(t)+(vniti(t)*deltime)
*
*     Calculating the width of the liquid
      w(t+1)=xnb(t+1)+xniti(t+1)
*
*     Write results to raw.dat
      write(1,*)t*deltime,jnb(t),jniti(t),vnb(t),vniti(t),xnb(t),
     Cxniti(t),w(t)
*
      endif
*
      if(xnb(t).gt.nbthickness) then
*
*       Write data points for plotting into output.dat
        do 21 k=1,t,200
        write(2,*)k*deltime,vnb(k),vniti(k)
*         write(2,*)k*deltime,w(k),xnb(k),xniti(k),vnb(k),vniti(k)
21      continue
*
*     Print important information with regards to Nb exhaustion
      write(3,*)"Calculated Parameters"
      write(3,*)"~~~~~~~~~~~~~~~~~~~~~~~~~~~~~~~~~~~~~~~~~~~~~~~~~~~~~~~~~~~~"
      write(3,*)"Density of Pure Nb:",rho_nb," #/m3"
      write(3,*)"Density of Pure NiTi:",rho_niti," #/m3"
      write(3,*)"Density of Pro-eutectic Nb:",rho_nb1," #/m3"
      write(3,*)"Density of Pro-eutectic NiTi:",rho_niti1," #/m3"
      write(3,*)"NiTi Liquidus Composition:",c2
      write(3,*)"Nb Liquidus Composition:",c3
      write(3,*)"Nb-Concentration Diff. Across Liquid:",nbconc," #/m3"
      write(3,*)""
      write(3,*)"Information Associated With Nb Exhaustion"
      write(3,*)"~~~~~~~~~~~~~~~~~~~~~~~~~~~~~~~~~~~~~~~~~~~~~~~~~~~~~~~~~~~~"
      write(3,*)"Time:",t*deltime," seconds"
      write(3,*)"Thickness of Nb Exhausted:",xnb(t)," m"
      write(3,*)"Thickness of NiTi Exhausted:",xniti(t)," m"
      write(3,*)"Eutectic Liquid Half-Width:",w(t)," m"
*
*     Print End-of-Program message
      write(3,*)""
      write(3,*)"Files Generated"
      write(3,*)"*******************************************************"
      write(3,*)"'raw.dat', 'output.dat', and 'results.dat'"
      write(3,*)" have been generated."
      write(3,*)""
      write(3,*)"'raw.dat' contains all time-evolution data."
      write(3,*)"Data is in the following sequence:"
      write(3,*)"Time, Nb-Flux, NiTi-Flux, Nb/L Velocity,"
      write(3,*)"NiTi/L Velocity, Nb/L Displacement,"
      write(3,*)"NiTi/L Displacement, Eutectic Liquid Width"
      write(3,*)""
```

```
      write(3,*)"'output.dat' contains plot-friendly data points."
      write(3,*)"Data is in the following sequence:"
      write(3,*)"Time (200-step interval), Eutectic Liquid Half-Width,"
      write(3,*)"Nb/L Displacement, NiTi/L Displacement,"
      write(3,*)"Nb Interface Velocity, NiTi Interface Velocity"
      write(3,*)""
      write(3,*)"'results.dat' contains most-recent input parameters"
      write(3,*)"and calculated values."
      write(3,*)""
      write(3,*)"END OF PROGRAM"
      write(3,*)"************************************************************"
      write(3,*)""
*
*     Close output files
      close(unit=1)
      close(unit=2)
      close(unit=3)
*
      stop
*
      endif
*
 20   continue
*
      end
```

Table B-1 Input parameters for simulating the melting kinetics before the complete melting of Nb (assume rate-limited by liquid phase diffusion).

Input Parameters	**Values**
Time Frame (secs)	60
Total Number of Steps	3E05
Initial Nb Interlayer Half-Thickness (m)	2.55E-05
Initial Liquid Width (m)	1E-08
Lattice Parameter of Nb (Angstroms)	3.307
Lattice Parameter of NiTi (Angstroms)	3.015
Braze Temperature (°C)	1185
NiTi Solidus Composition (at.% Nb)	7
Nb Solidus Composition (at.% Nb)	91
Nb Diffusion Coefficient (m^2/s)	1.55E-09
NiTi Diffusion Coefficient (m^2/s)	4.10E-09

Table B-2 Results from the melting kinetics calculation (before the complete melting of Nb, assume rate-limited by liquid phase diffusion).

Results Associated with Complete Melting of Solid Nb	**Values**
Thickness of Melted Nb (m)	2.55E-05
Thickness of Melted NiTi (m)	9.55E-05
Liquid Half-Width (m)	1.21E-04
Elapsed Time (secs)	33.51

APPENDIX C

Numerical calculations on melting kinetics after complete melting of the solid Nb, on the assumption that it is rate-limited by diffusion in the liquid, were written in FORTRAN 77. An explicit finite-difference scheme using the 2^{nd}-order Runge-Kutta method was applied to Eq. (3.14) – (3.19). The FORTRAN code, input parameters and summarized results are listed below.

```
      PROGRAM eutectic_late_stage
*-----------------------------------------------------------------------
*     Program created by Kebin Low
*     CHEMS Department, MSU
*     July 27th, 2007
*
*     This program performs numerical iterations to simulate
*     the NiTi-Nb eutectic half- width evolution as a function of time
*     after exhaustion of the Nb interlayer.
*
*     The program assumes:
*     (1) Density of solid and liquid phases are the same;
*     (2) The NiTi/L and Nb/L interfaces attempt to maintain
*         their respective liquidus compositions;
*     (3) A linear concentration gradient hence exists across
*         the 2 solids;
*     (4) Fick's 1st law holds in the eutectic liquid;
*     (5) Dissolution process is diffusion-controlled;
*     (6) Heat transfer does not play a rate-limiting role;
*     (7) Solid-state diffusion is negligible within the simulation
*         time-frame.
*-----------------------------------------------------------------------
*
*     Declarations
      implicit none
      integer*4 t,numstep
      real*8 jnb(300001),jniti(300001),xnb(300001),xniti(300001)
      real*8 w(300001),vnb(300001),vniti(300001),cte_nb,cte_niti,temp
      real*8 latticenb,latticeniti,deltime,tottime
      real*8 nbconc(300001),c1,c2,c3,c4,rho_nb,rho_niti
      real*8 diffusion_nb,diffusion_niti,rho_nb1,rho_niti1
*
*     Print on-screen menu
      write(*,*)""
      write(*,*)"-----------------------------------------------------"
      write(*,*)"This program performs numerical iterations to simulate"
      write(*,*)"the NiTi-Nb eutectic half-width evolution"
      write(*,*)"as a function of time after the exhaustion of the"
```

```
      write(*,*)"Nb interlayer."
      write(*,*)"--------------------------------------------------"
      write(*,*)""
*
*     Prompt user inputs
      write(*,*)"Input desired time frame (sec):"
      read(*,*) tottime
      write(*,*)"Input desired total number of steps (0-300000):"
      read(*,*) numstep
*
*     Dividing the total time by the number of steps
      deltime=tottime/float(numstep)
*
*     Setting all time-variables to zero initially
      do 10 t=1,numstep
      nbconc(t)=0
      jnb(t)=0
      jniti(t)=0
      vniti(t)=0
      xniti(t)=0
      w(t)=0
 10   continue
*
*     Continue with user prompts
      write(*,*)"Input Liquid Half-Width Upon Nb Exhaustion (m):"
      read(*,*) w(1)
      write(*,*)"Input Lattice Parameter of Nb (angstrom):"
      read(*,*) latticenb
      write(*,*)"Input Lattic Parameter of NiTi (angstrom):"
      read(*,*) latticeniti
      write(*,*)"Input Braze Temperature (Degrees Celsius):"
      read(*,*) temp
      write(*,*)"Input NiTi Solidus Composition (atomic % Nb):"
      read(*,*) c1
      write(*,*)"Input Nb Solidus Composition (atomic % Nb):"
      read(*,*) c4
      write(*,*)"Input Self-Diffusion of NiTi (m^2/s):"
      read(*,*) diffusion_niti
*
*     Calculating the liq. comp. of Nb and NiTi at selected temp.
      c2=(1310-temp)*(float(26)/float(140))
      c3=(temp-(2468-(float(1298)*100/float(74))))/
     C(float(1298)/float(74))
*
*     Opening output files
      open(unit=1,file='output_late.dat',status='unknown')
      open(unit=2,file='results_late.dat',status='unknown')
*
*     Writing inputs into results_late.dat
      write(2,*)"Input Parameters"
      write(2,*)"~~~~~~~~~~~~~~~~~~~~~~~~~~~~~~~~~~~~~~~~~~~~~~~~~~~~~~~~~~~~~~"
      write(2,*)"Time Frame:",tottime," seconds"
      write(2,*)"Total Number of Steps:",numstep
      write(2,*)"Liquid Half-Width Upon Nb Exhaustion:",w(1)," m"
      write(2,*)"Lattice Parameter of Nb:",latticenb," Angstroms"
      write(2,*)"Lattice Parameter of NiTi:",latticeniti," Angstroms"
```

```
      write(2,*)"Braze Temperature:",temp," Degrees Celsius"
      write(2,*)"NiTi Solidus Composition:",c1," atomic % Nb"
      write(2,*)"NiTi Liquidus Composition:",c2," atomic % Nb"
      write(2,*)"Nb Liquidus Composition:",c3," atomic % Nb"
      write(2,*)"Nb Solidus Composition:",c4," atomic % Nb"
      write(2,*)"NiTi Diffusion:",diffusion_niti," m^2/s"
*
*     Calculating thermal expansion at braze temperature
      cte_nb=1+(7.3E-6*temp)
      cte_niti=1+(6.6E-6*temp)
*
*     Calculating the number density of Nb and NiTi
      rho_nb=2/(latticenb*1E-10*cte_nb)**3
      rho_niti=1/(latticeniti*1E-10*cte_niti)**3
*
      rho_nb1=((c4/100.0)*rho_nb)+(((100.0-c4)/100.0)*rho_niti)
      rho_niti1=((c1/100.0)*rho_nb)+(((100.0-c1)/100.0)*rho_niti)
*
*     Calculating the Nb concentration difference in #Nb/m^3
      nbconc(1)=(c3/(((c3/2.0)*((latticenb*1E-10*cte_nb)**3))
     C+((100.0-c3)*((latticeniti*1E-10*cte_niti)**3))))
     C-(c2/(((c2/2.0)*((latticenb*1E-10*cte_nb)**3))
     C+((100.0-c2)*((latticeniti*1E-10*cte_niti)**3))))
*
*     Print in-calculation message
      write(*,*)""
      write(*,*)"Please wait... Calculation in progress..."
*
*     Numerical iterations
      do 20 t=1,numstep
*
*     Calculating the NiTi flux in the liquid
      jniti(t)=diffusion_niti*nbconc(t)/w(t)
*
*     Calculating the NiTi/L interface velocity
      vniti(t)=jniti(t)/rho_niti1
*
*     Calculating the width of the liquid
      w(t+1)=w(t)+(vniti(t)*deltime)
*
*     Calculating the new concentration difference in #Nb/m^3
      nbconc(t+1)=nbconc(t)-((jniti(t)*deltime)/w(t+1))
*
20    continue
*
*     Write data points for plotting into output_late.dat
      do 30 t=1,numstep,200
      write(1,*)t*deltime,w(t)
30    continue
*
*     Print calculated values to results_late.dat
      write(2,*)""
      write(2,*)"Calculated Parameters"
      write(2,*)"~~~~~~~~~~~~~~~~~~~~~~~~~~~~~~~~~~~~~~~~~~~~~~~~~~~~~~~~~~~~"
      write(2,*)"Density of Pure Nb:",rho_nb," #/m^3"
      write(2,*)"Density of Pure NiTi:",rho_niti," #/m^3"
```

```
      write(2,*)"Density of Pro-eutectic Nb:",rho_nb1," #/m^3"
      write(2,*)"Density of Pro-eutectic NiTi:",rho_niti1," #/m^3"
      write(2,*)"Self-Diffusion of NiTi:",diffusion_niti," m^2/s"
*
*     Print End-of-Program message
      write(*,*)""
      write(*,*)"************************************************************"
      write(*,*)"'output_late.dat' and 'results_late.dat'"
      write(*,*)"have been generated."
      write(*,*)""
      write(*,*)"Data in 'output_late.dat' is in the following"
      write(*,*)"sequence:"
      write(*,*)"Time, Eutectic Half-Width"
      write(*,*)""
      write(*,*)"'results_late.dat' contains most-recent input"
      write(*,*)"parameters and calculated values."
      write(*,*)""
      write(*,*)"END OF PROGRAM"
      write(*,*)"************************************************************"
      write(*,*)""
*
*     Close output files
      close(unit=1)
      close(unit=2)
*
      stop
*
      end
```

Table C-1 Input parameters for simulating the melting kinetics after the complete melting of Nb.

Input Parameters	**Values**
Time Frame (secs)	80
Total Number of Steps	3E05
Liquid Half-Width Upon Nb Exhaustion (m)	1.20951E-04
Lattice Parameter of Nb (Angstroms)	3.307
Lattice Parameter of NiTi (Angstroms)	3.015
Braze Temperature (°C)	1185
NiTi Solidus Composition (at.% Nb)	7
Nb Solidus Composition (at.% Nb)	91
NiTi Diffusion Coefficient (m^2/s)	4.10E-09

Table C-2 Results from the melting kinetics calculation (after the complete melting of Nb).

Results Associated with Post-Exhaustion of Solid Nb	**Values**
Liquid Half-Width at Exhaustion of Solid Nb (m)	1.21E-04
Approximate Thickness of Melted NiTi (m)	5E-06
Final Liquid Half-Width (m)	1.26E-04
Approximate Time Taken to Attain Final Liquid Half-Width (secs)	15

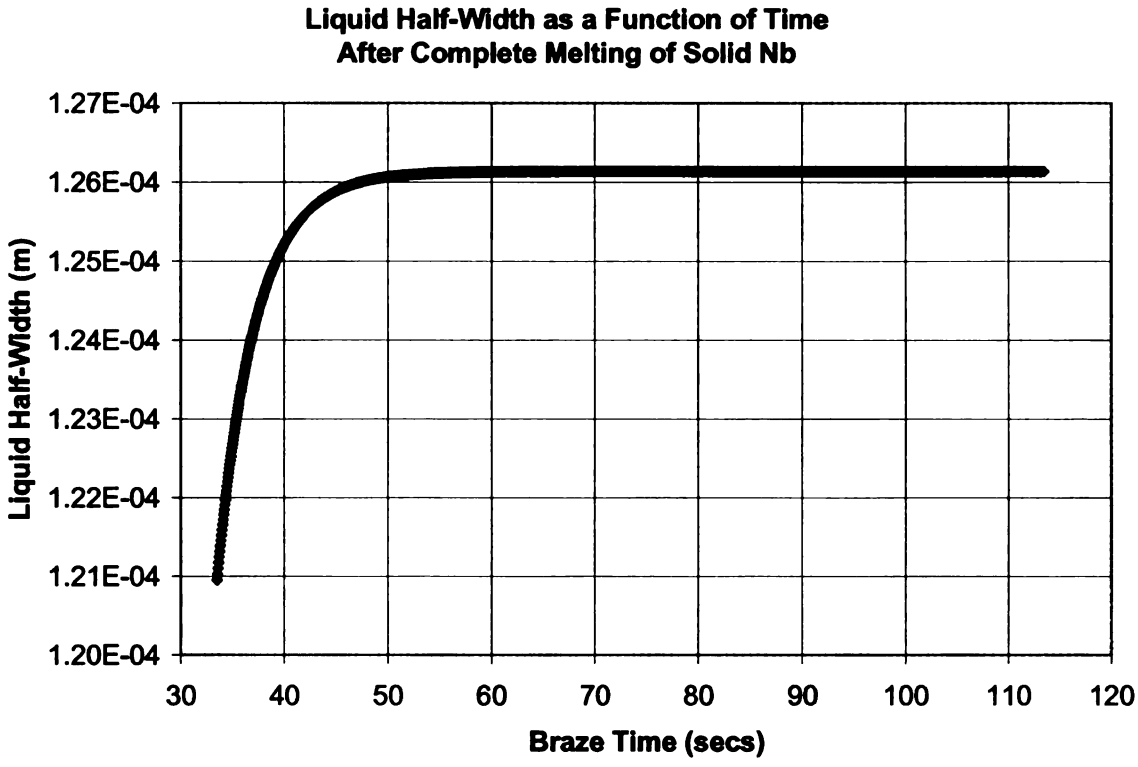

Figure C-1 Predicted liquid half-width as a function of braze time.

APPENDIX D

Numerical calculations on melting kinetics before complete melting of solid Nb, on the assumption that it is rate-limited by heat transfer, were written in FORTRAN 77. An explicit finite-difference scheme using the 2^{nd}-order Runge-Kutta method was applied to Eq. (3.20) – (3.21). The FORTRAN code, input parameters and summarized results are listed below.

```
      PROGRAM heat transfer
*-----------------------------------------------------------------------
*     Program created by Kebin Low
*     CHEMS Department, MSU
*     March 10th, 2008
*
*     This program performs numerical iterations to calculate
*     the NiTi-Liquid interface position and velocity
*     as a function of time if heat transfer, instead of diffusion,
*     is the rate-limiting factor for contact melting.
*
*-----------------------------------------------------------------------
*
*     Declarations
      implicit none
      integer*4 t,k,numstep
      real*8 meltthickness(300001),xniti(300001),vniti(300001)
      real*8 conduct,latent,cte_niti,tempext,tempint,tempdiff
      real*8 density,correctdensity,deltime,tottime
      real*8 delq(300001),nitithickness(300001)
      real*8 nbthickness,thicknesslimit
*
*     Print on-screen menu
      write(*,*)""
      write(*,*)"-----------------------------------------------------"
      write(*,*)"This program performs numerical iterations to"
      write(*,*)"calculate the NiTi-Liquid interface position and"
      write(*,*)"velocity as a function of time if heat transfer,"
      write(*,*)"instead of diffusion, is the rate-limiting factor"
      write(*,*)"for contact melting."
      write(*,*)"-----------------------------------------------------"
      write(*,*)""
*
*     Prompt user inputs
      write(*,*)"Input desired time frame (sec):"
      read(*,*) tottime
      write(*,*)"Input desired total number of steps (0-300000):"
      read(*,*) numstep
      write(*,*)""
```

```
      write(*,*)"Please Wait . . . "
      write(*,*)""
*
*     Dividing the total time by the number of steps
      deltime=tottime/float(numstep)
*
*     Setting all time-variables to zero initially
      do 10 t=1,numstep
      nitithickness(t)=0
      meltthickness(t)=0
      vniti(t)=0
      xniti(t)=0
      delq(t)=0
 10   continue
*
*     Continue with user prompts
      write(*,*)"Input Initial NiTi Plate Thickness (m):"
      read(*,*) nitithickness(1)
      write(*,*)"Input Limiting Thickness for NiTi Melting (m):"
      read(*,*) thicknesslimit
      write(*,*)"Input Thermal Conductivity of NiTi (W/m.K):"
      read(*,*) conduct
      write(*,*)"Input Latent Heat of Fusion of NiTi (J/g):"
      read(*,*) latent
      write(*,*)"Input External Temperature (Degrees Celsius):"
      read(*,*) tempext
      write(*,*)"Input NiTi-L Interface Temperature (Degrees Celsius):"
      read(*,*) tempint
      write(*,*)""
      write(*,*)"Calculation in Progress . . . "
      write(*,*)""
      write(*,*)"******************************************************"
      write(*,*)"'raw.dat' and 'results.dat'"
      write(*,*)"will be generated at the end of calculations."
      write(*,*)""
      write(*,*)"See 'results.dat' for details."
      write(*,*)"******************************************************"
*
*     Opening output files
      open(unit=1,file='raw.dat',status='unknown')
      open(unit=2,file='output.dat',status='unknown')
      open(unit=3,file='results.dat',status='unknown')
*
*     Writing inputs into results.dat
      write(3,*)"Input Parameters"
      write(3,*)"~~~~~~~~~~~~~~~~~~~~~~~~~~~~~~~~~~~~~~~~~~~~~~~"
      write(3,*)"Time Frame:",tottime," seconds"
      write(3,*)"Total Number of Steps:",numstep
      write(3,*)"Initial NiTi Thickness:",nitithickness(1)," m"
      write(3,*)"Thickness Limit for NiTi Melting:",thicknesslimit," m"
      write(3,*)"Thermal Conductivity of NiTi:",conduct," W/m.K"
      write(3,*)"Latent Heat of Fusion of NiTi:",latent," J/g"
      write(3,*)"External Temperature:",tempext," Degrees Celsius"
      write(3,*)"NiTi-L Temperature:",tempint," Degrees Celsius"
      write(3,*)""
*
```

```
*     Density of NiTi (g/m3)
      density=6.5
*
*     Calculating thermal expansion at braze temperature
      cte_niti=1+(6.6E-6*tempext)
*
*     Corrected density
      correctdensity=density/(cte_niti**3)
*
*     Calculating the temperature difference
      tempdiff=tempext-tempint
*
*     Print in-calculation message
      write(*,*)""
      write(*,*)"Please wait... Calculation in progress..."
*
*     Numerical iterations
      do 20 t=1,numstep
*
*     Check if NiTi thickness limit has been exceeded
      if(meltthickness(t).lt.thicknesslimit) then
*
*     Calculating change in heat
      delq(t)=(conduct*tempdiff*deltime)/nitithickness(t)
*
*     Calculating thickness of NiTi melted
      xniti(t+1)=(delq(t)/latent)/(correctdensity*100)
      nitithickness(t+1)=nitithickness(t)-xniti(t+1)
      meltthickness(t+1)=meltthickness(t)+xniti(t+1)
*
*     Calculating the velocity of NiTi-L interface
      vniti(t+1)=xniti(t+1)/deltime
*
*     Write results to raw.dat
      write(1,*)t*deltime,delq(t),meltthickness(t),vniti(t)
*
      endif
*
      if(meltthickness(t).gt.thicknesslimit) then
*
*       Write data points for plotting into output.dat
        do 21 k=1,t,200
        write(2,*)k*deltime,delq(k),meltthickness(k),vniti(k)
21      continue
*
*     Print important information with regards to Nb exhaustion
      write(3,*)"Information Associated With Nb Exhaustion"
      write(3,*)"~~~~~~~~~~~~~~~~~~~~~~~~~~~~~~~~~~~~~~~~~~~~~~~~~~~~~~~"
      write(3,*)"Time:",(t-1)*deltime," seconds"
      write(3,*)"Thickness of NiTi Melted:",meltthickness(t-1)," m"
      write(3,*)"Final Interface Velocity:",vniti(t-1)," m/s"
*
*     Print End-of-Program message
      write(3,*)""
      write(3,*)"Files Generated"
      write(3,*)"**************************************************"
```

```
      write(3,*)"'raw.dat', 'output.dat', and 'results.dat'"
      write(3,*)" have been generated."
      write(3,*)""
      write(3,*)"'raw.dat' contains all time-evolution data."
      write(3,*)"Data is in the following sequence:"
      write(3,*)"Time, Change in Heat, NiTi Melt Thickness and Velocity"
      write(3,*)""
*     write(3,*)"'output.dat' contains plot-friendly data points."
*     write(3,*)"Data is in the following sequence:"
*     write(3,*)"Time (200-step interval), Change in Heat,"
*     write(3,*)"NiTi Melt Thickness and Velocity"
*     write(3,*)""
      write(3,*)"'results.dat' contains most-recent input parameters"
      write(3,*)"and calculated values."
      write(3,*)""
      write(3,*)"END OF PROGRAM"
      write(3,*)"************************************************************"
      write(3,*)""
*
*     Close output files
      close(unit=1)
      close(unit=2)
      close(unit=3)
*
      stop
*
      endif
*
 20   continue
*
      end
```

Table D-1 Input parameters for simulating the melting kinetics before the complete melting of Nb (assume rate-limited by heat transfer).

Input Parameters	**Values**
Time Frame (secs)	0.1
Total Number of Steps	50000
Initial NiTi Thickness (m)	3.175E-03
Thickness Limit for NiTi Melting (m)	9.6E-05
Thermal Conductivity of NiTi (W/m-K)	41
Latent Heat of Fusion of NiTi (J/g)	357
External Temperature (°C)	1185
NiTi-Liquid Temperature (°C)	1170

Table D-2 Results from the melting kinetics calculation (after the complete melting of Nb, assume rate-limited by heat transfer).

Results	**Values**
Thickness of NiTi Melted (m)	9.54E-06
Elapsed Time (secs)	1.12E-04

BILIOGRAPHY

Akari T., Hirose A., Uchihara M., Kohno W., Honda K., Kondh M., *Materials*, **38(428)** (1989), p478.

Alemany M. M. G., Rey C., Gallego L. J., *Journal of Chemical Physics*, **109(13)** (1998), p5175.

Alkorta J., Martínez-Esnaola J. M., Gil Sevillano J., *Acta Materialia*, **54** (2006), p3445.

Bastin G. F., Rieck G. D., *Metallurgical Transactions*, **5** (1974), p1827.

Bird R. K., Hoffman E. K., "*Evaluation of the Transient Liquid Phase (TLP) Bonding Process for Ti_3Al-Based Honeycomb Core Sandwich Structure*" in *NASA Report*, **(NASA/TP-1998-208421)**, (1998).

Broughton W. R., Hinopoulos G., "*Evaluation of the Single-Lap Joint Using Finite Element Analysis*" in *National Physical Laboratory Report*, **CMMT(A) 206** Report No. 15 (1999), p1.

Callister W. D., "Phase Transformations in Metals" in Materials Science and Engineering – An Introduction, (John Wiley and Sons, New York, 2003), p298.

Campbell C. E., Boettinger W. J., *Metallurgical and Materials Transactions A*, **31A** (2000), p2835.

Chau E. T. F., Friend C. M., Allen D. M., Hora J., Webster J. R., *Materials Science and Engineering* A, **438-440** (2006), p589.

Chuprina V. G., Shalya I. M., *Powder Metallurgy and Metal Ceramics*, **41**(1-2) (2002), p85.

Darken L. S., Gurry R. W., "*Liquids*" in *Physical Chemistry of Metals*, (McGraw-Hill, New York, 1953), p110.

Davidson M. J., Biberger M., Mukherjee A. K., *Scripta Metallurgica et Materialia*, **27(12)** (1992), p1829.

Duerig T. W., Melton K. N., Proft J. L., "*Wide Hysteresis Shape Memory Alloys*" in *Engineering Aspects of Shape Memory Alloys*, edited by T. W. Duerig, K. N. Melton, D. Stockel, C. M. Wayman, (Butterworth-Heinemann, Essex, UK, 1990), p130.

Einziger R. E., Mundy J. N., Hoff H. A., *Physical Review B*, **17**(2) (1978), p440.

Eyring H., *Journal of Chemical Physics*, **4** (1936), p283.

Firstov G. S., Van Humbeeck J., Koval Y. N., *Materials Science and Engineering A*, **378** (2004), p2.

Flegler S. L., Heckman J. W., Klomparens K. L., Scanning and Transmission Electron Microscopy: An Introduction, (Oxford University Press, New York, 1993), p192.

Flemings M. C., "*Plane Front Solidification of Polyphase Alloys*" in *Solidification Processing*, (McGraw-Hill, New York, 1974), p93.

Gale W. F., Orel S. V., *Journal of Materials Science*, **31** (1996), p345.

Gale W. F., Guan Y., *Journal of Materials Science*, **32** (1997), p357.

Getazheev K. A., Savintsev P. A., *Soviet Physics Journal*, **13**(5) (1970), p620.

Grummon D. S., Zhang J., Pence T. J., *Materials Science and Engineering A*, **273-275** (1999), p722.

Grummon D. S., Shaw J. A., Foltz J. W., *Materials Science and Engineering A*, **438-440** (2006), p1113.

Gupta C. K., Suri A. K., "*Properties and Applications of Niobium*" in *Extractive Metallurgy of Niobium*, (CRC Press, Florida, 1994), p1.

Gupta K. P., *Phase Diagrams of Ternary Nickel Alloys, Part 2 Section D2*, (Indian Institute of Metals, Calcutta, India, 1991), p163.

Hall T. A., U. S. Patent No. 5242759, 1993.

Hillert M., "*Projected and Mixed Phase Diagrams*" in *Phase Equilibria, Phase Diagrams and Phase Transformations: Their Thermodynamic Basis*, (Cambridge University Press, UK, 1998), p226.

Hirose A., Akari T., *Metals* (in Japanese), **59(8)** (1989), p61.

Honma T., "*TiNi-Based Shape Memory Alloys*" in *Shape Memory Alloys*, edited by Funakubo H., (Gordon and Breach Science Publishers, New York, 1987), p61.

Hsieh S. F., Wu S. K., *Journal of Alloys and Compounds*, **266** (1998), p276.

Hsu Y. T., Wang Y. R., Wu S. K., Chen C., *Metallurgical and Materials Transactions A*, **32(3)** (2001), p569.

Hume-Rothery W., Raynor G. V., "*The Atomic Radii and Some Physical Properties of the Elements*" in *The Structure of Metals and Alloys – 3rd Edition*, (The Institute of Metals, London, 1954), p60.

Iida T., Guthrie R. I. L., "*Surface Tension*" in *The Physical Properties of Liquid Metals*, (Claredon Press, Oxford, 1988), p134.

Iida T., Guthrie R. I. L., "*Diffusion*" in *The Physical Properties of Liquid Metals*, (Claredon Press, Oxford, 1988), p199.

Iida T., Guthrie R. I. L., "*Viscosity*" in *The Physical Properties of Liquid Metals*, (Claredon Press, Oxford, 1988), p147.

Jax V. P., *Zeitschrift für Metallkunde (in German)*, **62**(H4) (1971), p279.

Jia D., Liu W., Han M., Wang D., Dong Z., *Zeitschrift für Metallkunde*, **91** (2000), p258.

Johnson A. D., Martynov V. V., Minners R. S., *Journal de Physique IV*, **C8 (5)** (1995), p783.

Kapgan M., Melton K. N., "*Shape Memory Alloy Tube and Pipe Couplings*" in *Engineering Aspects of Shape Memory Alloys*, edited by T. W. Duerig, K. N. Melton, D. Stockel, C. M. Wayman, (Butterworth-Heinemann, Essex, UK, 1990), p137.

Krell A., Shädlich S., *Materials Science and Engineering A*, **307** (2001), p172.

Lehnert T., Crevoiserat S., Gotthardt R., *Journal of Materials Science*, **37 (8)** (2002), p1523.

Li M. G., Sun D. Q., Qiu X. M., Sun D. X., Yin S. Q., *Materials Science and Engineering A*, **424** (2006), p17.

Lieberman D. S., Wechsler M. S., Read T. A., *Journal of Applied Physics*, **26 (4)** (1955), p473.

Lindquist P. G., Wayman C. M., "*Shape Memory and Transformation Behavior of Martensitic Ti-Pd-Ni and Ti-Pt-Ni Alloys*" in *Engineering Aspects of Shape Memory Alloys*, edited by T. W. Duerig, K. N. Melton, D. Stockel, C. M. Wayman, (Butterworth-Heinemann, Essex, UK, 1990), p58.

London B., Fino J., Pelton A., Fuller C., Mahoney M., *"Friction Stir Processing of Nitinol"* in *"Proceedings of The Minerals, Metals and Materials Society Conference – San Francisco, California, USA"*, (2005), p67.

MacDonald W. D., Eagar T. W., *"Transient Liquid Phase Bonding Processes"* in *The Metal Science of Joining*, edited by Cieslak M. J., Perepezko J. H., Kang S., Glicksman M. E., (The Minerals, Metals and Materials Society, 1992), p93.

MacDonald W. D., Eagar T. W., *"Low Temperature Transient Liquid Phase Bonding of Ti-6Al-4V"* in *"Proceedings of the 3rd International Conference on Trends in Welding Research – Gatlinburg, Tennessee, USA"*, (1992), p1083.

MacDonald W. D., Eagar T. W., *Metallurgical and Materials Transactions A*, **29A** (1998), p315.

Maksimovich G. G., Lyutyi E. M., Shirokov V. V., Druzhinina I. P., Per'kova G. N., *Soviet Materials Science*, 18(2) (1982), p150.

Massalski T. B., *Binary Alloy Phase Diagrams 2nd Edition* (American Society for Metals, Metals Park, Ohio, 1990).

Matsumoto S., Tokunaga T., Ohtani H., Hasebe M., *Materials Transactions (Special issue on "Materials Science of Bulk Metallic Glasses")*, **46(12)** (2005), p2920.

Mei J., Davenport J. W., *Physical Review B*, **42(15)** (1990), p9682.

Melton K. N., *"Ni-Ti Based Shape Memory Alloys"* in *Engineering Aspects of Shape Memory Alloys*, edited by T. W. Duerig, K. N. Melton, D. Stockel, C. M. Wayman, (Butterworth-Heinemann, Essex, UK, 1990), p21.

Miyazaki S., Ohmi Y., Otsuka K., Suzuki Y., *Journal de Physique*, **43** (1982), pC4-255.

Miyazaki S., Imai T., Igo Y., Otsuka K., *Metallurgical Transactions*, **17A** (1986), p115.

Mueller M. H., Knott H. W., *Transactions of the Metallurgical Society of AIME*, **227** (1963), p674.

Munro R. G., *Journal of American Ceramic Society*, **80**(8) (1997), p1919.

Murai M., U. S. Patent No. 4952044, 1990.

Myneni G. R., Agnew S. R., American Institute of Physics Conference Proceedings, 671 (2003), p227.

Nakata Y., Tadaki T., Shimizu K., *Materials Transactions JIM*, **32** (1991), p580.

Nakata Y., Tadaki T., Shimizu K., *Materials Transactions JIM*, **32** (1991), p1120.

Nevitt M. V., *Transactions of the Metallurgical Society of AIME*, **218** (1960), p327.

Niemann J. T., Garrett R. A., *Welding Journal*, **53**(8) (1974), p351s.

Nishida M., Wayman C. M., Honma T., *Metallurgical Transactions*, **17A** (1986), p1505.

Oliver W. C., Pharr G. M., *Journal of Materials Research*, **7**(6) (1992), p1564.

Otsuka K., Wayman C. M., *"Introduction"* in *Shape Memory Materials*, edited by Otsuka K., Wayman C. M., (Cambridge University Press, Cambridge, UK, 1998), p1.

Otsuka K., Ren X., *Progress in Materials Science*, 50 (2005), p511.

Owczarski W. A., *Welding Journal*, **42**(2) (1962), p78s.

Ozeki K., Yuhta T., Aoki H., Fukui Y., *Bio-Medical Materials and Engineering*, **13**(3) (2003), p271.

Piao M., Miyazaki S., Otsuka K., *Materials Transactions JIM*, **33(4)** (1992), p346.

Piao M., Miyazaki S., Otsuka K., Nishida N., *Materials Transactions JIM*, **33(4)** (1992), p337.

Piao M., Otsuka K., Miyazaki S., Horikawa H., *Materials Transactions JIM*, **34(10)** (1993), p919.

Plietsch R., Ehrlich K., *Acta Materialia*, **45**(6) (1997), p2417.

Porter D. A., Easterling K. E., "*Solidification*" in *Phase Transformations in Metals and Alloys – 2nd Edition (Reprinted)*, (Nelson Thornes, Cheltenham, UK, 2001), p185.

Prima S. B., *Metally*, **5** (1992), p120.

Prima S. B., Tret'yachenko L. A., Petyukh V. M., *Powder Metallurgy and Metal Ceramics*, **34** (1995), p155.

Proft J. L., Duerig T. W., "*The Mechanical Aspects of Constrained Recovery*" in *Engineering Aspects of Shape Memory Alloys*, edited by T. W. Duerig, K. N. Melton, D. Stockel, C. M. Wayman, (Butterworth-Heinemann, Essex, UK, 1990), p115.

Rhines F. N., "*Ternary Four-phase Equilibrium, Class I*" in *Phase Diagram in Metallurgy – Their Development and Application*, (McGraw-Hill, New York, 1956), p159.

Rhines F. N., "*Ternary Four-phase Equilibrium, Class II*" in *Phase Diagram in Metallurgy – Their Development and Application*, (McGraw-Hill, New York, 1956), p176.

Rhines F. N., "*Ternary Four-phase Equilibrium, Class III*" in *Phase Diagram in Metallurgy – Their Development and Application*, (McGraw-Hill, New York, 1956), p186.

Rhines F. N., "*Congruent Transformation in Ternary Systems*" in *Phase Diagram in Metallurgy – Their Development and Application*, (McGraw-Hill, New York, 1956), p193.

Roy A. K., Chhabra R. P., *Metallurgical Transactions A*, **19A** (1988), p273.

Saburi T., Tatsumi T., Nenno S., *Journal de Physique*, **43** (1982), pC4-261.

Saburi T., Yoshida M., Nenno S., *Scripta Metallurgica*, **18** (1984), p363.

Savintsev P. A., Akhkubekov A. A., Getazheev K. A., Rogov V. I., Savvin V. S., Soviet Physics Journal, 14(4) (1971), p467.

Schetky L. M., Wu M. H., "*Issues in the Further Development of Nitinol Properties and Processing for Medical Device Applications*" in "*Proceedings of the Materials and Processes from Medical Devices Conference, Anaheim, California*", (2004), p271.

Schlossmacher P., Haas T., Schuessler A., *Journal of Physics Colloquium*, **C5 (Supplementary)** (1995), p251.

Schwartz M. M., "*Vacuum Brazing*" in *Modern Metal Joining Techniques*, (John Wiley and Sons, New York, 1969), p278.

Seki M., Yamamoto H., Nojiri M., Uenishi K., Kobayashi K. F., *Journal of Japan Institute of Metals*, **64(8)** (2000), p632.

Shaw J. A., Grummon D. S., Foltz J. W., *Smart Materials and Structures*, **16** (2007), p S170.

Shiue R. H., Wu S. K., *Materials Transactions*, **46(9)** (2005), p2057.

Sinclair C. W., Purdy G. R., Morral J. E., *Metallurgical and Materials Transactions A*, **31A** (2000), p1187.

Sisco F. T., Epremian E., "*Physical and Mechanical Properties*" in *Columbium and Tantalum*, (John Wiley and Sons, New York, 1963), p198

Sneddon I. N., *International Journal of Engineering Science*, **3** (1965), p47.

Su C. Y., Chou C. P., Wu B. C., Lih W. C., *Materials Science and Technology*, **15** (1999), p316.

Surbled P., Clerc C., Le Pioufle B., Ataka M., Fujita H., *Thin Solid Films*, **401 (1-2)** (2001), p52.

Tuah-Poku I., Dollar M., Massalski T. B., *Metallurgical Transactions A*, **19A** (1988), p675.

Vadovic C. J., Colver C. P., *Physical Review B*, **1(12)** (1970), p4850.

Van der Eijk C., Fostervoll H., Sallom Z. K., Akselsen O. M., "*Plasma Welding of NiTi to NiTi, Stainless Steel and Hastelloy C276*" in "*Proceedings for ASM Materials Solutions 2003 Conference, Pittsburgh, Pennsylvania*", (2003).

Wang G., Zhou Z., Zhang C., *Acta Metallurgica Sinica (in Chinese)*, **41**(7) (2005), p703.

Wechsler M. S., Lieberman D. S., Read T. A., *AIME Transactions*, **197** (1953), p1503.

Wilcox B. A., Allen B. C., *Journal of the Less-Common Metals*, **13** (1967), p186.

Winzek B., Sterzl T., Quandt E., *"Proceedings of the International Conference on Solid-State Sensors and Actuators, Transducers '01 – Eurosensors XV, Munchen, Germany"*, (Springer-Verlag, Berlin, Heidelberg, 2001), p706.

Wollants P., De Bonte M., Roos J. R., *Z Metallkunde*, **70** (1979), p113.

Wu M. H., "*Fabrication of Nitinol Materials and Components*" in "*Proceedings for International Conference on Shape Memory and Superelastic Technologies, Kunming, China*", (2001), p285.

Yan P., Wallach E. R., *Intermetallics*, **1** (1993), p83.

Yang G., Hao S., *Journal of Alloys and Compounds*, **297** (2000), p226.

Yang T. Y., Shue R. K., Wu S. K., *Intermetallics*, **12** (2004), p1285.

Yung K. C., Zhu H. H., Yue T. M., *Smart Materials and Structures*, **14** (2005), p337;

Zadno G. R., Duerig T. W., "*Linear Superelasticity in Cold-Worked Ni-Ti*" in *Engineering Aspects of Shape Memory Alloys*, edited by T. W. Duerig, K. N. Melton, D. Stockel, C. M. Wayman, (Butterworth-Heinemann, Essex, UK, 1990), p21.

Zhang C. S., Zhao L. C., Duerig T. W., Wayman C. M., *Scripta Metallurgica*, **24 (9)** (1990), p1807.

Zhao L. C., Duerig T. W., Justi S., Melton K. N., Proft J. L., Yu W., Wayman C. M., *Scripta Metallurgica*, **24 (2)** (1990), p221.